Dynamics of Stratospheric Sudden Warming Events: Data Analysis and Modelling

Submitted by

Robin Nicholas Beaumont

to the University of Exeter as a thesis for the degree of Doctor of Philosophy in Mathematics, May 2014.

I certify that all material in this thesis which is not my own work has been identified and that no material is included for which a degree has previously been conferred upon me.

.....

Robin Nicholas Beaumont

Abstract

The polar vortex is a large scale cyclone located in the middle atmosphere near to the planet's geographic poles. These vortices form during the hemispheric winter and break down in the spring of the following year. They may also break down in mid winter, causing a sudden stratospheric warming event (SSW). The vortex is thought to be preconditioned leading up to these warming events, resulting in the breakdown of the vortex. Integral diagnostics are used to investigate the stripping of air from the vortex as part of this preconditioning.

Contour diagnostics of mass and circulation are calculated using ERA-40 reanalysis data for the stratosphere. The edge of the vortex is easily identifiable in these diagnostics as a high gradient of Ertel's potential vorticity (PV), and the warming events are also clearly visible. From these the amount of air removed from the vortex is determined from the balance equation of the mass integral. These terms show that there are significant amounts of air removed from the vortex, with several stripping events identifiable in them through the winter, especially in those during which a major sudden warming event occurred. These stripping events can be seen in corresponding PV maps, where tongues of PV can be seen to be stripped from the vortex and mixed into the surrounding surf zone of turbulent air.

From the integral diagnostics a Lagrangian measure of the meridional circulation in the stratosphere is also calculated.

In the final part of the thesis a shallow water model is used to investigate a quantitative link between forcing and the amount of stripping of the vortex. It is found that when the forcing is large enough there is significant stripping of mass from the vortex. This does not lead to SSWs in all cases, and the total amount of

stripping is not found to be proportional to the maximum amplitude of the forcing.

Acknowledgements

I would like to thank Dr. Frank Kwasniok and Prof. John Thuburn for their help and suppport thoughout the course of my PhD. Their supervision was invaluable. I'm also very grateful to my examiners, Prof. Mitchell Berger and Prof. John Methven, for managing to wade their way through my thesis, especially in its uncorrected state.

I would also like to thank Anna-Lujz for putting up with my moaning and constant pessimism, and Toffee for providing the optimism.

Contents

List of Figures

List of Tables

Chapter 1

Introduction

1.1 The Polar Vortex

The stratosphere is the part of the Earth's atmosphere which lies above the troposphere, between the tropopause and the stratopause. It typically lies between 10km and 50km in altitude.

During the winter, the pole is in a state of perpetual polar night. This causes a strong temperature gradient between the polar region and the tropics due to the difference in radiative heating between the two regions. The southern winter is colder than that of the north, so is closer to radiative equilibrium (Andrews et al., 1987). The negative temperature gradient between the tropics and the pole gives rise to strong westerly winds in the stratosphere due to the mechanism of thermal wind balance. The thermal wind equation, and the negative gradient of temperature give

$$\frac{\partial u}{\partial z} > 0 \tag{1.1}$$

meaning that the strength of the westerly winds increase with height, with the strongest winds being encountered at the top of the vortex.

This region of strong westerly winds makes up the 'polar night jet', which is commonly referred to as the polar vortex.

The structures of the Northern and Southern hemispheric vortices differ from each other. As well as the southern vortex being colder, it is larger in size than its

northern counterpart (Schoeberl et al., 1992).

The vortex extends from the lower stratosphere ($\sim$ 20 km) up to the stratopause ($\sim$ 50 km). It forms at the start of the hemispheric winter and breaks down again in the following spring as the polar night draws to a close, and so the temperature gradient driving the winds of the polar night jet starts to wane.

The movement of air within the stratosphere is predominantly horizontally layer-wise. It is this mainly horizontal mixing, as well as the stratified nature of the temperature profiles of the air in the stratosphere, from which it derives its name. Consequently, in addition to height and pressure, another useful vertical quantity is that of potential temperature. Potential temperature is defined as

$$\theta = \left(\frac{p}{p_0}\right)^{-\kappa} T \tag{1.2}$$

where T is temperature, p is pressure, p_0 is a constant reference pressure, generally taken to be 1000 hPa, and $\kappa = \frac{R}{c_p}$ is a constant defined as the gas constant R divided by the specific heat capacity at constant pressure c_p. The physical interpretation of this quantity is the temperature at which the parcel of air would be if it was adiabatically brought to the reference pressure p_0.

Potential temperature is related to entropy through the equation

$$S = c_p \ln \theta + C \tag{1.3}$$

where S is entropy and C is a constant of integration. This means that, as the radiative heating is weak and slow in the stratosphere, isentropic surfaces, which correspond to surfaces of potential temperature, are approximately equal to material surfaces.

In studies of the dynamics of the polar vortex, a useful quantity to study is Ertel's Potential Vorticity (PV). The PV is defined as

$$Q = \frac{\boldsymbol{\zeta} \cdot \nabla \theta}{\rho} \tag{1.4}$$

where $\boldsymbol{\zeta}$ is the absolute vorticity, ρ is density and θ is potential temperature as defined above. The principle of potential vorticity inversion states that given the isentropic distribution of PV, the mass below isentropic surfaces and the potential

temperature on the lower boundary, the remaining dynamical fields can be derived (McIntyre, 2003). This makes PV a useful quantity for examining dynamical flows.

Another attractive feature of PV is that, in a flow where the motion is adiabatic $\left(\frac{D\theta}{Dt} = 0\right)$ and in which there is an absence of friction, then the PV is materially conserved, that is,

$$\frac{DQ}{Dt} = 0. \tag{1.5}$$

In the winter stratosphere this condition is approximately true on timescales of 6 to 10 days, meaning that on these timescales the PV can be seen as being a materially conserved quantity. For longer timescales the effects of radiative heating must be taken into account. This is especially true in the higher levels of the stratosphere.

This makes PV on isentropic surfaces an extremely useful quantity in examining the stratosphere. Maps of this quantity make the vortex clearly visible as an area of high PV located over the pole. Figure 1.1 shows a typical undisturbed vortex which is clearly visible in the centre of the figure.

The edge of the polar vortex is characterised by anomalously high gradients of PV. This edge of the undisturbed vortex typically lies at latitudes in the region of 70 degrees in the winter hemisphere.

The area surrounding the vortex from the vortex edge to the subtropics, roughly 20 degrees latitude, is an area of horizontally well mixed air referred to as the surf-zone (McIntyre and Palmer, 1983, 1984). The surf zone is well mixed due to the breaking of planetary waves which occurs in this region. This breaking of waves has been likened to the breaking of waves on a beach, hence the term surf zone.

1.2 Stratospheric Sudden Warmings

Stratospheric Sudden Warmings (SSWs) are events which occur in the winter stratosphere, where the strong zonal-mean zonal westerly winds weaken or change direction. This is accompanied by an increase in the stratospheric temperature by tens of degrees. The generally accepted definition of an SSW is the definition given by the World Meteorological Organisation (WMO) in which an SSW is said to have

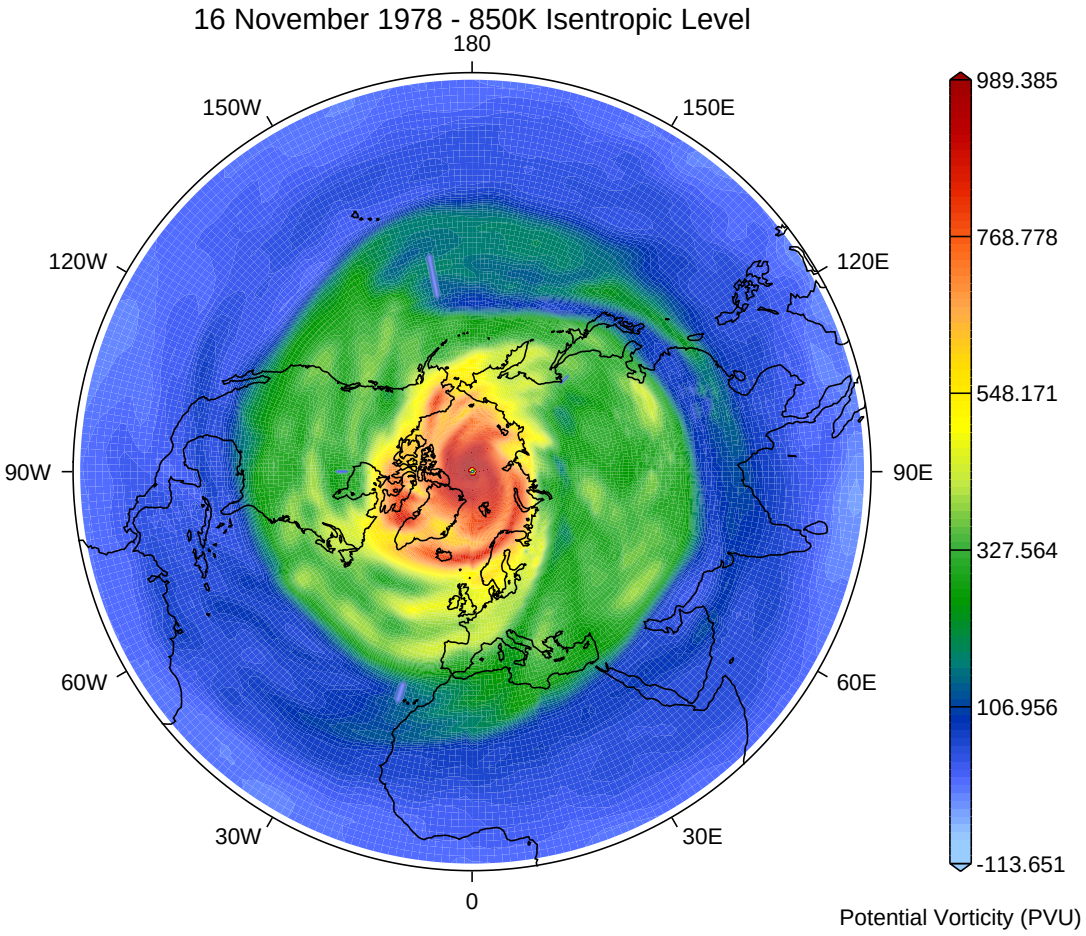

Figure 1.1: Potential vorticity on the 850 K isentropic surface for 16th November 1978.

occurred when the zonal-mean of the temperature at 10hPa increases between 60° and 85° in the winter hemisphere (Andrews et al., 1987).

Stratospheric sudden warmings are divided into 4 distinct categories.

The first of these categories is *Major Warming*. These occur when the zonal-mean temperature at or below 10 hPa between 60 and 85 degrees in the winter hemisphere increases, as in the WMO definition of an SSW. In major warmings this is accompanied by a reversal of the zonal-mean zonal wind in the same area. A feature of major warmings is that there is a breakdown of the polar vortex where

the circulation becomes highly asymmetric. This is visible in maps of PV and is accompanied by a rise in winter polar stratospheric temperatures by up to 60 K. These events occur in both the Northern and Southern hemispheric vortices.

Canadian Warmings are similar to major warmings, however, unlike major warmings they occur only in the Northern hemisphere with no counterpart in the Southern vortex. Canadian warmings also differ from major warmings in that the vortex is displaced from the pole when the Aleutian cyclone moves north (Labitzke, 1977; Labitzke and Naujokat, 2000). This subcategory of warming is distinct from major warmings because, while they can lead to a reversal of the temperature gradient between 60 and 80 degrees and a reversal of the zonal winds over the pole, the vortex itself remains intact.

Warmings which do not lead to a reversal of the zonal-mean zonal wind are referred to as *Minor Warmings*. These warmings occur much more frequently than major warmings and occur in both the Southern and Northern vortices. They also do not feature the dramatic breakdown of the vortex which is seen in major warmings.

The last category of warming is that of *Final Warmings*. These warmings are characterised by the final breakdown of the vortex, and occur at the end of the life of the vortex in the hemispheric spring. Following final warmings the westerlies of the vortex are replaced by the summer easterly winds which are dominant throughout the hemispheric summer. They too have a reversal of the zonal-mean zonal wind, although the vortex does not return to its pre-warming state as it does with mid-winter warmings. Final warmings vary in intensity, and can be classed as either major or minor warmings.

The reason for the stratospheric temperature increase from which the events derive their name is descent of air near the pole. This descending air then warms adiabatically as illustrated by the accompanying descent of isentropic surfaces.

Several minor warmings can occur over the course of a Northern hemisphere winter but major warmings occur less regularly. There have been winters noted where two major warmings have occurred and between 1989 and 1998 there was a period

of 9 consecutive winter periods in which no major warmings were noted. These were followed by 4 winters of high stratospheric activity (Charlton and Polvani, 2007; Labitzke et al., 2005). Despite this, major warmings occur at an average rate of 0.62 per year in the Northern hemisphere. September 2002 saw the only observed major warming to have occurred in the Southern hemispheric vortex.

Major warmings are often divided into two sub-classes. These are referred to as 'Wave-1' and 'Wave-2' due to the dominant zonal wavenumber 1 or 2 vertically propagating Rossby waves, visible in the geopotential height fields during the warming. Wave 1 events, also called *Displacement events*, are characterised by a displacement of the vortex from the pole at the time of the warming followed by its return to the pole as the vortex recovers. Wave 2 events are also referred to as *Splitting events* as they are characterised by a splitting of the vortex into 2 distinct smaller sub-vortices, sometimes referred to as 'daughter vortices'. As the vortex recovers one of these sub-vortices breaks down as the other strengthens and recovers to the pre-warming state. The dynamics of the two types of major warming are different, with vortex splitting events being mainly barotropic and vortex displacements mainly baroclinic (Esler and Matthewman, 2011; Matthewman and Esler, 2011). The biggest differences between the two classes of major SSW are visible after the date of the warming. Vortex splits are in general stronger than displacements with larger wind and temperature anomalies observed (Miller et al., 2013).

Rossby waves were first connected with sudden warmings by Matsuno (1971). The reason for the rarity of SSWs in the southern hemisphere is thought to be the smaller amplitude of propagating Rossby waves disturbing the vortex in the region.

The vortex can take a considerable time to return to its climatological state following the breakdown, up to several months in some cases (Hitchcock et al., 2013). This period is longer for a split vortex than it is for a displaced vortex (Charlton and Polvani, 2007). It has been noted that the disturbance associated with splits is more barotropic, whereas that of displacements is more baroclinic (Matthewman and Esler, 2011; Matthewman et al., 2009). These disturbances

disrupt the lower stratospheric vortex more efficiently in the case of splits, which gives a possible explanation of the longer lived weak vortex period following these events (Hitchcock et al., 2013).

In the period of time leading up to the occurrence of major warmings it has been suggested that a certain "preconditioning" of the vortex takes place, along with the presence of a wave number 1 forcing (Labitzke, 1981; Limpasuvan et al., 2004), allowing the vortex to break down and an SSW to take place. This preconditioning is discussed further in section 1.4.

There have recently been several attempts to classify all winters for which data is available as featuring either a displacement event, a splitting event or neither of these (Charlton and Polvani, 2007; Labitzke and Naujokat, 2000; Mitchell et al., 2013; Seviour et al., 2013). Some of these studies used the WMO definition to identify the occurrence of an SSW, while others have tried to refine the definition because zonal-mean measures can often 'smear' and miss features which are not zonally symmetric. Several of the authors have also not made the distinction between major warmings and Canadian warmings, instead including them with displacement events. Here the classifications of major warmings into only either splitting or displacement as in Charlton and Polvani (2007) and Mitchell et al. (2013) will be used.

The classifications of Charlton and Polvani (2007) use the WMO definition to identify when an SSW has occurred. They are then classified as splits if there are two vortices present and the larger one has less than twice the circulation of the smaller, otherwise it is classified as a displacement event. In contrast Mitchell et al. (2013) used a vortex following coordinate to detect periods when the vortex was displaced from the pole or split into two. The classification by Mitchell et al. (2013) identifies more events than Charlton and Polvani (2007), and some events were classified as different types in each study. Despite this most of the dates of the onsets of warmings were similar between the two, with only several days difference in most common events. In this thesis the classifications and dates of Charlton and Polvani (2007) will primarily be used, but those of Mitchell et al. (2013) will

occasionally be referred to for comparison.

1.3 Vortex Erosion

The vortex edge acts as a barrier to mixing of air, largely isolating the air within the vortex from that of the surrounding surf zone. This means that the air within the vortex is chemically distinct from that outside. In particular the vortex is associated with anomalously low ozone concentrations, with the southern vortex exhibiting larger anomalies than the northern vortex.

While the vortex edge acts as a barrier to transport of air from the cold area within the vortex to the warmer air of the surf zone there is still some transport of air across the vortex edge through the ejection of filaments of high PV air from the vortex into the surf zone. These filaments then become mixed into the air of the surf zone, steepening the PV gradient and increasing the mixing barrier at the edge (McIntyre and Palmer, 1983, 1984; Waugh et al., 1994).

The process causing this stripping of filaments of vortex air is thought to be the upward propagation of Rossby waves; these waves originate in the troposphere and propagate upward into the stratosphere where they break, pulling tongues of air from the vortex edge as they do so (McIntyre and Palmer, 1983, 1984, 1985; Waugh et al., 1994). As the PV gradient on the edge of the vortex increases the vortex becomes more resistant to this wave breaking process and therefore undergoing less filamentation under weak forcing amplitudes. This process of stripping of the vortex is also thought to be the process under which the vortex becomes preconditioned in the lead up to SSW events.

As the vortex becomes eroded and the edge of the vortex sharpens a so called 'PV step' develops (see Dritschel and McIntyre (2008) their Fig. 1) where the high PV gradients of the vortex edge and the subtropical edge of the surf zone are contrasted by the relatively shallow gradients at the vortex centre and the surf zone itself.

There have also been observations showing that air near to the centre of the vortex is moved toward the vortex edge, meaning that air from deep within the

vortex and not just close to the edge can become mixed into the surf zone. This air then appears to be replaced by downwelling of air from higher altitudes within the vortex (Waugh et al., 1994). Consequently a significant proportion of the air within the vortex may be ejected without a significant loss of mass within the vortex.

There have been several numerical simulations of the vortex, where an initial vortex is disturbed in an attempt to investigate vortex erosion. Several of these studies use simulated wave like forcing by imposing a wave like orography on the bottom boundary (eg. Juckes, 1989; Juckes and McIntyre, 1987). Others embedded a vortex within an external straining flow, simulating erosion of the vortex by another adjacent vortex (eg. Legras and Dritschel, 1993; Legras et al., 2001). These simulations show filamentation on the vortex edge similar to that seen in high resolution analyses and aircraft observation flights, and show what may be happening at scales smaller than that resolvable in analysis datasets.

While the erosion of model vortices has been quantified in several studies, the pattern and amount of stripping in the real polar vortex has not been identified. One of the main aims of this thesis is the quantification of this stripping from observational data.

In chapter 5 a model will also be used to attempt to find a quantitative link between forcing and the erosion of the vortex.

1.4 Preconditioning of the Polar Vortex

Preconditioning of the polar vortex is the process of making the vortex susceptible to SSWs. The preconditioning of the vortex prior to the onset of SSWs is not well understood. It is thought, though, that Rossby waves play an important role in this preconditioning.

There are several theories of how the vortex might become preconditioned allowing an SSW to occur. One of these says that as Rossby waves propagate upward they increase in amplitude until reaching a critical level when they break. This then causes strong mixing which reverses the temperature gradient and the zonal-mean wind become easterly. These zonal-mean easterlies inhibit the upward propagation

of waves causing them to break at lower altitudes, which in turn causes the easterlies to propagate downward as the SSW progresses (eg. Esler and Matthewman, 2011; Matthewman and Esler, 2011).

As the PV gradient at the edge of the polar vortex becomes sharpened it acts as a wave guide for the propagation of Rossby waves. These waves propagate along gradients of PV, and as the PV gradient increases the waves become focused poleward, allowing them to more easily affect the polar vortex as they propagate to higher altitudes. A diagnostic for this is the so called 'refractive index' (Butchart et al., 1982), which is a measure of the equatorward refraction of these waves.

Another theory is the weakening of the vortex due to erosion. This is similar to the break down of a model vortex when placed inside an external straining flow once it reaches some critical value (e.g. Legras et al., 2001). In this experiment, filaments of air are stretched and pulled from the model vortex, eroding it until it finally breaks down. The air that is moved out of the polar vortex may take the form of filaments of PV being pulled from the vortex in a similar way, resulting in the preconditioning of the vortex prior to a sudden warming event, such as observed by Charlton and Polvani (2007).

1.5 Interaction of the Stratosphere and Troposphere

While much of the attention in the study of SSWs is focused on the stratosphere, the effects of these anomalies, despite their name, are not confined to the stratosphere. At the time of the stratospheric warming and reversal in zonal winds, a corresponding cooling can be observed in the mesosphere (though the systematic zonal wind signal here is not known), and a warming of the thermosphere. Coinciding events have also been observed as high as the ionosphere (eg Andrews et al., 1987; Zülicke and Becker, 2013).

Several studies have also identified mesospheric precursors to SSWs in several events, between 2 and 10 days prior to the onset of the warming in the stratosphere

(eg Zülicke and Becker, 2013).

Of particular interest in this atmospheric coupling around the time of SSWs is the effect that SSWs have on the circulation of the troposphere. Understanding how these interactions and the intensity of SSWs are affected by climate change, as well as a better understanding of the onset of SSWs, are of importance for prediction of tropospheric weather systems.

The role of upward propagation of Rossby waves, originating from the troposphere, into the stratosphere in the breakup of the polar vortex was first identified by Matsuno (1971). Despite this mechanism having been well understood for a long time, until recently there was very little understanding of the effects of the stratosphere on the troposphere, particularly during stratospheric warming events. Over the last two decades there has been much interest in the dynamical relationship between the stratosphere and the troposphere, in particular what effect stratospheric anomalies such as SSWs have on tropospheric weather as well as the effect that climate change will have on both the interactions and the strength and frequency of the anomalies. Several studies (Baldwin and Dunkerton, 2001, 1999; Mitchell et al., 2013; Thompson and Wallace, 2001) have identified a propagation of anomalies in the northern annular mode (NAM) downward in altitude from the stratosphere to the troposphere following certain warming events. The NAM is a measure of the variability from the climatological mean of the geopotential. In the stratosphere the NAM can be interpreted as a measure of the strength of the vortex, so negative NAM values coincide with times during which the vortex is weak, ie. SSW events.

The propagation of these signals associated with stratospheric anomalies into the troposphere has been observed to have effects on tropospheric circulation, such as affecting the intensity and locations of storms, increasing the probability of cold spells over Northern Europe and an increase in tropospheric blocking at high latitudes (Thompson and Wallace, 2001; Tomassini et al., 2012; Woollings et al., 2010).

The effects and strength of the propagation of the signals down to the tro-

posphere is not uniform between displacement events and splitting events. The signals which can be seen in the troposphere following SSW events depend on the criteria used both to identify the occurrence of an SSW and to classify the warming as a splitting or a displacement. There are some differences between the two types of events which are common to the classifications, however. For example, splitting events seem to have a longer lasting influence on the troposphere than displacement events. Splitting events also seem to have a stronger influence on the troposphere, with the corresponding tropospheric signal in the NAM lasting for a period of roughly 60 days following the onset of the SSW.

Using the criteria of Charlton and Polvani (2007), Cohen and Jones (2011) found that the tropospheric signal following splittings and displacements was similar. The sea level pressure anomalies for both types of event showed a positive anomaly over the arctic with a corresponding negative anomaly over the ocean basins. They did find systematic differences in the signal observed in the troposphere prior to the onsets of the two types of event. The main features of vortex displacements are a strengthened Siberian high pressure anomaly and a corresponding increased Aleutian low. Splitting events mainly show high pressure anomalies across mid latitudes of the Northern Pacific and an equatorward shift in the main storm tracks.

The criteria of Mitchell et al. (2013) found that the largest signal seen in the troposphere prior to the onset of the warming was seen before displacement events, and the effects of the two types of events differed. For example displacements seem to result in cold spells over the high latitudes of Northern America, while splitting events result in increased blocking events over the Atlantic and Pacific basins.

While these coinciding signals across different sections of the atmosphere have been well observed, the mechanism by which the stratospheric anomalies affect the troposphere is not fully understood.

Several theories for the mechanism by which these stratospheric anomalies are able to propagate into the troposphere have been suggested. One such theory is that of reflection of upward propagating waves from the troposphere when wave reflecting surfaces form in the stratosphere (Perlwitz and Harnik, 2003). The effect

of stratospheric shear-modulated eddies on the downward propagation of the NAM has also been suggested as another method by which the anomalies could travel downward from the stratosphere (Wittman et al., 2007).

It is known that stratospheric anomalies in PV can affect the height of the tropopause, with negative PV anomalies resulting in a lowered tropopause and positive anomalies corresponding to a tropopause of increased height (Ambaum and Hoskins, 2002). This means that when the vortex moves from being located over the pole, such as a displaced or a split vortex, the tropopause at the pole will be lowered, while that in the region of the vortex (or vortices in the case of a split) will be raised. The exact location and strength of the vortex/vortices is an important factor in the influence which it/they may have on the tropopause height in this case, and may be important in understanding the nature of the stratospheric effects.

It is likely that the downward propagation of the effects of SSWs into the troposphere is governed by a combination of these mechanisms.

This means that understanding the onset of SSWs is important for prediction of tropospheric weather conditions over the hemispheric winter.

1.6 Diagnostics

Various diagnostics of the flow in the stratosphere have been used to investigate the dynamics and structure of the vortex, especially around the time of the onset of SSW events. The simplest of these diagnostics involves taking the Eulerian zonal-means of various quantities of interest such as zonal-mean zonal wind, which is used in the WMO definition of sudden warmings, as well as the mean meridional circulation.

The Lagrangian view of a flow looks at the motion of a fluid following individual parcels of fluid. This is contrasted with the Eulerian description which looks at the motion of fluid parcels through points in space.

The transformed Eulerian mean (TEM) can give a slightly more Lagrangian view of the stratospheric circulations. The TEM can be thought of as the inter-

action between a zonally symmetric flow and the action of eddies (Andrews et al., 1987). The eddy flux term in the TEM equations ($\nabla \cdot \mathbf{F}$ where $\mathbf{F}$ is the Eliassen-Palm (EP) flux) can be related to the wave activity ($\mathcal{A}$) and the diabatic and frictional effects (D) through the approximate equation

$$\frac{\partial \mathcal{A}}{\partial t} + \nabla \cdot \mathbf{F} \approx D. \tag{1.6}$$

However the use of Eulerian mean based diagnostics can be unreliable, blurring features which have high zonal asymmetry. This is especially true in the case of a highly disturbed vortex which is no longer centred over the pole, such as following sudden warming events. This becomes problematic when this period is the one of particular interest.

The averaging process can also cause the edge of the vortex and other sharp gradients of potential vorticity to become less well defined. Small scale features such as filaments of high PV air being mixed from the vortex into the surf zone will also be smeared out. Additionally the association between changes in circulation of the middle atmosphere and certain non-conservative processes are not well represented in Eulerian mean diagnostics (Thuburn and Lagneau, 1999).

This means that a more Lagrangian approach is needed to examine the stratospheric circulation in a more reliable way. The modified Lagrangian mean (MLM) approach is able to overcome many of the disadvantages of the Eulerian approaches, though this does come at the expense of ease of calculation of some of the diagnostics. MLM diagnostics are defined as the integral over an area bounded by a material contour

$$\int_S \eta \, \mathrm{d}S \tag{1.7}$$

where S is the surface bounded by the contour, often taken to be PV on surfaces of constant potential temperature.

Several modified Lagrangian mean diagnostics have been examined for model data, such as the mass within a PV contour, and the circulation around the contour (eg Nakamura, 1995; Thuburn and Lagneau, 1999). These Lagrangian diagnostics are able to better capture quantitatively the evolution of the vortex over the course

of the winter, such as changes in area and mass. They are also able to capture the PV gradient of the vortex edge and separate it from the surf zone, as these diagnostics give a clear view of the vortex in PV space, overcoming one of the main disadvantages of the Eulerian diagnostics.

The information obtained from Eulerian zonal-mean diagnostics was compared to that obtained from the Lagrangian diagnostics by Thuburn and Lagneau (1999) in a two dimensional shallow water model vortex. It was found that the Eulerian mean diagnostics become dominated by transient reversible PV deformation. The Eulerian diagnostics also fail to differentiate between small scale PV mixing and large scale eddies. Conversely the Lagrangian diagnostics give a much better picture, displaying a clear view of the sharp gradients of PV at the vortex edge. The Lagrangian diagnostics were also used to define a reference state which is directly comparable to the Eulerian diagnostics with the difference that it only evolves through friction, diabatic heating and irreversible PV mixing. This means that it is not changed by reversible perturbations to the flow. The Lagrangian diagnostics therefore give a much better picture of what is happening within the vortex and at the edges than the Eulerian mean diagnostics do.

Only some of these diagnostics have been applied to observational data for the real wintertime vortex. In particular the time evolution of the mass within a PV contour can give information about how much air is removed from the vortex when tongues of air are pulled into the surf zone and mixed into the surrounding area. This has not so far been used to give a quantitative estimate of how much air is removed from the vortex, and how often, in the lead up to SSW events.

It is important to note that integral diagnostics such as equivalent latitude (Butchart and Remsberg, 1986) and mass and circulation integrals (Thuburn and Lagneau, 1999) give information about total vortex area, and are not able to give any information about whether a particular warming event is a displacement or a splitting event. This is because they take into account only PV values; in the case of a splitting event they take the sum of the two separate vortices. It is therefore important to consider the diagnostics in addition to the PV maps of the vortex to

describe a full picture of the state of the vortex.

These diagnostics have been widely applied to model output, but because they cannot be calculated without knowledge of PV fields they have not been widely applied to atmospheric data. In the first part of this thesis MLM diagnostics will be used to quantify stripping from the real vortex using the ERA-40 dataset.

1.7 Meridional Circulation in the Stratosphere

The strongest circulations in the wintertime stratosphere are the zonal winds, especially those of the polar vortex. In the meridional direction the circulation is dominated by the so called Brewer-Dobson circulation. This large scale overturning circulation is driven by breaking waves and is characterised by the upward movement of air in the tropics where tropospheric air enters the stratosphere, subsequent poleward movement of air and downward movement at the poles (Holton et al., 1995).

The Brewer-Dobson meridional circulation is driven by the breaking of atmospheric waves. Gravity waves reach a critical amplitude in the lower stratosphere of the winter pole and so break, leaving only westward propagating waves to propagate higher. As the waves beak they deposit momentum. This wave breaking and depositing of momentum in the stratosphere causes the strong winds of the polar night jet to slow. As a result the pressure gradient is no longer in balance with the Coriolis force. Consequently the air moves poleward and subsequently downward, inducing cooling of the air at the stratospheric pole. The sinking air is then replaced by poleward flow from the tropics, which in turn is replaced by upward propagating air (Shepherd, 2007).

The Eulerian mean meridional circulation and Lagrangian mean meridional circulation are very different, and in some circumstances have different signs (Dunkerton, 1978).

Several studies have looked at the Lagrangian views of the meridional circulation in the winter stratosphere, both for the Northern and Southern hemispheric vortices. Fisher et al. (1993) used a Lagrangian approach to examine the descent

of air from the mesosphere into the wintertime stratosphere in the Southern hemispheric winter of 1991. Their results were able to explain the low levels of methane in interior of the vortex, as the descent of air within the vortex means that low methane air from the mesosphere reduces the amount of methane within it.

Sutton (1994) looked at the Lagrangian circulation over the course of winter in the middle atmosphere. Tracer trajectories were computed in a global primitive-equation model to track the positions of fluid parcels over the winter period for both the Northern and Southern winters. The trajectories showed that the air within the vortex descends within both the Northern and Southern polar vortices, while the surrounding air ascends. The meridional poleward movement of air was found to be stronger in the Northern winter than in the Southern winter due to the increased wave activity in the Northern hemisphere.

The MLM integral diagnostics calculated in this thesis for the ERA-40 data will be used to calculate a Lagrangian measure of the meridional circulation in the winter stratosphere.

1.8 Thesis Summary

The main focus of this thesis is the erosion of the polar vortex in the lead up to SSW events, in particular through the stripping of tongues of air from the vortex. This erosion is studied in relation to the preconditioning of the vortex.

Chapter 2 gives a brief description of the ERA-40 dataset which is used in the following chapters.

In chapter 3 the ERA-40 dataset is used to calculate modified Lagrangian mean diagnostics of the vortex for various levels within the stratosphere. These are examined in an effort to investigate how and when tongues of air are pulled from the vortex, in particular on the lead up to major warming events.

Chapter 4 looks at the Lagrangian 'meridional circulation' relative to contours of PV to examine both the horizontal and vertical movement of air around the times of SSWs.

In chapter 5 a shallow water model is used, motivated by the findings of chapters

3 and 4 to investigate the removal of tongues of air in response to wave 1 amd 2 forcings of various amplitudes. The model SSWs produced are also compared to those seen in chapter 3.

Chapter 2

The ERA-40 Dataset

The ERA-40 dataset is a 45 year re-analysis dataset produced by the European Centre for Medium-Range Weather Forecasts (ECMWF) covering the period from September 1957 to August 2002 (Uppala et al., 2005). The dataset is useful for examining weather systems over historical periods such as the polar vortex.

2.1 ERA-40

Operational analyses are produced by assimilating observations into the forecasting model to produce an initial state. This state is then used to run the model forward in time to produce a forecast. Analyses can be thought of as our 'best estimate' of the state of the atmosphere at a given time. This means that they are potentially useful for studying the atmosphere as they represent a timeseries historical states of the atmosphere. However, the data assimilation systems used to produce these analyses are updated in order over time to get a more accurate initial state with which to begin running the forecasting model. Due to this and the fact that the forecasting system itself undergoes improvements over time, an extended timeseries of analysis data will in general feature inconsistencies over the time period. This drives a need for re-analysis datasets, where modern forecasting models and data assimilation systems are used to rerun extended historical periods using the original observational data to produce a consistent historical dataset which can be used for

historical climatological studies.

As well as improvements in the forecasting models and data assimilation systems over time the accuracy and number of global observations changes and improves. The ERA-40 dataset uses operational analyses from ECMWF, NCEP and the Japan Meteorological Agency along with data from several other institutions. A variety of observations are used in the ERA-40 dataset, including satellite observations, aircraft, balloon and radiosonde data.

The ERA-40 model is run at a T159 spectral resolution which is approximately equal to a 40km grid spacing in the horizontal direction. In the vertical direction the model uses 60 surfaces with roughly 1.5km between these surfaces in most of the stratosphere.

The main limitations of the ERA-40 dataset are the fact that the analyses show a larger amount of tropical moisture than those of observations from 1991 onward, the Brewer-Dobson circulation is too intense causing the stratospheric 'tape recorder' to run too fast, and the fact that the amount of precipitation is larger than that of evaporation (Uppala et al., 2005).

2.2 Pre-Processing

In spherical latitude-longitude grids those points near to the equator are spaced longitudinally further apart than those further from the equator. This means that there are lots of points spaced closely together near to the pole, though the latitudinal distance remains constant. In a reduced Gaussian Grid the number of grid points around each circle of constant latitude varies, with the number reducing as the distance to the pole decreases. For example the N80 reduced Gaussian Grid has 160 latitudinal coordinates, with those close to the equator having 320 longitudinal points and those closest to the pole having 18. This reduces the amount of space required for storing data, and makes the distance between the grid points more similar (though not identical) for all latitudes.

In this study data at a spectral resolution of T159 as well as data on the N80 reduced Gaussian Grid from the ERA-40 dataset are used. The data is retrieved from

the British Atmospheric Data Centre (BADC, http://badc.nerc.ac.uk/home/).

The data fields used here are primarily the potential vorticity, temperature and geopotential height fields as well as the horizontal velocity fields. These data are obtained on pressure levels at 6 hourly intervals for the period of the Northern hemispheric winter (here taken to be the 5 month period from 1st November to 31st March). The data are provided on 23 pressure levels from 1000hPa to 1hPa. PV fields on potential temperature surfaces are also used to compare the reults of the interpolation from pressure levels onto isentropic levels.

The pressure level data are pre-processed before the data analysis in chapter 3 and chapter 4 is undertaken.

The potential vorticity, geopotential height and velocity data fields are linearly interoplated from the pressure surfaces onto isentropic surfaces using the data in the temperature fields. This is done rather than using the data provided already on isentropic surfaces in the ERA-40 dataset because the highest isentropic surface provided is $\theta = 850$K. This level is far below the highest isobaric surface provided which is 1hPa, which allows much higher isentropic surfaces to be calculated.

The values of the interpolated isentropic surfaces are at 50K intervals from 450K to 1050K.

Comparing the interpolated data with those provided on the isentropic surfaces in ERA-40 shows that the two are in good agreement.

Chapter 3

Integral Diagnostics of the Polar Vortex

3.1 Introduction

Stratospheric sudden warmings (SSWs) are of interest for their effects on tropospheric weather. In many of the stronger events the signals can be seen to propagate downward and penetrate into the troposphere (Baldwin and Dunkerton, 2001; Thompson et al., 2002). It has been suggested in several studies (eg. Charlton and Polvani, 2007; Esler and Matthewman, 2011; Labitzke and Naujokat, 2000; Matthewman and Esler, 2011) that prior to the vortex undergoing splitting SSW events the vortex becomes "preconditioned" where the vortex becomes small and the magnitude of the winds decrease.

The preconditioning of the vortex is investigated here in terms of removal of air from the vortex by means of tongues of air being pulled from the vortex and wrapped up into the area of well mixed air surrounding the vortex, called the 'surf-zone'. Integral diagnostics of the vortex are calculated from ERA-40 Re-Analyses in an attempt to quantify the amount of air removed from the vortex in these stripping events. This quantification will enable us to look at the role of these stripping events in the preconditioning of the stratospheric vortex for sudden warming events and to see a) if there is any difference in the way the stripping

occurs between displacement and splitting SSWs, b) if more stripping means that an SSW is more likely and c) how much stripping occurs, and the timing of this stripping.

It was shown in Esler and Matthewman (2011); Matthewman and Esler (2011) that as the topographic forcing is increased for a model vortex the system undergoes a bifurcation from a state in which no SSW can occur into one in which a SSW does occur. This is related to the question of preconditioning of the vortex, and in particular major stripping of mass from the vortex. As mass is stripped from the vortex it is possible that a bifurcation threshold is passed, allowing the vortex to transition into a state in which a SSW may occur.

Nakamura (1995) and Thuburn and Lagneau (1999) both calculated expressions for the balance of the mass within a PV contour $Q = Q^*$ on surfaces of constant potential temperature θ, which can be expressed in terms of vertical movement of air across potential temperature surfaces and horizontal movement of air across PV contours, as well as expressions for the circulation around a PV contour. These diagnostic quantities - mass, circulation and 'stripping' term - have two desirable properties for examining stripping of the polar vortex. The first of these is that they are approximately Lagrangian invariant, meaning that they are only changed though non-conservative processes. The second is the fact that these quantities are vortex centred. Together these properties mean that the diagnostics can accurately capture features such as the sharp gradients of PV making up the vortex edge and the relatively shallow PV gradient of the adjacent surf zone, as well as the movement of air between these two regions.

In this chapter the surface integration scheme and the form of the integral diagnostics are defined in section 3.3. The timeseries of these calculated from the ERA-40 reanalysis are then examined in section 3.4 and the conclusions from these are examined in section 3.5.

3.2 Potential Vorticity

Potential vorticity is often used as a diagnostic quantity in the study of the atmosphere, and in particular the polar vortex, since it is an approximately material invariant quantity which may only be changed by diabatic, frictional or mixing processes. In finite resolution data these processes include those occurring at unresolved scales. Due to the fact that these effects take place on timescales larger than those of potential vorticity advection, PV is approximately conserved on timescales of 6 to 10 days (Matthewman, 2009). The isentropic distribution of potential vorticity is an extremely useful quantity for studying flows such as the polar vortex. Given this quantity along with the mass under each constant θ surface and the distribution of θ on the lower boundary, the potential vorticity invertibility principle states that all the dynamical information for the flow is able to be diagnosed, such as wind fields, geopotential heights, temperature fields etc. (eg. McIntyre, 2003). This means that for balanced flows the potential vorticity field holds information about all the dynamical fields of the flow at any instant in time.

Also, looking at potential vorticity fields plotted on isentropic surfaces it is easy to identify the polar vortex from the surrounding surf zone (see Figure 3.17 for example), as it appears as a large positive area of potential vorticity located over the winter pole. In general, isentropic potential vorticity maps are very useful for making dynamical processes easier to identify (Hoskins et al., 1985).

Ertel's Potential Vorticity (PV) is defined as

$$Q = \frac{(\boldsymbol{\zeta} + 2\boldsymbol{\Omega}) \cdot \nabla\theta}{\rho} \tag{3.1}$$

where $\boldsymbol{\zeta}$ is the relative vorticity, $\boldsymbol{\Omega}$ is the angular velocity vector, θ is potential temperature and ρ is density (Ertel, 1942). In spherical coordinates and using the hydrostatic approximation this can then be expressed as

$$\begin{aligned} Q = &\frac{g}{a\cos\phi}\frac{\partial v}{\partial p}\frac{\partial\theta}{\partial\lambda} - \frac{g}{a}\frac{\partial u}{\partial p}\frac{\partial\theta}{\partial\phi} - \\ &\left\{\frac{g}{a\cos\phi}\left[\frac{\partial v}{\partial\lambda} - \frac{\partial}{\partial\phi}\left(u\cos\phi\right)\right] + gf\right\}\frac{\partial\theta}{\partial p} \end{aligned} \tag{3.2}$$

where p is the pressure. Using the small slope approximation (which states that

potential temperature surfaces are approximately parallel to height surfaces)

$$\nabla\theta = \frac{\partial\theta}{\partial z}\mathbf{e}_r \tag{3.3}$$

this can further be written as

$$Q = -\,g\,(\zeta + f)\,\frac{\partial\theta}{\partial p} \tag{3.4}$$

where ζ is the z component of $\boldsymbol{\zeta}$ and f is the z component of $\boldsymbol{\Omega}$.

This equation is true when the Rossby number and Burger numbers are both ~ 1. This condition is approximately true in the stratosphere.

The PV values provided by ECMWF in the ERA-40 Reanalysis data will be used in the following diagnostics.

Ertel's potential vorticity is used in studies of the atmosphere, in particular in studies of the polar vortex, although it has the unfortunate property that it increases exponentially with height. This is not a problem when only one vertical surface is being studied, but can become problematic when examining multiple surfaces since there is no way of identifying equivalent PV contours between any two surfaces. In particular the potential vorticity values of the air which makes up the vortex are higher on higher isentropic surfaces, and the vortex edge takes a different value of PV on each surface. In general the potential vorticity can take the form

$$Q = \frac{\boldsymbol{\zeta}\cdot\nabla f\,(\theta)}{\rho} \tag{3.5}$$

where taking $f\,(\theta) = \theta$ recovers the definition of Ertel's potential vorticity. In particular Lait (1994) introduced an alternative form of potential vorticity which was generalised by Müller and Günther (2003) to take the form

$$\Pi_L = \frac{\boldsymbol{\zeta}\cdot\nabla\theta}{\rho}\left(\frac{\theta}{\theta_0}\right)^{-\alpha} \tag{3.6}$$

where θ_0 is the reference potential temperature, taken to be some constant value and α is a constant which may be chosen based on the profile of the temperature for the conditions under consideration. Taking $\alpha = 4$ as used by Nakamura (1995), which corresponds to a θ profile similar to that typically observed in the

stratosphere, provides a convenient way of identifying equivalent contours across different isentropic surfaces. In this chapter the modified PV Π_L will be used as an objective method of identifying equivalent contours but when numerical values of PV are given these will be the usual Ertel's PV as given in the ERA-40 data. This value of α gives similar values of Π_L for PV contours in similar positions in relation to the vortex on the different θ levels examined here. This seems to make it a reasonable choice for the value of the parameter in this case.

3.3 Integral Diagnostics

In this section the integral diagnostics to be calculated will be discussed. These integral diagnostics are modified Lagrangian mean quantities. These are partially Lagrangian quantities that are changed only by non conservative processes.

These quantities are an improvement over the Eulerian mean diagnostics which were used previously, which fail to capture various aspects of the atmosphere, such as the smearing of the vortex edge and irreversible PV mixing (Thuburn and Lagneau, 1999). By looking at the progression of the equivalent latitude calculated at various Q values over the course of the winter is it possible to see features of SSW events which may occur during that period.

3.3.1 Equivalent Latitude

Butchart and Remsberg (1986) defined the quantity equivalent latitude ϕ_e as

$$\phi_e = \arcsin\left(1 - \frac{A_{Q,\theta}}{2\pi a^2}\right) \tag{3.7}$$

where

$$A_{Q,\theta} = \int_{S_{Q,\theta}} dS. \tag{3.8}$$

Here $S_{Q,\theta}$ is the section of the θ surface where the PV is greater than Q. The boundary of this surface will be denoted by $\Gamma_{Q,\theta}$. The equivalent latitude can be interpreted as the latitude circle, the area to the North of which occupies the same area as that for which the PV is larger than Q.

This quantity, unlike the mass and circulation (defined below) is not a Lagrangian invariant quantity, for instance the area may decrease if the depth of an isentropic surface increases. In the winter stratosphere however, to a good approximation this quantity can be considered as being approximately invariant in the absence of non conservative processes.

3.3.2 Mass Integral

Defined by Thuburn and Lagneau (1999) is an expression for the mass within a PV contour Q, which takes the form

$$\mathcal{M}_{Q,\theta} = \int_{S_{Q,\theta}} \sigma \, \mathrm{d}S \tag{3.9}$$

where σ is the isentropic mass density, and again $S_{Q,\theta}$ is the surface representing the inside of the PV contour Q on the isentropic surface θ. Here we are following the convention used in Thuburn and Lagneau (1999) of defining the inside of a PV contour Q to be the region where PV is larger than Q.

Using the hydrostatic approximationthe expression can be transformed to the form

$$\mathcal{M}_{Q,\theta} = \int_{S_{Q,\theta}} \rho \frac{\partial z}{\partial \theta} \, \mathrm{d}S = -\frac{1}{g} \int_{S_{Q,\theta}} \frac{\partial p}{\partial \theta} \, \mathrm{d}S \tag{3.10}$$

in which the integrand, and therefore the integral, is much easier to calculate from the ERA-40 data than the form given in Equation (3.9). This is the form which will be calculated below.

Timeseries plots of the mass $\mathcal{M}_{Q,\theta}$ give a clear view of how the structure of the vortex changes over the course of the winter making the vortex edge and formation of the surf zone easily identifiable. Being Lagrangian invariant, changes in mass can be attributed purely to non conservative processes. Using the mass budget, derived in the next section it also allows an estimation of the amount of mass removed from the vortex.

3.3.3 Balance Equation for $\mathcal{M}_{Q,\theta}$

The evolution of the mass $\mathcal{M}_{\mathcal{Q},\theta}$ in time takes the form

$$\frac{\partial}{\partial t}\mathcal{M}_{\mathcal{Q},\theta} = \mathcal{V}_{\mathcal{Q},\theta} - \int_{S_{Q,\theta}} \frac{\partial\left(\sigma\dot{\theta}\right)}{\partial\theta}\,\mathrm{d}S \tag{3.11}$$

This expression is derived from the definition of $\mathcal{M}_{Q,\theta}$ (Equation (3.9)) and taking the time derivative of this. The derivation can be found in section A.2. Here the cross contour mass transport $\mathcal{V}_{Q,\theta}$ is defined as

$$\mathcal{V}_{\mathcal{Q},\theta} = -\frac{\partial}{\partial Q}\int_{S_{Q,\theta}} \sigma\dot{Q}\,\mathrm{d}S + \frac{\partial}{\partial Q}\int_{S_{Q,\theta}} \sigma\dot{\theta}\frac{\partial\widetilde{Q}}{\partial\theta}\,\mathrm{d}S. \tag{3.12}$$

The term $\widetilde{Q}$ in Equation (3.12) is simply the PV to be integrated over, since PV appears in the limits of integration and the integrand itself, so the $\sim$ is adopted to remove ambiguity between the two terms.

Equation (3.12) represents the net mass flux across the PV=Q contour(s), and the remaining term on the right hand side of Equation (3.11) represents the mass transport across isentropic surfaces. The separation of terms here differs from the separation in the expression for the mass budget given by Nakamura (1995) in his equation (2.3). There the contours of PV are vertical between isentropic levels, meaning that the mass flux across PV contours can be expressed simply as $\frac{\partial}{\partial Q}\int_{S_{Q,\theta}} \sigma\dot{Q}\,\mathrm{d}S$. Where the contours of constant PV are sloped across isentropic levels the additional term on the right hand side of $\mathcal{V}_{Q,\theta}$ ($\frac{\partial}{\partial Q}\int_{S_{Q,\theta}} \sigma\dot{\theta}\frac{\partial\widetilde{Q}}{\partial\theta}\,\mathrm{d}S$) is required to calculate the cross contour mass flux. To our knowledge this separation of the terms in Equation (3.12) is novel, and has not been given in the literature. This separation is important when PV contours differ significantly from the vertical, as is the case in the real stratosphere, as mass transport vertially through PV contours becomes more important.

The physical interpretation of each of the terms that make up the expression for $\mathcal{V}_{\mathcal{Q},\theta}$ depends upon the definition of potential vorticity Q used (see Equation (3.6)). When combined into the term $\mathcal{V}_{\mathcal{Q},\theta}$, however, the interpretation becomes independent of the definition of PV, since the other terms in the mass balance equation are

independent of PV, making it a more useful quantity to use here than Nakamura's form. This is another important and useful feature of the separation given here.

This definition of $\mathcal{V}_{\mathcal{Q},\theta}$ also agrees with that given by Thuburn and Lagneau (1999) (using the identity Equation (A.2)) who give

$$\mathcal{V}_{\mathcal{Q},\theta} = \oint_{\Gamma_{Q,\theta}} \sigma\left(\boldsymbol{v} - \boldsymbol{v}_c\right) \cdot \widehat{\boldsymbol{n}} \mathrm{d}s \tag{3.13}$$

$$= \oint_{\Gamma_{Q,\theta}} \frac{1}{|\nabla_\theta Q|} \left(\sigma\dot{Q} - \sigma\dot{\theta}\frac{\partial Q}{\partial \theta}\right) \mathrm{d}s \tag{3.14}$$

where $\widehat{\boldsymbol{n}}$ is the unit normal vector to $\Gamma_{Q,\theta}$, $\boldsymbol{v}$ is the velocity of the flow and $\boldsymbol{v}_c$ is the velocity of the PV contour, which can be shown to be equal to the definition given here.

In the calculation of the terms in the balance equation (3.11) it is required to compute the value of $\dot{\theta}$, the radiative heating rate. To calculate this the MIDRAD radiation scheme of Shine and Rickaby (1989), implemented by John Thuburn, was used to compute $\dot{T}$ which was then transformed into $\dot{\theta}$ using temperature profiles from the ERA-40 data.

The values of $\dot{T}$, and hence $\dot{\theta}$, produced by the radiation scheme were found to have a net cooling bias, due to the fact that the long wave cooling was up to a factor of 50% too large. To correct this, we used the fact that, globally,

$$\int \sigma\dot{\theta}\, \mathrm{d}S = 0 \tag{3.15}$$

on a surface of constant pressure. Using the small slope and hydrostatic approximations this can be expressed as

$$\int \frac{\partial p}{\partial \theta}\dot{\theta}\, \mathrm{d}S \approx 0. \tag{3.16}$$

The value of $\dot{\theta}$ is then corrected so that

$$\int \frac{\partial p}{\partial \theta}\dot{\theta}_c\, \mathrm{d}S = 0 \tag{3.17}$$

where $\dot{\theta}_c = \dot{\theta} + c\left(p\right)$ is the corrected value of $\dot{\theta}$ and $c\left(p\right)$ is the correcting factor for each pressure level.

3.3.4 Circulation

The absolute circulation around a PV contour Q can be expressed as

$$\mathcal{C}_{Q,\theta} = \oint_{\Gamma_{Q,\theta}} \boldsymbol{v}_{abs} \cdot \mathrm{d}\boldsymbol{r}. \tag{3.18}$$

Using Stokes' theorem it can be shown that $\mathcal{C}_{Q,\theta}$ can be expressed in the form of an area integral, which is much easier to calculate numerically than the contour integral form. It then takes the form

$$\mathcal{C}_{Q,\theta} = \int_{S_{Q,\theta}} (\boldsymbol{\zeta} + 2\boldsymbol{\Omega}) \cdot \frac{\nabla\theta}{|\nabla\theta|} \,\mathrm{d}S. \tag{3.19}$$

Again invoking the small slope approximation this can further be simplified to

$$\mathcal{C}_{Q,\theta} = \int_{S_{Q,\theta}} \sigma\widetilde{Q} \,\mathrm{d}S \tag{3.20}$$

$$= \int_{S_{Q,\theta}} (\zeta + f) \,\mathrm{d}S. \tag{3.21}$$

The form expressed in Equation (3.20) is then easily calculated from the ERA-40 data.

3.3.5 Balance Equation for $\mathcal{C}_{Q,\theta}$

The time evolution of the circulation $\mathcal{C}_{Q,\theta}$ can be expressed as

$$\frac{\partial \mathcal{C}_{Q,\theta}}{\partial t} = Q\mathcal{V}_{Q,\theta} + \oint_{\Gamma_{Q,\theta}} \boldsymbol{X} \cdot \mathrm{d}\boldsymbol{l} + \oint_{\Gamma_{Q,\theta}} \dot{\theta}\frac{\partial \boldsymbol{v}}{\partial\theta} \cdot \mathrm{d}\boldsymbol{l} \tag{3.22}$$

$$\begin{aligned} &= Q\mathcal{V}_{Q,\theta} + \oint_{\Gamma_{Q,\theta}} \boldsymbol{X} \cdot \mathrm{d}\boldsymbol{l} \\ &+ \int_{S_{Q,\theta}} \frac{1}{a\cos\phi}\left(\frac{\partial}{\partial\lambda}\left(\dot{\theta}\frac{\partial v}{\partial\theta}\right) - \frac{\partial}{\partial\phi}\left(\cos\phi\,\dot{\theta}\frac{\partial u}{\partial\theta}\right)\right)\mathrm{d}S \end{aligned} \tag{3.23}$$

The derivation of this expression is given in Appendix A.3. The term $\oint_{\Gamma_{Q,\theta}} \boldsymbol{X} \cdot \mathrm{d}\boldsymbol{l}$ in principle gives an estimate of gravity wave drag and other frictional effects experienced by the PV contour Q, and it can be diagnosed from equation (3.23) as a residual given $\mathcal{V}_{Q,\theta}$ calculated from equation (3.11) and the last term in Equation (3.23). Again, the form given in Equation (3.23) has not, to our knowledge, been given in the literature.

3.3.6 Consistency Check

Taking the mass integral $\mathcal{M}$ along with the circulation $\mathcal{C}$ it is possible to derive a balance equation for the derivatives, in Q space, of the two quantities despite them being independent. This balance equation takes the form

$$\frac{\partial \mathcal{C}_{Q,\theta}}{\partial Q} = Q \frac{\partial \mathcal{M}_{Q,\theta}}{\partial Q} \tag{3.24}$$

as derived by Thuburn and Lagneau (1999). This can either be used as a check that the two quantities $\mathcal{M}_{Q,\theta}$ and $\mathcal{C}_{Q,\theta}$ have been calculated correctly, or it can be used to compute the distribution of $\mathcal{M}_{Q,\theta}$ or $\mathcal{C}_{Q,\theta}$ given the full distribution of the alternate quantity.

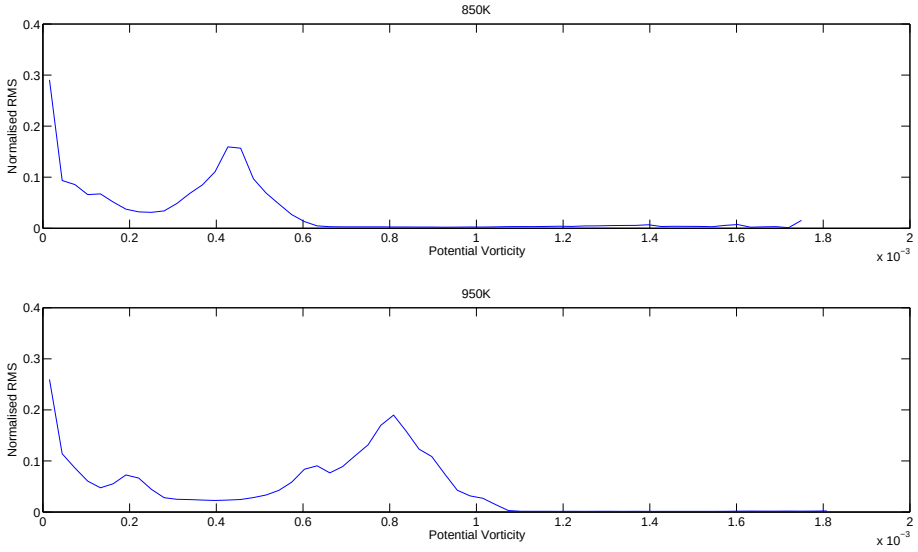

Figure 3.1: Root mean square of the residual of $Q\frac{\partial \mathcal{M}_{Q,\theta}}{\partial Q} - \frac{\partial \mathcal{C}_{Q,\theta}}{\partial Q}$ divided by the root mean square of $Q\frac{\partial \mathcal{M}_{Q,\theta}}{\partial Q}$ for the a)850k and b)950K isentropic levels between 15.2 PVU and 1749.8 PVU

Here we have chosen to use the equation as a consistency check, and thus verified that our calculation for both quantities satisfies this relation to a good degree of accuracy. This gives confidence that the two quantities have been calculated correctly, and also that the resolution of the data is good enough for the purposes used in these diagnostics.

Figure 3.1 shows the root mean square of the residual of the continuity check (Equation (3.24)), normalised by dividing by $Q\frac{\mathcal{M}_{Q,\theta}}{\partial Q}$ for both the 850K and 950K isentropic levels for the duration of the 1978−9 winter. The value of this normalised error term is relatively small; for most of the PV values it takes values of the order 10^{-2} or smaller, with only a small number of PV contours taking values slightly larger than this.

The large values of the normalised error occur at the lower potential vorticity contours, which represent air which lies very close to the equator. It should be noted that the values of Q near to the equator approach 0 meaning that the values of the normalised error will increase in this area. The region is far away from the area of interest, meaning that this has no impact on the values calculated for the PV contours which make up the polar vortex, and the air immediately around it. Therefore it is of little significance that the values of this error on the outer PV contours are relatively larger than those for the rest of the winter hemisphere.

3.3.7 Numerical Evaluation of Surface Integrals

In order to calculate these continuous quantities from the finite resolution ERA-40 data an approximation for computing surface integrals from finite Gaussian gridded data is required. In this section the routine for calculating these integrals is described.

On the Gaussian grid the coordinates of the grid points $(\lambda_i, \phi_j)\,; i = 1, ..., N_{\text{lon}}; j = 1, ..., N_{\text{lat}}$ are defined as $\lambda_i = 2\pi\,(i-1)\,/N_{\text{lon}}$ and ϕ_j are defined by the Gaussian latitudes with $\phi_j > \phi_{j+1}$.

To approximate the continuous integral expression the following sum is used

$$\int_S h\,(\lambda, \phi)\,dS = \sum_{\substack{i,j \\ \widetilde{Q}(\lambda_i,\phi_j)\geq Q}} w_{ij} h\,(\lambda_i, \phi_j) \tag{3.25}$$

where

$$w_{ij} = \frac{2\pi a^2}{N_{lon}}\left(\sin\frac{\phi_{j+1}+\phi_j}{2} - \sin\frac{\phi_j+\phi_{j+1}}{2}\right) \qquad j = 2, N_{lat}-1 \tag{3.26}$$

$$w_{i1} = \frac{2\pi a^2}{N_{lon}}\left(1 - \sin\frac{\phi_1+\phi_2}{2}\right) \tag{3.27}$$

$$w_{iN_{lat}} = \frac{2\pi a^2}{N_{lon}} \sin \frac{\phi_{N_{lat}-1} + \phi_{N_{lat}}}{2} \tag{3.28}$$

for one hemisphere with a equal to the radius of the earth, taken here to be $6.371\text{x}10^6 m$.

3.4 Results

The results of the calculations for the surface integral diagnostics will be presented in this section. Firstly composites of mass and circulation will be presented to identify the features of a typical winter, followed by a series of case studies of 7 winters, 5 of which included a single warming event, one included 2 warmings and one in which no warmings were observed. Table 3.1 gives a list of the winters to be looked at in these case studies. The table also gives the dates of warmings as identified by Charlton and Polvani (2007) and Mitchell et al. (2013), these dates will be indicated in the following plots (not including the composites) with those of Charlton and Polvani (2007) indicated by a red line and Mitchell et al. (2013) with a magenta line. The data used is ERA-40 6 hourly data which is explained in chapter 2.

To identify when an SSW occurs Charlton and Polvani (2007) use the WMO definition (a reversal of the zonal mean zonal wind at 60° North and 10hPa). These were then classified as a split if two vortices exist with circulations having a ratio of $2:1$ and a displacement if not. Mitchell et al. (2013) calculated the area, centroid latitude and aspect ratio of the vortex. They then used a hierarchical clustering algorithm to classify the vortex as split, displaced or stable. If within 5 days of the date of the warming the event changed from split to displaced it was classed as a mixed event.

Before looking at the results, a note on the reliability of the data is needed. The radiation scheme includes an error in the long wave cooling rate. Although this has been compensated for, this may have an effect on the reliability of the calculation of $\mathcal{V}_{Q,\theta}$ and $\oint_{\Gamma_{Q,\theta}} \boldsymbol{X} \cdot \mathrm{d}\boldsymbol{l}$ which involve calculation of $\dot{\theta}$. As seen below the results of at least the calculation of $\mathcal{V}_{Q,\theta}$ seem not to be heavily influenced by this error.

Winter	Charlton and Polvani (2007)	Mitchell et al. (2013)
1978-9	22nd February S	18th February S
1979-80	29th February D -	15th February S 16th March D
1981-2	4th December D -	- 21st January S
1983-4	24th February D	26th February D
1984-5	1st January S	25th December S
1987-8	7th December S 14th March S	1st December M 10th March D
1990-1	-	-

Table 3.1: Winters and their classifications. D denotes a displacement warming event, S a splitting SSW and M a mixed event defined by Mitchell et al. (2013) to be one which changes in state between split and displacement.

3.4.1 Composite Plots

Figure 3.2 shows a composite of the mass $\mathcal{M}_{Q,\theta}$ for the $\theta = 850$ K isentropic level from 1st November to 31st March for the winters in Table 3.1. The pole is at the bottom of the figure, where the higher PV contours also lie.

At the bottom of the plot the gradient of the PV can be seen to increase as the PV contours become more densely packed. This can be interpreted as the edge of the vortex which is characterised by a high gradient of PV.

From the start of November the mass within the vortex increases steadily until the end of the month when it remains fairly similar for the duration of the winter until it starts to decrease again at the end of February. The mass between the contours surrounding this increases over the course of the winter, and can be identified as the surf zone.

A composite of the circulation $\mathcal{C}_{Q,\theta}$ for $\theta = 850$ K for the same period is shown in Figure 3.3. In all figures showing the circulation the higher valued PV contours appear increasing toward the bottom of the figure.

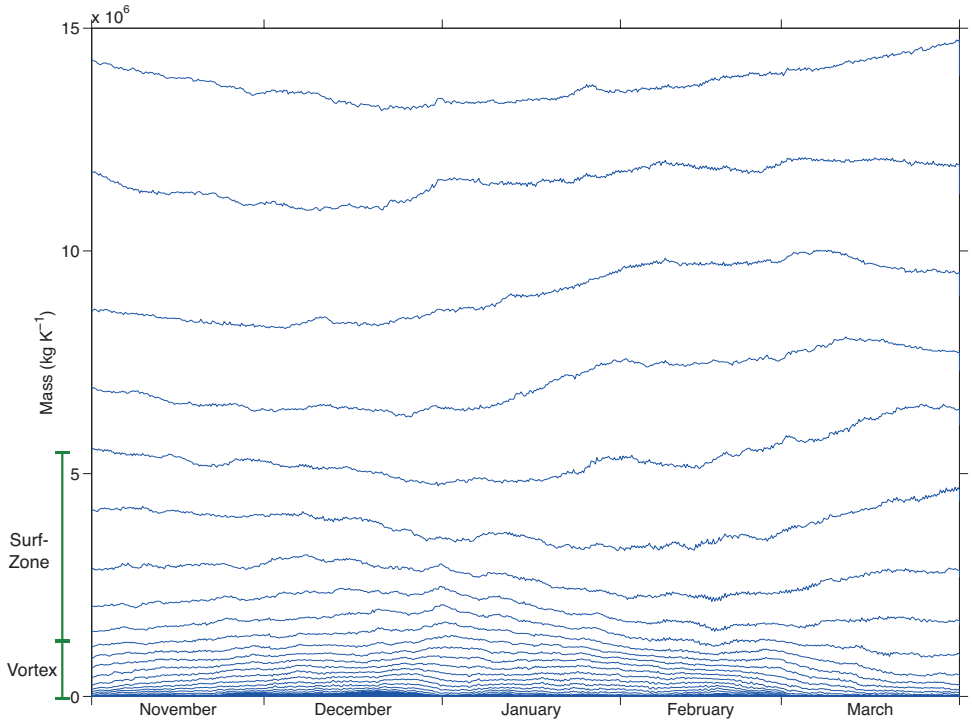

Figure 3.2: Composite of $\mathcal{M}_{Q,\theta}$ from 1st November to 31st March for $\theta = 850$ K. 31 evenly spaced PV contours are plotted between -43.6 PVU and 1838 PVU.

The edge of the vortex is not as well defined in this plot as it is for the previous mass composite. In this plot the contours on the very edge of the vortex have circulation values of roughly 700 m^2 s^{-1}at the start of the winter.

While it does not show the difference between the vortex edge and the surf zone as clearly as the mass does, the circulation does provide a much clearer view of the area inside the vortex, and changes in circulation over the winter are slightly clearer in some cases. Many of the changes that are seen in either plot can be seen in the other, as would be expected from the mass-circulation relation Equation (3.24).

Due to the added detail of the circulation the mid winter period of relatively steady levels of mass appears to have a more changeable circulation with an average of decreasing circulation over the period, though at a much slower rate than the decrease in circulation toward the end of the winter.

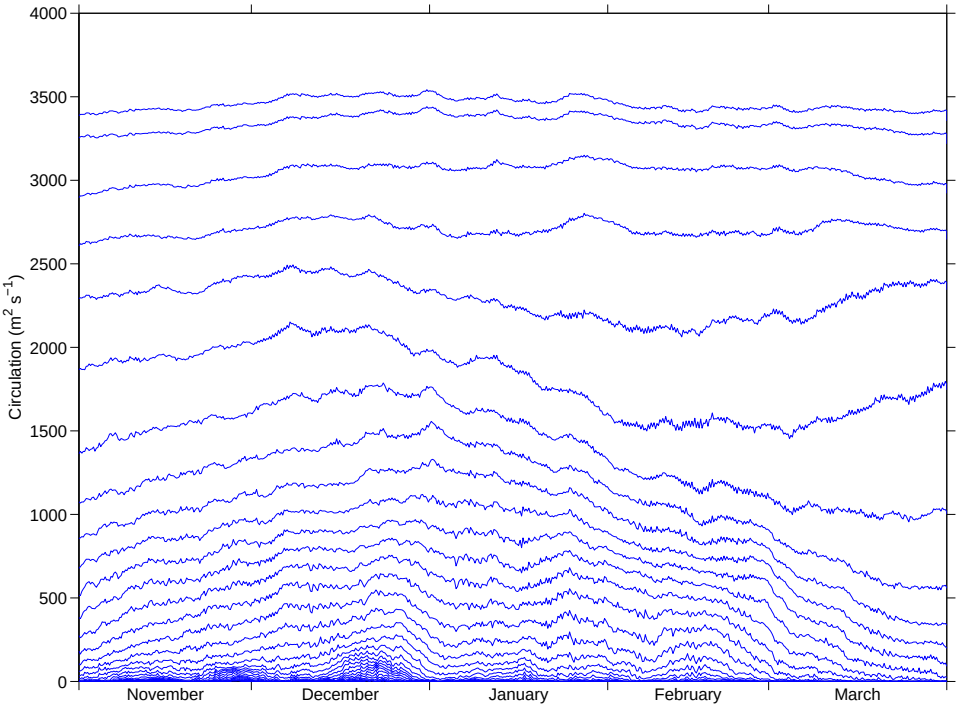

Figure 3.3: Composite of $\mathcal{C}_{Q,\theta}$ from 1st November to 31st March for $\theta = 850$ K. 31 evenly spaced PV contours are plotted between -43.6 PVU and 1838 PVU.

For the $\theta = 950$ K isentropic level the composite of mass is shown in Figure 3.4. The plot looks similar to the $\theta = 850$ K level plot with the vortex being immediately identifiable as the area of tightly packed PV contours at the bottom of the figure. The gain in mass at the start of the winter occurs at a similar rate for both 850 K and 950 K levels.

Toward the end of February the drop in mass observed on the lower levels can be seen, and is slightly sharper on this higher level especially on the innermost PV contours at the very bottom of the figure.

The contours surrounding the vortex appear to change in the opposite sense to those of the vortex, that is they appear to decrease in mass at the start of the winter and increase toward the end. From the start of January the contours far from the vortex edge start to increase in mass, and this signal appears to

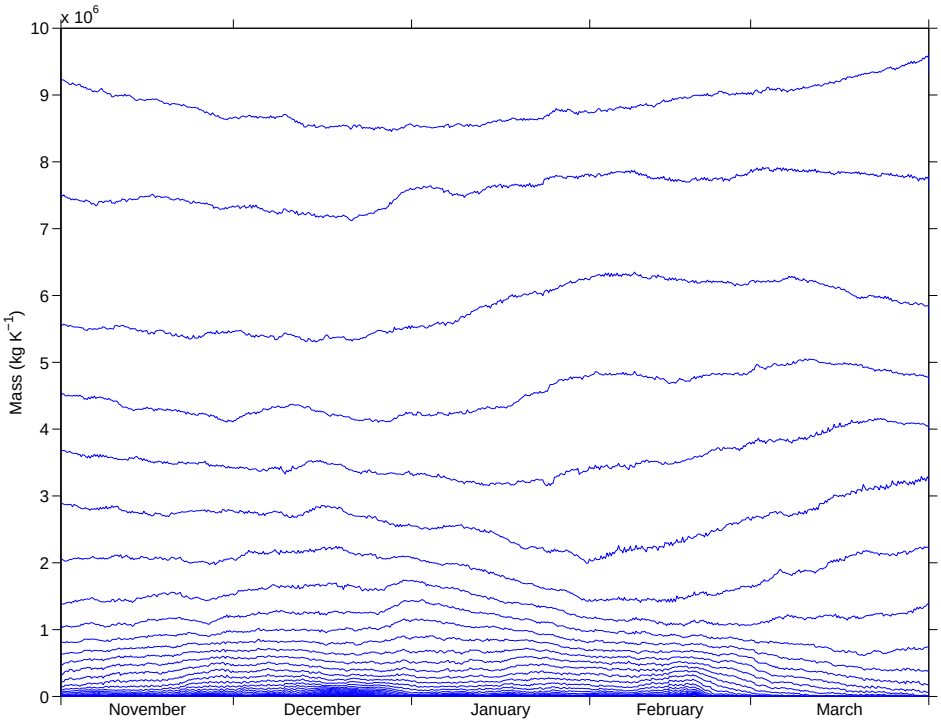

Figure 3.4: Composite of $\mathcal{M}_{Q,\theta}$ from 1st November to 31st March for $\theta = 950$ K. There are 39 PV contours plotted evenly spaced in PV space between 426.8 PVU and 3101.2 PVU.

propagate toward higher valued contours closer to the vortex edge over the course of the following month. This can also be seen on the lower 850 K isentropic level in Figure 3.2 though the increases in mass are lower than at the higher level and the propagation of the signal toward the vortex edge is slower, taking until nearly the end of February to reach the contours near the vortex while equivalent contours appear to start to increase at the start of February for $\theta = 950$ K.

The composite of the circulation on the $\theta = 950$ K level, unlike the corresponding mass, is notably different from the 850 K level (Figure 3.5). The circulation is slightly larger on the contours making up the vortex edge, taking values of just under 1000 m^2 s^{-1}.

The circulation increase in the early part of the winter is similar in rate to that

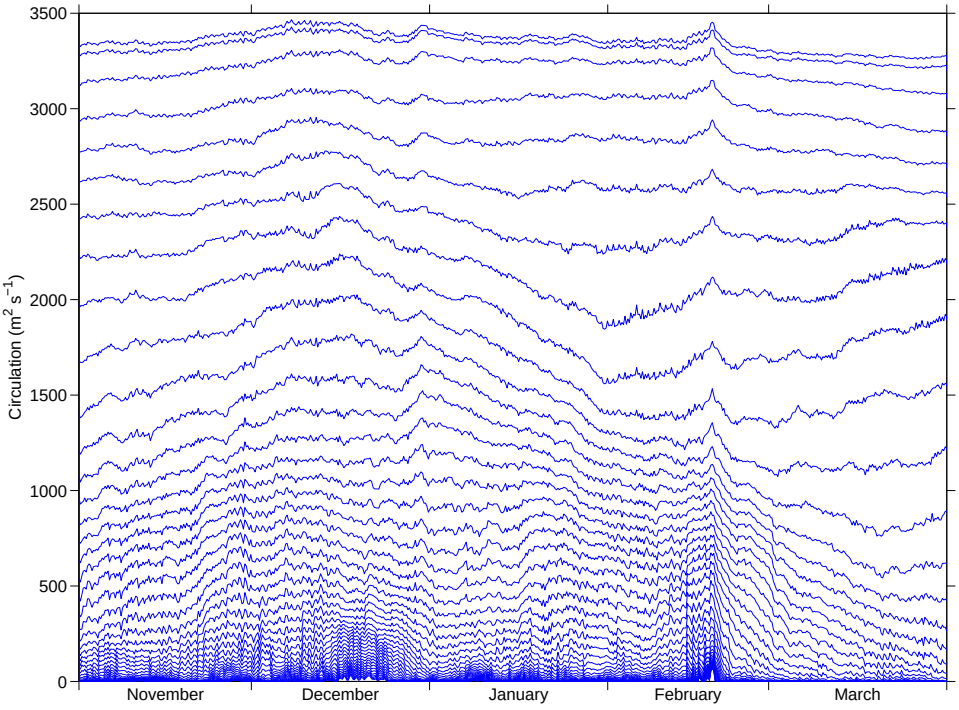

Figure 3.5: Composite of $\mathcal{C}_{Q,\theta}$ from 1st November to 31st March for $\theta = 950$ K. There are 39 PV contours plotted evenly spaced in PV space between 426.8 PVU and 3101.2 PVU.

for 850 K, with a larger drop in mid February over a larger area than the mass on this level.

The contours outside the vortex can be seen to increase in mass significantly between February and the end of March, between 1x10^{6}kg K^{-1}and 4x10^{6}kg K^{-1}. The corresponding increase in circulation is less clear than that for the mass. There are fewer contours which appear to show as large an increase in circulation than the corresponding mass increase.

On the 600 K level (Figure 3.6) the composite changes in mass are less obvious than on the higher levels. The increase in mass of the vortex at the start of winter, from the start of November to mid December, can still be seen and appears to last for a longer time than it does on the higher isentropic levels; for $\theta = 850$ this period

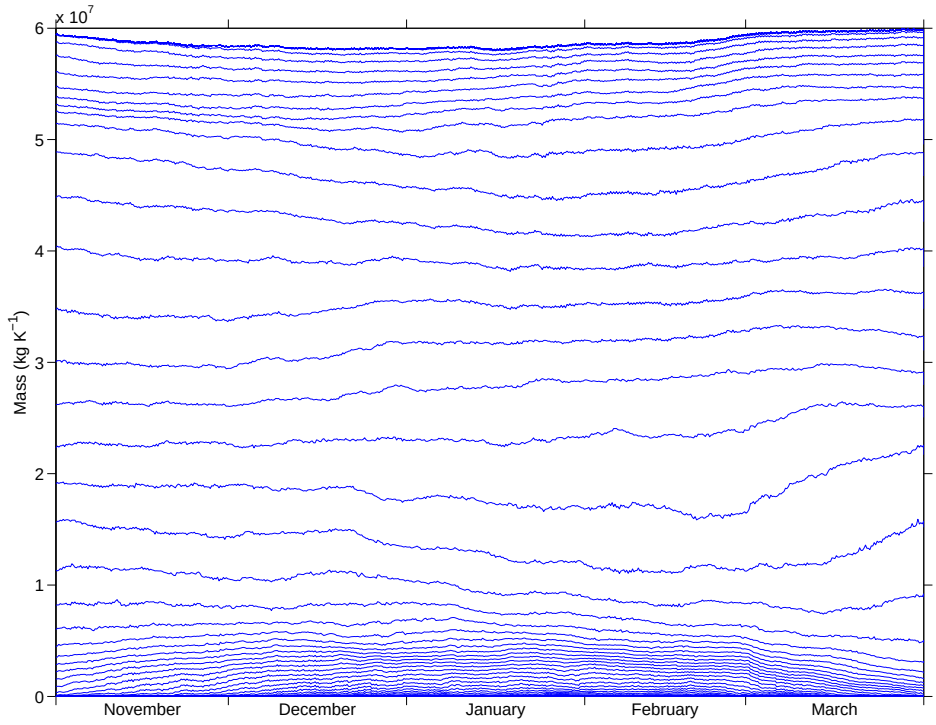

Figure 3.6: Composite of $\mathcal{M}_{Q,\theta}$ from 1st November to 31st March for $\theta = 600$ K. The plot shows 30 PV contours equally spaced from 0.5 PVU and 213.65 PVU.

lasts until the end of November, but on the 600 K level it is extended until mid December. Following this the vortex retains a relatively constant amount of mass for the middle part of the winter.

The decrease in mass of the high valued PV contours which make up the vortex and its edge toward the end of the winter does not begin until the start of March. This is later than the corresponding effect can be seen on the higher 850K surface.

There doesn't appear to be any significant rise in mass in the lower valued PV contours at the start of the winter for $\theta = 600$ K as there is for 850 K and 950 K. Toward the end of the winter some of the contours immediately around the vortex begin to increase in mass, though the range of contours is much smaller than that on the 850 K and 950 K surfaces. This increase occurs at the end of February which is much later than on the 850K and 950K surfaces as can be seen above.

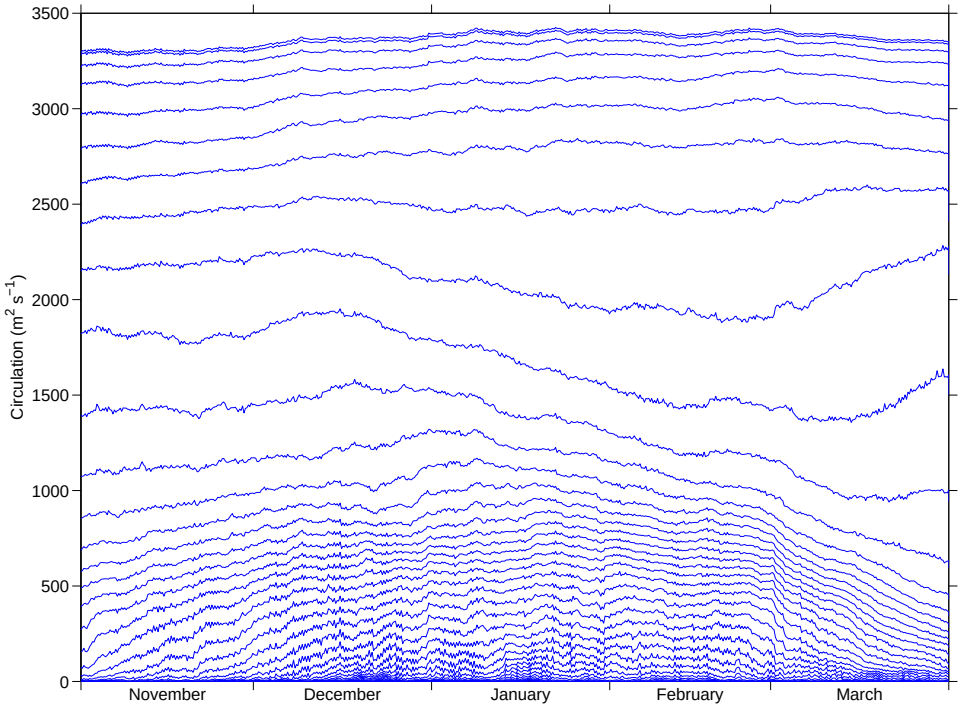

Figure 3.7: Composite of $\mathcal{C}_{Q,\theta}$ from 1st November to 31st March for $\theta = 600$ K. The plot shows 30 PV contours equally spaced from 0.5 PVU and 213.65 PVU.

The circulation on $\theta = 600$ K (Figure 3.7) of the contours in and immediately around the vortex increases at a higher rate from 1st November to mid December than seen in Figure 3.3 or Figure 3.5. The starting values of the contours at the edge of the vortex is around 500 m^2 s^{-1}, just over half that on the 950 K level, but by mid December the values of these contours are around 1000 m^2 s^{-1}, around the same as the equivalent contours on the 850 K and 950 K surface.

The circulation doesn't begin to decrease at the end of the winter until the end of February, at the same time as the mass starts to decrease. A similarly reduced number of contours surrounding the vortex increase in circulation coinciding with the decrease of those making up the vortex.

The composites of mass $\mathcal{M}_{Q,\theta}$ and circulation $\mathcal{C}_{Q,\theta}$ show a general increase in their respective values from the start of November in the contours making up the

vortex and its edge. This increase continues until the start of December for the higher 950 K level but continues until the middle of December on the lower 600 K level.

After this initial increase in mass the vortex remains relatively unchanging over the middle part of the winter. The circulation also maintains a similar level over this period but shows some small changes. Toward the end of the winter the mass and circulation of the contours making up the vortex decreases until the end of March. On the 950 K level this occurs can be seen to start just after the middle of February and seems to propagate downward until it can be seen on the 600 K level at the end of February.

Accompanying this decrease within the vortex the contours surrounding the vortex can be seen to increase in mass. The signal of this can be seen at the end of December on contours far from the vortex on the 950 K level. This then propagates toward the vortex edge over the course of the next month and similar patterns can be seen on the lower levels, though for a smaller range of contours.

In the following part of this section several case studies (described above) will be examined to try to identify systematic features of splitting and displacement SSW events.

3.4.2 1978-9

Figure 3.8 shows the equivalent latitude calculated for the winter of 1978-1979 for 25 PV values between -43.6 PVU and 1367.6 PVU on the 850 K isentropic level. This is the same one as calculated by Butchart and Remsberg (1986) and was chosen because the vortex splitting event which occurred in this particular winter was a particularly dramatic one, so any features picked out by the equivalent latitude will hopefully be more prominent and easier to identify.

In Figure 3.8 the splitting event at the end of February can clearly be seen. This is characterised by the area of the vortex decreasing in the period immediately after the sudden warming for a period of approximately 2 weeks. The other main features of the figure are the equatorward movement of the outer PV contours over

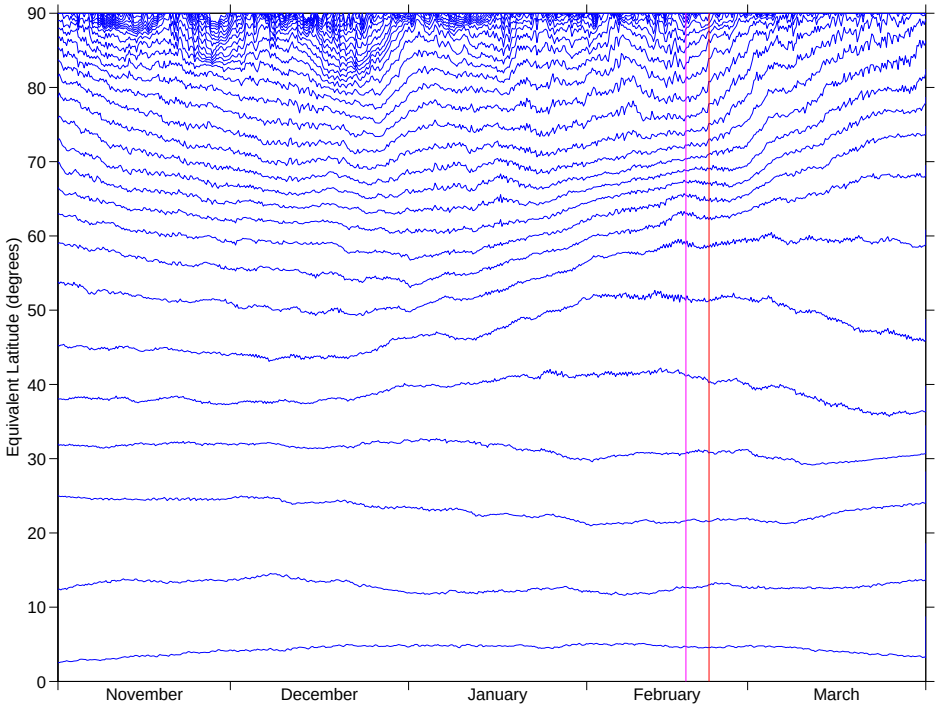

Figure 3.8: Equivalent latitude for the winter from 1st November 1978 to 31st March 1979. There are 22 contours plotted from −43.6 PVU to 1367.6 PVU.

the course of the winter. For instance from early December some of the lower PV contours move towards the equator, and with reference to PV maps for the winter it can be seen that this corresponds to the event of a tongue of PV being stripped from the vortex at about 9th December. The same can be seen in late December for the tongue of air stripped from the vortex at about 22nd December and again in mid and late January.

Another prominent feature of Figure 3.8 is the shrinking of the area of the vortex at the time leading up to the vortex splitting event which occurred around 22nd February 1979 as identified by Charlton and Polvani (2007). This is seen in the figure as increasing equivalent latitude from the start of January to the event of the splitting in mid February. It is also possible to observe a sharpening of the PV gradient at the vortex edge, seen as a greater concentration of the contour

lines towards the top of the figure. The date of the onset of this warming is also identified by Mitchell et al. (2013) as being the 18th of February. This is close to the date of Charlton and Polvani (2007) and both class this event as a vortex split.

Dates of sudden warmings given here will in general be those identified as the central dates by Charlton and Polvani (2007), but these will be compared occasionally with the classifications of Mitchell et al. (2013). When the classifications are similar the dates of Charlton and Polvani (2007) will be used to refer to the event.

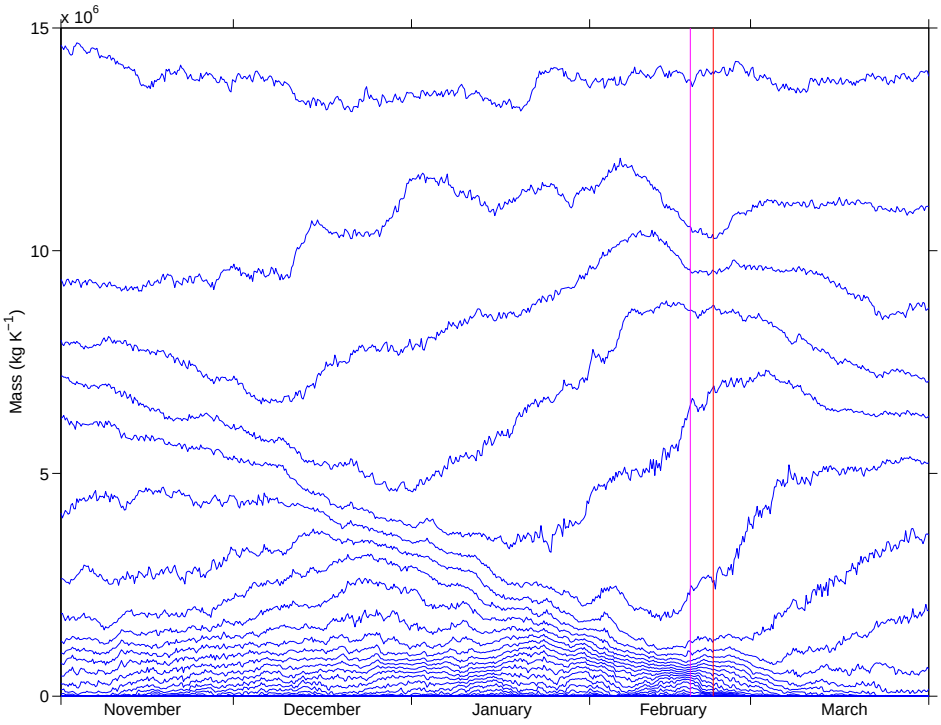

Figure 3.9: Mass integral $\mathcal{M}_{Q,\theta}$ for the winter 1st November 1978 to 31st March 1979 on the 850 K isentropic surface. A vortex splitting event occurred around 22nd February which can clearly be seen in the plot. The mass is plotted for 22 PV contours, evenly spaced between 15.2 PVU and 1250 PVU.

Figure 3.9 shows $\mathcal{M}_{Q,\theta}$ for the same winter (1978-9) as the equivalent latitude plot Figure 3.8 for a range of PV contours equally spaced between the values 15.2

PVU and 1250 PVU. Here the higher PV contours, and the pole, appear toward the bottom of the figure with lower valued contours containing more mass than the higher valued ones.

In the figure it is possible to see the decreasing mass of air inside the vortex in the lead-up to the warming event as air is stripped from the main vortex and mixed into the surrounding air. There is also a corresponding increase in the mass within the surrounding contours meaning that mass is being mixed from the tropics into the surf zone. This is a similar picture as that seen in the equivalent latitude plot (Figure 3.8), although the stripping of air in the lead up to the warming event is much clearer in Figure 3.9, where the mass inside some of the outer contours increases quite dramatically as the winter progresses.

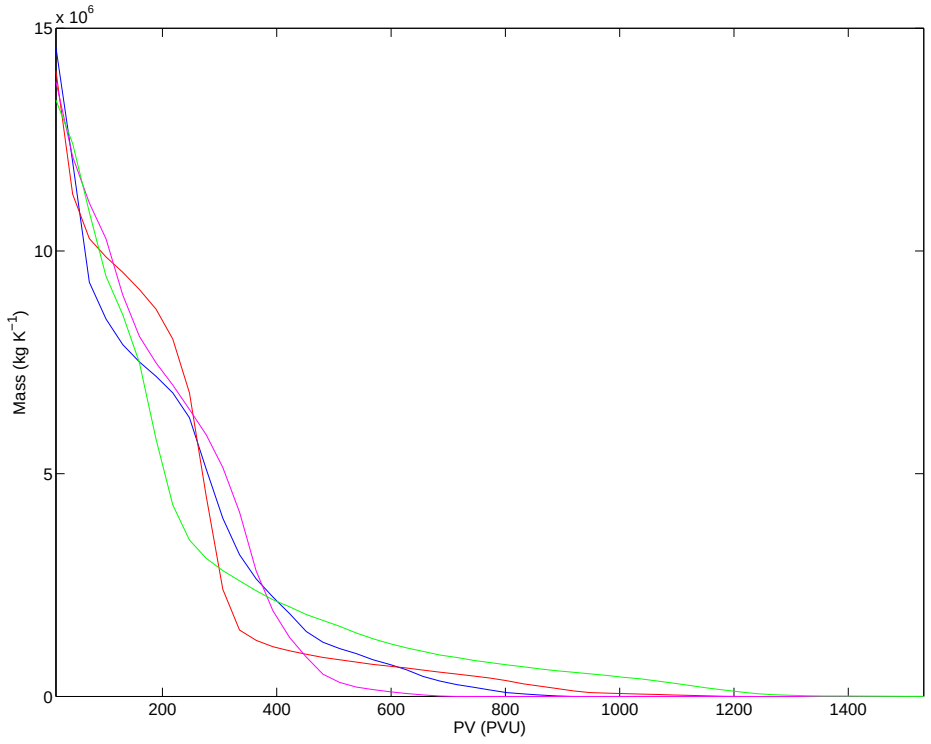

Figure 3.10: Potential Vorticity against Mass on $\theta = 850$ K for various times during the $1978 - 9$ winter. The blue line corresponds to early November, green to mid January, red is around the time of the SSW in late February and magenta is in mid March.

Figure 3.10 shows the Mass $\mathcal{M}_{Q,\theta}$ plotted as function of PV on the 850 K isentropic surface for various instants during the winter. In early November (blue line) the 'PV staircase' of alternating steep and relatively shallow PV gradients is clearly present. By mid January (green line) the maximum value of PV has increased and the PV increases more sharply toward the centre of the vortex. The 'step' that appears between around 50 and 300 PVU in early November is not as clearly visible in mid January, though some features still remain at around 150 PVU.

At the end of February (red line) the staircase structure can be seen again as well as the fact that the maximum value of PV has dramatically reduced since mid January. In mid March (magenta line) the maximum PV has again increased, though not to the same maximum value it attained in mid January. The difference in gradient between the vortex edge and the surrounding area of surf zone is much sharper than it is earlier in the winter.

Figure 3.11 shows the circulation $\mathcal{C}_{Q,\theta}$ for the winter of $1978-9$ on the same 850 K isentropic level. The plot shows a similar picture to those of the equivalent latitude ϕ_e and mass $\mathcal{M}_{Q,\theta}$ plots (Figure 3.8, Figure 3.9) with the warming event clearly visible at the end of February. Because of the mass-circulation balance equation (Equation (3.24)), it is not surprising that the two quantities show similar features with the circulation showing more resolution around the area of the vortex due to the factor of Q on the right hand side of the equation. While the vortex edge and formation of the surf zone are not quite as striking in the circulation there is much more detail about what is going on inside the vortex. This makes examining the two quantities side by side a useful way of looking at the progression of the vortex over the course of the winter, though plots of both quantities will only be included when each adds a slightly different view, otherwise just one of the plots will be shown with brief references to the other.

In Figure 3.11 the circulation of the contours inside the vortex increases initially until mid-December to early-January when it reaches its peak. The contours nearest to the outside of the vortex reach their maximum circulation rate earliest and

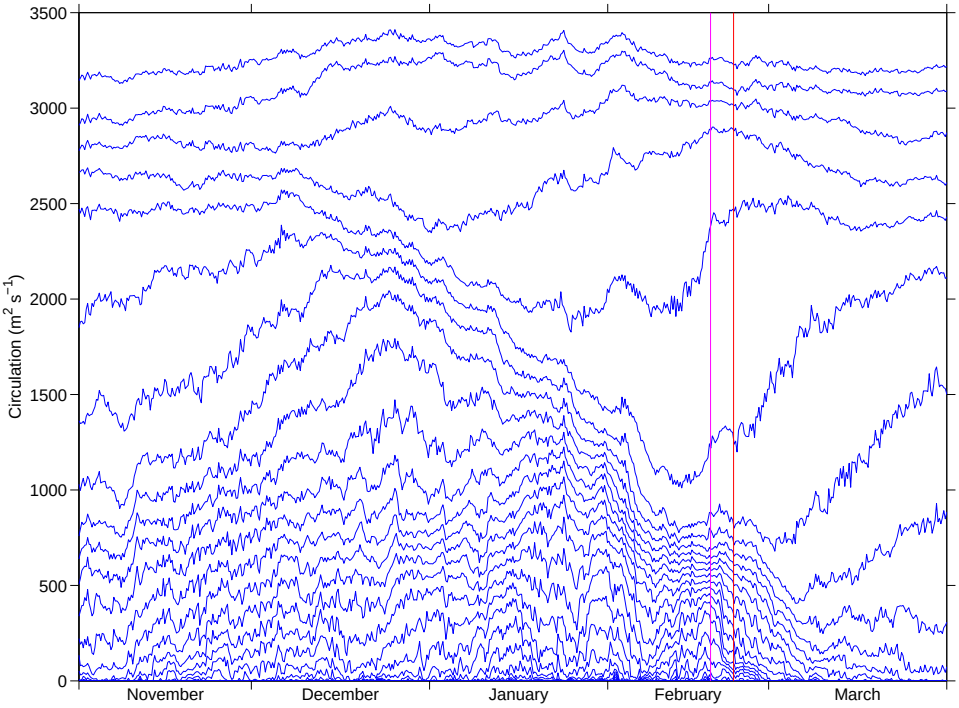

Figure 3.11: Timeseries of $\mathcal{C}_{Q,\theta}$ for 1st November 1978 to 31st March 1979 on the 850 K isentropic level. There are 18 PV contours are plotted equally spaced between 15.2 PVU and 1279.4 PVU

begin falling, followed by the inner contours. The circulation then stabilises briefly around mid-February in the lead up to the vortex splitting before it decreases as the warming progresses. Following the warming the circulation then starts to increase for the outer PV contours, though many of the inner PV contours disappear as the circulation goes towards zero.

The mass $\mathcal{M}_{Q,\theta}$ for $\theta = 950$ K is shown in Figure 3.12 for the same $1978-9$ winter. Similar features to those on the 850 K surface can be identified, though with some notable differences. Because σ is smaller on this higher isentropic level, the mass of air within the vortex is smaller than for 850 K. There also appears to be less contrast between the vortex and the surrounding air than there is for the is at 850K. As expected, the PV of the contours making up the edge of the vortex takes higher values than the 850 K surface.

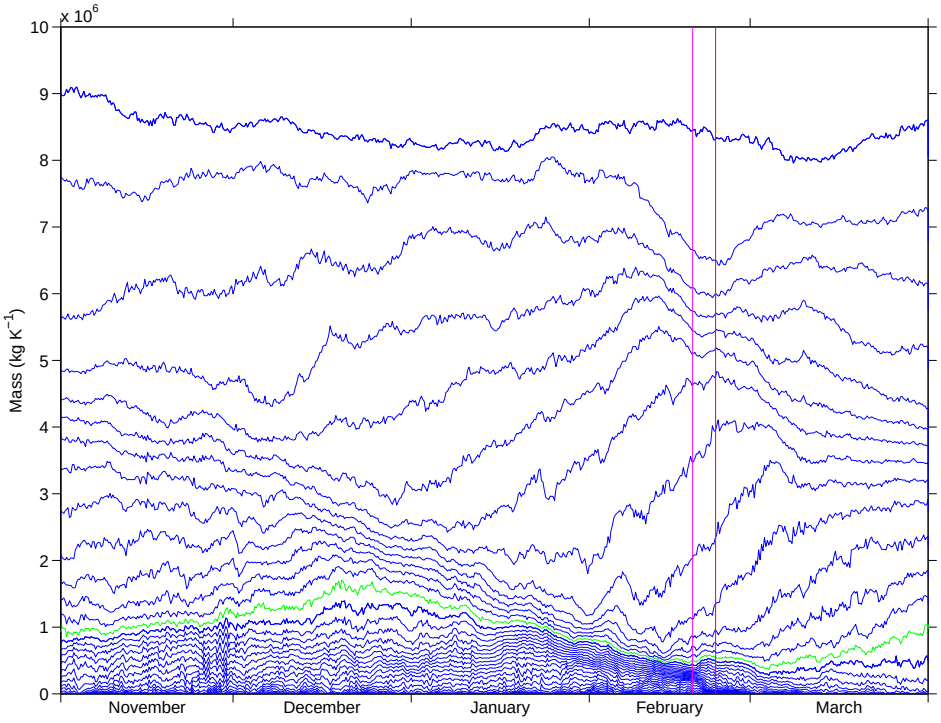

Figure 3.12: $\mathcal{M}_{Q,\theta}$ for the winter 1st November 1978 to 31st March 1979 on the 950 K isentropic surface. The splitting event around 22nd February can again be seen here. The mass is plotted for 39 PV contours, evenly spaced between 426.8 PVU and 3101.2 PVU. The green contour is the one shown in Figure 3.18.

The vortex seems to be more established at the start of November at 950K than it is for 850K where the mass of the vortex increases until late in November. After this the evolution of the vortex appears similar on both levels until the signal of the warming starts to become visible in the diagnostic. Over the course of the winter the gradient of PV making up the vortex edge gradually sharpens, becoming steeper until mid February when the breakdown of the vortex causes it to become shallower.

The relative change in mass within PV contours on this level is much larger over the course of the winter than for those on the lower level. The decrease in mass within the vortex associated with the warming seems to become visible earlier for

$\theta = 950$ K than for 850 K, especially on the inner contours of the vortex, but the vortex remains relatively intact until the signal of the warming becomes visible on 850 K when a similar picture occurs on both levels.

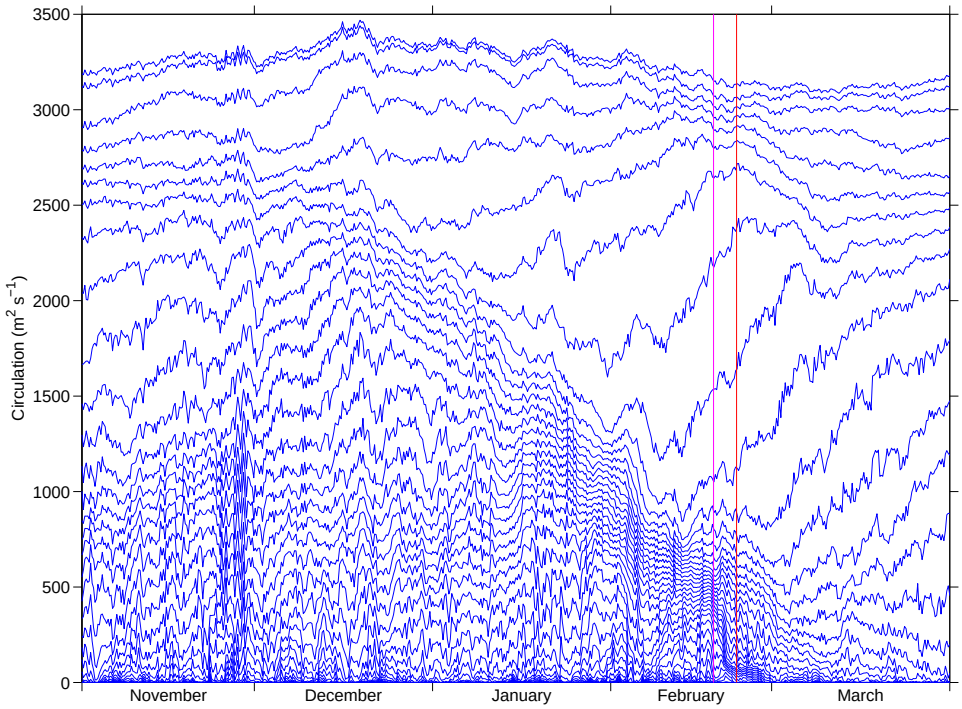

Figure 3.13: Timeseries of $\mathcal{C}_{Q,\theta}$ for 1st November 1978 to 31st March 1979 on the 950 K isentropic level. There are 31 PV contours are plotted equally spaced between 15.2 PVU and 2661.2 PVU.

The circulation on the 950 K surface (Figure 3.13) takes slightly larger values than those on the 850 K level. The value of the circulation on the contours making up the main part of the vortex take values roughly twice as large at the start of the winter, though when the circulation starts to decrease around the time of the sudden warming the circulations on the two separate levels becomes very similar. The circulation can be seen to decrease slightly earlier on the 950 K level than it can on the 850 K level on some of the outer contours similar to the way that the mass starts to decrease earlier on the higher level. Closer to the centre of the vortex the reduction of $\mathcal{C}_{Q,\theta}$ becomes more synchronised between the two levels. Following

the splitting the circulation increases at a similar rate on the higher level as it does on the 850K level. The outer contours start to decrease in circulation from mid-December, slightly earlier than they do for $\theta = 850$ K, with a much sharper decrease occurring on this level. There are some contours on the outside of the vortex whose circulation starts to rise before the sudden warming, though there doesn't appear to be a significant amount more than on the 850 K level.

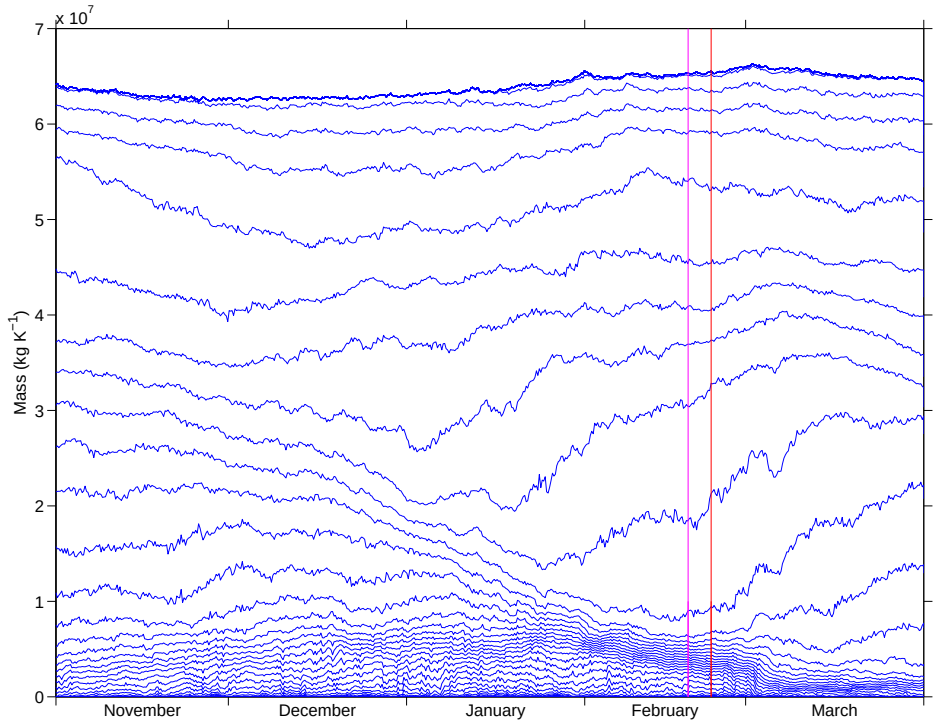

Figure 3.14: $\mathcal{M}_{Q^*,\theta}$ from 1st November 1978 to 31st March 1979 on the 600 K isentropic surface. The plot shows 30 PV contours equally spaced from 0.5 PVU and 213.65 PVU.

Figure 3.14 shows the plot for the same period as the previous two figures on the 600 K isentropic level. Comparing this to the other two, the effect of the splitting event towards the end of February can be seen less clearly on this level, though it is still possible to identify the signature of the splitting event at the end of February as identified in the plots on the two higher levels. Unlike the other two levels, however, in which the signal of the warming can be seen to occur at roughly

the same time, on this level the signal cannot be seen to occur until slightly later, around the 28th February. Comparing PV maps for the three different isentropic levels for the period in question reveals that the vortex appears to split nearly simultaneously on all levels, as noted in Matthewman et al. (2009). The difference in the signal appearing in the $\mathcal{M}_{Q,\theta}$ plots is not caused by the split occurring later on the lower level, but the fact that the two 'daughter' vortices appear to be longer loved on the 600K surface than they are for 850K and 950K. The smaller vortex which breaks down allowing the other to recover to it pre-warming state seems to become eroded much later and at a faster rate on the lower level, while on the upper levels the higher PV air in the centre of the vortex appears to mix into the rest of the air in the interior giving the vortex a more uniform PV structure inside. This vortex will then break down slightly earlier, but at a slower rate than it does at 600K.

The other obvious feature of the plot is the fact that the values of the potential vorticity are much smaller here than on the higher levels, as well as the fact that there is a much higher mass per unit θ of air within the vortex than on the higher levels. There is also a much smaller relative change in $\mathcal{M}_{Q,\theta}$ due to the erosion of the vortex during the warming event than there is on the higher levels.

The poleward trend of outer PV contours resulting in a sharpening of the gradient on the edge of the vortex that can be seen on the other levels is also present here. This will be investigated below with a view to determining whether this can be attributed to filaments of air being removed from the vortex by the external flow which results in the preconditioning of the vortex prior to the sudden warming. After the occurrence of the sudden warming the mass within the vortex decreases similarly to the other levels along with a decrease in the PV gradient on the vortex edge.

On the 600 K level the circulation at the vortex edge is similar to that on the upper two surfaces (Figure 3.15). The changes in circulation on the vortex's outer contours is again smaller on this lower level, increasing in size on each of the higher levels in turn. The decrease in circulation that characterises the splitting events in

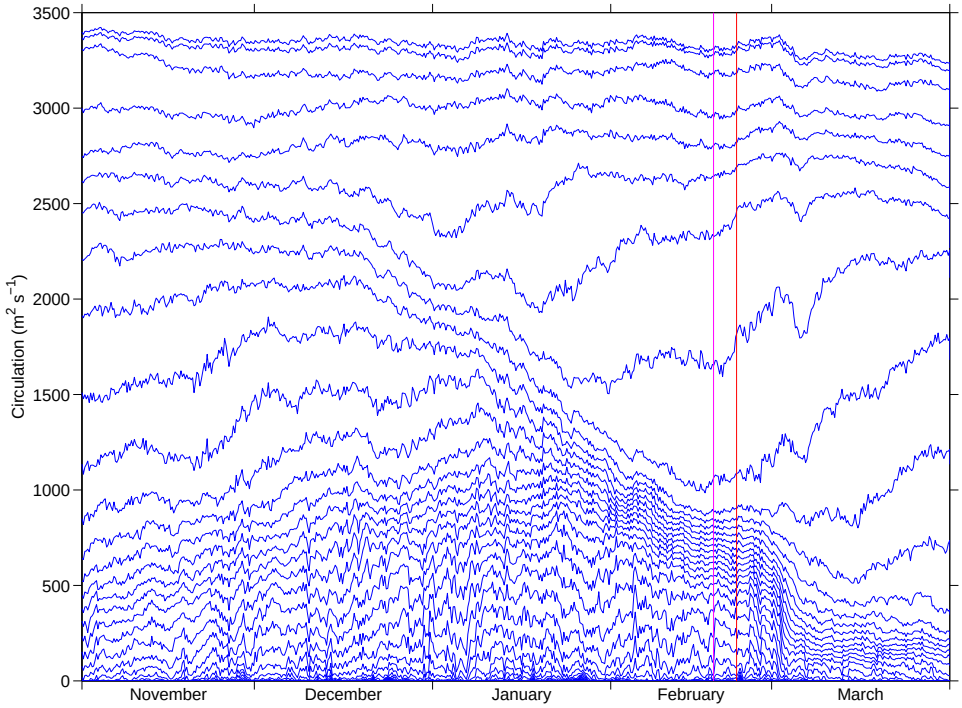

Figure 3.15: Timeseries of $\mathcal{C}_{Q,\theta}$ for 1st November 1978 to 31st March 1979 on the 600 K isentropic level. There are 34 PV contours are plotted equally spaced between -6.86 PVU and 235.7 PVU

these plots is seen much later on this level than on the upper levels as would be expected from the analogous plots of $\mathcal{M}_{Q,\theta}$; the splitting cannot be seen on this level until the very end of February and into the beginning of March while on the higher levels the signal is constrained to mid to late February. Unlike the other levels the PV contours on this surface which do decrease in circulation around the advent of the sudden warming do not increase again afterwards like they do on the surfaces above them.

There is a period immediately before the signal of the warming starts to become visible in this plot where the change in circulation slows right down, so that for a short period of time the circulation stays nearly steady. Following this the signal of the warming starts to become visible as the circulation decreases sharply. This plateau appears on both of the higher levels, but for a much shorter period of time.

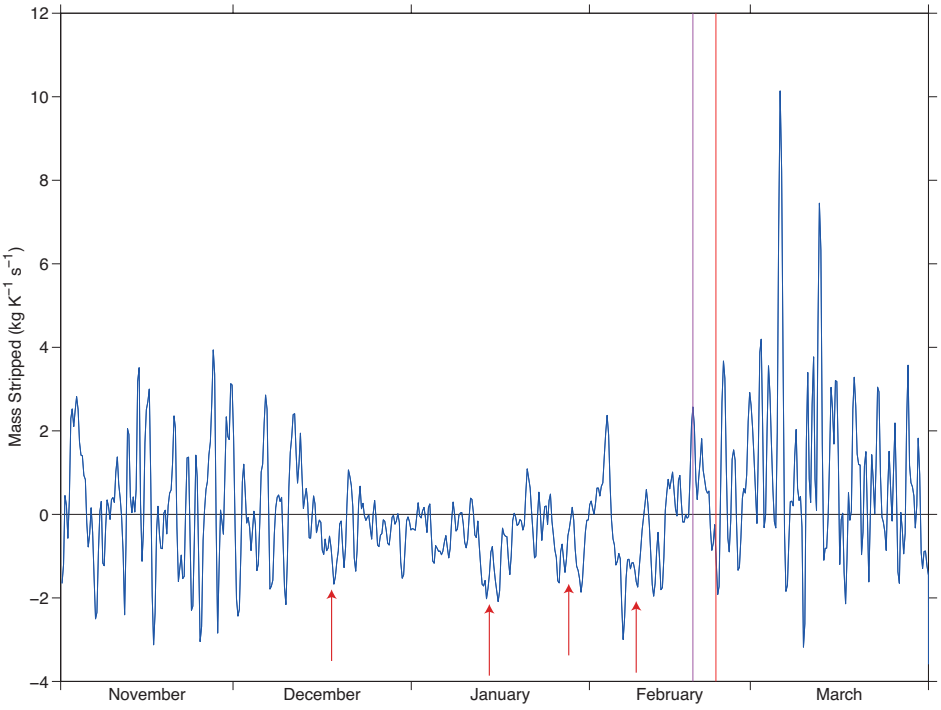

Figure 3.16: Timeseries of $\mathcal{V}_{Q,\theta}$ from 1st November 1978 to 31st March 1979 for 338.6 PVU on the 850 K isentropic surface (blue line). The black line is plotted at x = 0 to easier identify when $\mathcal{V}_{Q,\theta}$ changes from positive (influx) to negative (outflux).

Figure 3.16 shows a plot of $\mathcal{V}_{Q,\theta}$, (Equation (3.12)) for the winter of $1978-79$ on the 850 K isentropic surface for Q = 338.6 PVU. This PV value corresponds to a contour lying roughly at the edge of the vortex. This means that air crossing this contour can be interpreted as entering or leaving the vortex. Positive values of $\mathcal{V}_{Q,\theta}$ correspond to the mass of air inside the vortex increasing, while negative values correspond to air flowing out from the vortex and being mixed into the surrounding surf zone. Comparing Figure 3.16 to Figure 3.9 it appears that most of the changes to the mass of air within the vortex at this level is due to this 'stripping term' $\mathcal{V}_{Q,\theta}$.

It can be seen from Figure 3.16 that there are small amounts of air that are constantly moving into and out from the PV contour. It is possible that this is

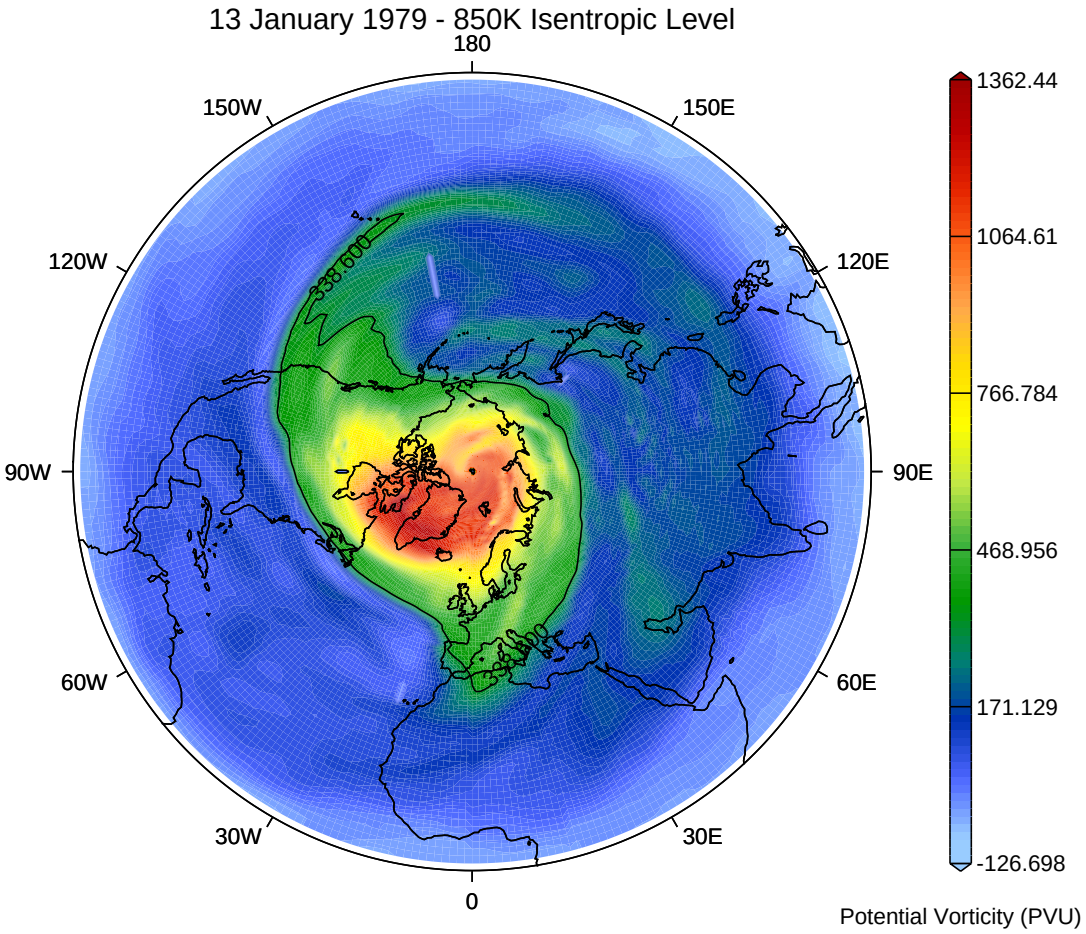

Figure 3.17: PV map for 13th January 1979 on the 850 K isentropic surface. The solid line shows $Q = 338.6$ PVU. A filament of PV can be seen being stripped from the vortex and mixed into the surrounding surf zone.

either noise in the data or fluctuations due to the diurnal cycle. It is possible to identify vortex stripping events in the plot by the fact that these are much longer lived than the regular fluctuations; on the scale of 5 to 10 days. One such event, for example, can be observed in mid January in Figure 3.16. Comparing this to the PV map Figure 3.17 for an instant during the identified stripping event it can

clearly be seen that this event corresponds to a filament of air (outlined in black) being pulled from the vortex, and examining a time series of PV maps reveals it being mixed into the surf zone surrounding the vortex. Other such events can be observed throughout the winter, reducing the size of the vortex as mass is removed from it, up until mid February when the vortex splitting SSW occurred for this winter.

After the warming the size of the vortex increases, although the PV gradient at the edge of the vortex does not return to the same level as at the start of the winter.

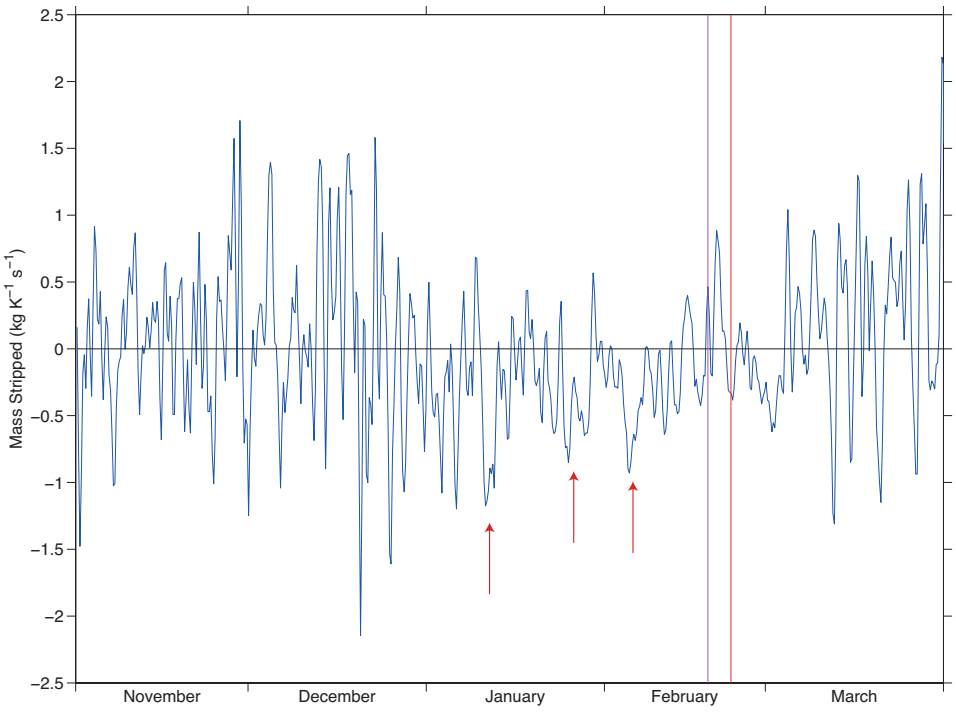

Figure 3.18: Timeseries of $\mathcal{V}_{Q,\theta}$ from 1st November 1978 to 31st March 1979 for the 779.6 PVU PV contour on the 950 K isentropic surface (blue line). The black line is plotted at $x = 0$. This contour is highlighted in green in Figure 3.12.

A similar plot for the $\theta = 950$ K surface is shown in Figure 3.18. Comparing this to the 850 K level a similar pattern of air being removed from and moved into the vortex facilitated by the stripping of PV filaments can be seen. This

mainly occurs between the start of December and the SSW event in February. In addition to this stripping of filaments, the plot of $\mathcal{V}_{Q,\theta}$ for this contour on the edge of the vortex points to vertical movement of air through diabatic effects. This is evidenced by the fact that, other than the period when stripping of PV filaments occurs, the stripping term appears predominantly positive. Compared to the mass (Figure 3.12) $\mathcal{V}_{Q,\theta}$ is much more positive than the change in mass would indicate. This means that the main contribution to $\mathcal{V}_{Q,\theta}$ is the third term in the mass balance Equation (3.11) which represents vertical movement of mass within the vortex.

Of course this positive bias could be due to the errors observed above, but together with this negative bias seen below (Figure 3.19) it is more probable that this is indicative of vertical movement of air downward within the vortex as noted by for instance Waugh et al. (1994).

This period of mainly positive $\mathcal{V}_{Q,\theta}$ is mainly at the start and end of the winter, with the period of preconditioning being much more negative in comparison.

In contrast to the 950 K level, plots for the outer contours of the vortex for the 600 K level, for instance Figure 3.19, are predominantly negative, indicating outflux of air. This mass leaving the vortex indicated by $\mathcal{V}_{Q,\theta}$ is larger than expected by looking at the amount that plots of $\mathcal{M}_{Q,\theta}$ would suggest. Figure 3.19 shows $\mathcal{V}_{Q,\theta}$ for the 600 K level in the winter of $1978-9$. It clearly shows a more negative trend than would be suggested by looking at Figure 3.14 of $\mathcal{M}_{Q,\theta}$; integrating $\mathcal{V}_{Q,\theta}$ on the 88.7PVU contour over the period of the winter (Figure 3.19) shows a movement of an amount of air out of the vortex of the order of 2.5x10^7 kg K^{-1}which, while the trend of the contour for the duration of the winter is to remove the mass of air inside it, is more than the amount of air inside the contour at the start of the winter.

The movement of air out of the vortex is distributed throughout the winter, not localised to any particular time period. This indicates that air is constantly being moved vertically within the vortex onto this isentropic surface to replace that being removed via stripping. Indeed, some of the mass moving from the vortex to the surf zone is due to vertical movement across the slanted edge of the vortex rather

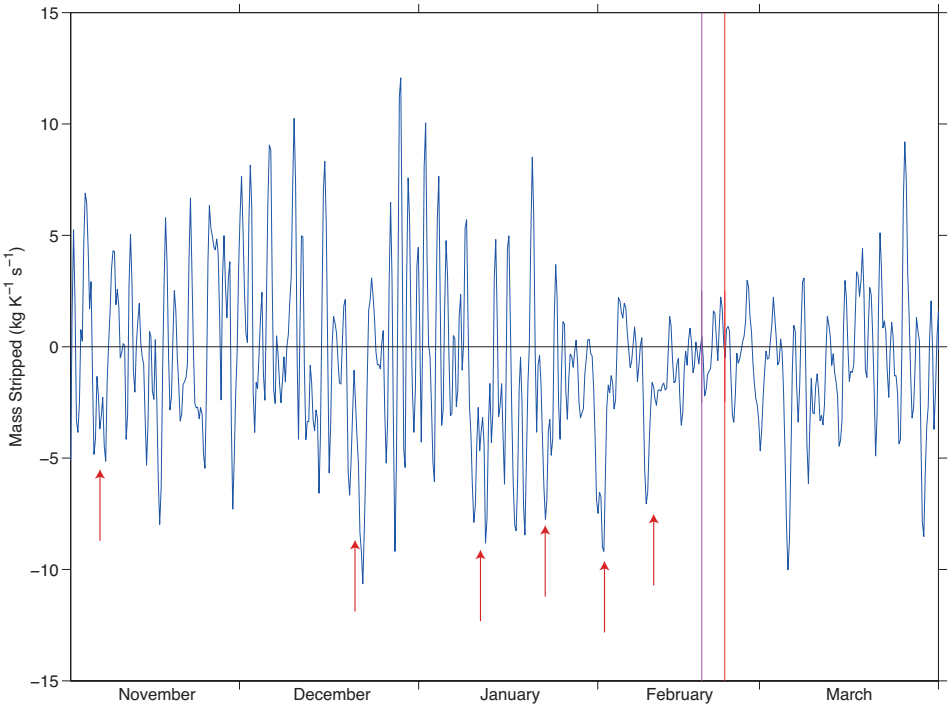

Figure 3.19: Timeseries of $\mathcal{V}_{Q,\theta}$ from 1st November 1978 to 31st March 1979 for 88.7 PVU on the 600 K isentropic surface.

than necessarily from horizontal movement across the boundary.

Various stripping events where significant quantities of mass are removed from the vortex can be seen throughout the winter among the movement of small quantities of air over the period of the winter as just noted above. As with the higher levels examined above, these can also be matched up to tongues of air being pulled from the vortex by looking at PV maps of the corresponding isentropic surface.

Timeseries plots of $\mathcal{V}_{Q,\theta}$ relating to corresponding PV contours on each of the three height surfaces examined, show that the more prominent stripping events can be identified as being common to each of the levels. They appear to occur at a similar time on all surfaces, although they do not seem to occur exactly simultaneously on all levels. There doesn't seem to be a preferred direction for the propagation of these events. Some events appear to occur first on the upper level and appear later on lower levels in plots of $\mathcal{V}_{Q,\theta}$, while others appear first on

the lower level and propagate up to the higher level. PV maps confirm this trend, where it is possible to see filaments starting to be removed on one level slightly before they become visible on the other levels and the propagation of these either upward or downward.

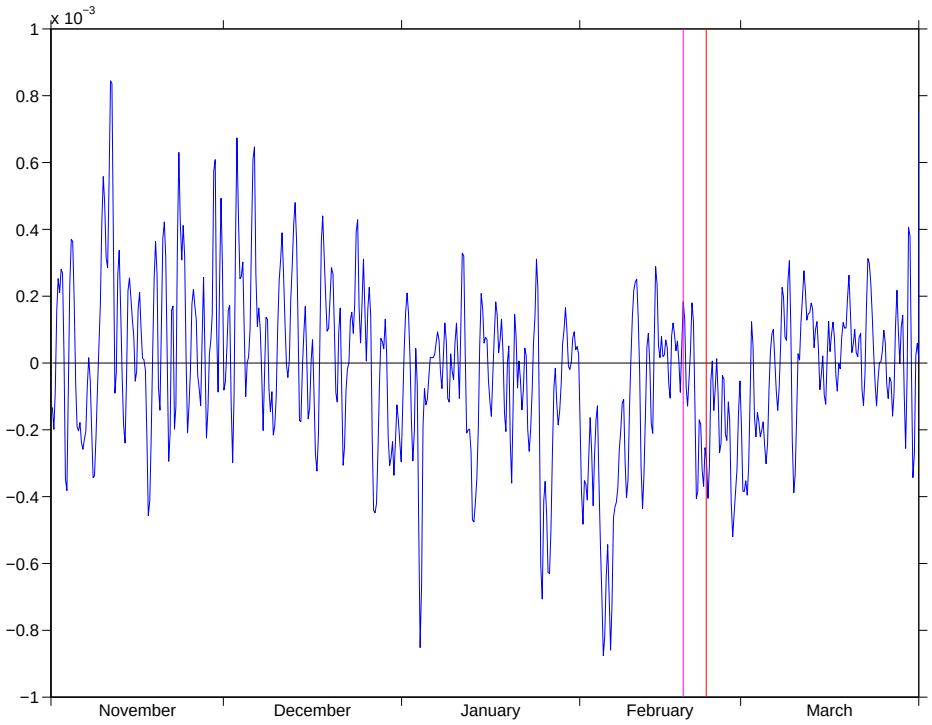

Figure 3.20: Timeseries of the frictional term from 1st November 1978 to 31st March 1979 for 338.6 PVU on the 850 K isentropic surface (blue line). The black line is plotted at x = 0 to easier identify changes from positive (influx) to negative (outflux).

The frictional term $\oint_{\Gamma_{Q,\theta}} \boldsymbol{X} \cdot \mathrm{d}\boldsymbol{l}$ (defined in subsection 3.3.5) was calculated from Equation (3.23) using the stripping term $\mathcal{V}_{Q,\theta}$ and circulation integral $\mathcal{C}_{Q,\theta}$. Plots of this term (for example Figure 3.20) showed a lot of noise, similar to what can be seen in plots of the $\mathcal{V}_{Q,\theta}$ term such as Figure 3.16. The noise in these plots largely masks any signal in the term making it very hard to spot interesting features. There are small periods similar to the stripping events observed in timeseries plots

of $\mathcal{V}_{Q,\theta}$, though these are much less defined than the stripping events. They are very similar in magnitude to the noise making it hard to tell if these are genuine events. The timing of these possible events doesn't seem to coincide well with either stripping or sudden warming events.

3.4.3 1984-5

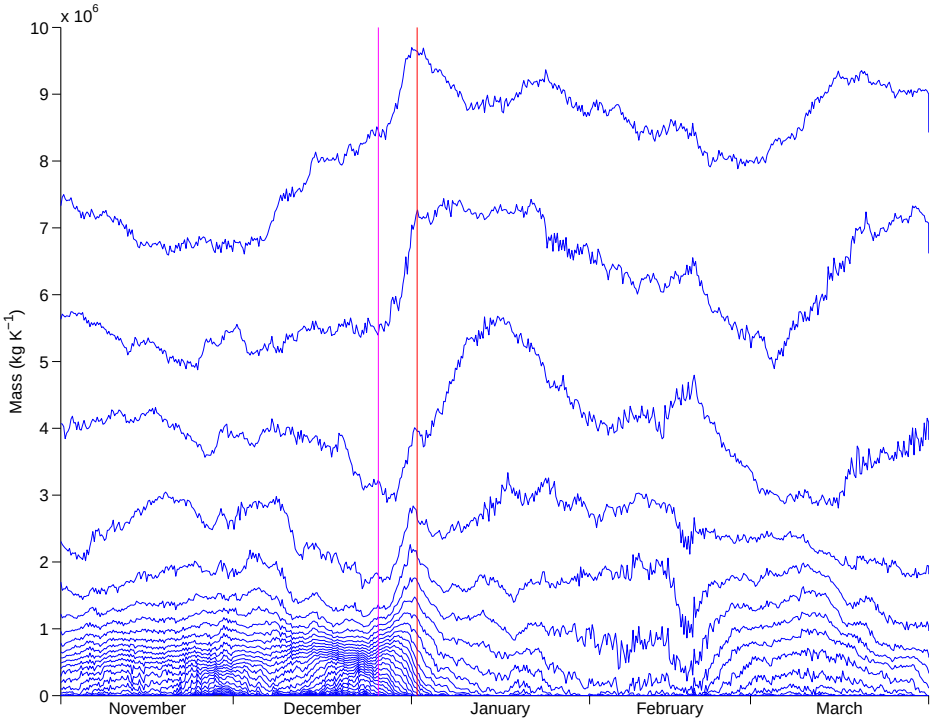

Figure 3.21: $\mathcal{M}_{Q,\theta}$ for the winter of 1984-5 from 1st November to 31st March on the 850K isentropic surface for 28 evenly spaced PV contours between 191.6 PVU and 1838 PVU

The winter of $1978-9$ has been well studied, in particular because it represents a particularly defined vortex splitting event, however the features observed above in the mass $\mathcal{M}_{Q,\theta}$ and the stripping term $\mathcal{V}_{Q,\theta}$ can be seen in many other winters which contain a single splitting SSW event.

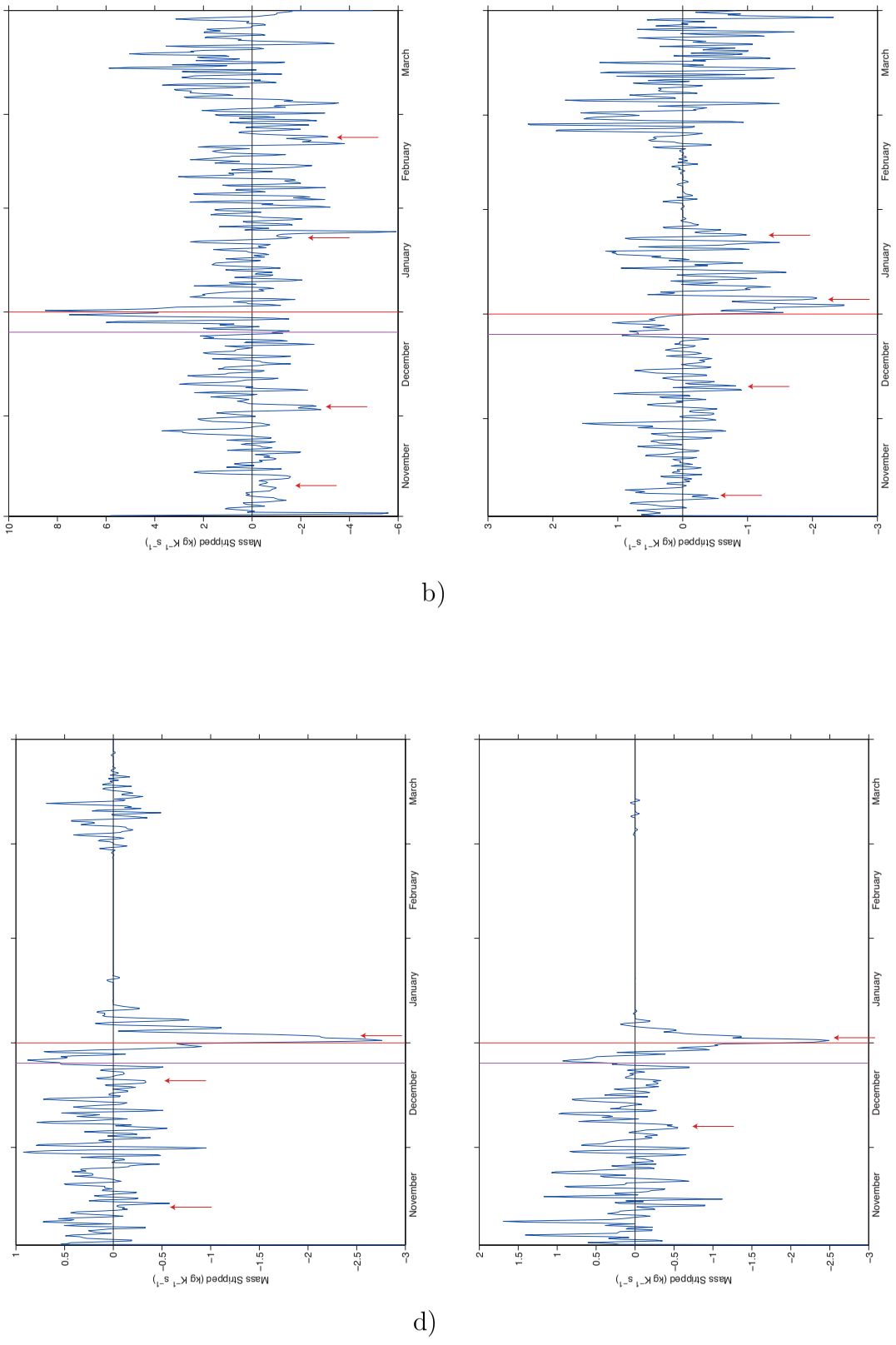

Figure 3.22: Timeseries of $\mathcal{V}_{Q,\theta}$ from 1st November 1984 to 31st March 1985 on the 850K isentropic surface for PV contours with values 250.4 PVU (a), 662 PVU (b), 838.4 PVU (c) and 956 PVU (d).

For example the winter of $1984-5$ is shown in Figure 3.21 and Figure 3.22 where a vortex splitting SSW event occurred around 1st January 1985 defined by the criteria of Charlton and Polvani (2007) and 25th December by Mitchell et al. (2013). The area of high PV gradient air making up the polar night jet can clearly be seen in Figure 3.21 up until the vortex split event occurs in late December/early January. Following the warming event the vortex reforms towards the end of February. After reforming the PV gradient is not as steep as it is in the pre-warming vortex, though a recognisable vortex is still visible in the plot of $\mathcal{M}_{Q,\theta}$.

Following the warming there is a period where the vortex is relatively undefined in the plot of $\mathcal{M}_{Q,\theta}$. Comparing this to maps of PV for the same period reveals that while there is still an area of high PV air over the pole, the vortex itself is not well defined. The PV values are lower than those at the start of the winter and are spread more thinly over the pole. Over the period of January they start to become drawn together and by the start of February a more recognisable vortex is visible located over the pole.

Figure 3.22 shows that, similarly to the winter of $1978-9$, the $1984-5$ winter also features several events where filaments of high PV air are moved toward the edge of the vortex and pulled from it in the lead up to the SSW event. There are several stripping events in the month or so leading up to the SSW event. Starting around the 1st January there is a fairly large stripping event lasting for roughly 15 days. This coincides with the splitting of the vortex and the breakdown of the smaller of the two daughter vortices.

While the splitting event around 1st January is clearly visible in the plot of $\mathcal{M}_{Q,\theta}$ on $\theta = 850$ K as in the $1978-9$ winter, on the $\theta = 600$ K surface there is little signal of the splitting event visible (see Figure 3.23). Towards the end of January the mass of the vortex can be seen to have been diminished, much like the signal of the splitting event seen earlier, although not by as much as can be seen in the corresponding plot for $1978-9$. The outer contours can be seen to move equatorward around this time also, which seems to occur with the decrease in mass

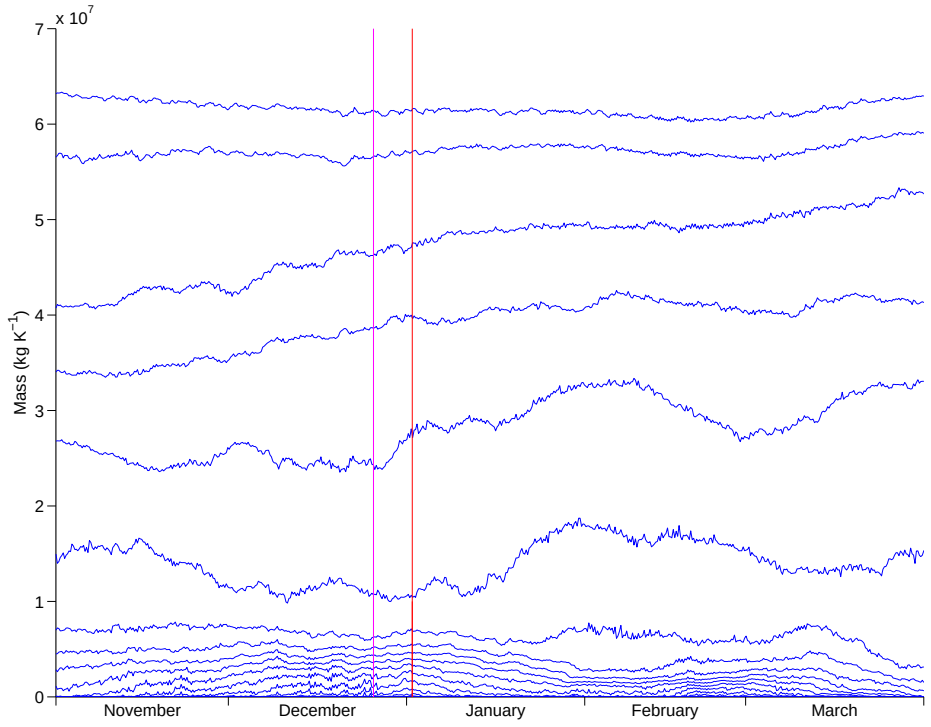

Figure 3.23: $\mathcal{M}_{Q,\theta}$ for the winter 1st November 1984 to 31st March 1985 on $\theta = 600$ K. 15 PV contours are plotted from -6.85 PVU to 198.95 PVU

inside the inner contours. This is only slightly more than can be seen in the winter of $1990-1$, which featured no major sudden warming events (see Figure 3.44).

Although the 950 K isentropic level is not shown here, the signal of the warming can be seen on this level with more change in mass than for $\theta = 850$ K similar to what is seen for the $1978-9$ between the two higher levels. This suggests that the smaller vortex was slower to break down on the 850 K level than higher in the stratosphere. Comparing $\mathcal{V}_{Q,\theta}$ on the various vertical levels also suggests a similar poleward movement of air within the vortex as those for the $1978-9$ winter.

3.4.4 1983-4

The two winters examined above are both winters in which vortex splitting events occurred. Vortex displacements, which are dynamically distinct from splitting events (Matthewman et al., 2009) are now examined in an attempt to identify

any differences in the pattern of stripping prior to the onset of the warming.

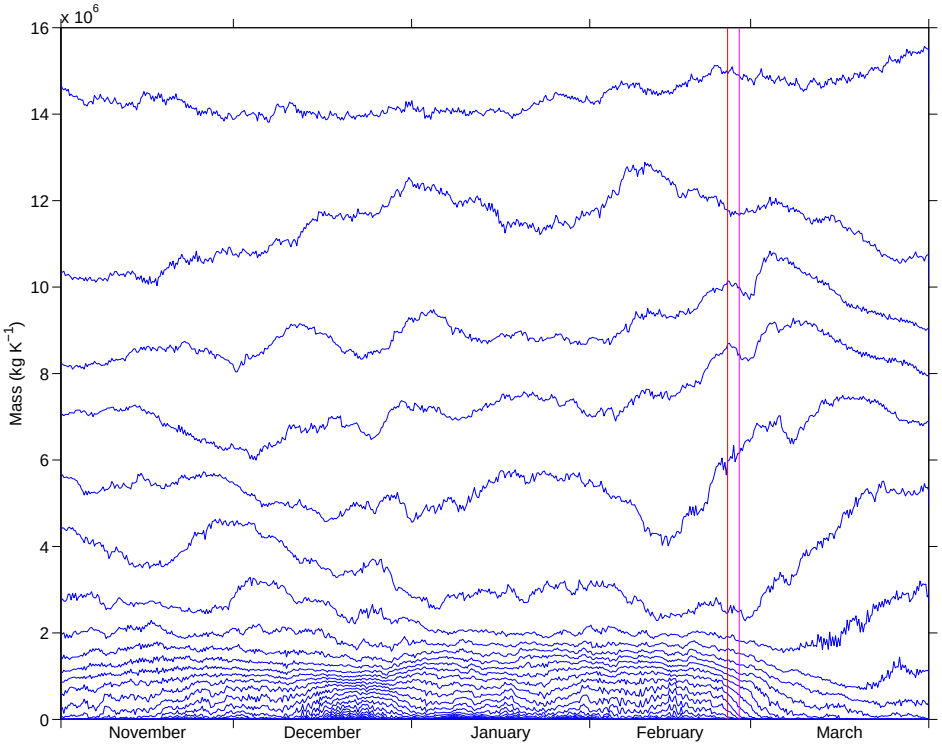

Figure 3.24: $\mathcal{M}_{Q,\theta}$ for the winter 1st November 1983 to 31st March 1984 on $\theta = 850$ K. 22 PV contours are plotted from 15.2 PVU to 1544 PVU

A particularly distinct vortex displacement event occurred around 24th February 1984 by the criterion of Charlton and Polvani (2007) and 26th February by those of Mitchell et al. (2013). Figure 3.24 shows the plot of $\mathcal{M}_{Q,\theta}$ for this winter on $\theta = 850$ K. Like the splitting events examined above, the signal of the vortex displacement event can be seen around the end of February when the mass of air and size of the vortex decrease following the displacement event. Unlike the events above, the downward movement of the PV contours in the plots does not extend to the contours around the vortex until near to the occurrence of the SSW, as they do in Figure 3.9 for example.

Most of the change in mass occurs in the early winter, while the vortex remains relatively stable throughout the mid winter. Just prior to the date of the

displacement event there is again a poleward trend of PV contours at the edge of the vortex, before the mass inside the main body of the vortex starts to decrease as the vortex returns from being displaced to be located once more over the pole.

One other feature of note in Figure 3.24 is that the mass of air within the inner contours of the main vortex is fairly constant throughout the period of the winter up until the displacement event occurred.

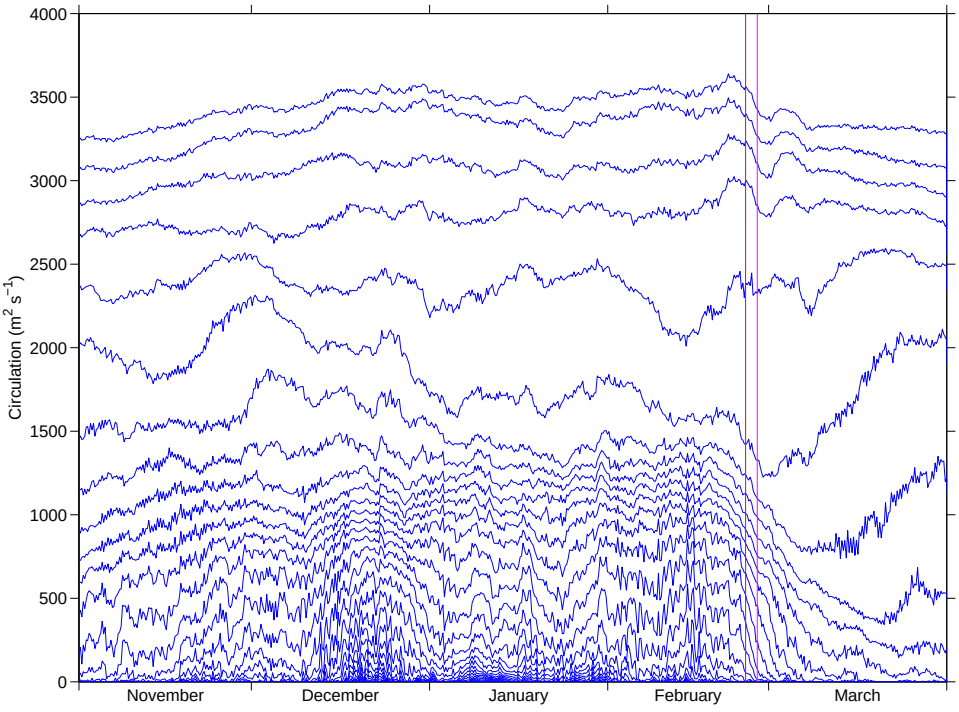

Figure 3.25: Timeseries of $\mathcal{C}_{Q,\theta}$ for 1st November 1983 to 31st March 1984 on the 850K isentropic level. There are 29 PV contours are plotted equally spaced between 74 PVU and 1720.4 PVU

The circulation $\mathcal{C}_{Q,\theta}$ on $\theta = 850$ K for $1983-4$ is shown in Figure 3.25. The vortex can be seen strengthening between the start of November and mid December where the circulation of the contours making up the vortex increases and the gradient of PV sharpens. This strengthening of the circulation of the contours making up the vortex is more gradual than the strengthening of the $1978-9$ winter. The circulation in the main part of the vortex remains fairly stable for most of the mid

winter period, from around mid December until the decrease in circulation caused by the onset of the displacement stratospheric sudden warming event around 24th February. Following the warming a large number of the PV contours from inside the vortex decrease to have zero circulation, only the outer contours start to increase in circulation again to reform the vortex before the final warming occurs. The outer contours do not show as much change for this winter as they do for $1978-9$, though this is common with the difference visible between the two mass plots seen above.

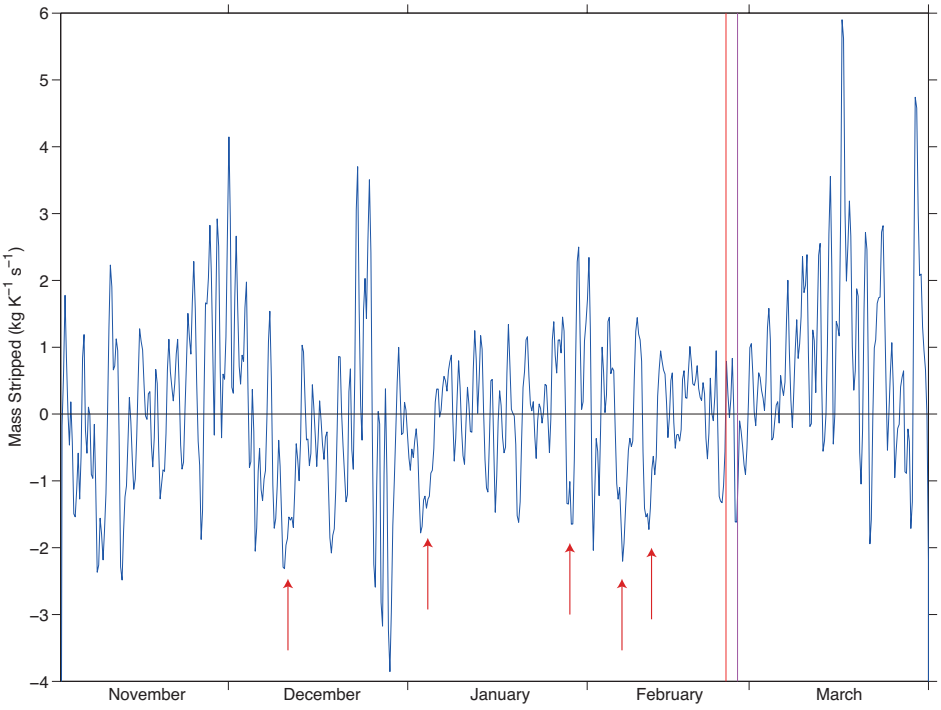

Figure 3.26: Timeseries of $\mathcal{V}_{Q,\theta}$ from 1st November 1983 to 31st March 1984 for 338.6 PVU on the 850 K isentropic surface.

Figure 3.26 is a timeseries for the stripping term $\mathcal{V}_{Q,\theta}$ for $1983-4$ on $\theta = 850$ K. This contour again lies on the vortex edge. The figure clearly shows several stripping events, similar to those seen in the vortex stripping events above. These events account for significant amounts of mass being removed from the vortex as well as some events where mass is added back into the vortex. The mass stripping

events seem to occur throughout the winter, though the events become more frequent in the month or so leading up to the warming, as well as several large events in the period prior to this. At the start of the winter the PV gradient on the edge of the vortex is not as defined as later in the winter. The stripping of filaments in the early winter acts to remove air from the contours on the edge and strengthen the PV gradient there.

Following the sudden warming event, and the subsequent breakdown of the vortex, there is a significant amount of air moved back into the vortex, as it reforms and starts to recover to its pre-warming state.

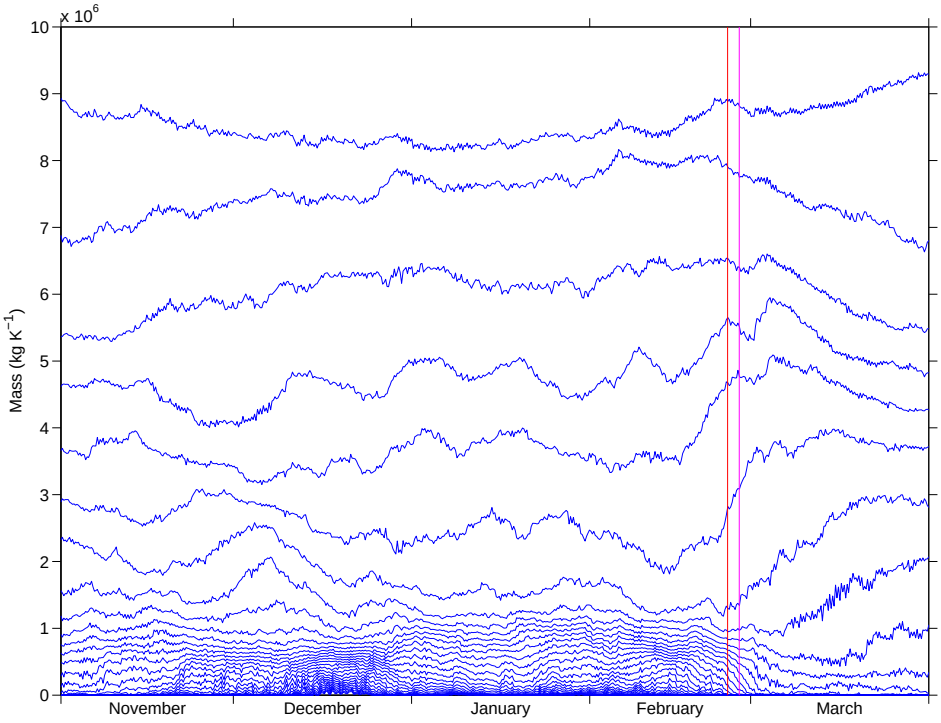

Figure 3.27: $\mathcal{M}_{Q,\theta}$ for the winter of 1983-4 from 1st November to 31st March on the 950K isentropic surface for 31 evenly spaced PV contours between 191.6 PVU and 2690.6 PVU

The pictures shown on both the 950 K and 600 K isentropic surfaces for the mass inside the vortex over the period of the winter (see Figure 3.27 and Figure 3.28) are both very similar to that on the 850 K surface. The dropping in mass as the

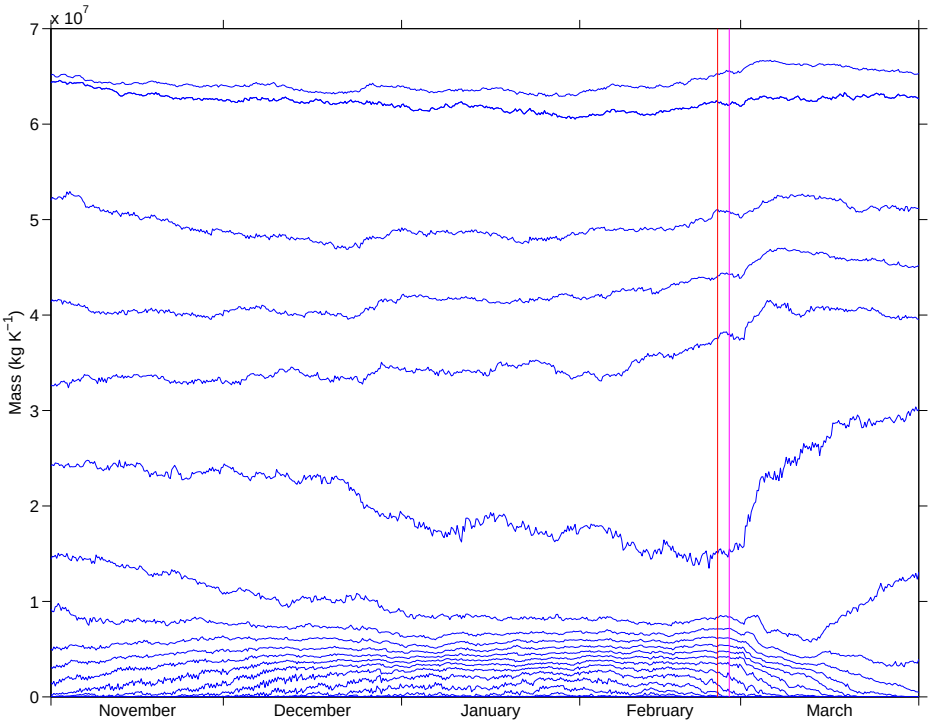

Figure 3.28: $\mathcal{M}_{Q,\theta}$ for the winter of 1983-4 from 1st November to 31st March on the 600K isentropic surface for 33 evenly spaced PV contours between -6.85 PVU and 228.35 PVU

vortex breaks down following the sudden warming occurs slightly earlier on the higher surfaces than on the lower surfaces, similarly to that found above for the winter of $1978-9$.

On the 950K surface there is a sharp increase in mass inside the inner PV contours toward the end of November, and again at the end of December for those near to the vortex edge. Other than this the features noted on the 850K surface can all be seen in this plot, though they appear much more defined on this higher level.

The plots of $\mathcal{V}_{Q,\theta}$ on $\theta = 950$ K have a positive bias, especially in the period following SSW events, similar to what was observed for the splitting events (Figure 3.29). Similarly the $\theta = 600$K level shows plots of $\mathcal{V}_{Q,\theta}$ which show a negative bias on the outer contours. After the sudden warming, between the end of

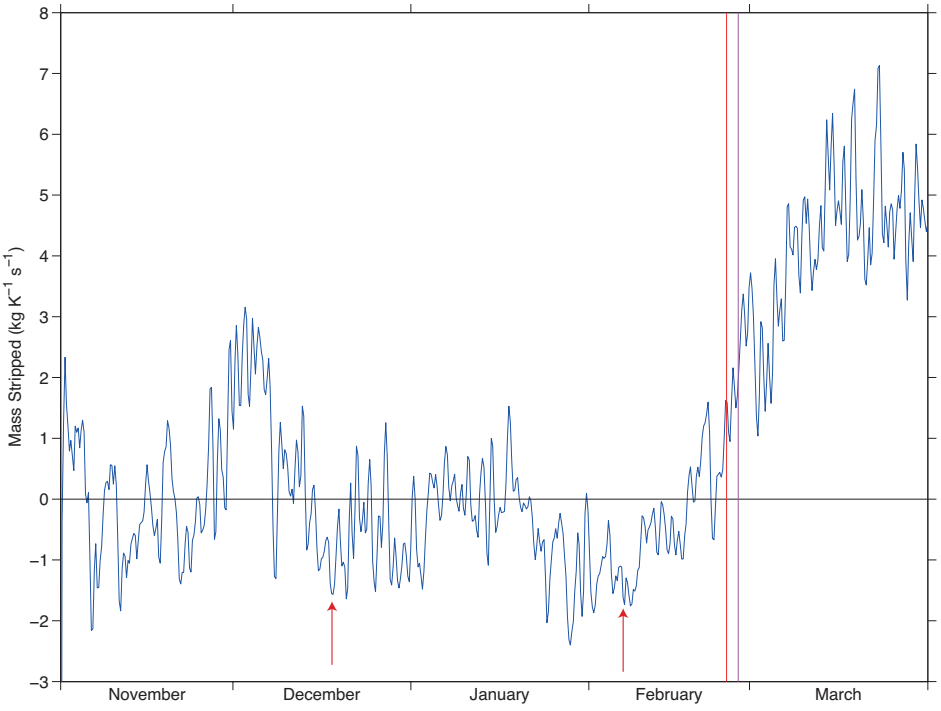

Figure 3.29: Timeseries of $\mathcal{V}_{Q,\theta}$ from 1st November 1983 to 31st March 1984 on the 950K isentropic surface for PV contour 603.2 PVU.

February the beginning of March, on contours nearer to the center of the vortex which in the previous period showed a more neutral balance between outflux and influx of mass there is a significant amount of mass mixed out of the vortex on the 600K level and in to it on the 950K level.

This positive bias on the higher isentropic levels and negative bias on the lower isentropic levels indicates downward movement of air within the vortex.

The $\theta = 950$ K level again shows the signal of the warming event appearing slightly earlier on this level than it does on the 850 K level for the event occurring in February 1984 (Figure 3.30). The contours on and around the edge of the vortex start to increase in circulation again about 10 days after the warming signal appears, the outer ones returning to near early winter levels but the vortex doesn't fully recover to its pre-warming circulation by the end of March and remains relatively undefined in Figure 3.30. The early winter gain in circulation and increase

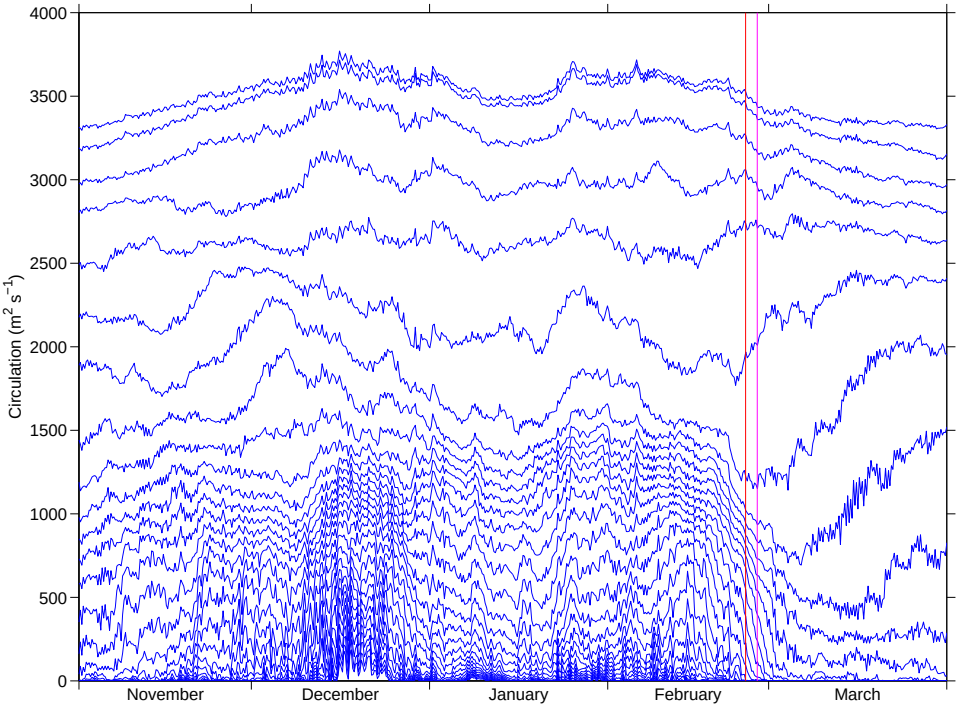

Figure 3.30: Timeseries of $\mathcal{C}_{Q,\theta}$ for 1st November 1983 to 31st March 1984 on the 950K isentropic level. There are 29 PV contours plotted equally spaced between 191.6 PVU and 2661.2 PVU

in PV gradient of the vortex is present, and like the signal of the warming seems to propagate downward to the lower level since the period of relatively stable circulation appears to start earlier here than for $\theta = 850$ K, appearing to begin in early December here in contrast to mid to late December lower down. In mid to late January there is another slight increase in circulation, though not as much as that in November and early December. This increase is larger than the corresponding increase for $\theta = 850$ K around the same time and the propagation downward from 950 K can be seen here as well.

Figure 3.31 shows that similarly the signal of the warming as well as the initial strengthening appear to occur slightly later again on the 600 K surface than both of the 850 K and 950 K surfaces. The period of relatively stable mid winter circulation on PV contours occurs between the start of January and the end of February when

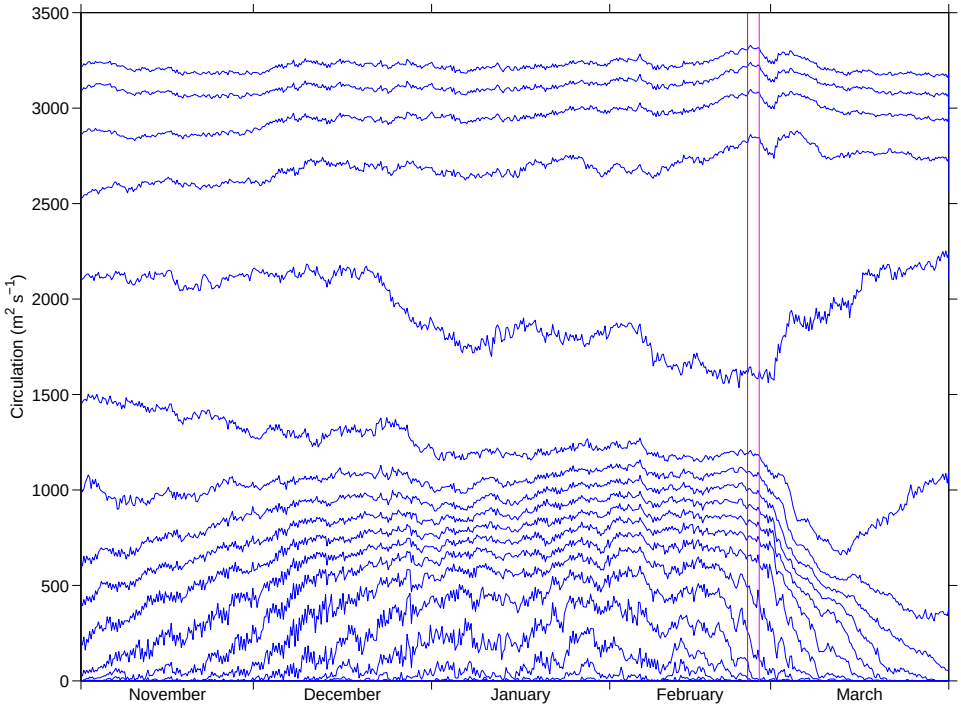

Figure 3.31: Timeseries of $\mathcal{C}_{Q,\theta}$ for 1st November 1983 to 31st March 1984 on the 600K isentropic level. There are 35 PV contours plotted equally spaced between 0.5 PVU and 250.4 PVU

the vortex breaks down. There is a slight growth of circulation around the start of February but much slower than the growth at the start of the winter as the vortex strengthens. The growth of circulation is much more steady on $\theta = 600$ K than it is higher in the stratosphere where the process is almost split into two phases on some surfaces, the first with steady growth in circulation over a period of a month or so, before a more rapid increase immediately before the plateau around the middle of December. The signal of the warming doesn't become visible on this level until the start of March. It is again more gradual than on the above levels, with the circulation on the contours inside the vortex still decreasing until the end of March.

3.4.5 1981-2

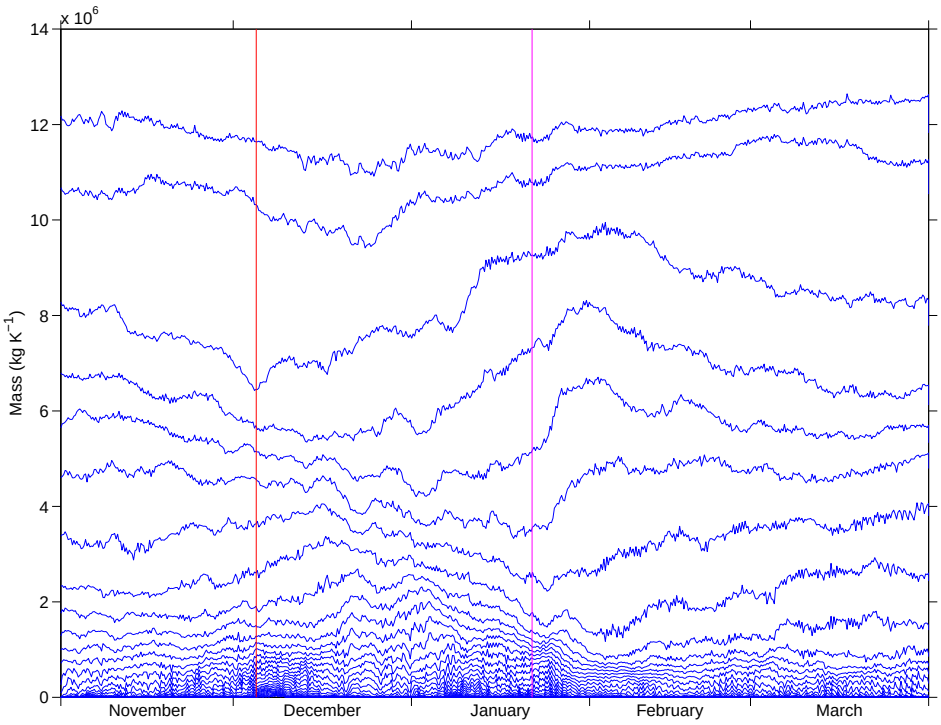

Figure 3.32: $\mathcal{M}_{Q,\theta}$ for the winter 1st November 1981 to 31st March 1982 on the 850 K isentropic level. 21 PV contours are plotted from 132.8 PVU to 1308.8 PVU

Charlton and Polvani (2007) identified a vortex displacement event to have occurred with a mid date of 4th December 1981. The mass $\mathcal{M}_{Q,\theta}$ on $\theta = 850$ K for the winter of $1981-2$ is plotted in Figure 3.32. In the figure there is not the clear signal that there was for the 2 splitting events and 1 displacement event above, that a sudden warming event has occurred. It is possible that this is due to the difference in dynamics between the two warming events; splitting events being barotropic, and displacement events being baroclinic (Matthewman and Esler, 2011). Also during a typical splitting event the vortex will split into two where one of the two 'daughter' vortices will breakdown and the other will move back over the pole and reform the vortex. This will cause the mass within the vortex to decrease since the air within one of the two has been mixed into the surf zone and no longer makes up the main vortex. During a typical displacement event the vortex will move to be

displaced from the pole before it moves back to be centred on the pole again. There is not necessarily any movement of a significant mass of air from the interior to the exterior of the vortex for the signal to show up in the plot of $\mathcal{M}_{Q,\theta}$. Another possible reason is that the vortex is not yet well formed as the warming is very early in the winter. This may result in the recovering vortex becoming stronger than the pre-warming vortex as following the SSW event the vortex seems to undergo a strengthening during early December.

It is also the case however that there was no event identified for December 1981 by Mitchell et al. (2013). There is, though, a splitting event identified on 21st January 1982 by Mitchell et al. (2013) which was not classified as a major warming by Charlton and Polvani (2007). Around this date the vortex can be seen to split into two distinct parts, although one of the resultant vortices is relatively undefined and breaks down within a couple of days. There is a reduction in mass seen in Figure 3.32 around the time of the Mitchell et al. (2013) splitting unlike the Charlton and Polvani (2007) displacement, which can be considered the signal of this event, though it is not quite as pronounced as the signals of the warmings common to the two criteria.

While the event is less defined in Figure 3.32 than other events a similar pattern as that observed in the lead up to the above events can still be seen here. The PV gradient on the edge of the vortex can be seen increasing prior to the splitting, as well as the decrease of the mass within it as the smaller weaker sub vortex breaks down.

The plots for $\mathcal{V}_{Q,\theta}$ are similar to those for the winters examined above, indicating that most of the change in $\mathcal{M}_{Q,\theta}$ for $\theta = 850$ K is due to stripping of PV filaments rather than diabatic effects moving air vertically throughout the vortex. The events that can be seen in the $\mathcal{V}_{Q,\theta}$ term can again be matched up to PV maps, where filaments of PV being removed and mixed into the surrounding air can clearly be seen. In Figure 3.33 b) there are various events, one of which can be seen in late January/early February, Figure 3.34 shows a PV map for 29th January 1982 with the solid black line corresponding to the same PV contour as the top right plot in

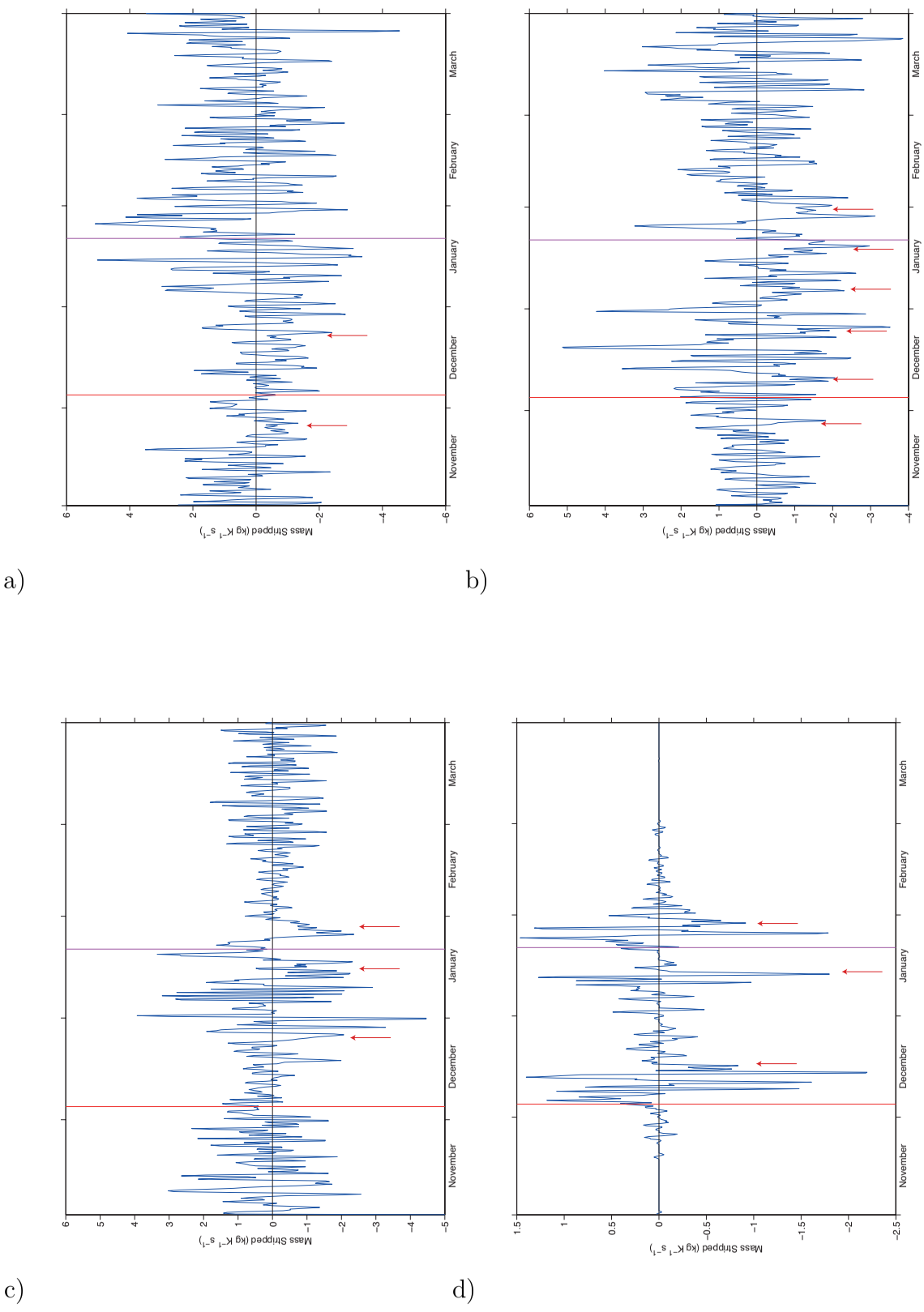

Figure 3.33: Timeseries of $\mathcal{V}_{Q,\theta}$ from 1st November 1981 to 31st March 1982 on the 850K isentropic surface for PV contours with values 250.4 PVU (a), 368 PVU (b), 662 PVU (c) and 956 PVU (d).

Figure 3.33. There is a portion of air at around 180° which is disconnected from the centre of the vortex and is being mixed into the surrounding air.

This effect can also be seen for other events picked out from plots of $\mathcal{V}_{Q,\theta}$ which can easily be matched up to events in the corresponding PV maps.

There are several stripping events in the lead up to the 'vortex displacement' on 4th December. These events are not as large as the corresponding events for previous winters but here the vortex is not as strong as it is where larger stripping events occur. It is possible that for this early winter SSW there is some 'competition' between the radiative growth of the vortex and the stripping, meaning that stripping is suppressed during this period of work.

Much larger events occur later in the winter once the vortex has recovered. Most of these larger stripping events occur in the period immediately before the 'splitting' event on 21st January. This is similar to the pattern of stripping in the lead up to the 1979 and 1984/5 splitting events, with a large stripping event immediately before the breakdown and several other large events at roughly 15 and 30 days previously.

The vertical structure of $\mathcal{M}_{Q,\theta}$ is similar to what is expected from winters examined above, albeit without the clear decrease in mass associated with the other sudden warmings in December. The increase in mass around the start of December occurs slightly earlier on the higher levels and propagates down through the stratosphere.

The vertical structure of $\mathcal{V}_{Q,\theta}$ is also similar to that of other winters. In the month or so before the sudden warming in January $\mathcal{V}_{Q,\theta}$ predominantly shows outward flux of mass from the vortex on all levels. Following this the trend on the higher levels is mainly positive and the lower levels is negative similar to what is observed above.

Figure 3.35 shows mass $\mathcal{M}_{Q,\theta}$ as a function of Q on the 850K isentropic level for various instants between November 1981 and March 1982. Between the initial early November (blue line) and the December 'displacement' SSW (red line) there is a significant increase in mass of some of the higher valued PV contours along

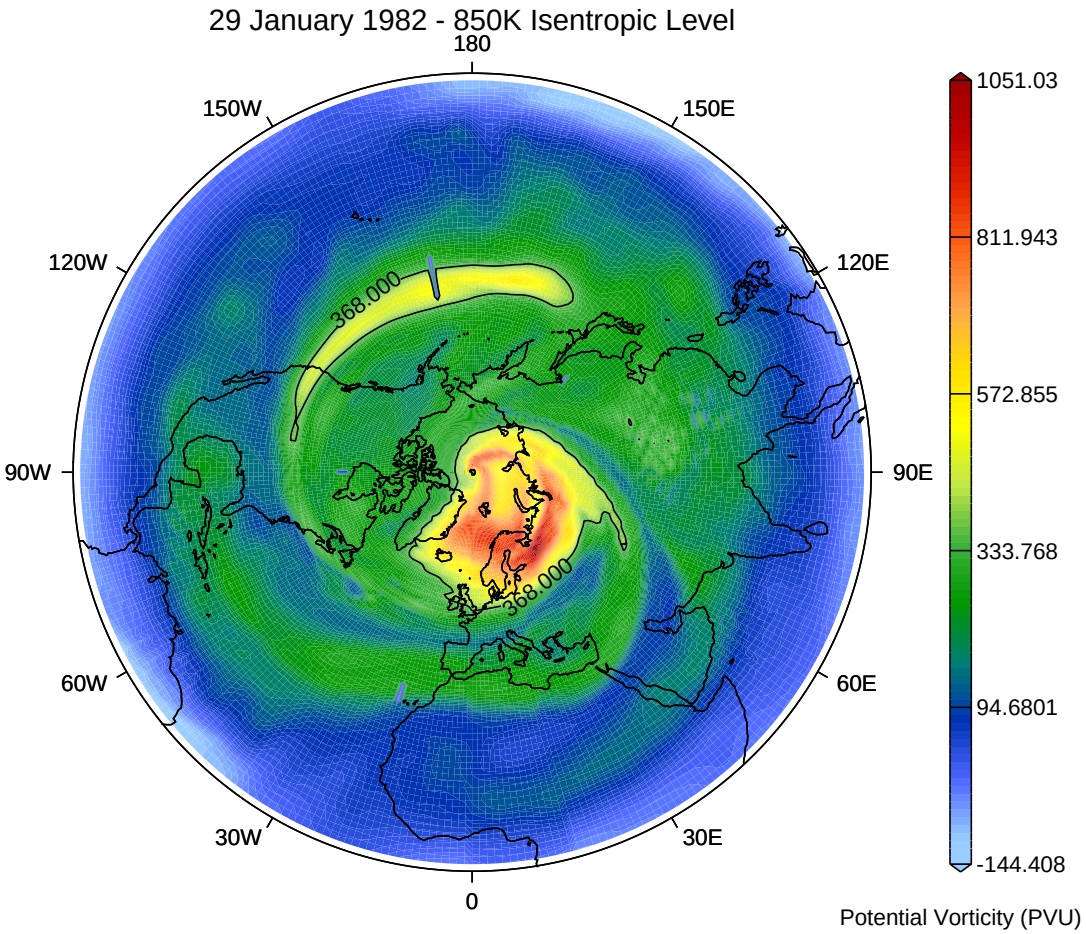

Figure 3.34: PV map for 29th January 1982 on the 850 K isentropic surface. The solid line shows $Q = 368$ PVU. A filament of PV can be seen being mixed into the air surrounding it.

with a much larger decrease in the lower valued contours. The profile of the red line shows several areas of high PV gradient interspersed with areas of lower PV gradient, again creating a PV staircase structure.

By the time of the 'splitting' SSW (magenta line) the staircase structure has largely disappeared with the higher valued (above 250PVU) PV contours decreasing in mass compared to the red line and the lower valued contours increasing to 'smooth out' the 'steps'. The PV gradient on the vortex edge does not change

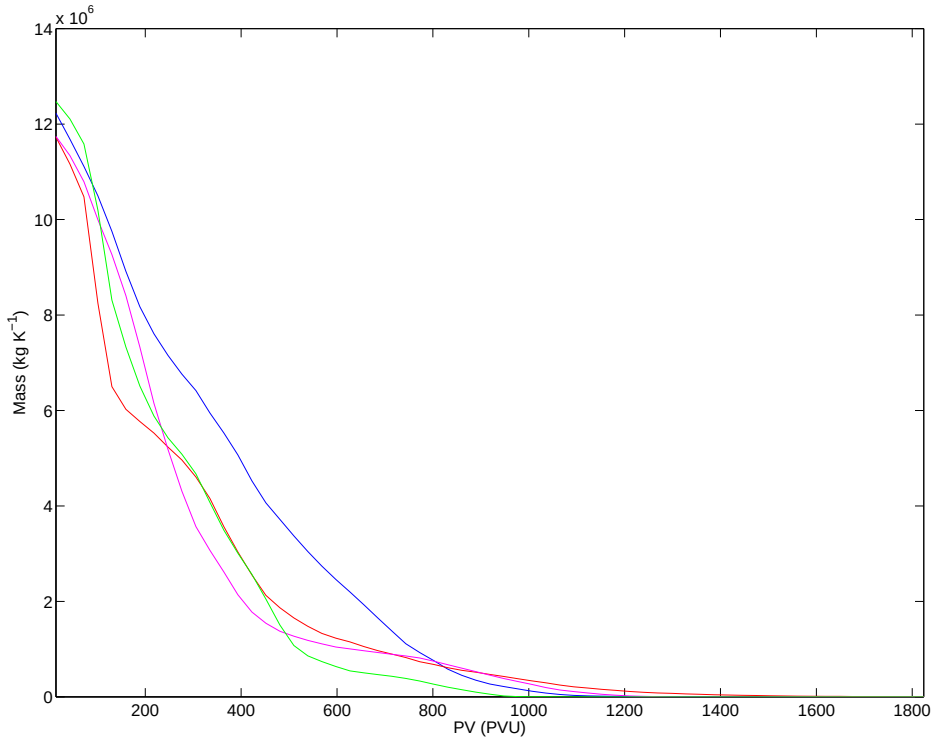

Figure 3.35: Potential Vorticity against Mass on $\theta = 850$ K for various times during the $1981-2$ winter. The blue line corresponds to early November (10th), red to the time of the SSW identified by Charlton and Polvani (2007) (3rd December), magenta to the Mitchell et al. (2013) SSW (24th Jan) and green is in mid March (15th).

much between the two cases.

The mass within the higher valued PV contours, 500PVU and above, decreases along with the contours between 100PVU and 300PVU. Between 300PVU and 500PVU there is an increase in mass of the PV contours, bringing back a weak staircase structure, though much less defined than it is around the time of the displacement SSW in early December.

3.4.6 1979-80

The differing criteria of Charlton and Polvani (2007) and Mitchell et al. (2013) also disagree on the classifications of the SSW(s) which occur in the winter of $1979-80$.

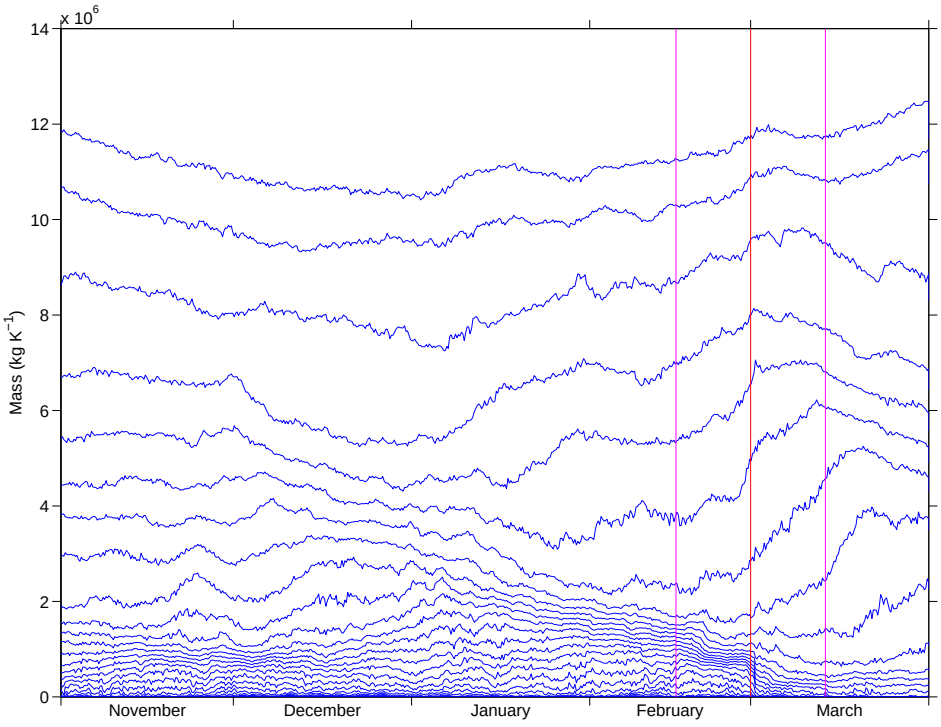

Figure 3.36: $\mathcal{M}_{Q,\theta}$ for the winter of 1st November 1979 to 31st March 1980 on the 850 K isentropic level for 17 PV contours between 132.8 PVU and 1073.6 PVU

The former classifies a single displacement to occur on 29th February 1980 while the latter classifies a splitting on 15th February 1980 and a displacement on 16th March of the same year.

A timeseries of $\mathcal{M}_{Q,\theta}$ for $\theta = 850$ K is shown in Figure 3.36. In Figure 3.36 the signal of a warming event can be seen to have occurred at the end of February. This coincides in timing with the classification of a late February displacement of Charlton and Polvani (2007). There is only a clear signal of one warming in this winter, further favoring this classification over that of Mitchell et al. (2013).

Comparing this, along with the 1984 displacement, with the splitting events of 1979 and 1985, the gradient of PV that makes up the vortex appears to be greater during the winters in which splitting events occurred than it is in winters containing displacement events. The PV throughout the surf zone surrounding the vortex is roughly the same for each type of event, though the maximum value of the PV on

a given surface is much higher in winters containing splitting events.

3.4.7 1987-8

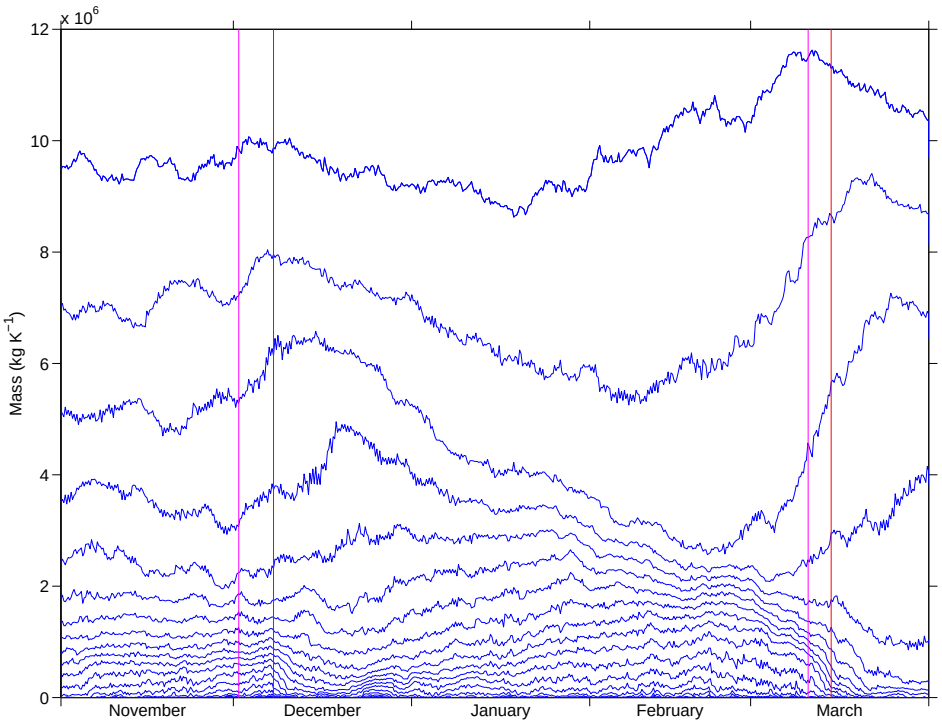

Figure 3.37: $\mathcal{M}_{Q,\theta}$ for the winter of 1st November 1987 to 31st March 1988 on the 850 K isentropic level for 17 PV contours between 132.8 PVU and 1073.6 PVU

Although the two sets of criteria differ in the number of events which occur in $1979-80$, they both identify two sudden warming events to occur in the $1987-8$ winter, though they disagree about the classifications of these events. The criteria of Charlton and Polvani (2007) identify two splitting events on 7th December 1987 and 14th March 1988, while those of Mitchell et al. (2013) identify a mixed event, where the vortex changes in state between split and displacement, to occur on 1st December 1987 and a displacement on 10th March 1988. The signals of these two events can clearly be seen in the timeseries of $\mathcal{M}_{Q,\theta}$ in Figure 3.37 where in early December and mid March the mass of air within the vortex can be seen to have depleted.

Following the early splitting/mixed event the vortex recovers more quickly than for the two splitting events of $1978-9$ and $1984-5$. For example the splitting event of early January 1985 (Figure 3.21) doesn't see the vortex fully recover until late February, with no clearly defined vortex visible in the intervening period. In contrast the splitting/mixed event of December 1987 sees a drop in mass of the vortex, followed by a recovery by late December and by January the vortex is almost fully recovered to its pre-warming state.

The other warming event which occurred in early winter $(1981-2)$ also shows a similarly fast recovery to its pre-warming state.

Following the splitting event the vortex slowly grows in mass, with the contours immediately surrounding the main area of steep PV gradients losing mass to become part of this area of highly concentrated PV contours. By mid February the vortex has become stronger than it was before the initial early winter event occurred. Once it reaches a peak in mass in mid to late February it starts to become eroded, undergoing a short phase of erosion in early March before the breaking in mid March.

The recovery following the early March warming is more like what can be seen in other winters with a longer period where the vortex remains relatively weak until the end of March.

The signal of the early winter vortex breakdown seems to appear at roughly the same time on the 950 K isentropic level as it does on the 850 K level (Figure 3.38). The 600 K level (Figure 3.40) still shows the delayed signal of the warming seen in other winters. This means that the breakdown appears on the two upper levels near simultaneously but takes a period of a few days to propagate down to the lower 600 K surface.

This seems to be the case with the later March event as well, with the breakdown appearing much later and occurring at a much slower rate at 600 K compared to 850 K and 950 K.

Following the December event, in the period of the weakened vortex where the vortex seems to be strengthening on the 850 K level there is another small dip in

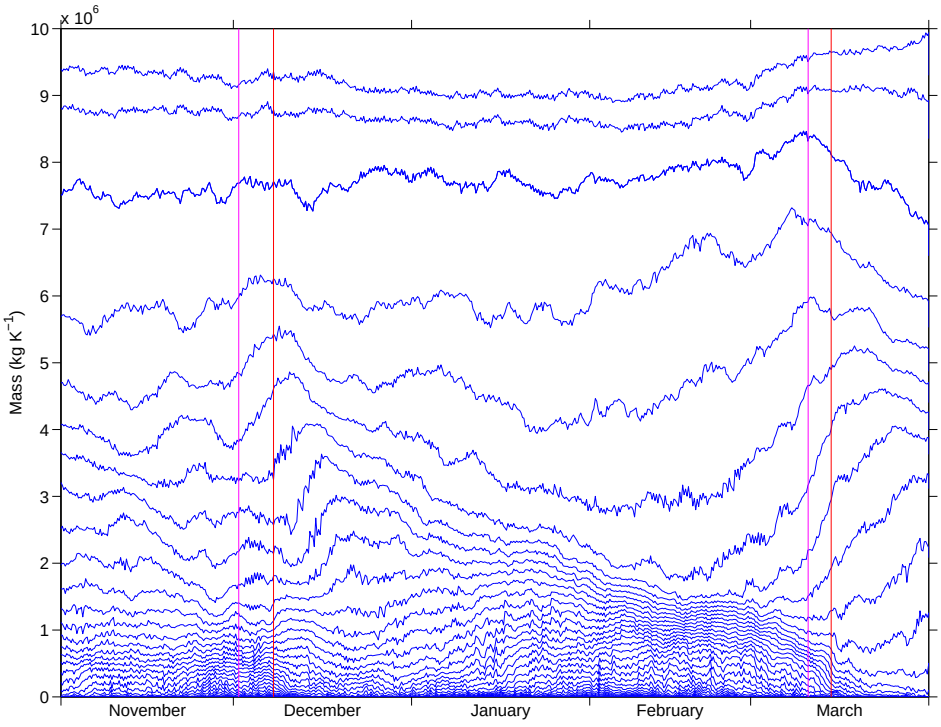

Figure 3.38: $\mathcal{M}_{Q,\theta}$ for the winter of 1st November 1987 to 31st March 1988 on the 950 K isentropic level for 42 PV contours between 15.2 PVU and 2661.2 PVU

mass inside the vortex on the 950 K level at the end of December before it starts to increase as it recovers on this level too.

The two phases in the March warming event don't seem to be present on the 950 K surface. Instead the breakdown seems to be more like one more gradual erosion of the mass within the vortex. The vortex does seem to start recovering on this level at the same time as it does on 850 K with some contours starting to grow in mass until the end of March.

Figure 3.39 shows the circulation for the winter of $1987-8$ at 850 K. In the circulation plot there is a dip around the end of December which coincides with the timing of the dip in $\mathcal{M}_{Q,\theta}$ for $\theta = 950$ K (Figure 3.38) but didn't appear to have a counterpart in the mass timeseries for 850 K. This dip occurs after the main loss in mass following the breakdown due to the sudden warming event.

The two phases of erosion in the March breakdown event are more pronounced

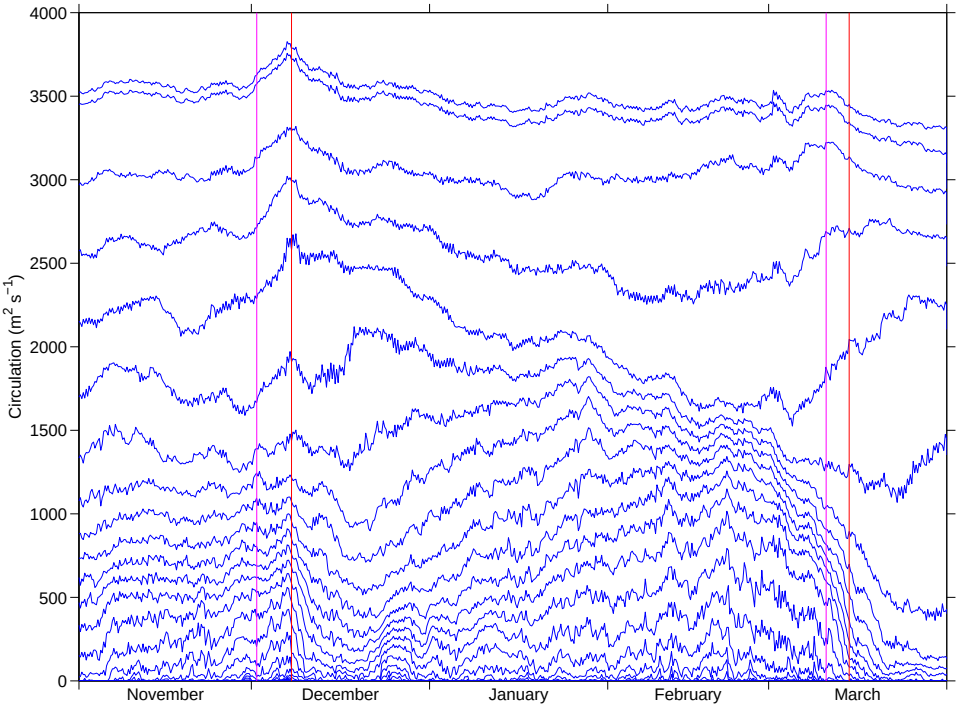

Figure 3.39: Timeseries of $\mathcal{C}_{Q,\theta}$ from 1st November 1987 to 31st March 1988 on the 850K isentropic level. There are 21 PV contours plotted equally spaced between 15.2 PVU and 1191.2 PVU

than they appear in the mass plots. The slowing down in erosion, and even a slight rise in circulation on some of the inner contours can be seen before a rapid reduction in PV for all contours making up the vortex.

There is a fairly rapid rise in the circulation inside the vortex immediately prior to the fall as the December event occurs. The fall in circulation seems to be much more rapid than the loss in mass for the same event. The initial gain in circulation which marks the start of the recovery is also much faster than the rest of the recovery period from late December to late February/early March.

From around mid December, just after the vortex splits, the contours closest to the vortex start to decrease in circulation bringing them closer to the vortex and increasing the PV gradient on the edge. These contours continue losing circulation until the vortex starts to displace from the pole, when these outer contours are

stripped from the vortex as it breaks down. These contours seem to be only loosely attached to the vortex as they do not follow the same rapid breakdowns as the other inner contours.

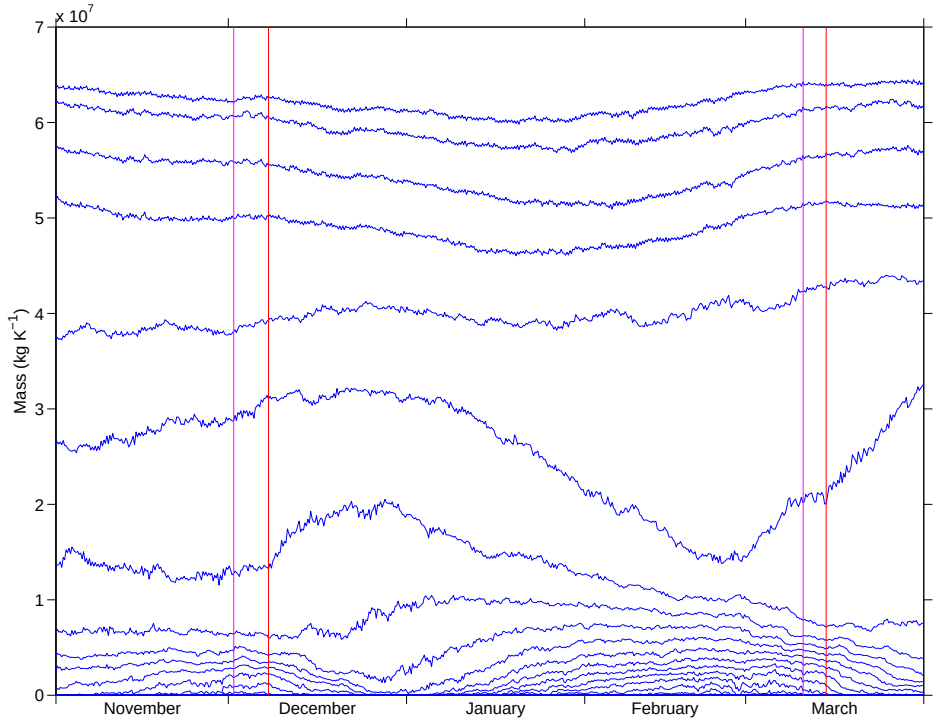

Figure 3.40: $\mathcal{M}_{Q,\theta}$ for the winter of 1st November 1987 to 31st March 1988 on the 600 K isentropic level for 17 PV contours between 0.5 PVU and 228.35 PVU

There seems to be a two stage element to the December splitting/mixed event for $\theta = 600$ K seen in Figure 3.40 where there is an initial decrease in mass at the start of December with a second drop in mass near to the end of December. The minimum in mass following this second stage roughly coincides in timing with the second small dip at 950 K. Following this the vortex starts regaining mass again and by mid January has attained its pre-warming mass. This seems to agree with the mixed classification of Mitchell et al. (2013), where it appears that the vortex indeed undergoes two stages of breakdown.

The late event, as well as occurring later than it does higher up, also happens much more gradually at 600 K. By the end of March the vortex itself doesn't seem

to have started recovering in the way it has higher up.

The contours surrounding the vortex aren't eroded as much as they are on the higher levels, and at a much slower rate. The erosion of the vortex also doesn't propagate toward the centre as it does higher up, but seems to occur almost simultaneously at all PV values.

3.4.8 1990-1

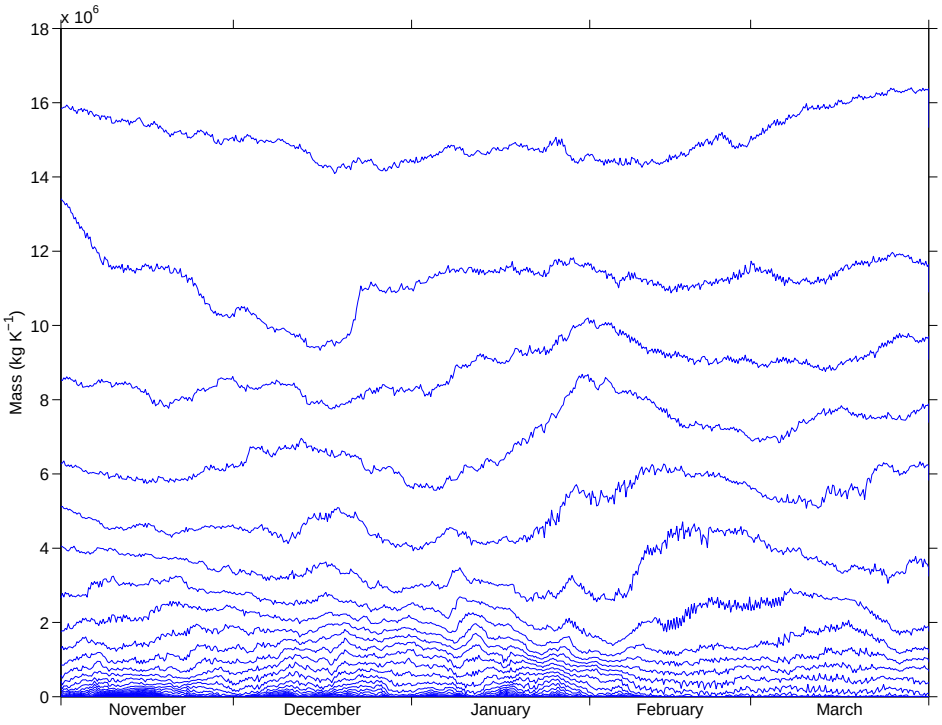

Figure 3.41: $\mathcal{M}_{Q,\theta}$ for the winter of 1st November 1990 to 31st March 1991 on the 850 K isentropic level for 28 PV contours between 15.2 PVU and 1602.8 PVU

So far all the winters examined have been ones in which sudden warming events have occurred. These are of main interest here, but examining winters in which no major warming took place is a useful way to try to differentiate between features in plots of $\mathcal{M}_{Q,\theta}$ and $\mathcal{V}_{Q,\theta}$ which can be seen as typical of an undisturbed polar vortex in the Northern hemisphere and those which are specific to either displacement or splitting events.

Figure 3.41 and Figure 3.43 show the plots of $\mathcal{M}_{Q,\theta}$ for the winter of $1990-91$ on the $\theta = 850$ K and $\theta = 950$ K isentropic surfaces respectively. This is a winter in which no major sudden warming events occurred by the criteria of either Charlton and Polvani (2007) or Mitchell et al. (2013). Figure 3.41 shows a vortex which looks similar to the undisturbed parts of some of the other winters examined at this vertical level, for example the early part of the winter of $1978-9$ up to the start of January, before the size of the vortex begins to decrease in mass in the run up to the late winter splitting event. There are notable differences however, for example the gradient of PV making up the edge and body of the vortex for the $1978-9$ winter is much steeper than for the $1990-91$ one. For the portion of the winters surrounding major warming events the picture described by the plots of $\mathcal{M}_{Q,\theta}$ are very different however, with much more change in the mass of the vortex seen in the disturbed vortices exhibiting warming events.

Examining plots of $\mathcal{V}_{Q,\theta}$ (Figure 3.45) there is much less movement of air across contours of PV within the vortex for this uneventful winter than in the disturbed winters which result in sudden warming events. Comparing Figure 3.45 to the same contour for $1978-9$ there is in the region of 3 times the mass of air moved across the PV contour for the period of the whole winter of $1978-9$ as there is in the winter of $1990-91$. Comparing Figure 3.45 to the winter of $1984-5$, there is also around 2 times as much mass movement though the contours for the earlier winter than for $1990-91$.

While the mass Figure 3.41 shows relatively little variation over the course of the winter with no clear events visible, the timeseries of circulation features much more relative change over the course of the winter. The change in the circulation is still less than in winters in which SSWs occurred but unlike in the mass plots it is possible to identify several small events over the period of the winter.

For example, at the start of December there is a small increase in circulation followed by another about 10 days later. At the end of January and the beginning of February there are two small drops in circulation where the circulation drops back to just below what it was at the start of November. This drop is not as large

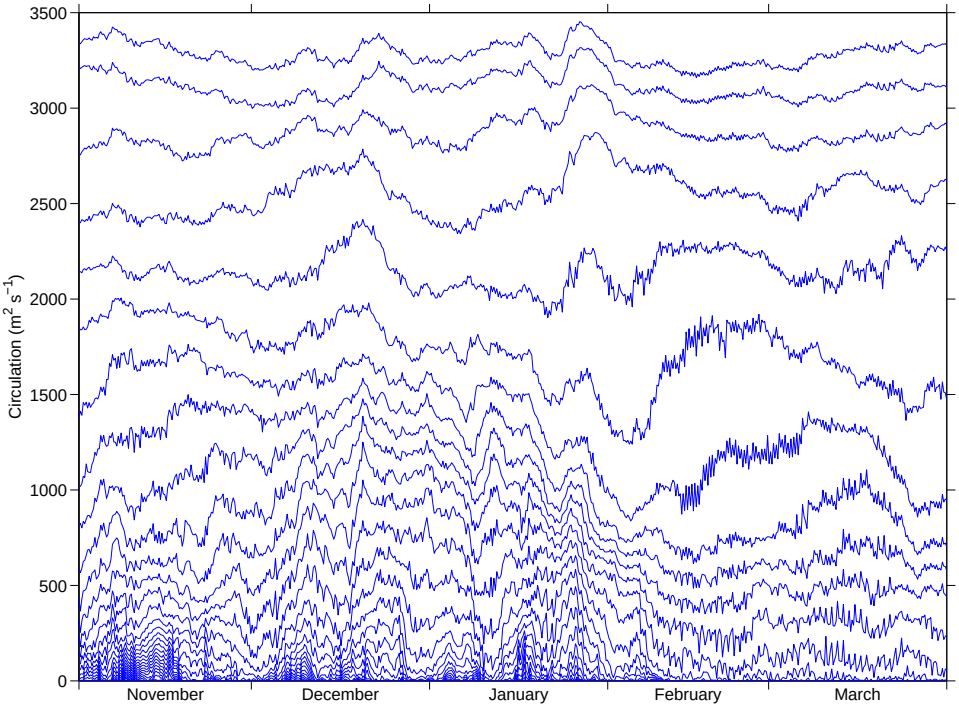

Figure 3.42: Timeseries of $\mathcal{C}_{Q,\theta}$ for the winter of 1st November 1990 to 31st March 1991 on the 850 K isentropic level for 31 PV contours between 15.2 PVU and 1779.2 PVU

and is less sudden than is seen around the time of major warmings and is more of a gradual reduction in the circulation of the vortex.

Although there are more features visible in the circulation plots than in the equivalent mass plots the changes in the circulation for the winter of $1990-91$ occur at a much slower rate than in other more eventful winters.

Figure 3.43 shows $\mathcal{M}_{Q,\theta}$ on the 950 K isentropic level. This figure shows that the vertical structure of the vortex on the higher levels is similar to that of eventful winters, other than the differences already noted for $\theta = 850$ K. The PV gradient of the vortex edge on the higher level is steeper than it is lower down, resulting in higher PV values making up the edge and centre of the vortex.

On the 600 K isentropic level the change in mass within a given contour of PV is very small over the course of this uneventful winter (see Figure 3.44). Again

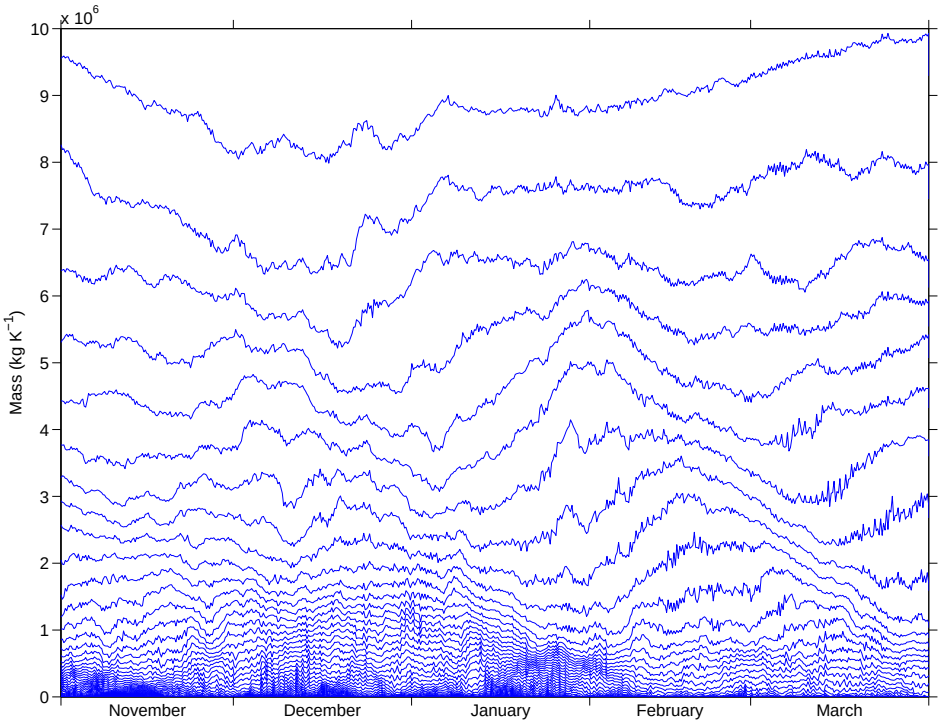

Figure 3.43: $\mathcal{M}_{Q,\theta}$ for the winter of 1st November 1990 to 31st March 1991 on the 950 K isentropic level for 42 PV contours between 15.2 PVU and 2484.8 PVU

this pattern matches that of the start of the eventful winter, up until the vortex starts to become disturbed leading up to the sudden warming. Once the vortex has strengthened, from about the start of December, the mass remains relatively constant until the end of March.

The picture of the stripping $\mathcal{V}_{Q,\theta}$ on the $\theta = 950$ K surface is quite different to some of the winters examined above. The trend is similar to that seen for the $1981-2$ winter, with a mainly negative trend towards the start of the winter and a mainly negative towards the end (Figure 3.46). There is still less mass moved across the edge of the vortex, which is where the contour in Figure 3.46 is located. As the change in mass within the vortex indicated by Figure 3.46 is larger than that indicated the change in $\mathcal{M}_{Q,\theta}$ Figure 3.43 this indicates that there must be significant vertical movement of air similar to that found above.

The 600 K level also shows a negative trend in the plot of $\mathcal{V}_{q,\theta}$ similar to that seen

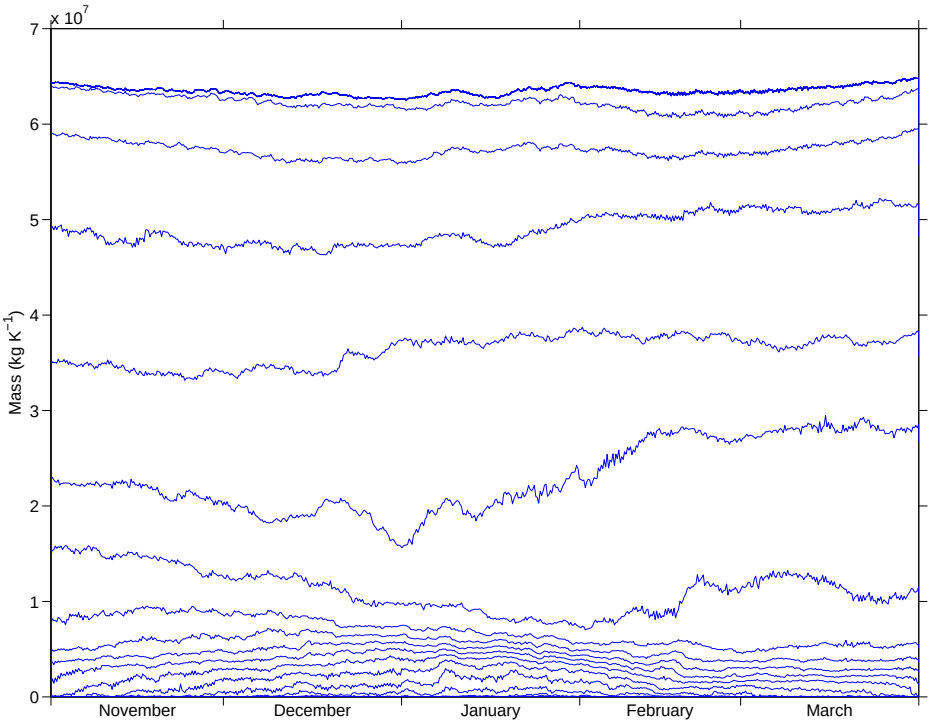

Figure 3.44: $\mathcal{M}_{Q,\theta}$ for the winter of 1st November 1990 to 31st March 1991 on the 600 K isentropic level for 28 PV contours equally spaced between 0.5 PVU and 206.3 PVU

in other winters. Together these indicate that air is moving vertically downward throughout the vortex. This vertical movement will be investigated in the next chapter.

3.5 Conclusions

The mass $\mathcal{M}_{Q,\theta}$, circulation $\mathcal{C}_{Q,\theta}$, stripping term $\mathcal{V}_{Q,\theta}$ and frictional term $\oint_{\Gamma_{Q,\theta}} \mathbf{X}\cdot\mathrm{d}\mathbf{l}$ have been calculated for several winters, both those in which major Sudden Stratospheric Warming events (SSWs) occur and those where no such events are present. Following most of these events the mass of air within the vortex dramatically decreases and the vortex becomes fairly undefined in plots of $\mathcal{M}_{Q,\theta}$. The events where this decrease is less visible, or not at all, are those events where the differing criteria

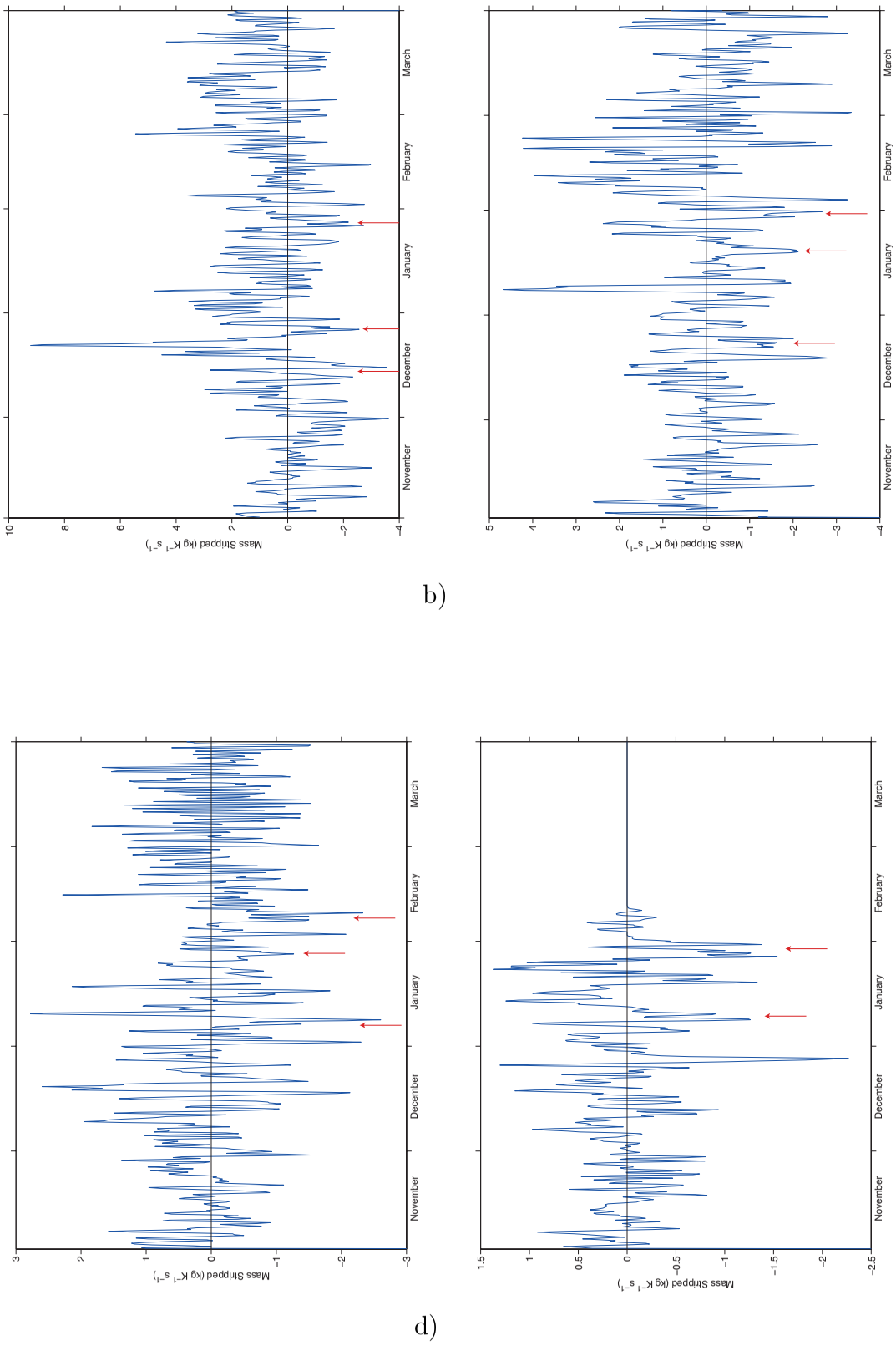

Figure 3.45: Timeseries of $\mathcal{V}_{Q,\theta}$ from 1st November 1990 to 31st March 1991 on the 850K isentropic surface for PV contours with values 44.6 PVU (a), 338.6 PVU (b), 662 PVU (c) and 956 PVU (d).

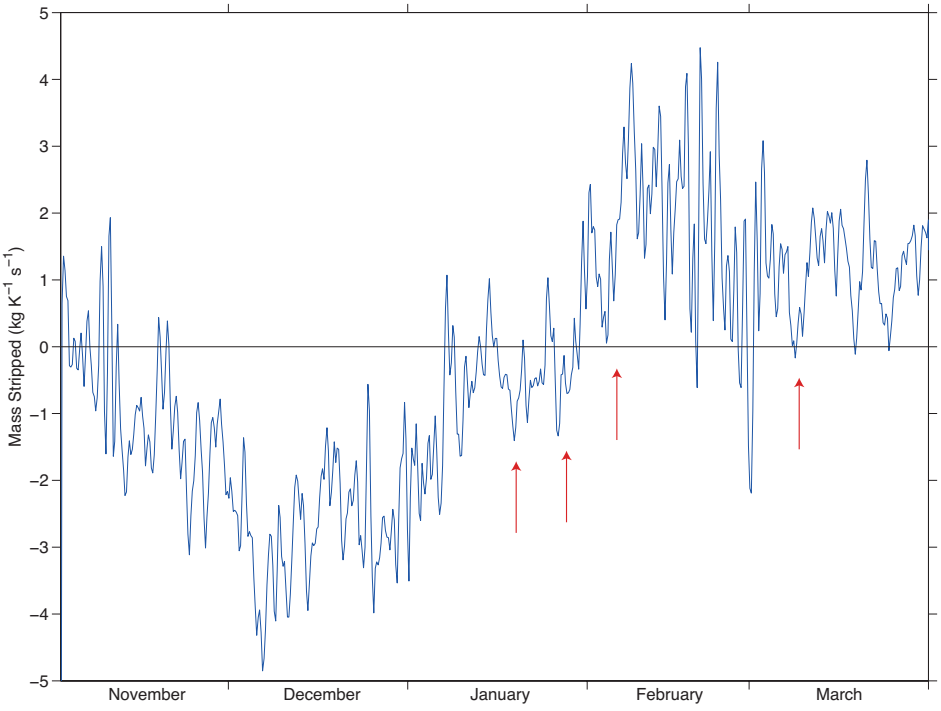

Figure 3.46: $\mathcal{V}_{Q,\theta}$ for the winter of 1st November 1990 to 31st March 1991 on the 950 K isentropic surface for $Q = 602.3$ PVU

of Charlton and Polvani (2007) and Mitchell et al. (2013) disagree on the occurrence of an SSW event, for example the vortex displacement event of 4th December 1981. Also the early winter events show less dramatic decreases in mass than those later in the winter.

The profiles of mass at the start of the winter, in early November, can vary significantly from year to year. The winters where warmings occurred early in the winter do have similar profiles of mass in early November. There doesn't seem to be any similarity between those that occurred later in the winter, or between those in which splitting or displacements occurred.

The behaviour of the vortex around the time of SSWs also differs significantly from year to year. This is similar to the findings of Matthewman et al. (2009), who noted that prior to the onset of SSWs there was a large amount of variability in the strength of the vortex, even when events were grouped into displacement and

splitting events.

In plots of the stripping term $\mathcal{V}_{Q,\theta}$ there are several events throughout the course of the winter where mass is removed from the vortex. These events in $\mathcal{V}_{Q,\theta}$ can be linked to events which occur in PV maps where tongues of air can be seen to be pulled from the vortex coinciding with the mass removal events in $\mathcal{V}_{Q,\theta}$. The amount of air pulled from the vortex in one of these tongues can be a significant proportion of the air within the vortex, typically in the order of 10% of the mass within the vortex.

Several of these stripping events can be identified in these diagnostics in the period leading up to the occurrence of sudden warmings. The diagnostics allow the proportion of air removed from the vortex in these events to be quantified.

Norton (1994) found, using a shallow water model integrated for 100 days, that in the region of 40% of the air within the vortex was removed over the course of the 100 days. This figure is found by comparing the relative size of the vortex before and after the integration. Here it is found that, while the change in mass of the vortex for several of the events is of a similar order to that found in the model of Norton (1994), the stripping term $\mathcal{V}_{Q,\theta}$ shows that much more mass than this, up to double in some cases, is removed from the vortex over the course of a typical winter. This mass is then replaced by downward movement of air within the vortex. This means that much larger amounts of vortex air than estimated by Norton (1994) can end up in the surf zone. This is still small in comparison to the amount of tropical/subtropical air making up the surf zone.

The centre of the vortex does not appear to be as isolated as suggested by Norton (1994) either, with air from the centre moving outward, and eventually into the surf zone in agreement with Waugh et al. (1994).

Using the classifications of Charlton and Polvani (2007), in the 10 days leading up to the dates of the warmings stripping events lasting for periods of roughly 5 days occur in all the winters for which the diagnostics have been calculated. The stripping event seen close to the sudden warming is one of the largest events in each winter, with up to 25% of the mass of the vortex stripped for the largest of

these such events.

These are not the only significant stripping events to occur in the period leading up to the sudden warming events. In those winters where sudden warmings occurred late in the winter, in late February and March, there are other large stripping events through the course of the winter lasting for several days of similar magnitudes to those immediately before the breakdown of the vortex.

In contrast, for winters where the warming events occur early, in December and early January, there are several smaller stripping events lasting around 2 days in length instead of the few larger events seen in the winters where warmings occur later.

There doesn't seem to be a significant difference in the pattern of stripping events in the lead up to vortex displacement and vortex splitting events as defined by Charlton and Polvani (2007). This is similar to the findings of Miller et al. (2013) who found that the biggest differences between the different types of warmings occurred following the date of the sudden warming, with only small differences visible before.

The classifications of Mitchell et al. (2013) also show a similar pattern of stripping in the lead up to sudden warming events with a much larger difference between early and late warming stripping than between displacement and splitting events. The events where the two criteria disagree as to whether a sudden warming occurs are those in which the signal of a warming is less visible in the stripping of filaments of high PV air, though these can still be distinguished from the general background pattern.

The reason for the lack of pattern in the stripping preceding splitting and displacement events seems to be the large amount of inter-event variability seen here and noted by Matthewman et al. (2009), who also noted that there were some splitting events which showed behaviour more characteristic of displacement events than splitting events.

The mass of air within the vortex doesn't seem to attain any fixed value, or "threshold" prior to the breakdown of the vortex, either for splitting or displace-

ment events. There is also not a certain amount of mass which is removed from the vortex via stripping of filaments of air before an SSW will occur.

It seems that large stripping events are a necessary, but not sufficient, condition for an SSW to occur; prior to all SSWs there is a large stripping event, the largest over the course of the winter, but there are several other stripping events of only slightly smaller magnitude which are not followed by SSWs. There are also large stripping events in winters in which no major SSWs occur. These are similar in magnitude to the stripping events which occur throughout winters in which SSWs occur late in the winter.

The circulation of the air at the vortex edge doesn't seem to feature a "threshold" value prior to an SSW event either, although the circulation at the vortex edge for the events identified as displacements on all isentropic levels is in general higher (around 1000-1200m^2 s^{-1}) than that immediately prior to those identified as splitting events (around 800-1000m^2 s^{-1}). This is in contrast to what is found by Matthewman et al. (2009) who found that immediately prior to splitting events the vortex appears stronger than it is in the lead up to displacement events. They did find, however, that there was a large amount of variability in the strength of the vortex prior to SSWs which is in agreement with the results seen here.

The Circulation $\mathcal{C}_{Q,\theta}$ gives a higher resolution view of the area inside of the vortex than the mass does. Correspondingly changes in circulation which are localised to the vortex are easier to see in the circulation than in the corresponding mass plot. The mass shows a clearer view of the formation of the surf zone and the vortex is more clearly separated from the rest of the air surrounding it meaning that it is often advantageous to examine both side by side despite the similarity in the features that both quantities exhibit due to Equation (3.24).

Chapter 4

Lagrangian Stratospheric 'Circulation' Plots

4.1 Introduction

The meridional circulation in the wintertime stratosphere is dominated by the Brewer-Dobson circulation, where air moves from equator to pole, with ascent in the tropics and descent near to the pole. Within the vortex air enters the stratosphere from the mesosphere where it descends (Sutton, 1994).

Both Eulerian and Lagrangian pictures of the meridional circulations have been studied, and have been found to be in some cases very different. In some circumstances the two circulations have been found to have opposite signs (Dunkerton, 1978).

Lagrangian diagnostics are useful when looking at the circulation of the wintertime stratosphere, especially that in and around the vortex, as the vortex is not always located over the pole, for example during SSWs. At these times the strong vortex located away from the pole will distort the view of the Eulerian zonal averages. Using Lagrangian diagnostics can give a view of the circulation relative to the vortex.

The meridional circulation has been calculated in various coordinate systems from ERA-40 data by eg Juckes (2001) and Egger and Hoinka (2014). Both of

these look at flow in the troposphere and lower stratosphere. It is shown by Juckes (2001) that it is possible for the circulation to appear in the opposite sense to the observed transport of tracers, due to the fact that the flow is not zonally symmetric in the atmosphere.

In this chapter the meridional movement of air relative to the vortex, in PV-θ space, will be calculated. In section 4.2 the components of this circulation will be derived. The monthly means of this circulation will be shown in section 4.3 and the conclusions will be presented in section 4.4.

4.2 Lagrangian Stratospheric 'Circulation' Plots

In this section the formulation of the horizontal and vertical components to be plotted will be explained.

It would be convenient if the meridional circulation could be described in terms of a mass overturning streamfunction, but due to the fact that the flow in ϕ, θ coordinates is not non-divergent this is not possible. Instead it will be described in terms of flux vectors.

The horizontal component of the 'circulation' is composed by first starting with the cross contour mass flux term

$$\mathcal{V}_{Q,\theta} \tag{4.1}$$

which represents the transport across contours of constant PV along an isentropic surface. This term is calculated as a residual of the mass evolution equation

$$\frac{\partial}{\partial t}\mathcal{M}_{\mathcal{Q},\theta} = \mathcal{V}_{\mathcal{Q},\theta} - \int_{S_{Q,\theta}} \frac{\partial\left(\sigma\dot{\theta}\right)}{\partial\theta}\,\mathrm{d}S \tag{4.2}$$

and is itself made up of two components

$$\mathcal{V}_{\mathcal{Q},\theta} = -\frac{\partial}{\partial Q}\int_{S_{Q,\theta}} \sigma\dot{Q}\,\mathrm{d}S + \frac{\partial}{\partial Q}\int_{S_{Q,\theta}} \sigma\dot{\theta}\frac{\partial\widetilde{Q}}{\partial\theta}\,\mathrm{d}S. \tag{4.3}$$

The first term on the right hand side of Equation (4.3) is the mass transport across the PV contour Q along the isentropic surface θ and the second term is the vertical

transport across a sloped PV contour onto the isentropic surface θ. Together they form the term $\mathcal{V}_{Q,\theta}$ which is the rate at which mass is 'stripped' from the region enclosed by the PV contour Q on the isentropic surface θ.

In this form it is not an intuitive quantity like velocity as it is not easy to visualise. The mass within higher valued PV contours, which lie closer to the pole, will be significantly less than that of the lower valued contours. The length of the lower valued contours will also be larger and possibly more deformed than those at the pole. The dimensions of $\mathcal{V}_{Q,\theta}$ are kg $K^{-1}s^{-1}$and it is more useful to have the components in dimensions of m s^{-1}. Rescaling $\mathcal{V}_{Q,\theta}$ will enable both of these weaknesses to be overcome.

Dividing by the length of the contour helps to reduce the difference in the mass flux across longer and shorter contours,giving the mass flux per unit length. This requires an expression for calculating the length of a PV contour that can be calculated easily from the ERA-40 data.

The length of a contour of PV is defined as

$$\ell = \oint_{\Gamma_{Q,\theta}} \mathrm{d}s. \tag{4.4}$$

Calculation of ℓ in the form of Equation (4.4) requires the computation of a contour integral. Contour integrals are difficult to compute numerically. The accuracy is affected by the accuracy of the interpolation scheme used and can be significantly time consuming to keep track of the geometry of the contour. In contrast surface integrals are much less sensitive to errors induced due to the interpolation; therefore it is desirable to express Equation (4.4) as a surface integral to make the calculation easier and more stable.

To make this transformation, we start with the identity

$$\frac{\partial}{\partial Q} \int_{S_{Q,\theta}} \eta \, \mathrm{d}S = - \oint_{\Gamma_{Q,\theta}} \frac{\eta}{|\nabla_\theta Q|} \, \mathrm{d}s \tag{4.5}$$

where η is an arbitrary scalar quantity.

Using this identity, and taking $\eta = |\nabla_\theta Q|$ Equation (4.4) can then be expressed as

$$\ell = \oint_{\Gamma_{Q,\theta}} \mathrm{d}s = -\frac{\partial}{\partial Q} \int_{S_{Q,\theta}} |\nabla_\theta Q| \, \mathrm{d}S = -\frac{\partial \mathcal{I}}{\partial Q}. \tag{4.6}$$

This expression for the contour length as the gradient in PV space of a surface integral is much easier to compute than Equation (4.4).

Equally $|\nabla_\theta Q|$ can be expressed in the form

$$|\nabla_\theta Q| = \sqrt{\left(\frac{1}{a}\frac{\partial Q}{\partial \lambda}\right)^2 + \left(\frac{1}{a\sin\lambda}\frac{\partial Q}{\partial \phi}\right)^2} \tag{4.7}$$

where λ is the longitude, ϕ the latitude and a is the radius of the earth taken to be 6.371x10^6 m. This then gives an expression for $\mathcal{I}$ as

$$\mathcal{I} = \int_{S_{Q,\theta}} \sqrt{\left(\frac{1}{a}\frac{\partial Q}{\partial \lambda}\right)^2 + \left(\frac{1}{a\sin\lambda}\frac{\partial Q}{\partial \phi}\right)^2}\, \mathrm{d}S. \tag{4.8}$$

The expression for the length of the contour ℓ is related to the equivalent length L_e of Nakamura (1996) and Haynes and Shuckburgh (2000). The equivalent length L_e of a contour is the contour length weighted by the variation of $|\boldsymbol{\nabla} Q|$ along the contour, making L_e the length the contour would have if $|\boldsymbol{\nabla} Q|$ were constant at its mean value along the contour. The two quantities are equal when $|\boldsymbol{\nabla} Q|$ is constant along the contour.

The dimensions of

$$\mathcal{V}_{Q,\theta}\frac{1}{\ell} \tag{4.9}$$

is then kg K^{-1}s^{-1}m^{-1}.

A further problem with the vertical structure of the cross contour mass transport is that the isentropic mass density on higher valued surfaces is smaller than that of lower surfaces. To compensate for this, and to express the horizontal component of the transport in dimensions of m s^{-1}, requires an expression for the isentropic mass density inside a PV contour. This is achieved by integrating the mass density σ over the surface $S_{Q,\theta}$ and dividing by the area of the surface, giving

$$\frac{1}{\widetilde{\sigma}} = \frac{\partial \int_{S_{Q,\theta}} \mathrm{d}S}{\partial \int_{S_{Q,\theta}} \sigma\, \mathrm{d}S} = \frac{\partial A}{\partial \mathcal{M}_{\mathcal{Q},\theta}} \tag{4.10}$$

where A is the area covered by the surface $S_{Q,\theta}$. This quantity has dimensions of m^2 K kg^{-1}.

This then gives us the horizontal component of the circulation

$$\vec{F}_{(\phi)} = \mathcal{V}_{Q,\theta}\frac{1}{\widetilde{\sigma}\ell} = -\mathcal{V}_{Q,\theta}\frac{\partial A}{\partial \mathcal{M}_{Q,\theta}}\frac{\partial Q}{\partial \mathcal{I}} \tag{4.11}$$

which now has dimensions of m s^{-1}.

The vertical part of the circulation is calculated by starting with the vertical movement of mass within a PV contour Q onto the isentropic surface θ

$$\frac{\partial}{\partial Q}\int_{S_{Q,\theta}} \sigma\dot{\theta}\,\mathrm{d}S. \tag{4.12}$$

This quantity suffers from some of the same problems as the horizontal component, namely that the contours of higher PV value will be smaller and contain less mass meaning that there will be less mass transport within them. Equation (4.12) also has dimensions of kg^2 m^2 K^{-1} where the full vertical component of the circulation should have units of m s^{-1}.

To scale this, and to compensate for the differing sizes of the PV contours, the gradient of PV with respect to area

$$\frac{\partial Q}{\partial A} \tag{4.13}$$

is used, having dimensions of K $kg^{-1}s^{-1}$. Combining this with Equation (4.12) then gives

$$\frac{\partial Q}{\partial A}\frac{\partial}{\partial Q}\int_{S_{Q,\theta}} \sigma\dot{\theta}\,\mathrm{d}S = \frac{\partial}{\partial A}\int_{S_{Q,\theta}} \sigma\dot{\theta}\,\mathrm{d}S \tag{4.14}$$

which has dimensions of kg m^{-2} s^{-1}.

To then express this as a velocity the average of the density of air inside the PV contour Q on the isentropic surface θ is used

$$\frac{1}{\widetilde{\rho}} = \frac{A}{\int_{S_{Q,\theta}} \rho\,\mathrm{d}S}. \tag{4.15}$$

To calculate the value of ρ the hydrostatic approximation is used

$$\frac{\partial p}{\partial z} = -\rho g \tag{4.16}$$

which can be used to give an expression for the density of

$$\rho = -\frac{1}{g}\frac{\partial p}{\partial z} = -\frac{\partial p}{\partial \Phi} \tag{4.17}$$

where $\Phi = gz$ is the geopotential. This gives the expression

$$\frac{1}{\widetilde{\rho}} = -\frac{A}{\int_{S_{Q,\theta}} \frac{\partial p}{\partial \Phi}\,\mathrm{d}S} \tag{4.18}$$

having dimensions $\mathrm{m}^3\ \mathrm{kg}^{-1}$. Here the density ρ rather than the pseudo density σ in isentropic coordinates is used in order to scale the vertical component in units of velocity. Combining this with Equation (4.14) then gives an expression for the vertical component of the circulation

$$\vec{F}_{(\theta)} = \frac{1}{\widetilde{\rho}}\frac{\partial Q}{\partial A}\frac{\partial}{\partial Q}\int_{S_{Q,\theta}} \sigma\dot{\theta}\,\mathrm{d}S = -\frac{A}{\int_{S_{Q,\theta}} \frac{\partial p}{\partial \Phi}\,\mathrm{d}S}\frac{\partial}{\partial A}\int_{S_{Q,\theta}} \sigma\dot{\theta}\,\mathrm{d}S \tag{4.19}$$

which has the required units of $\mathrm{m\ s}^{-1}$.

These vectors are plotted on axes of height as the vertical coordinate and equivalent latitude as the horizontal coordinate. The horizontal movement of air illustrated here is in potential vorticity space rather than physical space, but equivalent latitude ϕ_e is used as the horizontal coordinate as a means to relate the PV contours on different surfaces to each other. While $\phi_e(Q, \theta)$ can change with time, the mapping of Q to ϕ_e on the axis is invariant over each month shown.

In the atmosphere the horizontal scales are much larger than vertical scales, so the plots must be stretched to allow them to be readable. For the same reason the horizontal fluxes are much larger than vertical fluxes, so in order to preserve the apparent directions the components are stretched by the same factor.

When plotting the horizontal and vertical coordinates (F_ϕ, F_θ) they are rescaled by a factor of (S_y, S_z) so that the directions of the vectors in the figures resemble those in physical space. The scaling factors are then

$$S_y = \frac{\widehat{y}_p}{a\phi_p} \tag{4.20}$$

$$S_z = \frac{\partial \widehat{z}}{\partial z} \tag{4.21}$$

where $\widehat{y}_p$ is the total distance of the horizontal axis in the figure, ϕ_p is the latitude at the pole, $\widehat{z}$ is the vertical coordinate of the figure and z is the physical height coordinate. The plotted quantities are then $c(S_y F_\phi, S_z F_\theta)$ where c is a constant used to rescale the length of the vectors in each plot for graphical convenience, but

are kept constant throughout each winter period. The scaling factor is given in the November plot for each winter.

4.3 Results

In this section the Lagrangian 'circulation' plots will be presented. Firstly a schematic of the main features seen in the following plots will be discussed to aid with the discussion of the analysis of the plots in the following analysis. A composite plot of the circulation will then be discussed followed by a series of case studies of 7 winters, 5 of which included a single warming event, one included 2 warmings and one in which no warmings were observed. Table 4.1 gives a list of the winters to be looked at in these case studies. The data used is ERA-40 6 hourly data.

Winter	Charlton and Polvani (2007)	Mitchell et al. (2013)
1978-9	22nd February S	18th February S
1979-80	1st January S	25th December S
1981-2	4th December D -	- 21st January S
1983-4	24th February D	26th February S
1984-5	1st January S	25th December S
1987-8	7th December S 14th March S	1st December M 10th March D
1990-1	-	-

Table 4.1: Winters and their classifications. D denotes a displacement warming event, S a splitting SSW and M a mixed event defined by Mitchell et al. (2013) to be one which changes in state between split and displacement.

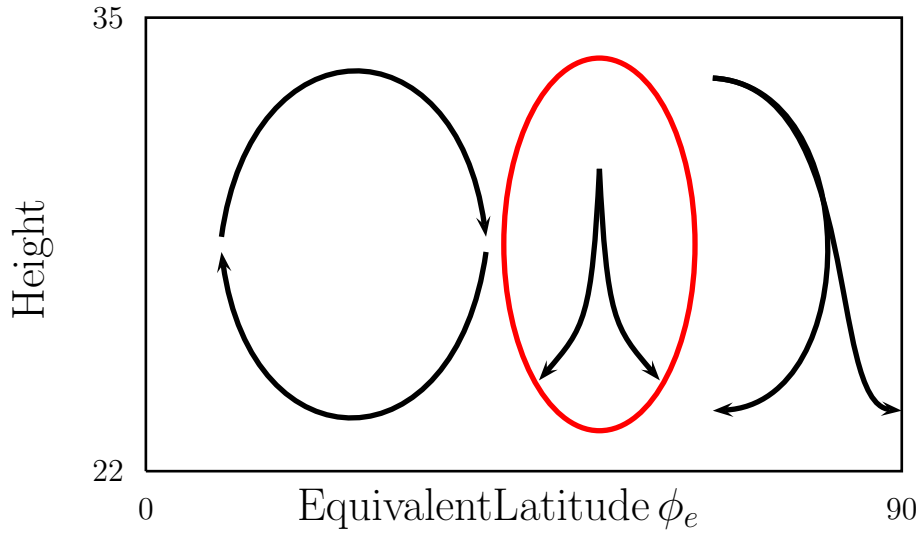

Figure 4.1: Schematic of the main features the Lagrangian 'Circulation' plots. The the region of the vortex (between the pole and $\sim 70^o$ there is descent everywhere with poleward movement at all times on higher levels and either poleward or equatorward movement on lower levels. The region south of this is the surf zone and features mainly descending air which is directed either poleward or equatorward. Between the southern edge of this and the equator has an area of air which looks to be moving clockwise in the plots.

4.3.1 Schematic

Figure 4.1 shows a schematic of the main features present in the monthly means of the circulation.

In the region near to the equator and up to around 50 degrees equivalent latitude is an area where the mass transport can be seen to be to form a 'rotating' (in the figure) area around a central point, usually located between 20 and 30 degrees equivalent latitude. Poleward of this is an area of mostly 'downward' moving transport which then either moves toward the vortex or the 'rotating' area, this varies over the course of the winter and seems to have a relationship to occurrences of SSW events. This area has a relatively low gradient of PV compared to the areas around it and seems to be consistent with the 'surf zone' area. The area of higher PV, possessing higher equivalent latitude, is the area which can be identified as the polar vortex. The transport within this region can be seen to either be

descending and directed toward the vortex centre, or to enter on higher levels, descend within the vortex and exit on lower levels. The sizes of the regions of poleward and equatorward mass transport again vary from month to month and will be discussed below.

These regions are not always well defined, and will vary in size and positioning as the winter progresses, and in the lead up and aftermath of a sudden warming event.

It is also important to note that isentropic surfaces change in height over time. This means that the apparent upward motion of air in θ space can also coincide with downward motion of air in physical space.

Similarly in the horizontal the arrows show movement of air across PV contours, which may themselves be moving, so apparent poleward movement in PV space can coincide with equatorward movement of air in physical space.

4.3.2 1978-9

Figures 4.2 to 4.6 show the PV-height 'Circulation' plots for monthly averages of the circulation described in section 4.2 for the winter of $1978-9$. The November monthly average of the vertical component of this circulation (Figure 4.2) is downward inside the vortex, as well as immediately outside, and upward in the subtropics. This is in agreement with the established dynamical theory, which says that the Brewer-Dobson circulation dominates the stratospheric dynamics, with air moving upwards in the subtropics before moving North and descending closer to the pole.

The horizontal component of the circulation, however, diverges from this expected behaviour.

The circulation illustrated in this flow looks in fact opposite to what would be generally expected, flowing generally equatorward between the equator and the 45 degrees North equivalent latitude contour. The reason for this apparent contradiction is that the data shown in these plots is flux of air relative to PV contours and is not the absolute motion of the air relative to the earth. It is

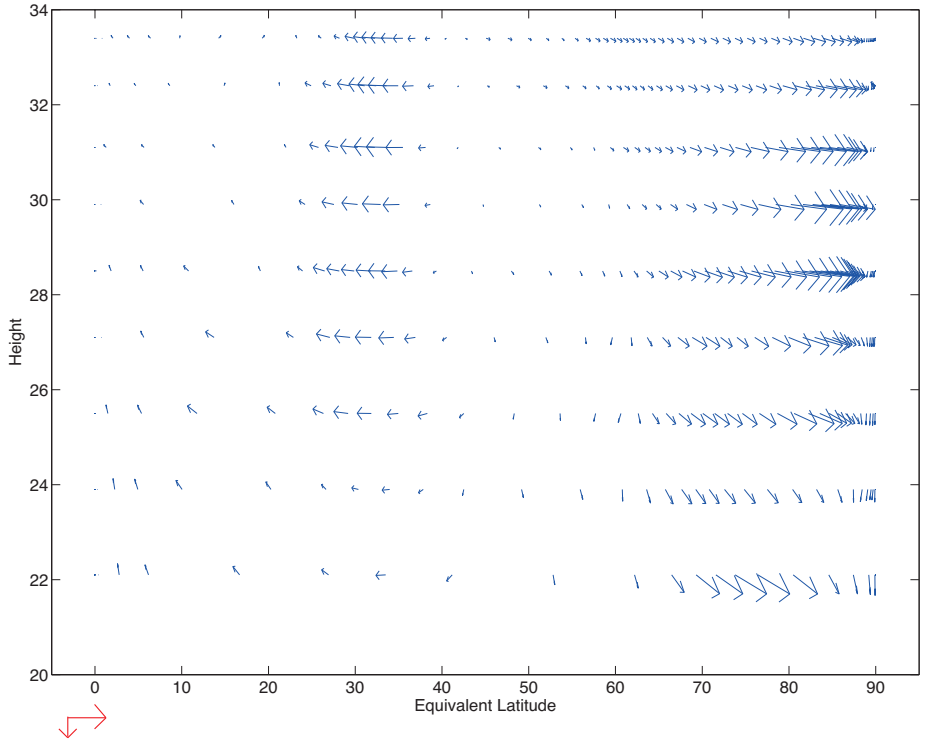

Figure 4.2: Circulation averaged over the month of November 1978. The red vectors at the bottom of the figure are each plotted with a magnitude of 7x10^{-}6 m s^{-1}. The scaling of all other figures will be given relative to this one.

important in evaluating these representations of the stratospheric circulation that the PV contours themselves are not fixed in the atmosphere and the equivalent latitude ϕ_e associated with a given contour will change as air crosses the contour. The figures plotted here give a representation of the cross contour mass transport.

The horizontal circulation within the vortex and just outside it is in the opposite direction to that in the subtropics, moving towards the higher PV rather than the equator.

Since the main area of interest here is the Northern hemisphere, to save on data storage space only data for the Northern hemisphere was saved. This means that the contours closest to the equator may cross into the Southern hemisphere. This means that in the calculations of the surface integrals only part of the contour will be counted. The calculations for the components of the circulation on these

contours thus produces erroneous values. This was verified as being sufficient for the purpose here as looking at PV maps reveals these contours near to the equator to have high zonal symmetry. Therefore the components from these contours are excluded from the plot and appear as dots at low ϕ_e values but do not affect the reliability of the adjacent contours.

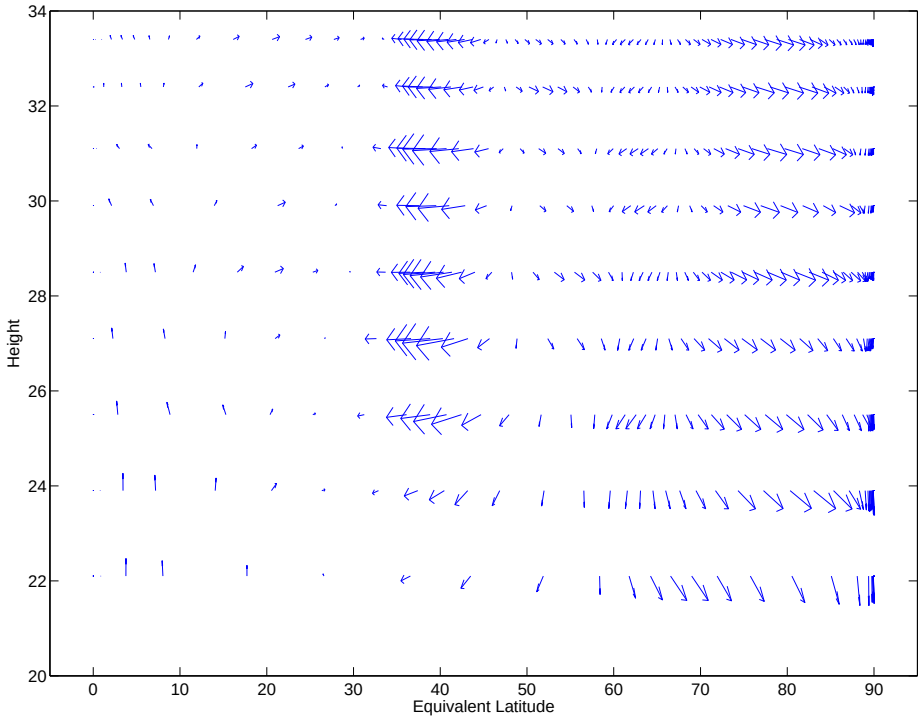

Figure 4.3: Circulation averaged over the month of December 1978.

The vertical components of the motions for December, and all the way through to March (Figure 4.3 to Figure 4.6) show a similar pattern to that of November. This agrees with what has been observed, eg Sutton (1994) where mesospheric air enters the stratosphere within the vortex and continues to descend.

In contrast, the horizontal components of the circulation for December are somewhat different to those of November. The subtropical air South of 30 degrees or so can be seen as heading generally towards the polar air with the exception of a few arrows very close to the equator. North of this, between 30 and $50-55$ degrees there is a band of air with a mostly equatorward trend. This trend is

stronger at lower altitudes with only weak equatorward movement on the higher altitudes. Further North of this band there is generally poleward flow again towards the vortex edge, where this flow seems to converge with that of the air within the vortex which moves in general outward towards the steep PV gradient area at the vortex edge. This together with the vertical components draws a picture of air that moves upward and poleward in the tropics and downward and equatorward in the surrounding air and close to the vortex edge.

This picture of the circulation is much more like what is expected from established dynamical pictures of the large scale circulation in the stratosphere (see Andrews et al., 1987).

Around the latitude of the vortex edge there are also a few arrows which show air moving with a much higher velocity than the surrounding air. These all occur at around 75 to 80 degrees where there are large arrows directed toward each other on all of the vertical levels plotted. This implies that there are significant amounts of cross contour mass flux into the area between the two PV contours indicated by each of the arrows.

By January the poleward part of the circulation has extended Northward towards nearly 50 degrees everywhere, except on the lowest surface plotted here. On this level the flow of air is still predominantly equatorward other than a small section close to the pole where flow is still toward higher PV air (see Figure 4.4). This section of poleward mass flux around the vortex that is forming and growing can be interpreted as the surf zone of well mixed air identified by McIntyre and Palmer (1983, 1984). On the tropical side of the surf zone the air rises and moves poleward before descending as it meets the air of high PV gradient on the vortex edge.

Within the vortex the majority of the horizontal movement of air is Southward towards the vortex edge where it meets the well mixed air of the surf zone. Near to the centre of the vortex there is still a small area where the horizontal movement is directed toward the vortex centre. There is also still equatorward flux in the area between the equator and the Southern side of the surf zone.

The surf zone appears in these plots as the region just outside the vortex edge

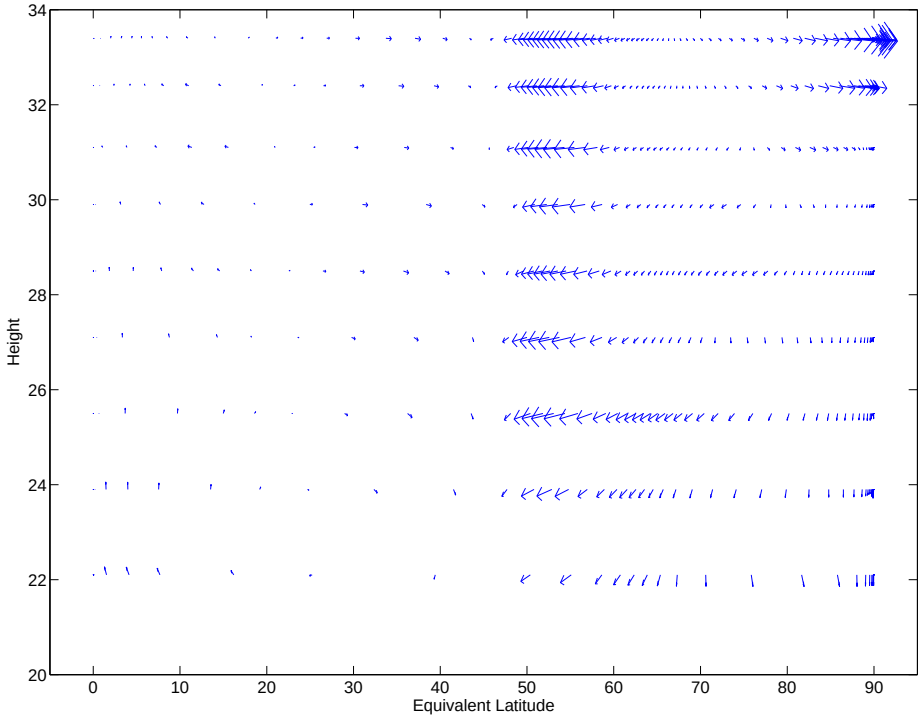

Figure 4.4: Circulation averaged over the month of January 1979.

characterised by the relatively low gradient of PV contours (ie widely spaced contours). Figure 4.5 shows that during February the surf zone, which is now well developed, can be seen to have spread North and can now be seen to occupy the area between about 25 and 65 degrees. The region is by now very well mixed and the mass flux within it is mainly poleward towards the contours making up the vortex edge, and downward everywhere towards the lower stratosphere. There is no longer ascent of air on the subtropical edge of the surf zone as there was in January, which has stayed at roughly the same latitude. Instead in February there is descent of air everywhere within the surf zone.

Along with the poleward advancement of the Northern edge of the surf zone, the edge of the vortex can be seen to have retreated North compared to that of previous months as it becomes preconditioned and undergoes a sudden stratospheric warming in late February. The vortex split occurs around 22nd February by the criteria of Charlton and Polvani (2007) and 18th February by those of Mitchell et al. (2013),

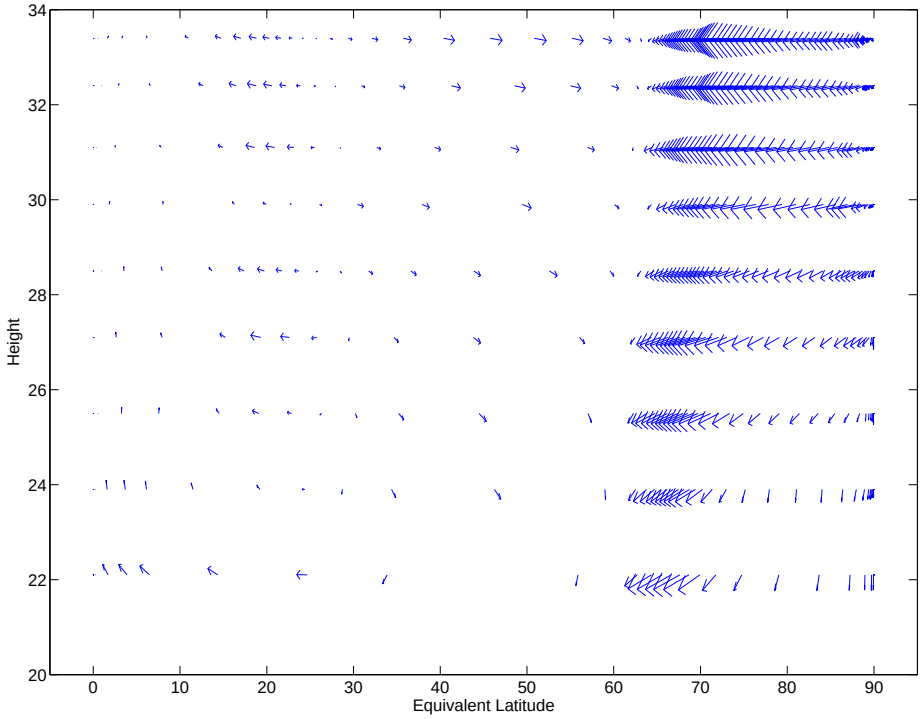

Figure 4.5: Circulation averaged over the month of February 1979.

so much of the signal of this in Figure 4.5 is dominated in the monthly average by the pre-warming vortex which occupies the stratosphere for three quarters of the month. This means that the signal of the warming which may be identifiable in these plots is much more likely to be visible in the monthly average of March than that of February.

The general picture for March (Figure 4.6) is one of downward and equatorward movement of air similar to that described in Figure 4.2 for November in the area outside the vortex. Within the vortex there is also equatorward movement in March in contrast to November where there was poleward movement. This is a result of the splitting event in late February and the subsequent breakdown of the smaller sub-vortex in late February/early March. This breakdown is followed by the reformation of the main vortex which will be significantly reduced in size compared to the early winter vortex.

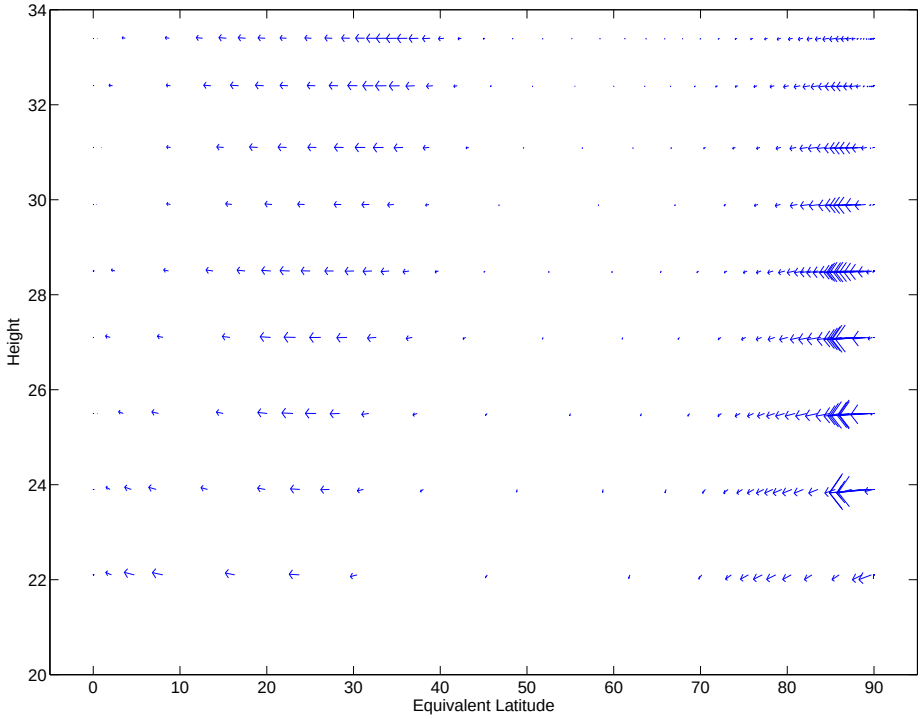

Figure 4.6: Circulation averaged over the month of March 1979.

4.3.3 1984-5

Figure 4.7 to Figure 4.11 show the circulation plots for the monthly averages from November 1984 to March 1985. This winter hosted a vortex splitting SSW which occurred around 1st January 1985.

In November of this winter on the surfaces below 29.9km there is an area of circulation directed upward and poleward in the subtropics, and downward and equatorward closer to the vortex edge. This forms an area where the air is moving clockwise around a point centred at around 30 degrees North and 25.5km altitude, moving clockwise in Figure 4.7. This area of clockwise movement of air can be seen throughout the winter in all monthly means of Figure 4.7. The centre around which this section of air moves stays at around 30 degrees equivalent latitude for the duration of the winter, the height of it however changes as the winter progresses. In January it has moved upward to lie between the 27km and 28.5km surfaces

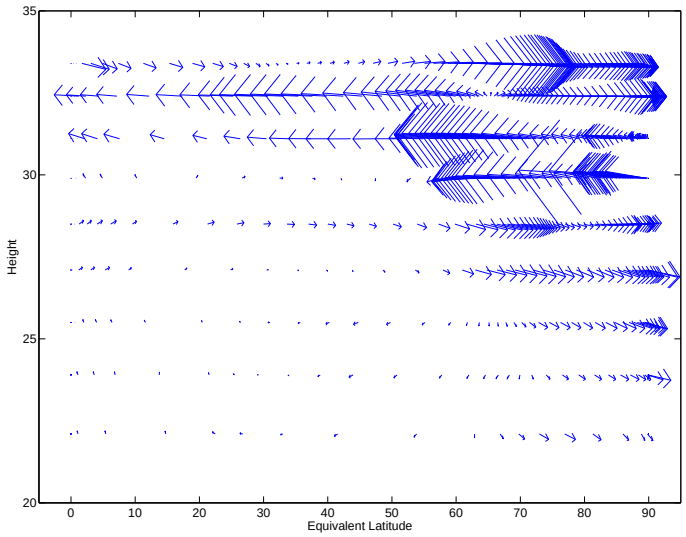

Figure 4.7: Circulation monthly average for November 1984. The vectors are scaled by a factor of 1.57 relative to Figure 4.2.

and by March it has moved upward to nearly the 29.9km surface. As the centre around which this circling air moves is pushed upward the area of poleward air above it remains similar, meaning that the area of equatorward directed air below it is increasing.

This area of circulation is much more similar to the Brewer-Dobson circulation where air rises in the tropics, where it enters the stratosphere, moves North then descends near to the pole. The circulation pictured here also features an equatorward part at lower altitudes. This part of the flow is generally weaker than the higher poleward part, especially in the pre-warming vortex. Following the sudden warming this lower equatorward part of the circulation starts to become larger in comparison to the pole directed part until in March the lower part is the larger of the two.

The air within the vortex mainly shows a downward movement similar to the $1978-9$ winter. For November this seems to be directed mainly poleward and to be of much larger magnitude than the circulation outside the vortex. December is similar, although some of the air nearer to the vortex edge is directed toward this edge and entering the surf zone which can by now be seen to be forming around

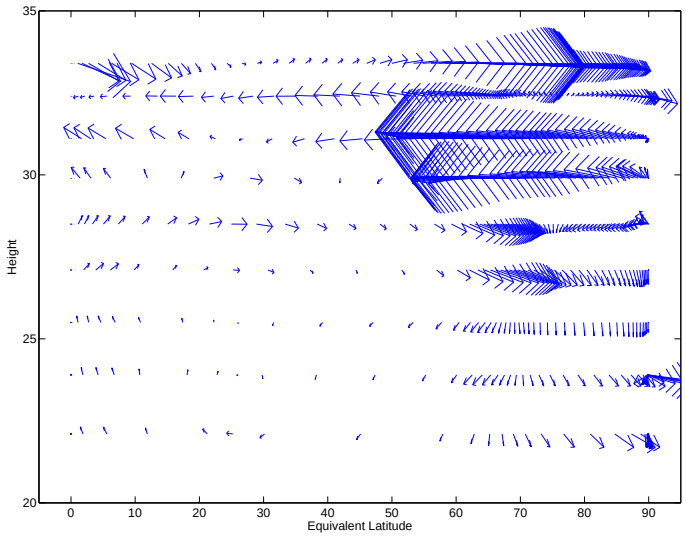

Figure 4.8: Circulation monthly average for December 1984.

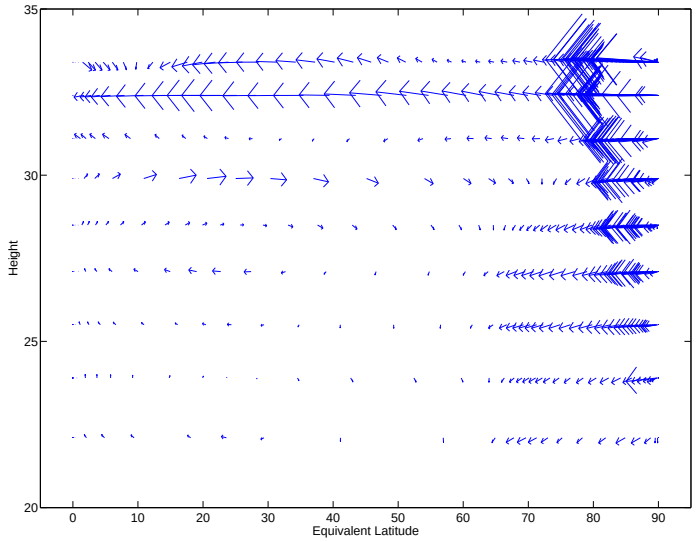

Figure 4.9: Circulation monthly average for January 1985.

the vortex.

The surf zone can be seen around the vortex as the area of downward mass flux between 35 degrees and the vortex edge which occurs at roughly 60 to 65 degrees. Between November and December it can seen to have developed, along with the

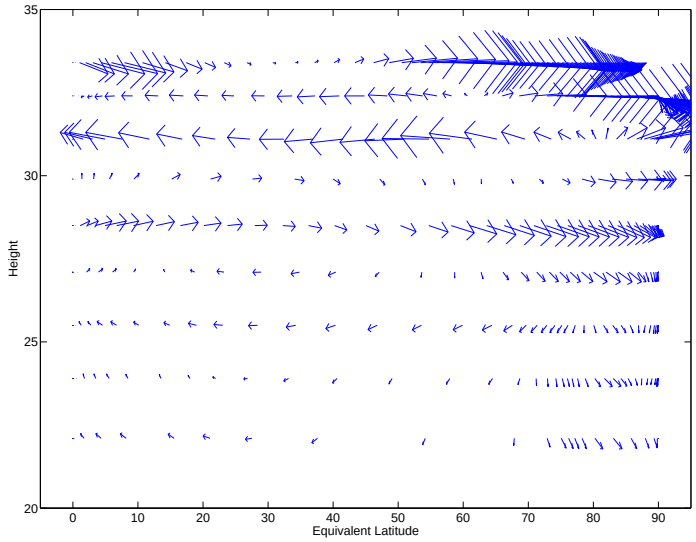

Figure 4.10: Circulation monthly average for February 1985.

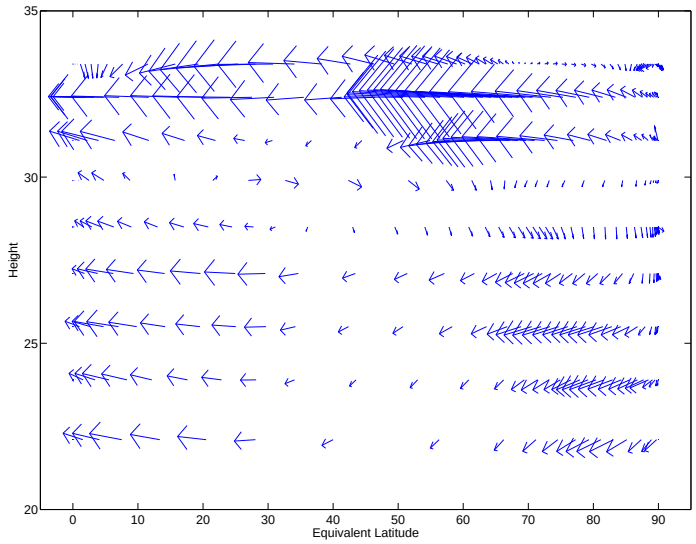

Figure 4.11: Circulation monthly average for March 1985.

sharpening of the gradient of PV at the vortex edge.

By January the air within the vortex is mostly moving towards the vortex edge and out into the surf zone. This is the result of the sudden warming which occurred on the 1st January, and the subsequent breakdown of the smaller of the

two sub-vortices which are the result of the splitting. By February the vortex edge has retreated to around 75 degrees and the surf zone occupies the majority of the Northern hemisphere.

On the upper levels, generally those above 29.9km there are what seems like erroneous circulations, with the vertical component of the circulation pointing upwards in sharp contrast to the components on the levels below. The horizontal components of the flow are also directed in many cases opposite to the components on the levels immediately below.

This area of 'upward' motion of air depicted on the higher altitudes, for the majority of the winter doesn't necessarily indicate upward motion of air in physical space. It is known that isentropic surfaces change in height throughout the course of the winter, especially so around the times of sudden warming events when anomalies in PV cause isentropic surfaces to increase or decrease in height in the area of the anomaly (Ambaum and Hoskins, 2002).

4.3.4 1979-80

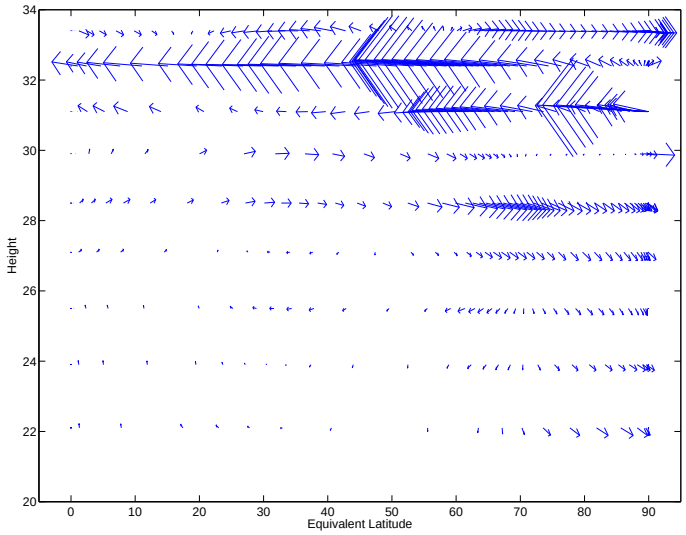

Figure 4.12: Circulation monthly average for November 1979. The vectors are scaled by a factor of 1.57 relative to Figure 4.2.

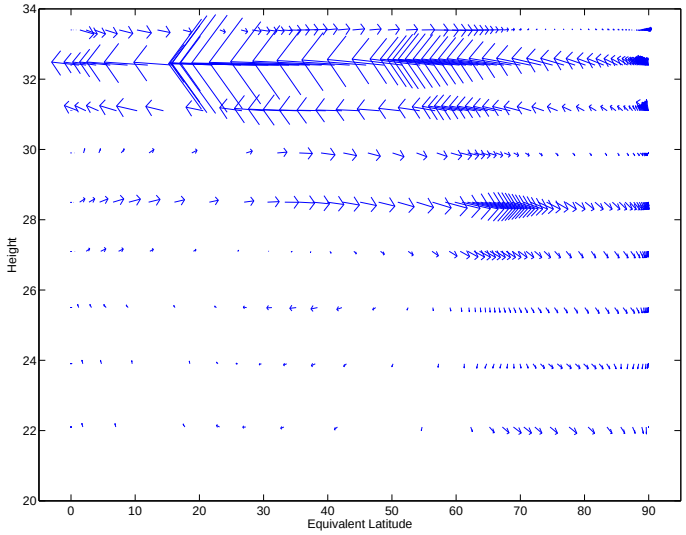

Figure 4.13: Circulation monthly average for December 1979.

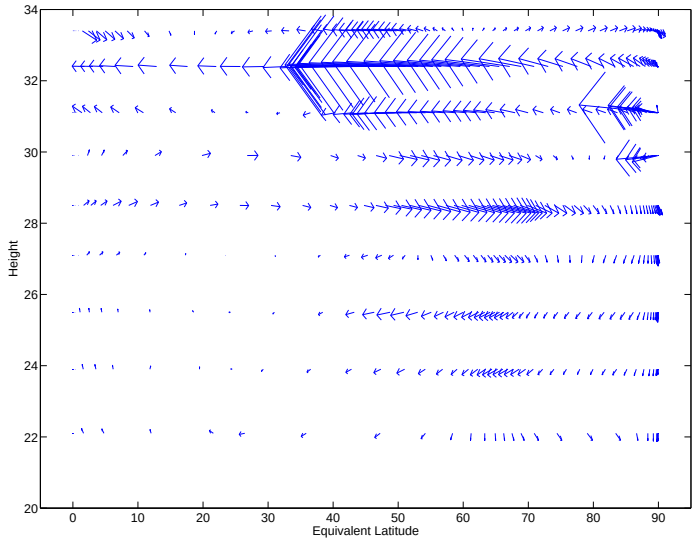

Figure 4.14: Circulation monthly average for January 1980.

In the winter of $1979-80$ (Figure 4.12 to Figure 4.16) Charlton and Polvani (2007) identified a vortex displacement to have occurred around the 29th February, while Mitchell et al. (2013) identified the same event as a splitting with a central date of 15th February. As can be seen from Figure 4.12 there is again an area of

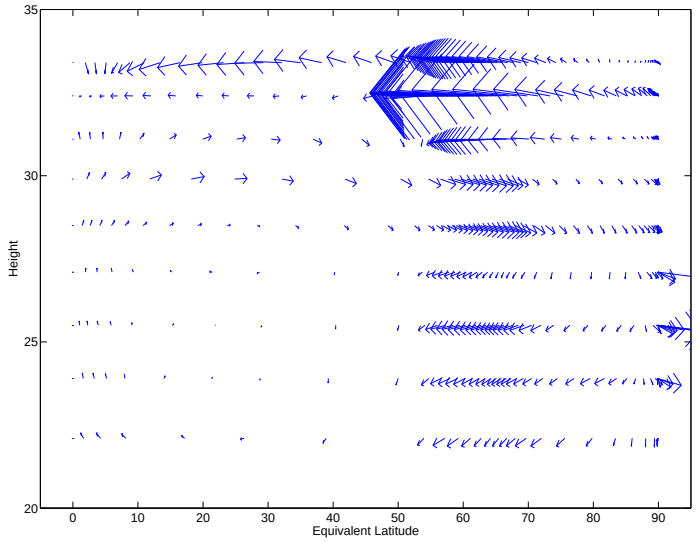

Figure 4.15: Circulation monthly average for February 1980.

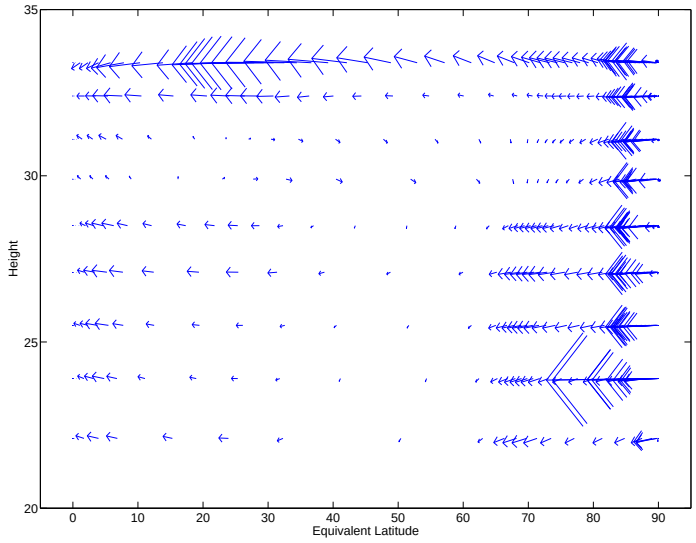

Figure 4.16: Circulation monthly average for March 1980.

clockwise rotation centred around 35 degrees North and just above 27km at the start of the winter. This is accompanied by the descending and mostly poleward movement of air within the vortex as in the two above winters. December looks very much similar to November, with air inside the vortex descending and moving

mostly poleward, with only a small amount of air near to the pole moving toward the vortex edge.

By January most of the mass flux inside the vortex has changed direction and is directed toward the vortex edge on the lower levels as mass is stripped from the vortex in the preconditioning leading up to the end of February warming. The point around which the rotating air is moving has also moved South to between 25 and 30 degrees equivalent latitude and is still located at around 27km in height.

In the monthly mean for February the area of clockwise rotation has moved upward again to between 27km and 28.5km and horizontally to around 25 degrees equivalent latitude. It has again increased by March, to now lie between 28.5km and 29.9km, at about 30 degrees equivalent latitude.

The formation of the surf zone and the sharpening of the gradient making up the vortex edge can be seen evolving over the period from November to February, and the dramatic reduction in the area of the vortex in the monthly mean for March following the breakdown of the vortex.

Following the warming at the end of February the mass flux within the vortex is all directed towards the edge as is seen in the months following the splitting events above.

4.3.5 1981-2

The winter of $1981-2$ (Figure 4.17 to Figure 4.21) featured an early warming by both the criteria of Mitchell et al. (2013) and Charlton and Polvani (2007) though both disagree on when it occurred and the classification of the event. Charlton and Polvani (2007) found a displacement around 4th December while Mitchell et al. (2013) defined a splitting around 21st January. In November, the month prior to the 'displacement' warming, the vortex edge seems to be less defined than in the month prior to later warmings seen above. This is to be expected as the vortex has undergone a much shorter period of strengthening prior to the onset of the warming than it would for later warmings.

The section of clockwise rotation of air is present in November at a similar

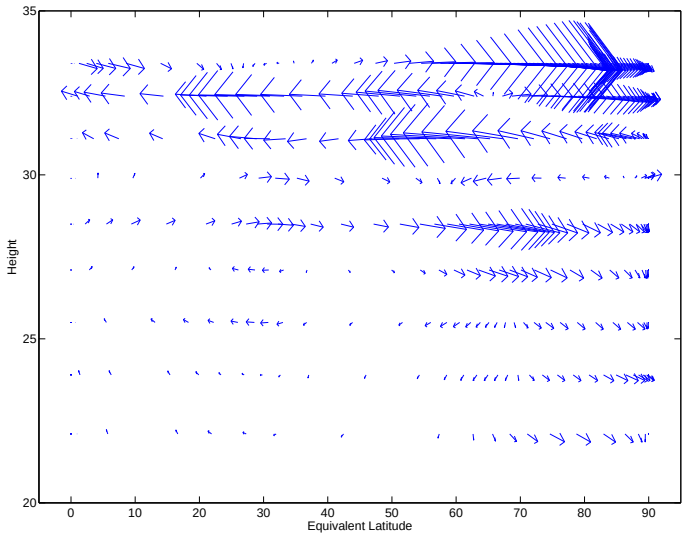

Figure 4.17: Circulation monthly average for November 1981. The vectors are scaled by a factor of 1.57 relative to Figure 4.2.

location to other winters; between 27km and 28.5km at around 30 degrees. Following the warming in December this centre has descended slightly, to lie roughly on the 27km surface. By the following month the centre has begun to rise again, and by March it has increased to between 28.5km and 29.9km. By this time the equatorward flow is also much larger compared to the poleward part than it is in the earlier parts of the winter.

Following the warming in early December, for the 25.5km surface and below there is net removal of mass from the vortex for the course of the following month. Above this there is still movement of mass into the vortex, but the vertical component has increased in relation to the horizontal velocity. The vortex edge has sharpened somewhat from the previous month, and the main area of movement is within the vortex.

By January the air within the vortex is descending much more strongly than the air outside is moving, in contrast to the previous months. The surf zone can be clearly seen with the vortex edge gradient becoming sharpened and the gradient of the surrounding area becoming decreased as the air becomes well mixed.

Toward the end of the winter the main flow of air is out of the vortex, with all

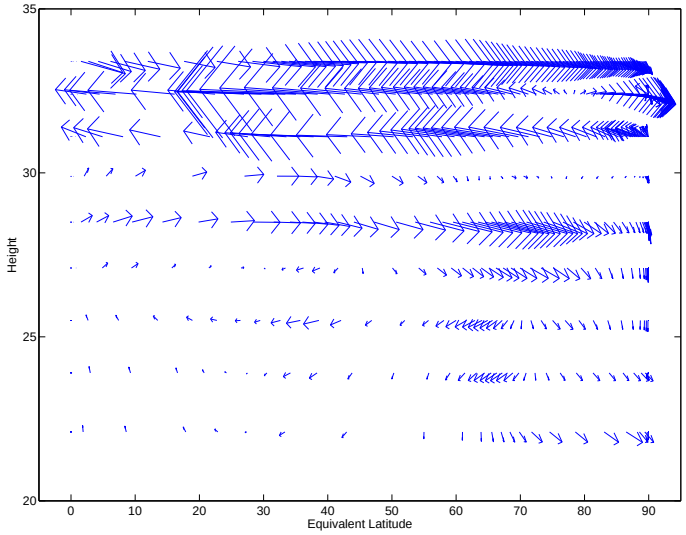

Figure 4.18: Circulation monthly average for December 1981.

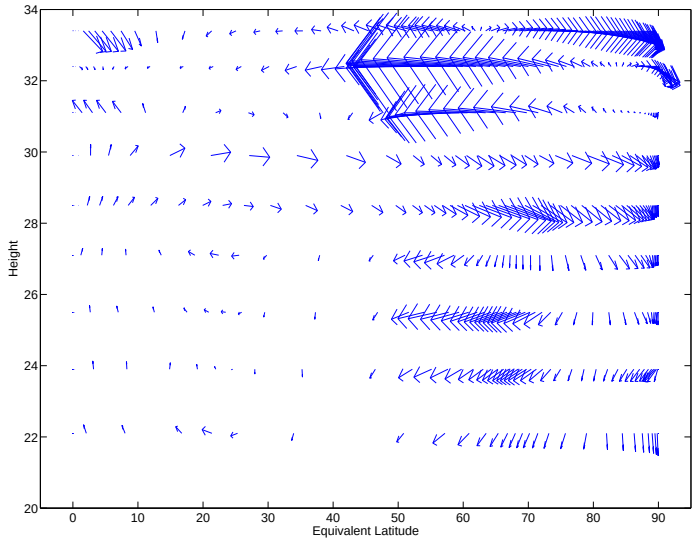

Figure 4.19: Circulation monthly average for January 1982.

levels up to and including 28.5km dominated by equatorward directed motion of air. The area of the vortex remains roughly constant over the whole winter, with the edge lying at roughly the same equivalent latitude from November to March, though the gradient making up the edge strengthens over this period. For the whole

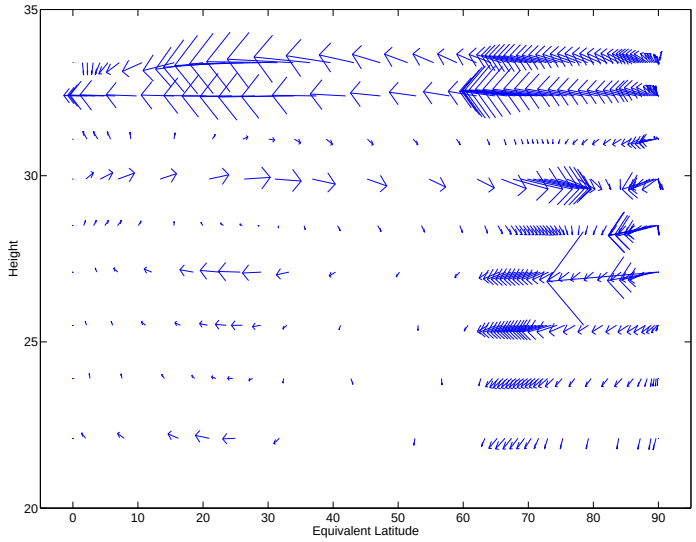

Figure 4.20: Circulation monthly average for February 1982.

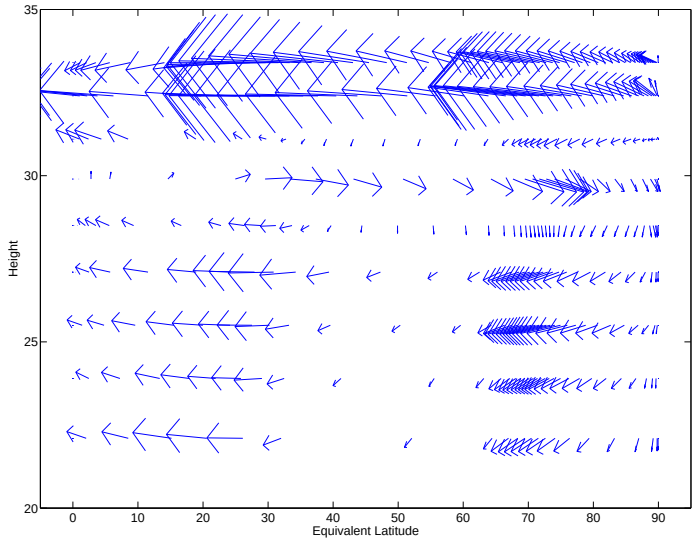

Figure 4.21: Circulation monthly average for March 1982.

time from the warming in early December the air inside the vortex is directed in general toward the vortex edge below 28.5km to be replaced by the air entering on the levels above this.

4.3.6 1983-4

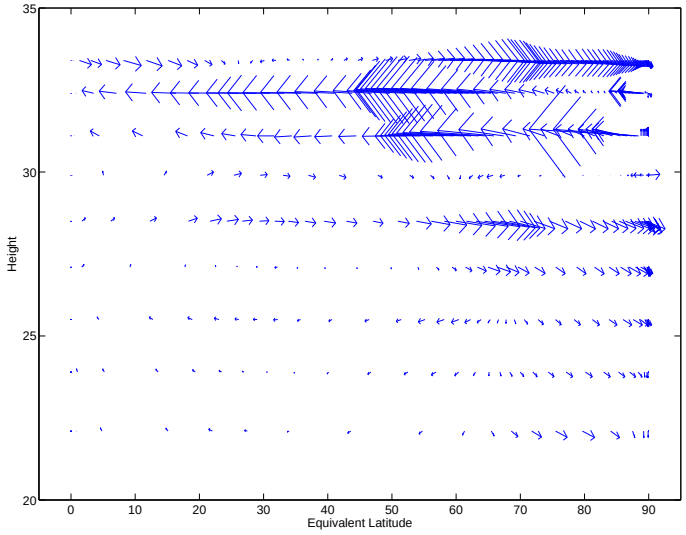

Figure 4.22: Circulation monthly average for November 1983. The vectors are scaled by a factor of 1.57 relative to Figure 4.2.

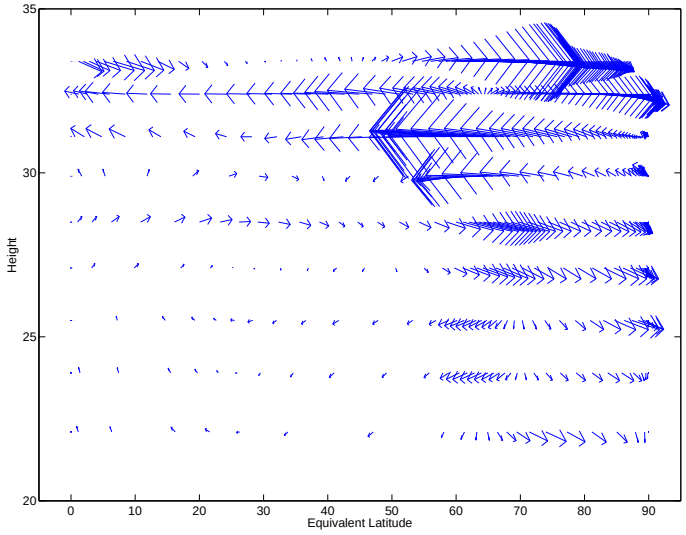

Figure 4.23: Circulation monthly average for December 1983.

The winter of $1983-4$ (Figure 4.22 to Figure 4.26) was a winter in which both criteria classified a displacement event of the 24th/26th February.

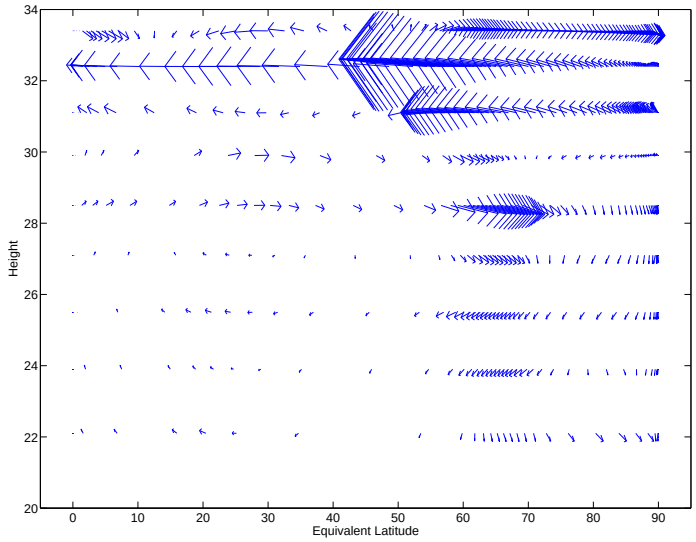

Figure 4.24: Circulation monthly average for January 1984.

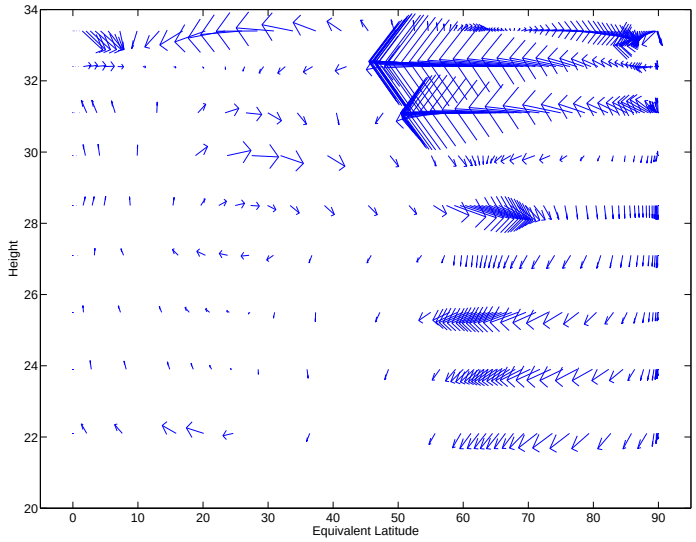

Figure 4.25: Circulation monthly average for February 1984.

The monthly mean for November 1983 looks similar to that of November 1979 which also features an end of February vortex displacement, with air above 27km moving toward the vortex up to 31.1km and air below 27km moving mainly equatorward. The centre around which the the rotating air moves is similarly located at

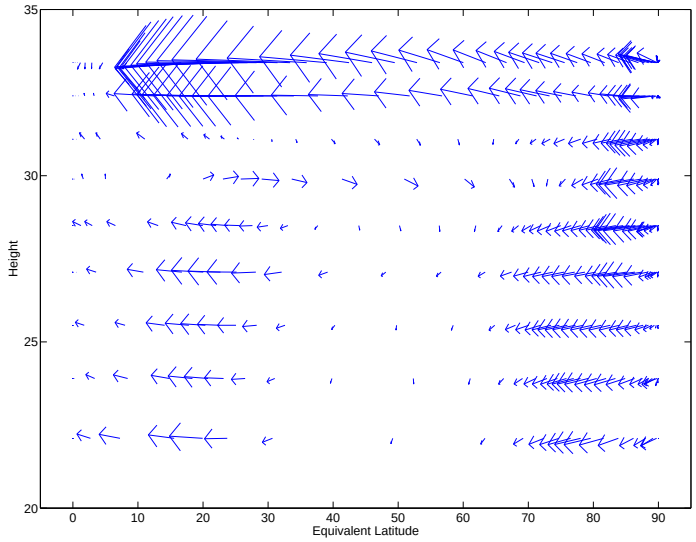

Figure 4.26: Circulation monthly average for March 1984.

around 30 degrees equivalent latitude and 27km altitude. Similarly to the $1979-80$ winter prior to the late February warming the centre for this circulation outside the vortex doesn't move any significant amount. Following the February 1984 warming this centre is still located at around $\phi_e = 30$ but has increased in height to between 28.5km and 29.9km.

For the first two months of the winter the vortex edge is relatively weak compared to the following months. All the mass flux within the vortex is directed toward higher PV. The mass flux outside on higher levels is directed strongly toward and across the vortex edge with weak equatorward movement on lower levels of air south of roughly 65 degrees. In January and February most of the mass flux within the vortex on the lower surfaces is directed toward the vortex edge.

Following the warming the picture differs quite a lot from the 1980 warming. All the mass flux within the vortex is directed toward the edge at a much stronger rate. Immediately outside the vortex, North of $\phi_e = 35$ degrees the mass flux is directed North toward the vortex edge.

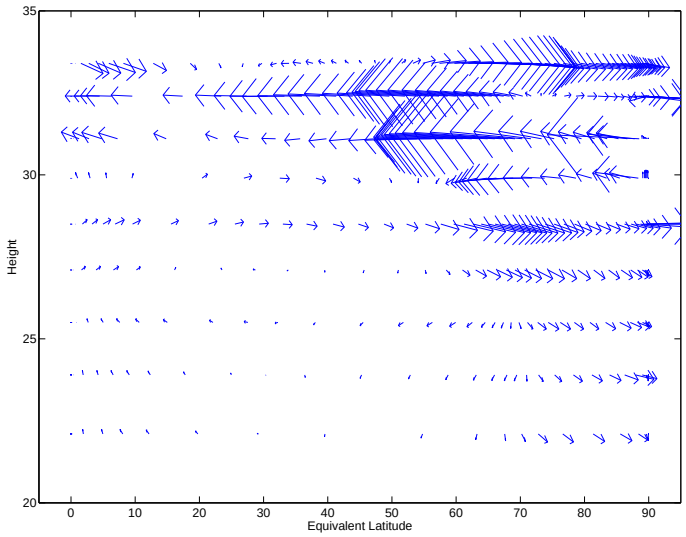

Figure 4.27: Circulation monthly average for November 1987. The vectors are scaled by a factor of 1.57 relative to Figure 4.2.

4.3.7 1987-8

1987−8 was a winter which featured two major sudden warming events, the first an early winter event classified by Charlton and Polvani (2007) as a vortex splitting on 7th December and by Mitchell et al. (2013) as a mixed event (a displaced vortex which then splits) on 1st December. The second was a late event classified by Charlton and Polvani (2007) as a vortex splitting on 14th March and by Mitchell et al. (2013) as a displacement on 10th March (Figure 4.27 to Figure 4.31).

The area of 'clockwise' mass flux outside the vortex stays at around 27km for most of the winter. Only in March does it increase significantly in height up to between 28.5km and 29.9km. It also stays at around $\phi_e = 30$ degrees for the first three months of the winter before slowly moving towards $\phi_e = 25$ degrees by the March monthly mean.

In November, the month leading up to the early warming event, the PV gradient at the edge of the vortex is not very sharp, similar to that of the 1981 early warming. It has sharpened by December but is located further North than it is for the undisturbed parts of other winters. The area of circulation is somewhat disrupted

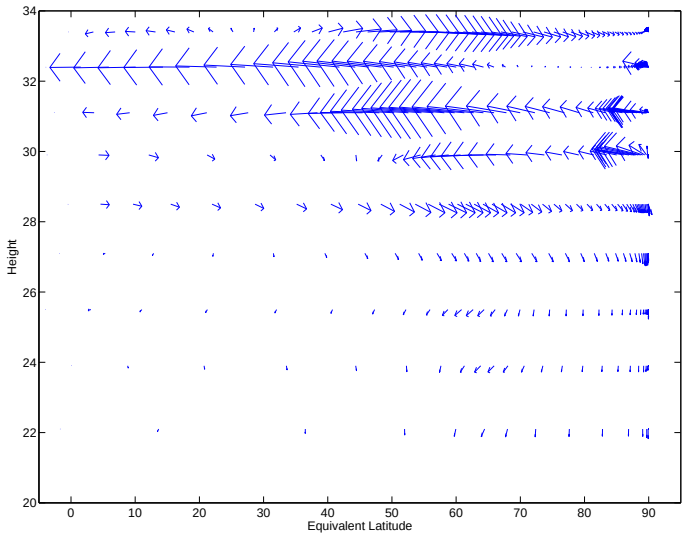

Figure 4.28: Circulation monthly average for December 1987.

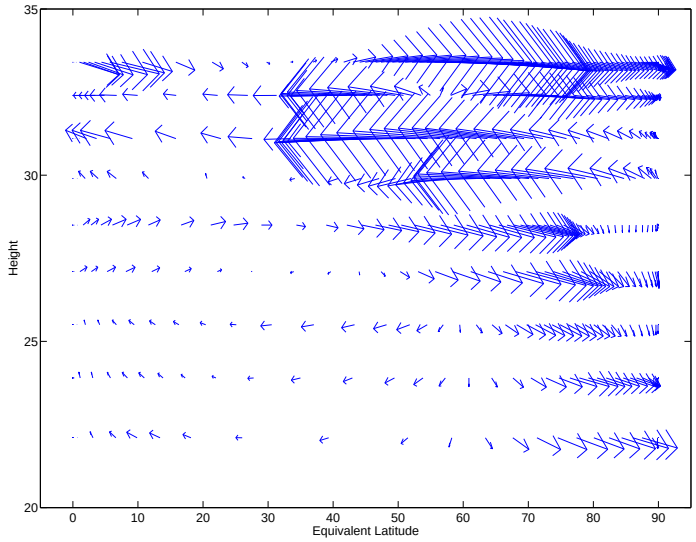

Figure 4.29: Circulation monthly average for January 1988.

following the warming with air North of roughly 20 degrees on the 23.9km surface moving toward higher PV in direct contrast to the air immediately above and below it in Figure 4.28.

The vortex edge has not returned to its original equivalent latitude, although

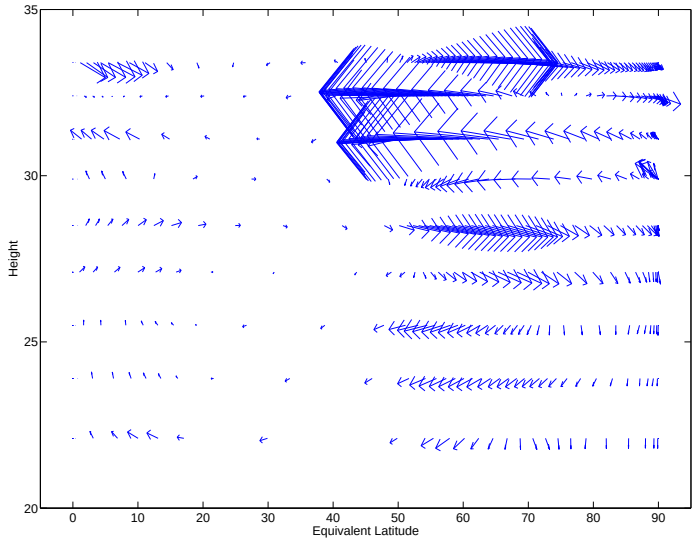

Figure 4.30: Circulation monthly average for February 1988.

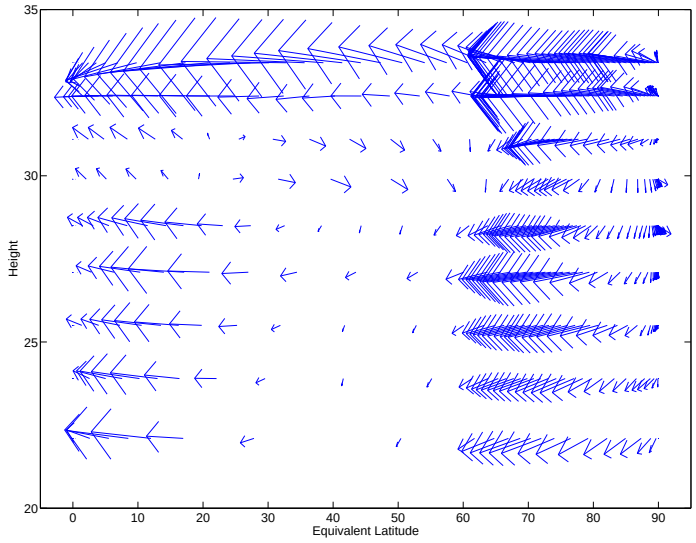

Figure 4.31: Circulation monthly average for March 1988.

the air around it is moving toward the vortex edge and by February the edge has fully recovered to its usual position between 60 and 70 degrees. The surf zone appears fairly well formed early in the winter, but by February it is much more developed than it seems to be for most other winters here.

The air within the vortex is moving poleward and downward in November but following the warming in December the air on the lower levels is mostly directed toward and across the vortex edge. In January a pattern similar to November has returned, with most of the air inside the vortex directed toward the pole, though the vertical component of the motion is much smaller than the horizontal component compared to other months of the winter. February is similar to December with air on the lower levels changing to flow equatorward while the air above is still directed mostly poleward. By March all mass flux from within the vortex is directed equatorward. The area of 'clockwise' mass flux is still present in the surrounding air, so air between 20 and 60 degrees on the upper levels is still directed toward the vortex edge. The rest of the air outside the vortex is directed toward the equator.

4.3.8 1990-1

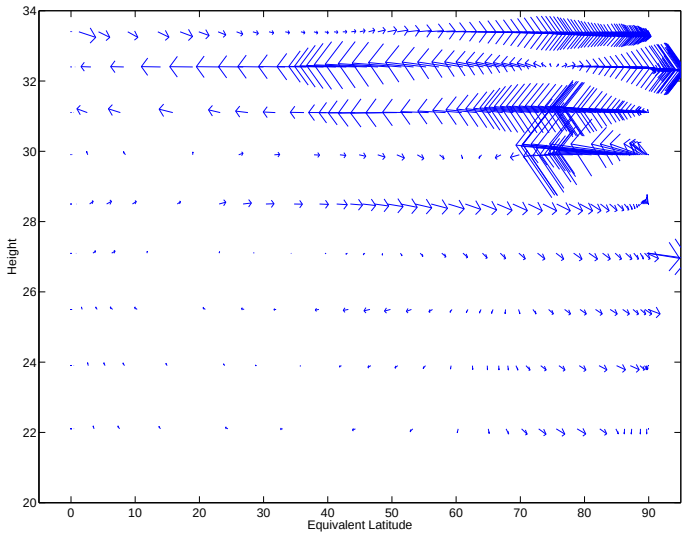

Figure 4.32: Circulation monthly average for November 1990. The vectors are scaled by a factor of 1.57 relative to Figure 4.2.

No major sudden warming events occurred in the winter of 1990−91 (Figure 4.32 to Figure 4.36). It is interesting to examine this winter beside the other winters to compare the progression of an undisturbed vortex with a disturbed one.

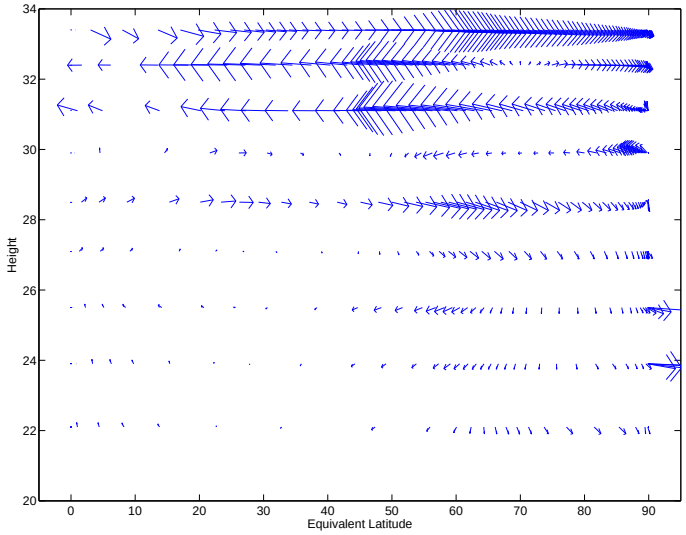

Figure 4.33: Circulation monthly average for December 1990.

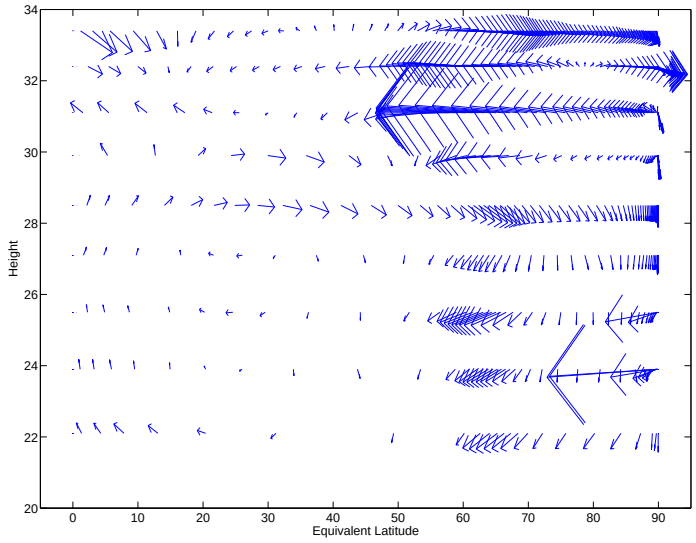

Figure 4.34: Circulation monthly average for January 1991.

In November of this winter the region of circulating air is further North than it appears in the other winters here where major warmings have occurred. This region appears at between 35 and 40 degrees North, but is still around 27km in height similar to that of the disturbed winters above. This then moves South as

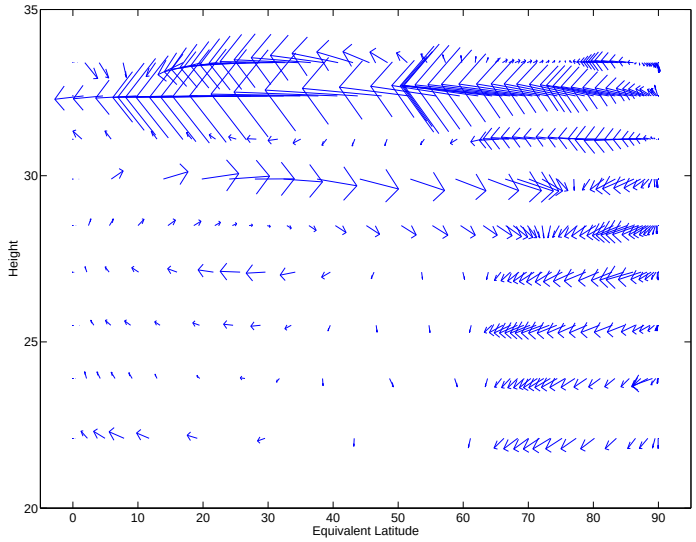

Figure 4.35: Circulation monthly average for February 1991.

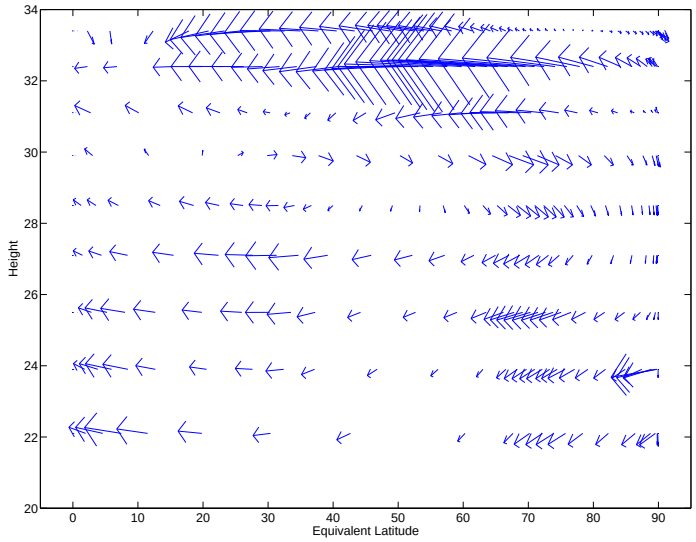

Figure 4.36: Circulation monthly average for March 1991.

the winter progresses, to between 20 and 25 degrees in February and March. The height remains the same in December and starts to increase gradually in January. In January and February the centre is between 27km and 28.5km and toward the end of the winter in March it has reached nearly 30km. Again this is similar to

what can be seen for some of the winters displayed above.

Similar to the other winters above the vortex is strengthening through November and December, with the air within and immediately outside it directed downward and toward higher PV on average for November. In December this is still the case for the Northern most contours, but those nearer to the vortex edge below 27km and immediately outside it are directed equatorward. The edge is not well defined in the November monthly mean but by December it can be seen quite well and in January it is well defined as expected from other plots. The air within the vortex is has a particularly strong vertical component on the intermediate levels, with slight poleward tendency on the levels above and equatorward tendency on the ones below.

During February most of the air in and around the vortex is directed toward the edge as it is receding toward the pole slightly from its position in January and weakened slightly by March. In March the picture looks fairly similar to the uneventful parts of the above winters with poleward flow in higher levels and equatorward flow on the lower ones.

4.4 Conclusions

The monthly mean circulation of air in PV-z space has been calculated and examined for several eventful winters as well as one uneventful winter. There are some differences between the patterns seen for individual years, but overall there are several features which appear common to all winters as well as several systematic differences between early and late warmings, similar to those seen in the integral diagnostics (chapter 3).

At the start of the winter, comparing the months of November for the winters examined it seems that the distribution of PV contours is similar, with similar maximum values encountered on each level. The pattern of the circulation is also fairly similar for most of the winters. As the winter progresses this changes, with some winters having significantly higher PV values than others for significant periods of time. The vortex edge occurs around the same PV values for all winters,

and stays around the same value over the course of the whole winter although it may change in equivalent latitude as the size of the vortex changes.

In November the vortex is not well formed. As it strengthens there is cross contour flux from the surrounding air which causes the area and mass of the vortex to increase. This can be seen in the November plots in Figures 4.2 to 4.32 where arrows North of about 60 to 70 degrees equivalent latitude on lower levels, and all the way to the equator on some of the higher surfaces, point toward the vortex edge. There is still a section of clockwise (in these plots) circulation in these months, though the area of equatorward movement is smaller than that of a more well developed vortex edge.

The area of downward mass flux within the vortex is in agreement with the findings of Juckes (2001) who found descent around the pole when examining the isentropic-mean mass stream function. The circulations seen here on the lower levels are directed equatorward for most of the winter, compared to the poleward movement seen by Juckes (2001) at the higher levels, which correspond to the lowest levels in the circulations presented here.

The monthly means for months where sudden warming events occur or have occurred in the last few days of the previous month show a sudden outward movement of air, as the vortex loses mass as it breaks down. This effect is visible for all sudden warming events other than the early vortex displacement event of December 1981. As noted the lack of mass reduction in the 1981 warming could be explained by the fact that the vortex is not well formed by this point in the winter and there is no reason why a displaced vortex should necessarily require a reduction in mass to regain its pre-warming position located over the pole. Reference to the mass plots in chapter 3 shows that the vortex doesn't lose mass following the warming in the same way as later warmings do.

Egger and Hoinka (2014) found that in their December-January-February (DJF) means there is movement toward higher PV contours for vortex air, and equatorward movement outside on the higher levels. This is similar to what is seen on the lower levels here in non-warming months, with air within the vortex directed

toward the vortex centre and non-vortex air mostly directed toward the equator. The picture differs in the months following SSWs, where all air is directed toward the equator. The post-warming circulation, which differs from the DJF mean of Egger and Hoinka (2014), is only visible for short periods following warmings, and as such the circulation mostly looks similar to the DJF mean.

Following the month where the signal of the breakdown from the sudden warming can be seen the vortex starts to reform and strengthen again. This can clearly be seen following the sudden warming events (such as March 1979 or January 1984 for example) by the poleward directed arrows on the poleward side of the surf zone and the southern most parts of the vortex. This disrupts the overall pattern of the flow which is seen over most normal non-warming months with downward and equatorward movement near to the vortex edge, and upward and poleward flux closer to the equator.

The equatorward part of the flow also seems to strengthen in the period following the warming, with most of the lower levels showing strong equatorward movement in relation to the rest of the flow.

Comparing early and late warmings there are several differences in the pictures of the circulation shown by the plots here. The convention used here is that warmings occurring in December are referred to as early warmings, and those occurring later from 1st. January onward are referred to as late warmings. In the winters looked at here the early warmings are the 'displacement' event of early December 1981 and the splitting/mixed event of early December 1987. In the period following these warmings, the circulation shows there is some removal of air from the vortex on lower levels. The contours closest to the vortex centre on these levels do not show much equatorward cross contour flux, indeed, some of the contours in December 1981 (Figure 4.18) show significant poleward movement or air across PV contours for the period immediately following the warming. On upper levels there is still cross contour flux of air into the vortex. This is likely to be because the vortex is not fully formed by the time the sudden warming occurs; therefore there will very quickly be influx of air into the vortex after the warming event. The

stripping and radiative growth of the vortex will be compensating to some extent for the effects of each other making the net effect a reduced influx of air to the vortex.

In comparison, the periods following warmings which occurred later in the winter have mass flux inside the vortex directed equatorward in ϕ_e, with only small amounts directed toward the pole. This removal of air, unlike that of the early warming also occurs on all levels. The ejection of air from the vortex indicating its breakup extends only as far as the surf zone, where the section of 'clockwise' rotating air is still visible. The air on the lower poleward side of it however is directed toward the vortex edge unlike it is in non-warming months. The difference between the splitting and displacement events seen for the early warmings doesn't appear to exist for later warmings, instead all of the warmings occurring later in the winter show similar features to each other.

In both early and late warming events the edge of the vortex can be seen to move poleward in terms of ϕ_e following the breakdown of the vortex. It then begins its recovery in the month following this to return to its usual place between $\phi_e = 65$ and 70 degrees.

Chapter 5

Investigating Stripping in a Shallow Water Model of the Polar Vortex

5.1 Introduction

Shallow water models have long been used to investigate vortex dynamics, especially those of the polar vortex. There have been two main approaches to investigation of vortex erosion in these experiments. Some studies have imposed a wave-like forcing on the lower boundary, while others have embedded a vortex in an external flow.

The main advantage of using a shallow water model over more realistic, multilayer models is that a larger area of the parameter space is able to be explored. As much of the motion in the stratosphere is along isentropic surfaces shallow water models are also well suited to investigating stratospheric dynamics.

Studies which have imposed wave-like forcings (eg Juckes, 1989; Juckes and McIntyre, 1987; Polvani et al., 1995) have done so by placing a time varying mountain on the bottom boundary. These have provided information about how Rossby waves cause the formation of filaments of vortex air near to vortex edge.

Mixing in a model vortex under wave-like forcing has been investigated (eg

Norton, 1994; Sobel and Plumb, 1999), and the effect of the amplitude in single and multi-level models (eg Esler and Matthewman, 2011; Matthewman and Esler, 2011; Polvani and Saravanan, 2000). The amount of mass mixed from the vortex into the surf zone has been found to be much less than that mixed from the tropics into the surf zone.

The other main approach is to embed a vortex in an external flow (eg. Legras and Dritschel, 1993; Legras et al., 2001; Mariotti et al., 1994). This simulates the effects that other vortices have on the erosion of the polar vortex. In the presence of these external flows, if the external shear is weak enough then the contours near to the edge of the vortex start to become stripped and eroded while the centre of the vortex remains intact. This increases the PV gradients at the edge of the vortex, which is maintained by further stripping. If the external strain is above a certain level the vortex then breaks down completely.

These experiments show that when the external strain growth is slow enough the vortex goes through a series of equilibrium states until it breaks down when the strain reaches a critical level.

In chapter 3 the transport of mass out of the polar vortex was investigated using the ERA-40 reanalysis data. The data shows that there are several periods where mass is stripped from the vortex in the period leading up to the onset of SSWs. This suggests that the vortex may undergo several quasi-steady states in the lead up to these events. This is similar to what is seen in the experiments of Legras et al. (2001) in the progression through equilibrium states. This forms one of the hypotheses which will be investigated in this chapter.

The main questions of interest in the following experiments are

- When the forcing increases at a slow enough rate does the vortex go through a series of quasi steady states?
- What is the criteria for the vortex to break; is there some threshold forcing amplitude above which the vortex breaks down?
- Is there a systematic difference between the response to wave 1 and wave 2 forcings?

In section 5.2 the details of the model and experiments will be explained. The results are presented in section 5.4 and in section 5.5 the conclusions are presented.

5.2 Experimental Details

Stripping is investigated using the Finite Element Shallow Water Model of John Thuburn. The model uses a finite element based method to solve the rotating shallow water equations on a sphere similar to the finite volume model of Thuburn et al. (2013).

The model solves the dynamical equations (see below) on an unstructured grid. The numerics of the model are formulated in such a way that the PV evolves as if the PV conservation law

$$\frac{\partial}{\partial t}(\Phi Q) + \nabla \cdot (\mathbf{u}\Phi Q) = 0 \tag{5.1}$$

itself were to be integrated rather than the dynamical equations (5.2) and (5.3). This means that an accurate and conserving advection scheme may be used while maintaining desirable PV advection properties.

In the model there are no explicit diabatic effects or frictional terms. This means that mass transport across contours of potential vorticity are down to small scale mixing within the advection scheme. When features of PV contours reach scales which are below those resolved by the model they become mixed into the background flow.

The dynamical equations take the form

$$\frac{\partial \Phi}{\partial t} + \nabla \cdot (\Phi \mathbf{u}) = 0 \tag{5.2}$$

$$\frac{\partial \mathbf{u}}{\partial t} + \mathbf{k} \times (\Phi \mathbf{u} Q) + \nabla \left(\Phi + \Phi_s + \frac{1}{2}\mathbf{u} \cdot \mathbf{u} \right) = 0 \tag{5.3}$$

where $\Phi = gh$ is the geopotential height, Φ_s is the geopotential of the orography, $\mathbf{u}$ is the velocity and Q is the potential vorticity. The prognostic variables of the model are $\mathbf{u}$ and Φ. In the Shallow Water equations the potential vorticity (PV) can be formulated as

$$Q = \frac{f + \zeta}{\Phi} \tag{5.4}$$

where f is the Coriolis parameter and ζ is the relative vorticity.

The orography Φ_s of the flow consists of a zonally symmetric part ($\overline{\Phi}$) corresponding to the initial condition plus a time-varying mountain (Φ_{pert}) which imposes a wave-like forcing on the flow. The orography then takes the form

$$\Phi_s = \overline{\Phi} + \Phi_{pert}. \tag{5.5}$$

The mountain then takes the form

$$\Phi_{pert} = gH^*T(t)M(\phi, \lambda). \tag{5.6}$$

where H^* is the maximum height of the mountain, $T(t)$ is a time dependence which is used to grow the mountain from 0 to its maximum height H^* and takes the form

$$T(t) = \begin{cases} 0.5\left(1 - \cos\left(\frac{\pi t}{\tau}\right)\right) & 0 \leq t < \tau \\ 1 & \tau \leq t. \end{cases} \tag{5.7}$$

Here τ is a parameter controlling the rate of growth of the mountain. This has the effect of growing the mountain smoothly up to the final height of H^* at time $t = \tau$. $M(\phi, \lambda)$ is the shape of the mountain which takes the form

$$M\left(\phi, \lambda\right) = \exp\left(-\left(\frac{(\phi - \phi_0)}{\Delta\phi}\right)^2\right)\cos\left(\lambda\right) \tag{5.8}$$

for wave-1 forcing and

$$M\left(\phi, \lambda\right) = \exp\left(-\left(\frac{(\phi - \phi_0)}{\Delta\phi}\right)^2\right)\cos\left(2\lambda\right) \tag{5.9}$$

for wave-2 forcing where $\phi_0 = \frac{\pi}{3}$ and $\Delta\phi = \frac{\pi}{12}$. This creates a mountain centred at 60^o North which grows in time up to a maximum height H^*. The longitudinal part ($\cos\left(\lambda\right)$) creates a mountain of wave-1/wave-2, while maintaining the zonal average of geopotential.

This mountain is similar in size and shape to the wave-1/wave-2 component of the geopotential in the wintertime stratosphere.

The fluid on top of the orography Φ_s then takes a constant depth, having geopotential Φ = 4x10^4 m^2 s^{-2} meaning that the total fluid depth is $\Phi + \Phi_s$ (see Figure 5.1).

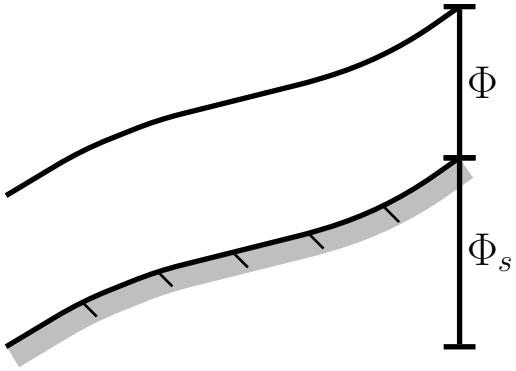

Figure 5.1: Orography plus fluid depth

The basic orography $\overline{\Phi}$ and initial velocity $\overline{u}$ are set by first starting with a zonally symmetric velocity similar to that which would be found in the winter stratosphere. This is then integrated numerically to find the streamfunction ψ and, using the v equation from the shallow water equations,

$$fu + \frac{1}{a}u^2 \tan(\phi) + \frac{1}{a}\frac{\partial \Phi}{\partial \phi} = 0, \tag{5.10}$$

the geopotential $\overline{\Phi}$.

The specified form of the velocity $\overline{u}(\phi)$ is

$$\begin{aligned}\overline{u}(\phi) = 4.5 \sin\left(\frac{20\phi - 3\pi}{7}\right) \exp\left(\frac{11\phi + 5}{10}\right) - 6 \exp\left(-\frac{(\phi - 0.29)^2}{0.015}\right) \\ +12 \exp\left(-\frac{(\phi + 0.02)^2}{0.02}\right) - 4.5 \sin\left(\frac{\pi}{7}\right) \exp\left(-\frac{11\pi + 10}{20}\right) \exp\left(-\frac{\left(\phi + \frac{\pi}{2}\right)^2}{0.015}\right).\end{aligned} \tag{5.11}$$

This profile is chosen to be similar to that observed in a typical Northern hemisphere polar winter while being constrained to be equal to 0 at both the North and South poles for continuity. Figure 5.2 shows several examples of stratospheric zonal mean wind flows in dotted lines along with the initial velocity of Equation (5.11) plotted with a solid line.

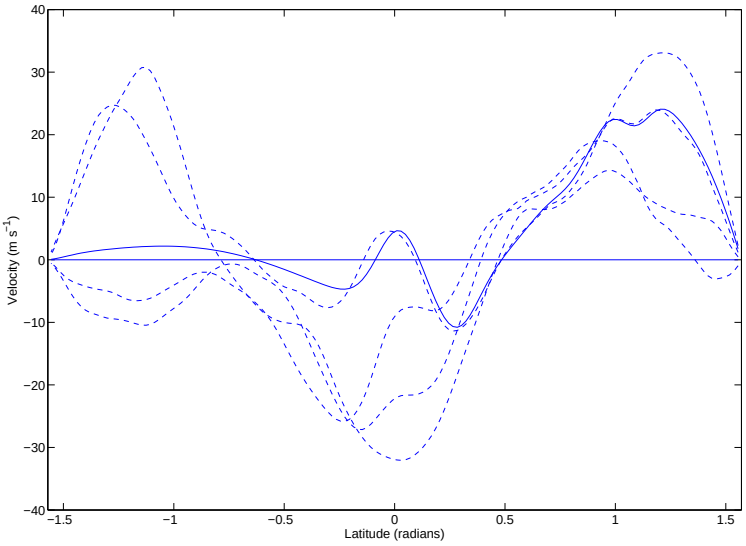

Figure 5.2: Zonal mean winds for several different instants during several winters at $p = 10$hPa plotted with dashed lines, and the specified velocity (Equation (5.11)) plotted with solid line.

5.3 Diagnostics

The diagnostics which will be used here are the same as calculated in the previous chapters. The formulations of these, however are slightly different in the Shallow Water regime compared to the Small Slope, Hydrostatic regime used previously.

5.3.1 Equivalent Latitude

Equivalent latitude is defined as

$$\phi_e = \arcsin\left(1 - \frac{A}{2\pi a^2}\right) \tag{5.12}$$

$$A = \int_{\widetilde{Q} \geq Q} \mathrm{d}S \tag{5.13}$$

where the surface $S_{Q,\theta}$ used before is now simplified to the area where $\widetilde{Q} \geq Q$ since in the Shallow Water regime there is only one surface. The calculation of this is the same as in the previous cases where whole grid boxes with the criteria $\widetilde{Q} \geq Q$ are counted and those where $\widetilde{Q} < Q$ are not.

5.3.2 Mass

The Mass integral is here defined as

$$\mathcal{M}(Q) = \int_{\widetilde{Q} \geq Q} \Phi \, \mathrm{d}S \tag{5.14}$$

as in Thuburn and Lagneau (1999). This is in fact a volume (multiplied by the gravity term g which is constant) and not a mass, but if density is taken to be constant unity then this quantity will have all the features of a true mass integral.

Since there is no diabatic heating, the 'stripping term' from previous chapters is equal to the change in mass of a particular PV contour Q.

5.3.3 Circulation

The circulation $\mathcal{C}(Q)$ around a potential vorticity contour Q is defined as

$$\mathcal{C}(Q) = \oint_{\widetilde{Q}=Q} \mathbf{v}_{abs} \cdot \, \mathrm{d}\mathbf{r}. \tag{5.15}$$

Using Stokes' theorem this can be transformed to

$$\mathcal{C}(Q) = \int_{\widetilde{Q} \geq Q} \zeta + f \, \mathrm{d}S \tag{5.16}$$

and combined with the definition of PV above (Equation (5.4)) the circulation can be written in the form

$$\mathcal{C}(Q) = \int_{\widetilde{Q} \geq Q} \Phi \widetilde{Q} \, \mathrm{d}S \tag{5.17}$$

which is the form which will be calculated in the model.

5.3.4 SSWs in the Shallow Water Scheme

The WMO definition of an SSW states that an SSW has occurred when the zonal mean temperature gradient between 60 and 85 degrees North at 10hPa is reversed, accompanied by a reversal of the zonal mean zonal winds in the same region.

In order to identify if a simulated sudden warming occurs in this shallow water regime, and if so at what point it can be said to occur, the sign of the zonal mean

zonal winds at 60 degrees North will be calculated. Using Stokes' theorem this can be expressed as an area integral of the relative vorticity

$$\oint_{\phi=60} \mathbf{u} \cdot \mathrm{d}\mathbf{l} = \int_{\phi \geq 60} \boldsymbol{\nabla} \times \mathbf{u} \cdot \widehat{\boldsymbol{n}} \, \mathrm{d}S = \int_{\phi \geq 60} \zeta \, \mathrm{d}S. \tag{5.18}$$

An SSW can then be defined to have occurred if/when the value of this integral changes sign.

5.3.5 Wave Activity

Wave activity diagnostics for the model can be calculated using the integral diagnostics outlined above.

From Thuburn and Lagneau (1999), the balance equation for the wave activity in a shallow water model takes the form

$$\frac{\partial \mathcal{A}}{\partial t} + \nabla \cdot \mathcal{F} = S \tag{5.19}$$

where S represents lower boundary forcing and sources and sinks due to irreversible mixing, and the wave activity

$$\mathcal{A} = -h_e u_e \cos\phi - \frac{h}{2\pi a} \int_{Q_{ref}}^{Q} \left(Q - \widetilde{Q}\right) \frac{d}{d\widetilde{Q}} m_{ref}\left(\widetilde{Q}\right) \mathrm{d}\widetilde{Q} \tag{5.20}$$

where $m_{ref}(Q)$ is the mass within the PV contour Q in a zonally symmetric reference state and subscript e indicates departures from the reference state. Assuming $Q_{ref}(\phi)$ is monotonic then $m_{ref}(Q) = \mathcal{M}_{ref}(Q)$.

Using the mass-circulation balance equation

$$Q \frac{\partial \mathcal{M}}{\partial Q} = \frac{\partial \mathcal{C}}{\partial Q} \tag{5.21}$$

Equation (5.20) can be written as

$$\mathcal{A} = -h_e u_e \cos\phi - \frac{h}{2\pi a} \left[Q \left(\mathcal{M}_{ref}(Q) - \mathcal{M}_{ref}(Q_{ref}) \right) - \left(\mathcal{C}_{ref}(Q) - \mathcal{C}_{ref}(Q_{ref}) \right) \right]. \tag{5.22}$$

If the reference state is a PV-conserving mass rearrangement of the actual state then Equation (5.22) can be further simplified to

$$\mathcal{A} = -h_e u_e \cos\phi - \frac{h}{2\pi a} \left[Q \left(\mathcal{M}(Q) - \mathcal{M}(Q_{ref}) \right) - \left(\mathcal{C}(Q) - \mathcal{C}(Q_{ref}) \right) \right]. \tag{5.23}$$

This expression consists of two terms, one of which $h_e u_e \cos\phi$ approximately represents gravity waves while the other $\frac{h}{2\pi a}\left[Q\left(\mathcal{M}\left(Q\right)-\mathcal{M}\left(Q_{ref}\right)\right)-\left(\mathcal{C}\left(Q\right)-\mathcal{C}\left(Q_{ref}\right)\right)\right]$ is the approximate contribution from Rossby waves. The magnitude of the 'Rossby wave' term is several orders of magnitude larger than the 'gravity wave' term, so in calculations of $\mathcal{A}$ it is sufficient to only calculate the contribution from the Rossby wave term. Moreover the Rossby wave term is easy to calculate once $\mathcal{M}$ and $\mathcal{C}$ are calculated, which are quantities of interest in themselves.

Since the initial state is a balanced flow the reference state is taken to be the initial state meaning that $Q_{ref} = Q_{initial}$.

5.3.6 $\psi - Q$ Plots

Plots of the streamfunction ψ against the PV Q are able to show when the flow departs from free mode form. When the flow is not in free mode form, that is the PV is not a function of the streamfunction, the spread of the points about a compact curve $Q = Q\left(\psi\right)$ shows how far from free mode form the flow is (Read et al., 1986).

The streamfunction in spherical co-ordinates can be written as

$$\boldsymbol{u} = \widehat{\boldsymbol{r}} \times \nabla\psi \tag{5.24}$$

$$= \frac{1}{a}\frac{\partial\psi}{\partial\phi}\widehat{\boldsymbol{\lambda}} - \frac{1}{a\cos\phi}\frac{\partial\psi}{\partial\lambda}\widehat{\boldsymbol{\phi}} \tag{5.25}$$

where $\widehat{\boldsymbol{\lambda}}$, $\widehat{\boldsymbol{\phi}}$ and $\widehat{\boldsymbol{r}}$ are the unit vectors in the λ, ϕ and r directions respectively.

Equation (5.25) is easily calculated from the model by integrating the horizontal velocity components, which are prognostic variables in the model.

5.4 Model Results

5.4.1 Investigating how the rate of growth of the mountain affects the onset of model SSWs

In this section effect which the rate of growth of the mountain has on the onset of model SSWs is investigated. In particular how does the time at which a model

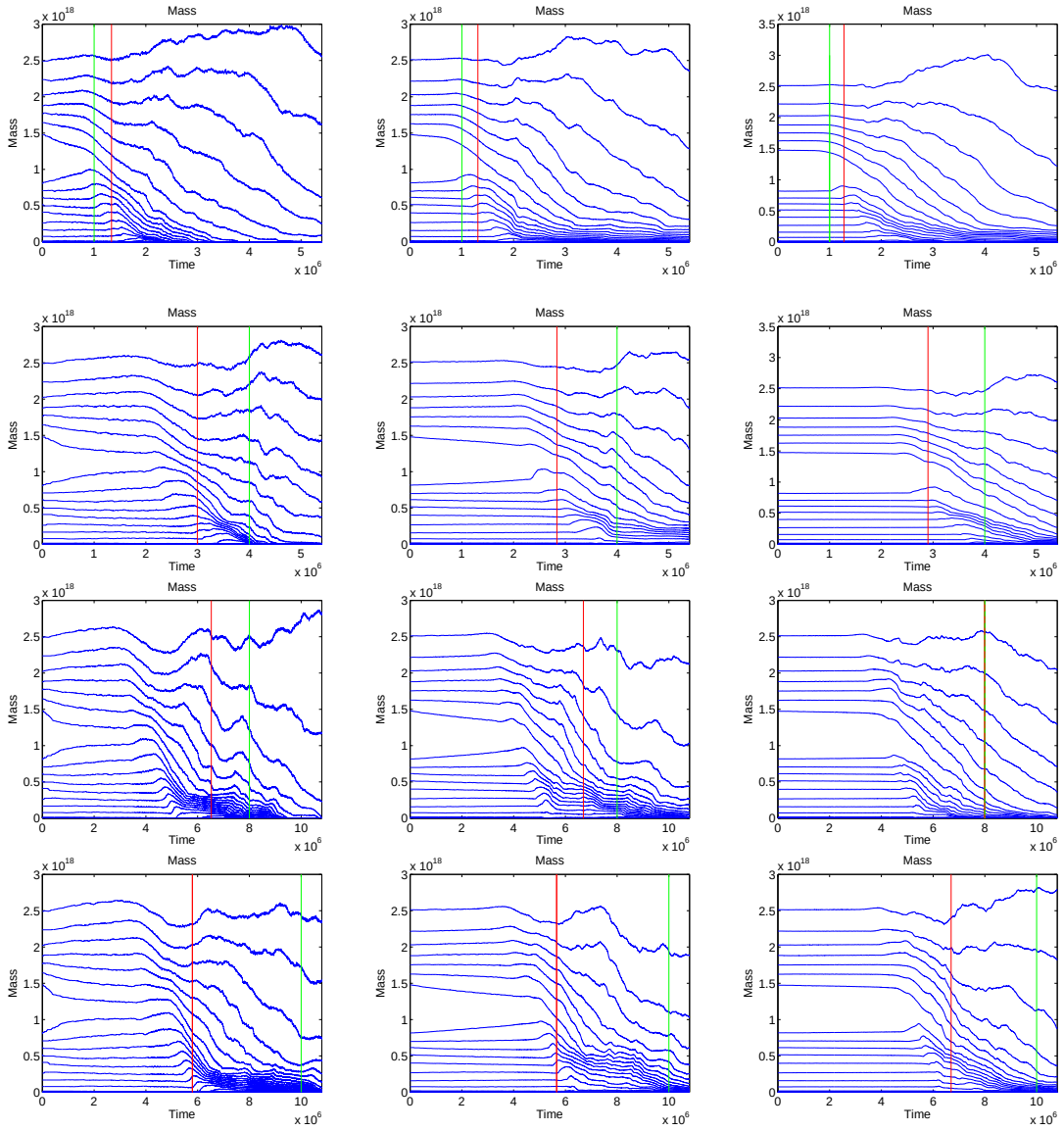

Figure 5.3: Northern hemisphere plots of mass for various model resolutions and rates of mountain growth, with maximum height of 2000m. The left most column is on the cubed sphere with a resolution of 13824 grid boxes (208km), the middle column is the same with 55296 boxes (104km) and the right most has 221184 grid boxes (52km). The mountain has a time varying part of the form $\frac{1}{2}(1-\cos\left(\pi\frac{t}{\tau}\right))$. The top row has $\tau = 1\text{x}10^6$, the second is $\tau = 4\text{x}10^6$, third $\tau = 8\text{x}10^6$ and the bottom row has $\tau = 1\text{x}10^7$. The PV contours are equally spaced in PV space, from $2.56\text{x}10^{-9}$ s m^{-2} to $9.6\text{x}10^{-9}$s m^{-2}. The red line corresponds to the onset of an SSW and the green to the time when the mountain reaches its maximum height. Note that in the case of $\tau = 8\text{x}^6$ at a resolution of 52km the red and green lines are at almost exactly the same point.

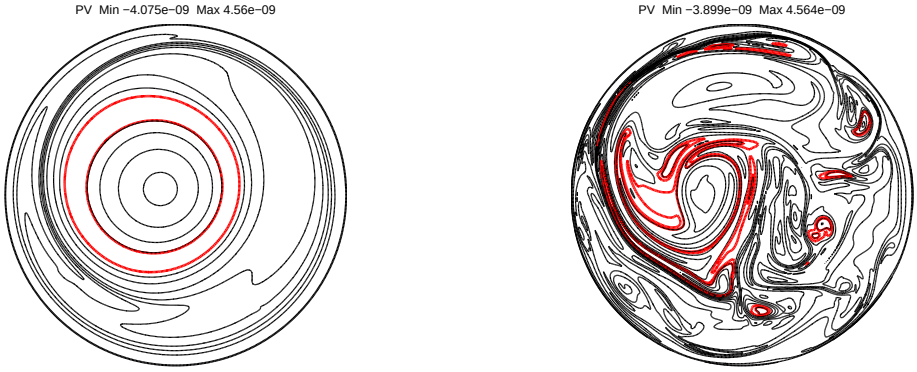

Figure 5.4: PV maps for before and after the onset of the model SSW for the τ = 8x10^{6}s case of the 52km run in Figure 5.3. The black contours are evenly spaced, and the red contours indicate those shown in Figure 5.6

SSW occurs change with the growth rate of the mountain and does it occur when the mountain reaches some particular predefined height.

The effects that the resolution of the model has on the onset of SSWs is also investigated. The transfer of mass across PV contours is due to fine scale features of the flow reaching small scales unresolved by the finite sized grid used in the model. This means that the resolution of the model has a large effect on this rate of mass transport.

The model was run at several different resolutions and rates of mountain growth, with the maximum height of the mountain H^* = 2000m. The timeseries of mass for the Northern Hemisphere from these runs are shown in Figure 5.3 (see caption for details). All model runs start with the same zonally symmetric PV field defined above. For the lower resolution runs there is significant leakage of mass across the PV contours from the start of the run which decreases after around 1x10^{6}s, though is still present for the entirety of the model run. As the resolution increases this leakage reduces significantly until there is almost none in the highest resolution runs shown in the far right hand column of Figure 5.3. Despite this feature the effects of the growth on the forcing are clearly identifiable in the timeseries of mass with the vortex breaking down and simulating a sudden warming at some point after the effects of the forcing begin to take effect. The timeseries of mass also

becomes smoother as the resolution increases.

As the resolution of the model increases the vortex breaks down slightly later than at lower resolutions. It is possible that this could be because at lower resolutions there is more transfer of mass across the vortex edge via numerical leakage meaning that the criteria for the vortex to break down may be met sooner in the case of the lower resolution vortex. As with the signal for vortex breakdowns and sudden warming events seen in the ERA-40 data (see chapter 3) the signal of the vortex breakdown propagates toward the centre of the vortex, so appears sloped in the plots of $\mathcal{M}(Q)$ as it occurs later on the higher valued PV contours near the vortex centre than on the lower valued ones at the vortex edge. There is also a slight rise in the mass within the contours near to the edge of the vortex in the immediate lead up to the breakdown similar to what can be seen in the reanalysis data. This small increase in mass starts on the outer contours and as with the loss in mass it propagates from the contours on the vortex edge toward the centre of the vortex. The speed of this propagation toward the vortex interior is slower than the propagation of the loss of mass toward the same contours, with the contours on the edge retaining the extra mass for a longer time than those closer to the centre. These two signals reach some of the inner-most contours at roughly the same time, increasing the gradients of PV very close to the vortex centre.

This signal of the vortex breakdown is preceded by a period of relative stability where the mass within the contours of the higher resolution runs remains unchanging. This can be seen in the centre and right hand columns here; the lower resolution left hand column has too much numerical leakage in the early part of the model run so there is no period of stability but a steady change in mass is seen instead.

In the period before the rapid loss in mass of the vortex a surf zone-like structure forms in the area around the vortex. As the surf zone forms tongues of air from the tropics can be seen to be mixed into it (eg see left hand plot in Figure 5.4). In the early parts of the simulation there is much more tropical air mixed into the surf zone than vortex air, similar to what was found by Norton (1994) and Polvani

et al. (1995). This is not very visible in Figure 5.3 as the features of the tongues of air have not yet reached scales small enough for mass to be mixed across them, though especially in the bottom two rows of Figure 5.3 the tropical contours start to change in mass before the contours making up the vortex. As the vortex starts to become eroded though the amount of vortex air making up the surf zone increases significantly. This differs from the findings of Norton (1994) and Polvani et al. (1995) who found that for the entirety of the simulation there was little vortex air making up the surf zone compared to tropical air. In these studies the mountain was located at 45^o north compared to the 60^o North used here. The more Northern location of the mountain, which stimulates stripping of more Northern contours, is likely to be the reason for the difference in the relative amount of vortex air in the surf zone.

The signal of the breakdown of the vortex that can be seen in Figure 5.3 is very similar to what is seen in the ERA-40 data in chapter 3, with a slight increase in mass before the loss of mass as the vortex breaks down. Following the simulated SSW events the vortex does not recover in the way seen in the ERA-40 plots of $\mathcal{M}_{Q,\theta}$, since for the vortex to recover some 'diabatic' effects would be required to move mass back into the vortex. In some cases the model vortex becomes completely eroded. The period leading up to the SSW is also unlike the ERA-40 equivalents; in the period before warmings the vortex undergoes changes in mass in the ERA-40 diagnostics but in the case of the current model the mass of the vortex remains relatively steady in the period before SSW starts to occur (eg. the first 1x10^{6}s in the top right plot in Figure 5.3. As the forcing is different to that in the case of ERA-40 for this period the difference between the two is to be expected. The fact that the simulated warmings appear similar to those seen in the ERA-40 data gives confidence for the choice of the shallow water equations to investigate stripping in the polar vortex. This means that the results obtained from studying the shallow water model vortex can be applied to the real polar vortex.

The speed of the propagation of the signal of the SSW from the edge of the vortex toward the centre appears to decrease along with the growth rate of the

mountain, taking longer for the signal to reach the centre as the growth rate decreases. For example in the case of the fastest growing mountain ($\tau = 1\text{x}10^6$s) the signal of the breakdown takes approximately $1\text{x}10^6$s to propagate to the vortex centre after it starts to appear on the outer contours. Compared with this the same signal takes roughly $1.5\text{x}10^6$s to propagate for $\tau = 4\text{x}10^6$s. This means that while the rate of propagation from the vortex edge to the centre of this signal is related to the growth rate of the mountain, the two are not directly proportional.

The initial leaking of mass out of the vortex that can be seen at lower resolutions toward the start of the model runs, before the effects of the mountain start to become visible, appears to occur at a similar rate independently of the rate of growth of the mountain. At the highest resolution shown (52km) this leakage appears to have disappeared almost entirely, which means that this resolution appears sufficient for the numerical experiments carried out below while still being able to carry out a sufficient number of model runs to explore a larger area of parameter space.

Decreasing the growth rate of the mountain by increasing the value of τ also has the effect of delaying the onset of the sudden warming. As well as the signal of the SSW becoming visible later in time, it can also be seen to start occurring at lower mountain height values when the mountain is grown more slowly. This can be seen by looking at plots of mass $\mathcal{M}(Q)$ against the height of the mountain h (Figure 5.5), where the breaking of the vortex doesn't occur until after the mountain has reached its maximum height of 2000m for the fastest growth rate, but appears at as low as half this height, $h = 1000$m, for the slowest growing mountain in the test cases.

There doesn't appear to be a clear difference between a 'preconditioning' of the vortex and the SSW, though in the case of the slower growing mountain there is a period where mass appears to be stripped from the vortex before the onset of the SSW. This will be examined in subsection 5.4.2 in an attempt to determine whether this mass removal is acting to precondition the vortex or whether it is a part of the SSW occurring.

In the slowest growing of the test cases for the 104km resolution there appears to be a second period where $\mathcal{M}(Q)$ for the vortex remains relatively stable, at around $8\text{x}10^6$s. This doesn't appear to occur at the highest resolution where the mass of the vortex decreases at a relatively steady rate.

Figure 5.6 shows the total amount of mass removed from two particular PV contours (those highlighted in red in Figure 5.4) at various resolutions. These contours lie on or around the vortex edge and so are a good indication of air moving into or out from the vortex. The left and right columns correspond to the same PV contour (the outer red contour in Figure 5.4); the left hand column shows mass removed against time and the right against mountain height. This contour corresponds to one on the vortex edge of the surf zone. The middle column corresponds to a contour at the edge of the vortex (the inner red contour in Figure 5.4) and shows mass removed against time. Each row corresponds to different growth rates of the mountain, and the various lines on each plot are different resolutions; the red line corresponds to a resolution of 416km, the green to 208km, the blue has 104km and the magenta line corresponds to a resolution of 52km, all of which correspond to a cubed sphere grid.

The leakage of mass across contours of PV which was observed above (Figure 5.3) is very evident in Figure 5.6. This leakage is reduced as the resolution is increased, as can be seen by the mass stripped becoming minimal at the higher resolution runs until the mountain has grown to a suitable level to initialise more mass removal. The removal which is then initiated seems to be the start of the breakdown of the vortex, though this will be further investigated below.

The plots of mass removed from the contour on the vortex edge (middle column in Figure 5.6) show an increase of mass within this contour (ie. negative removal of mass) prior to the loss of mass as the vortex breaks down and the sudden warming like event occurs. The maximum amount of mass acquired by this PV contour seems to be similar for a given resolution across each of the growth rates used in the test runs here, roughly $1\text{x}10^{17}$ m^4 s^{-2}. It is possible that there is a specific amount of mass added to this PV contour prior to the vortex breaking but this

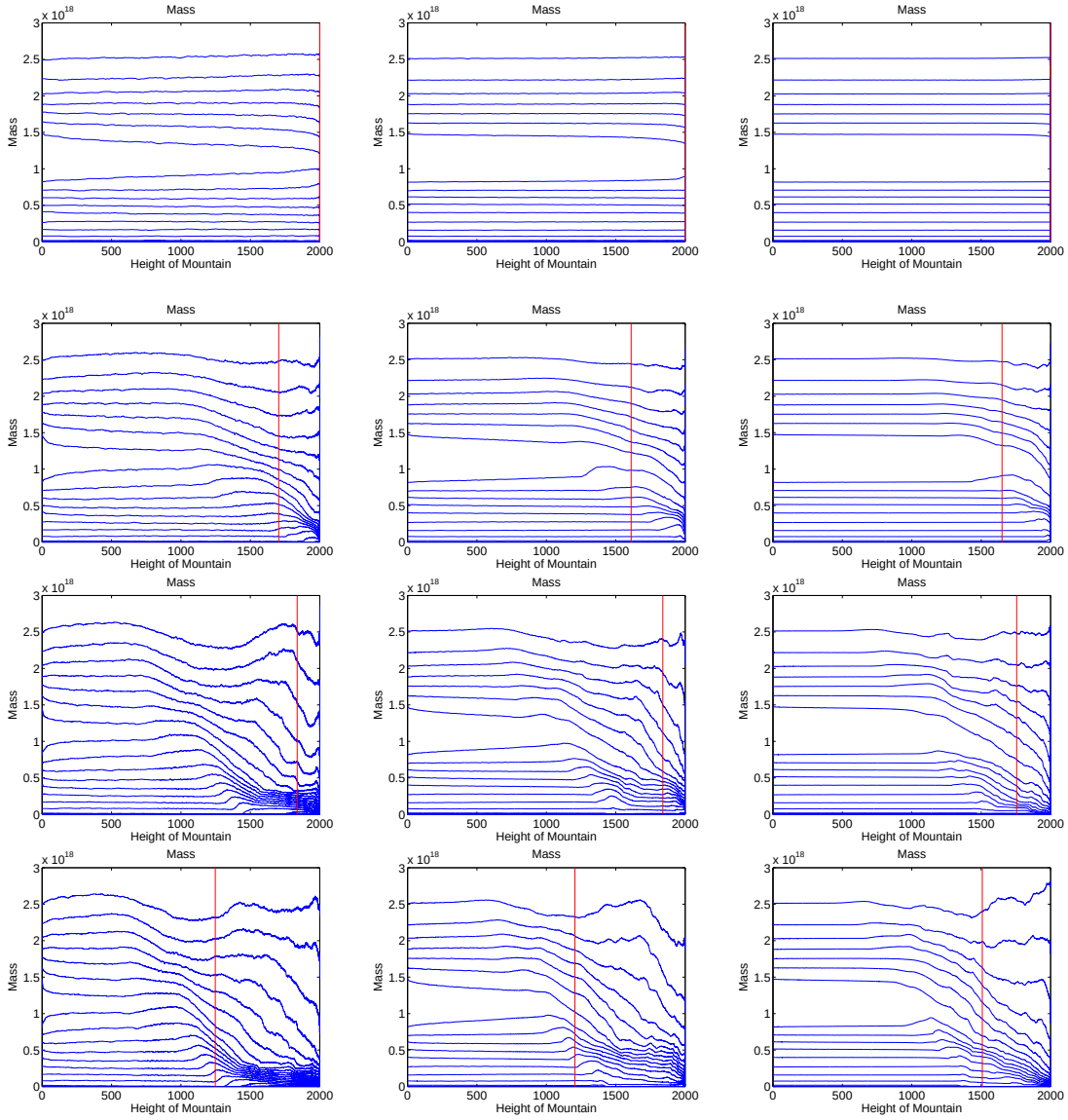

Figure 5.5: Northern hemisphere plots of mass against mountain height for various model resolutions and rates of mountain growth. The left most column is on the cubed sphere with a resolution of 208km, the middle column is the same with a resolution of 104km and the right most is 52km. The mountain has a time varying part of the form $\frac{1}{2}(1 - \cos(\pi \frac{t}{\tau}))$. The top row has τ = 1x10^6, the second is τ = 4x10^6, third τ = 8x10^6 and the bottom row has τ = 1x10^7. The PV contours are equally spaced in PV space, from 2.56x10^{-9} s m^{-2} to 9.6x10^{-9} s m^{-2}. The red lines mark the onset of an SSW.

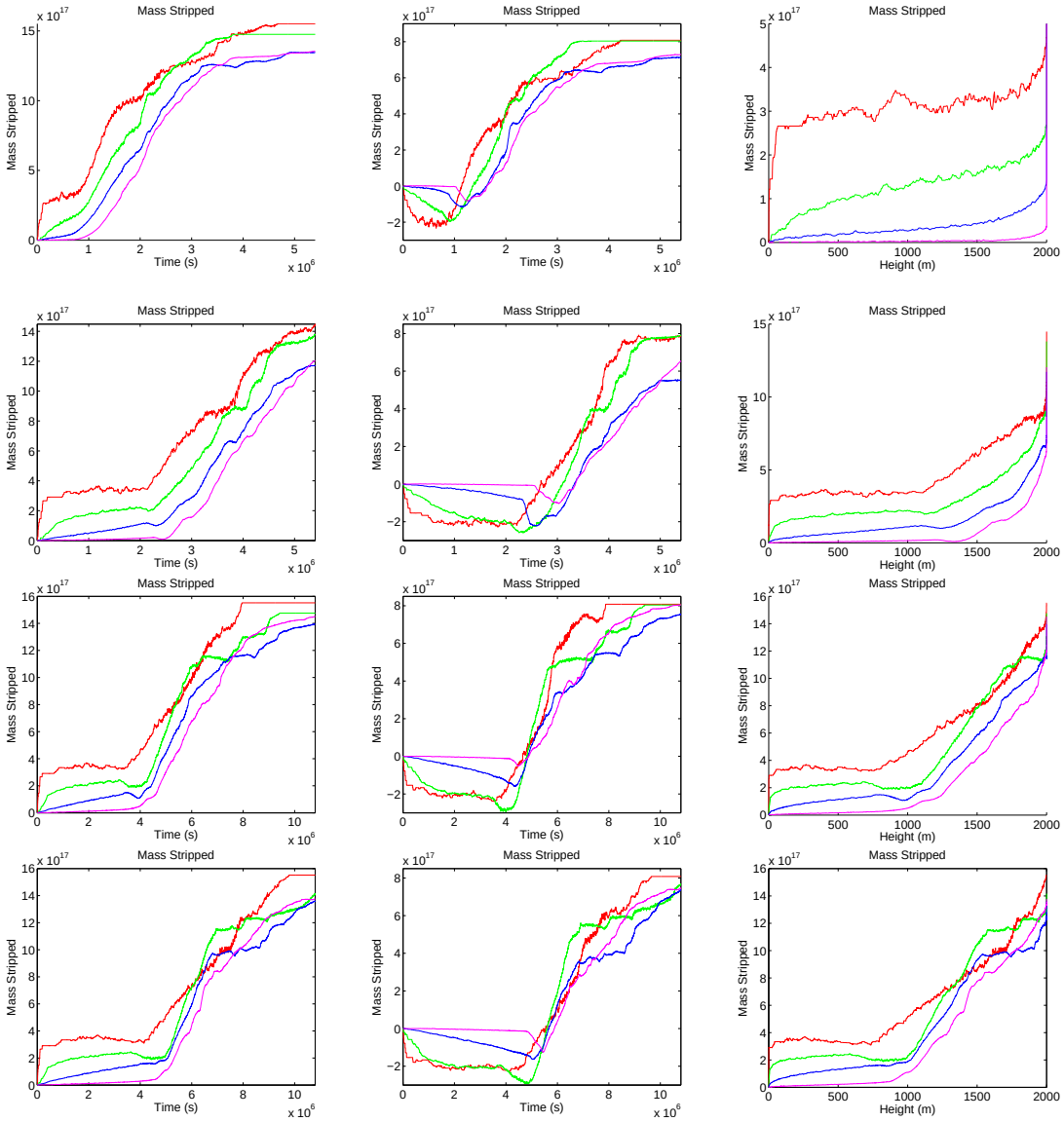

Figure 5.6: Plots of mass stripped (mass-initial mass) for various pv contours (columns) and values of $\tau = 1\text{x}10^6$ (row 1), $\tau = 4\text{x}10^6$ (row 2), $\tau = 8\text{x}10^6$ (row 3) and $\tau = 1\text{x}10^7$ (row 4). The left and right columns correspond to the outer red contour in Figure 5.4 and the middle column corresponds to the inside red contour indicated in Figure 5.4. The red line corresponds to a resolution of 416km, the green is 208km, the blue 104km and the magenta 52km.

will require more model runs to verify and will investigated below.

During the runs in which the mountain is grown more slowly, in particular the bottom rows of Figure 5.6, there also appears to be a small increase in mass prior to the initial removal of mass from the PV contour at the edge of the surf zone (left and right columns in the figure). As the resolution increases this increase becomes smoother and smaller in magnitude, with the increase disappearing on the outer contour for the higher resolutions.

As the resolution increases the initial loss in mass decreases until it appears that the effects of the mountain become more clearly distinguishable from the effects of the low resolution mass leakage.

It appears that the slower the mountain is grown, the larger the amount of mass removed from the vortex before it reaches its maximum height of 2000m. This mass loss is also slower when the mountain is grown more slowly. It will be investigated in the next section how this links to the height of the mountain at any given time.

5.4.2 Investigating the effect of different mountain heights on the rate of mass removal for a Wave 1 forcing

After completing the experiments in the previous section, it appears that as the mountain is grown at a slower rate the model SSW starts to occur at lower mountain heights. In this section the mountain is grown, with a value of $\tau = 8 \times 10^6$, to several intermediate heights. In this case

$$T(t) = \begin{cases} 0.5\left(1 - \cos\left(\frac{\pi t}{\tau}\right)\right) & H \leq H_{max} \\ 1 & H = H_{max} \end{cases} \tag{5.26}$$

where H is the current height of the mountain and H_{max} is the maximum mountain height. The effect of these differing heights on the onset of SSWs is investigated, and the rate and amount of stripping related to differing mountain heights.

Figure 5.7 shows the total amount of mass removed from each of the two red contours in Figure 5.4 for several different mountain heights. These contours lie around the vortex edge and any change in mass of these contours can be interpreted

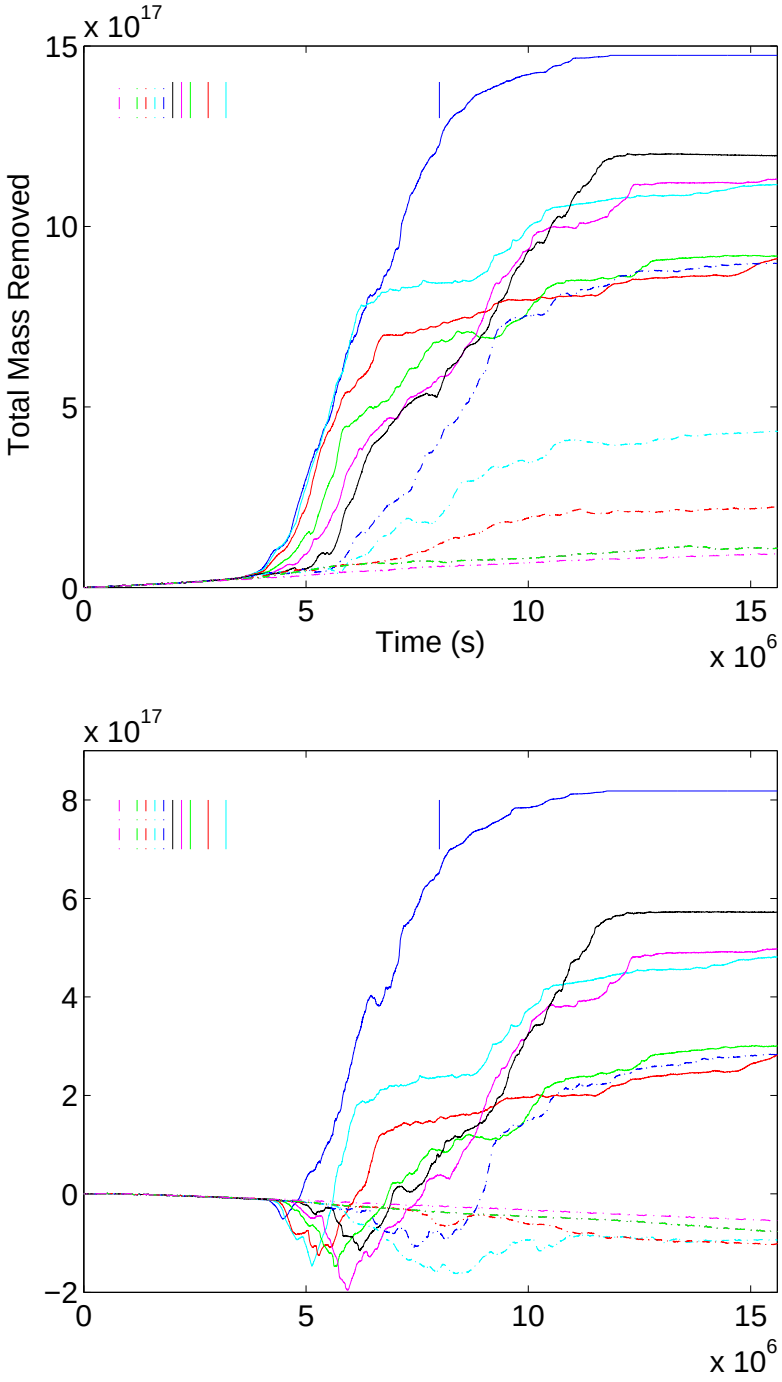

Figure 5.7: Mass removed from two PV contours on the edge of the vortex for wave 1 simulations. The top figure corresponds to the outer red contour in Figure 5.4 and the bottom figure to the inner red contour. The mountain was frozen at various heights (the solid blue line is the full 2000m mountain, the solid cyan line 800m, the solid red line is 700m, 600m (solid green line), 550m (solid magenta), 500m (black), 450m (dashed blue line), 400m (dashed cyan line), 350m (dashed red line), 300m (dashed green line), 200m (dashed magenta line). The mountain is grown with a value of $\tau = 8\text{x}10^6$s.

as change in mass of the vortex. The vertical lines at the top of the plots show the times when each of the mountains reach their maximum heights.

When the mountain is grown to only low heights there is a relatively small amount of mass removed from the vortex. For example when the mountain is grown to a height of 200m the mass flux occurs at a very low rate, though the air surrounding the vortex still becomes very turbulent after enough time has passed, and tongues of air can be seen to form at the edge of the vortex.

When the mountain is grown to a height of 350m the amount of mass removed from the vortex is very similar to the 200m case for roughly the first 70 model days. After this the outward mass flux for the case of the 350m mountain run increases. When the mountain is grown to larger final heights the initial mass loss is again very similar to the 200m mountain mass flux for the first $4.5\text{x}10^6$s before starting to accelerate. This increasing of the rate of mass loss occurs much longer after the mountain has reached its full height for the lower maximum mountain heights than it does for larger maximum heights. This suggests that the forcing does not initiate stripping directly, but initiates a process which then results in removal of mass from the vortex at some time later.

After a period of roughly 140 model days many of the runs have reached a stage where no or little further mass flux out of the contour occurs. In this case the flow is not steady, but the mass $\mathcal{M}(Q)$ becomes almost unchanging at the edge of the vortex.

The PV contour shown in the bottom panel of Figure 5.7 initially experiences an increase in mass, with the 200m mountain case experiencing a gradual steady increase in mass for the period of the model run. When the mountain is grown to a height greater than 200m the contour experiences a larger increase in mass, which persists for longer times when the final mountain height is smaller. For those runs with a final mountain height over 450m, following an initial gain in mass the contour then begins to decrease in mass to a level below that of the starting level.

As well as the period of the mass gain being longer as the final height of the mountain becomes smaller, the amount of mass gained by the PV contour also

seems to increase, attaining a maximum when the final height of the mountain is 550m.

Close to the end of the model runs the amount of mass within the PV contour again appears to reach a steady state, much like the outer contour shown in the top panel, for most final mountain heights although there are some which appear to still be losing mass. For the runs where the mountain height is less than 450m the amount of mass within the PV contour is larger at the end of the winter than at the start as the period where mass starts to be rapidly removed from the vortex doesn't appear to have initiated for these low forcing amplitudes.

There doesn't seem to be any threshold in the amount of mass removed from or added to either of the PV contours shown here before the rate of stripping starts to increase above the level of the 200m mountain, rather it is the size of the forcing and not the amount of mass removed from or gained by the PV contour that is responsible for the contour starting to lose mass more rapidly.

Once the rate of mass loss from the contour increases, between 4.5x10^{6}s and 5x10^{6}s, the average rate of loss is similar for all runs with a mountain of 500m or more and continues at this rate for a period of 10 model days for all but the 2000m mountain which proceeds at this rate for nearly double this time.

Figure 5.8 shows PV against mass for various instants during the 550m wave1 mountain run. The red line coincides in timing with the point where the inner contour of Figure 5.7 reaches its maximum mass. Comparing this to the initial PV-$\mathcal{M}$ profile (blue line) shows that there is one main area where contours decrease in mass, between 2.5×10^{-9} and 3.5×10^{-9} s m^{-2}, and two areas, a small one at higher PV values and a larger one at lower PV contours, which gain mass compared with the initial state.

From conservation of circulation

$$\int \mathrm{d}\mathcal{C} = 0 \tag{5.27}$$

then for any 2 Q values Q_1 and Q_2 where the circulation is constant, and if circulation is conserved, then using the relation

$$\frac{\partial \mathcal{C}_{Q,\theta}}{\partial Q} = Q \frac{\partial \mathcal{M}_{Q,\theta}}{\partial Q} \tag{5.28}$$

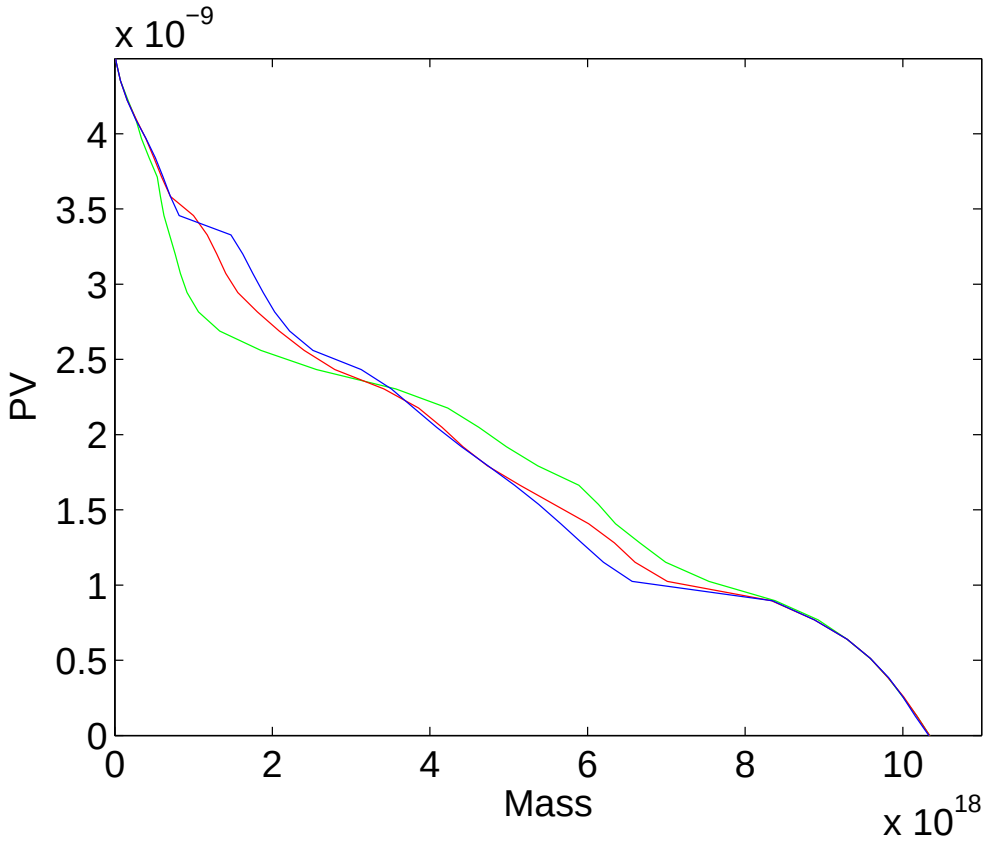

Figure 5.8: PV Q against mass $\mathcal{M}(Q)$ for various instants for the wave 1 550m mountain. The blue line is the initial condition, the red line is 68 days and the green line is 105 days.

this can be expressed as

$$\int_{Q_1}^{Q_2} Q \, \mathrm{d}\mathcal{M} = 0 \tag{5.29}$$

This means that the area under the curves in PV-$\mathcal{M}$ space (Figure 5.8) must remain constant for all instants during the model run. It then follows that if the mass within some PV contours decreases, there must be other region(s) in PV space where the mass increases to compensate. Since the mass within PV contours in the southern hemisphere (not shown in Figure 5.8) is almost constant over the entirety of the model run, when there is stripping of mass from the vortex there must be areas in the northern hemisphere which increase in mass to compensate for this.

Between the initial state of the model and the red line in Figure 5.8 there is

a small increase in mass in higher valued contours, which is much smaller than the increase in the lower valued contours corresponding with the increase in the contours in the region of the vortex edge.

By day 105 (the green line in Figure 5.8) the mass of the contours within the vortex (those above 2.4×10^{-9} s m^{-2}) has decreased quite significantly. Here there is no region of compensating mass increase in the higher valued PV contours, instead there is a large increase in mass within the 1×10^{-9} to 2.4×10^{-9} s m^{-2} region. This regions clearly corresponds to the surf zone region which is by this point well established.

Model SSWs

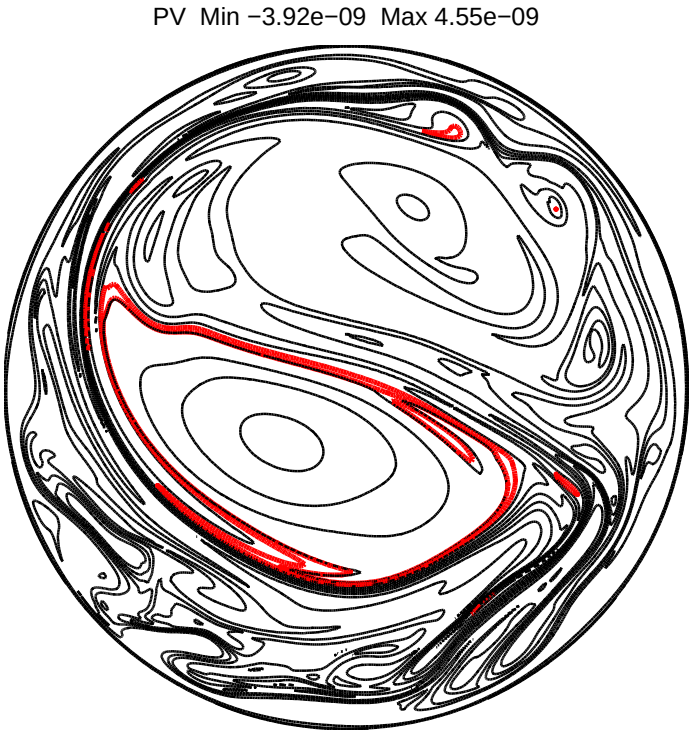

Figure 5.9: The displaced vortex following a simulated sudden warming for the case of a 600m forcing. The black contours are evenly spaced, with the two red contours corresponding to those plotted in Figure 5.7. The displaced vortex can be seen in the lower left part of the plot with the characteristic 'comma shape' that is seen in SSWs in the real atmosphere.

Using the criteria of Equation (5.18), when the mountain is grown to heights

Mountain Height	SSW time
2000m	72 days
800m	104 days
600m	126 days
500m	73 days
400m	-

Table 5.1: Dates of model SSWs for varying wave 1 mountain heights.

of 450m or higher the sign of Equation (5.18) reverses at some time during the experiment, indicating that an SSW-like event has occurred, and the vortex can be seen to have displaced from the pole (see Figure 5.9 for the 600m mountain for example). When the mountain is grown to lower heights (400m and below) the sign of Equation (5.18) does not change indicating that for these forcing amplitudes the model vortex does not undergo an SSW event.

As with the total amount of mass removed from the vortex the timing of the model equivalent of an SSW doesn't follow a linear relationship to the final mountain height. The 2000m mountain is the first to experience a model SSW around 70 days from the start of the run. As in the case of the ERA-40 data there doesn't seem to be a threshold for the amount of mass removed from the vortex (or equivalently the total mass within the vortex) for an SSW to occur. Shortly after the onset of the warming in the 2000m case an SSW occurs for the 500m mountain. The mass within the vortex at this point is much larger than that of the 2000m case.

Figure 5.9 also shows several areas where mass has been pulled from the vortex as a tongue of air is mixed into the surrounding air. In the top right of the figure there are several 'islands' of PV which started as vortex air. These have been disconnected from the vortex and are in the process of being eroded. These are similar to what can be seen in McIntyre and Palmer (1984) (their Figure 1).

The original hypothesis in performing these experiments was that the vortex progresses through several quasi-steady states. This does not seem to be the case

25 days

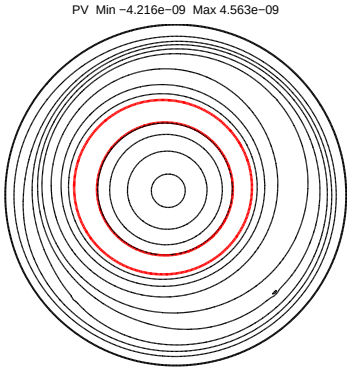

104 days

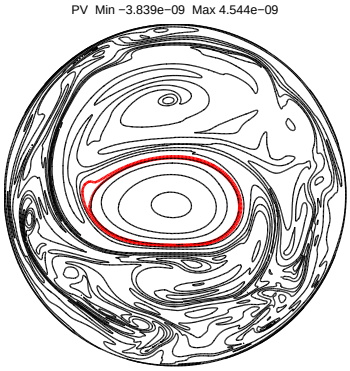

52 days

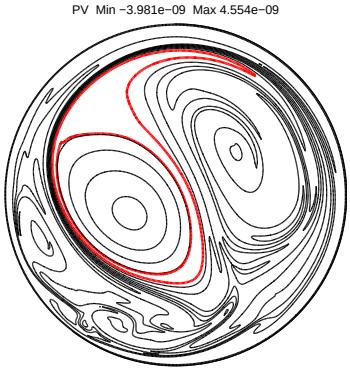

121 days

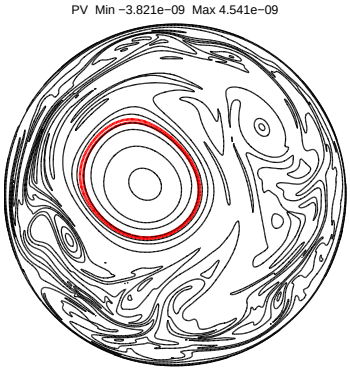

78 days

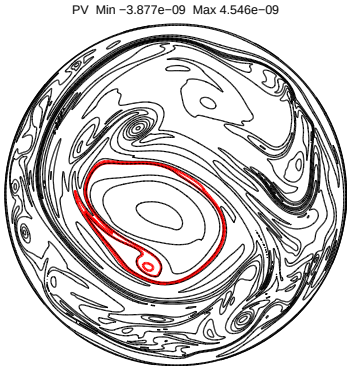

173 days

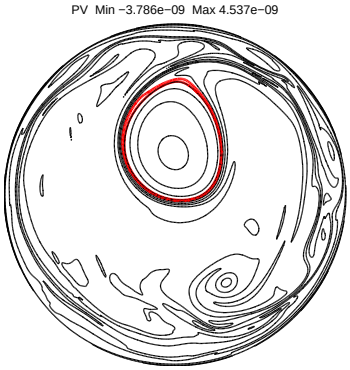

Figure 5.10: PV maps for the case of the 700m wave 1 mountain at several instants during the experiment for the days indicated.

since for even very small mountain heights there appears to be a small amount of mass removed from the vortex, as well as the fact that tongues of PV appear to form on the edge of the vortex, although these do not then appear to mix into the surrounding air to form a surf zone, or form a very thin one.

The period of rapid reduction in mass removal rate

Around the time of the sharp decrease in the rate of mass flux from the vortex in the case of the 700m mountain forcing the tongues of air attached to the vortex start to disappear; as time passes the existing tongues get pulled from the vortex and no new tongues form as they do in the other experiments. Instead the edge of the vortex appears to become sharper and more oval shaped than is typical up until this point (see Figure 5.10). The sharper vortex edge created by the removal of mass up to this point then appears to inhibit further tongues of air from forming leading to the dramatic reduction in the rate of removal of mass from the vortex. This is similar to what has been found in other shallow water experiments, and termed 'Rossby elasticity' due to the fact that the edge of the vortex becomes more 'elastic' (Juckes and McIntyre, 1987; Norton, 1994).

At the time of the initial decrease in the rate of mass removal in Figure 5.7, around $6x10^6$s, the tongues of air that are attached to the vortex have mostly disappeared and those which remain are very small compared to those present in the period of high mass removal. Over the next 35 days there is a much reduced rate of mass removal where the parts of the vortex which form into small tongues are pulled from the vortex but do not pull any more mass with them, therefore disappearing very quickly after forming. This then makes the vortex into a more regular oval shape, gradually losing the non-oval shaped elements as they become eroded. After $9x10^6$s (roughly 100 days) the vortex has lost all tongues attached to it, and the mass removal rate becomes almost negligible, around the same rate as that of the 200m mountain.

There are two periods after the mass removal rate has decreased where further tongues of air form and become eroded from the now more regularly shaped vortex. These tongues last for short periods of time before the vortex again does not have any tongues attached to it. One of these can be seen in Figure 5.10 at day 173.

In the cases of the other final mountain heights the same effect can be seen in the period where the rate of mass removal significantly decreases, around 115 model days in most cases. The tongues attached to the vortex disappear and the

edge seems to become a more regular oval shape, although in the case of the 2000m mountain the vortex has become almost completely eroded.

5.4.3 Wave Activity

As noted above the amplitude of the forcing does not appear to be proportional to the amount of mass stripped from the vortex. The wave activity $\mathcal{A}$ (Equation (5.23)), however, is a good measure of the accumulated forcing. It is possible that the wave activity will give a better measure of the amount of stripping of mass from the vortex.

The wave activity is related to the forcing by the relation Equation (5.19)

$$\frac{\partial \mathcal{A}}{\partial t} + \nabla \cdot \mathcal{F} = \mathcal{S} \tag{5.30}$$

where $\mathcal{S}$ includes the lower boundary forcing as well as mixing, diabatic and frictional forces.

Integrating these over the sphere then gives

$$\int \frac{\partial \mathcal{A}}{\partial t} \, \mathrm{d}S = \int \mathcal{S} \, \mathrm{d}S \tag{5.31}$$

since the integral of $\nabla \cdot \mathcal{F}$ over the sphere must vanish. This means that the space-time integral of the mountain forcing is related to the space integral of $\mathcal{A}$.

Using the initial zonally symmetric state as the reference state in Equation (5.23) the wave activity has been calculated for various model runs. Figure 5.11 shows the wave activity $\mathcal{A}$ for the wave 1 case with a mountain of height 700m. The gravity wave part of the wave activity ($-h_e u_e \cos\phi$) is roughly 10^4 times smaller than the Rossby wave part ($-\frac{h}{2\pi a}\left[Q\left(\mathcal{M}(Q) - \mathcal{M}(Q_{ref})\right) - \left(\mathcal{C}(Q) - \mathcal{C}(Q_{ref})\right)\right]$), meaning that this term can safely be neglected in the calculation of $\mathcal{A}$.

In the period up until the mountains reach their maximum heights the profiles of the wave activity are identical to that of the 2000m mountain. As the smaller mountains reach their maximum heights the profile then diverges from that of the larger forcing.

The wave activity begins very small, but after a period of 20 model days a wave 2 pattern starts to emerge. The terms in the wave activity equation in

10 days ctr=5.4×10^4

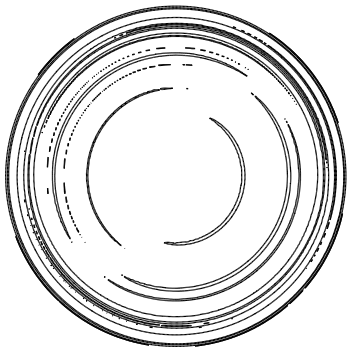

42 days ctr=2.0×10^5

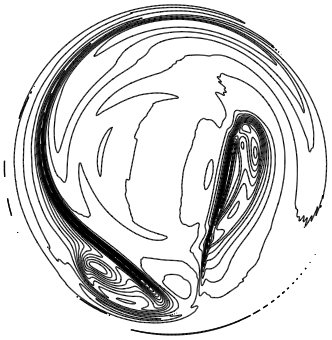

20 days ctr=1.1×10^5

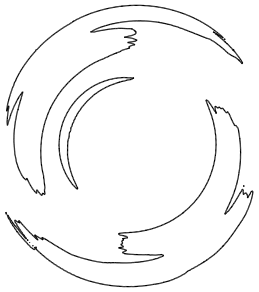

52 days ctr=2.0×10^5

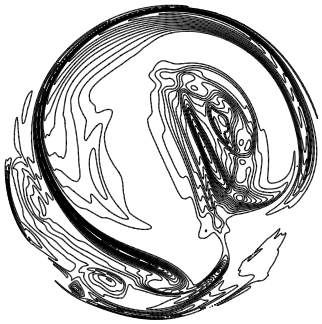

31 days ctr=1.1×10^5

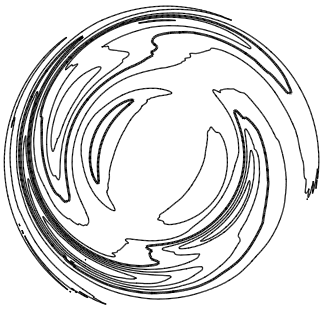

62 days ctr=2.2×10^5

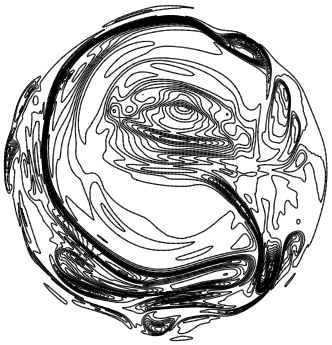

Figure 5.11: Wave activity $\mathcal{A}$ for various instants throughout the winter for the case of the 700m mountain for the days indicated. The contour interval is indicated by ctr, note that the spacing is much smaller for day 10 than for the other days.

Equation (5.23) are second order in disturbance quantities, so maps of $\mathcal{A}$ for a zonal wavenumber 1 disturbance will show wave 2 patterns, which is the case here for small amplitude forcing. As it starts to become more asymmetric $\mathcal{A}$ starts to pick out some of the anticyclones surrounding the vortex. For example at day 52 the area of the largest anticyclone is clearly picked out as well as several of the smaller ones.

These synoptic maps of wave activity $\mathcal{A}$ pick out many of the features seen in corresponding PV maps and don't seem to provide significantly more information than the PV does. The spatial integral of $\mathcal{A}$ is related to the time-space integral of mountain forcing. This means that if the time integral of mountain forcing is what is important in stripping then the integrated wave activity $\mathcal{A}$ may be a useful diagnostic quantity.

Figure 5.12 shows the mass removed from the vortex plotted against the wave activity integrated over the area of the Northern hemisphere $\int_{\phi>0} \mathcal{A}\,\mathrm{d}S$ for a selection of the final mountain heights from the wave 1 experiments. The figure shows the part of the graph for the initial part of the experiment where the integrated wave activity is increasing, in order to provide a monotonic x-coordinate. The points where the integrated wave activity reaches its maximum value for the 2000m and the 700m mountains are both very similar, with the wave activity for the 2000m mountain reaching its maximum a couple of days earlier than that for the 700m mountain.

On the inner PV contour (bottom plot in Figure 5.12 and Figure 5.7) the period where mass is being entrained into the vortex corresponds almost exactly to the period when the integrated wave activity is increasing. Other than the case of the 2000m mountain, where the mass flux changes from inward flux to outward flux slightly before the wave activity starts to decrease, the moment when the wave activity starts to decrease is the same moment as the change from inward to outward mass flux.

The rate of mass increase is approximately linearly correlated with integrated wave activity up until the wave activity becomes large, from around $8\text{x}10^{19}\text{m}^2\ \text{s}^{-1}$,

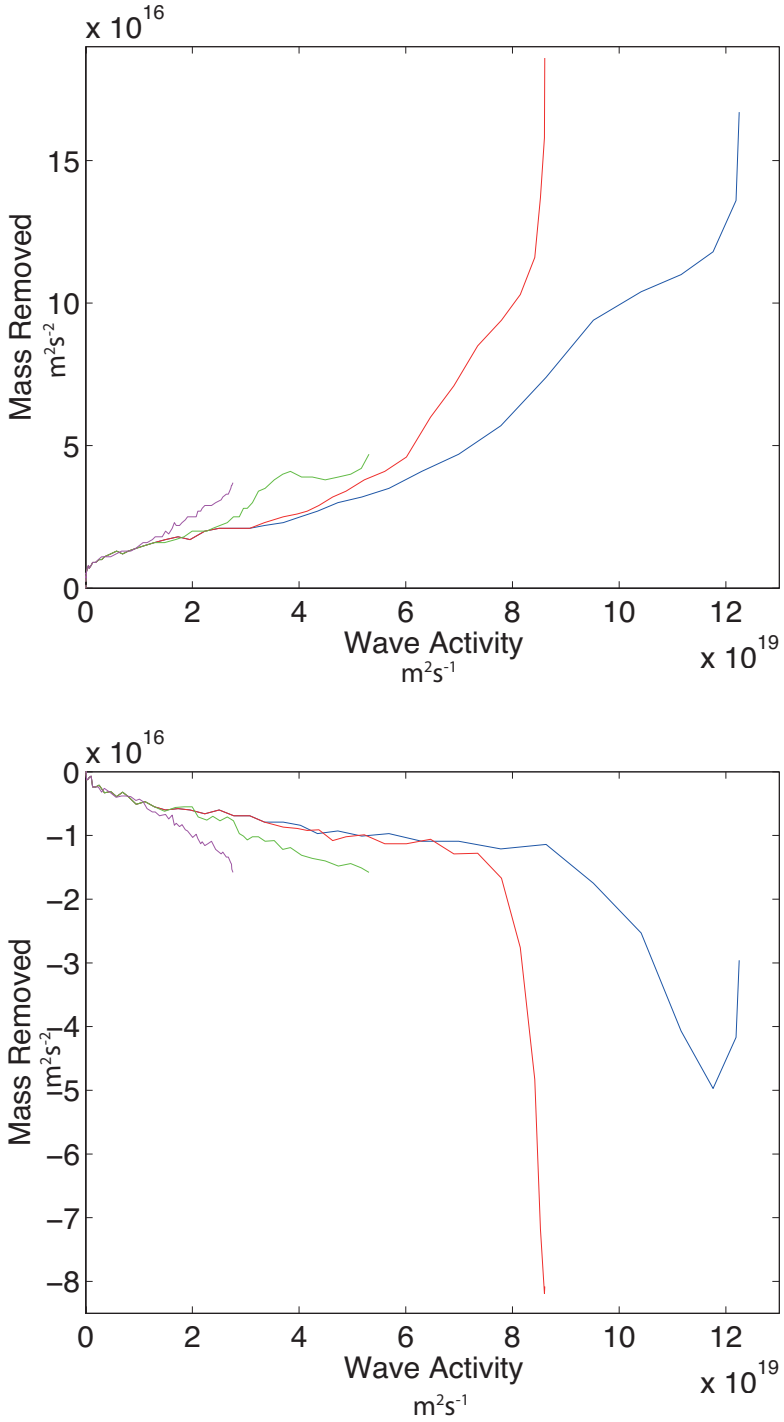

Figure 5.12: Total mass removed from the outer red PV contour (top) and the inner red contour (bottom) against wave activity $\mathcal{A}$ for period of the wave 1 experiments where the $\mathcal{A}$ is increasing for various mountain heights: 2000m (blue line), 700m (red line), 450m (green line) and 200m (magenta line). These figures correspond to the same contours as those in Figure 5.7. The negative values in the bottom figure here correspond to mass added to the contour.

when the rate of mass increase becomes significantly larger.

5.4.4 $\psi - Q$ plots

Scatter diagrams of the streamfunction ψ against PV Q can clearly show departure of the flow from free-mode form. It was hoped that departures from a compact curve, indicating departures from free mode form, may be a useful indicator of stripping.

In the case of these experiments the $\psi - Q$ plots (shown in Figure 5.13 for the 700m mountain) show that initially the points all lie on a compact curve indicating a steady flow state. As tongues of PV start to appear the points corresponding to the region of the tongue start to depart from the compact curve. This can be seen at day 34 in the 700m experiment. The $\psi - Q$ plot is also shown in Figure 5.14 along with the corresponding PV map for this instant. A tongue of air can clearly be seen to have formed at this point and the points corresponding to this tongue can be seen to correspond to those which have the largest departure from the compact line in $\psi - Q$ space. It is not clear what the size of this departure from the compact line means quantitatively.

The highlighted area of Figure 5.14 corresponds to the critical layer, also referred to by McIntyre and Palmer (1984) as the surf zone. In this region the waves at the vortex edge become irreversibly deformed and break, transporting mass from the vortex into the surrounding region. The area of departure from the compact curve at this point can be used as an indicator that tongues have started to form on the edge of the vortex, and that stripping is being initiated.

While it can be seen in this example, as well as for other experiments performed (not shown), that departure from the compact curve coincides with stripping of air from the vortex it is not possible to use these plots to quantify the amount or rate of stripping occurring. This would require an objective way of identifying the tongue of air in the model, which in practice is not possible.

The air within the vortex appears as the top part of the $\psi - Q$ plots, being the air having the highest PV values. This part of the plots remains relatively

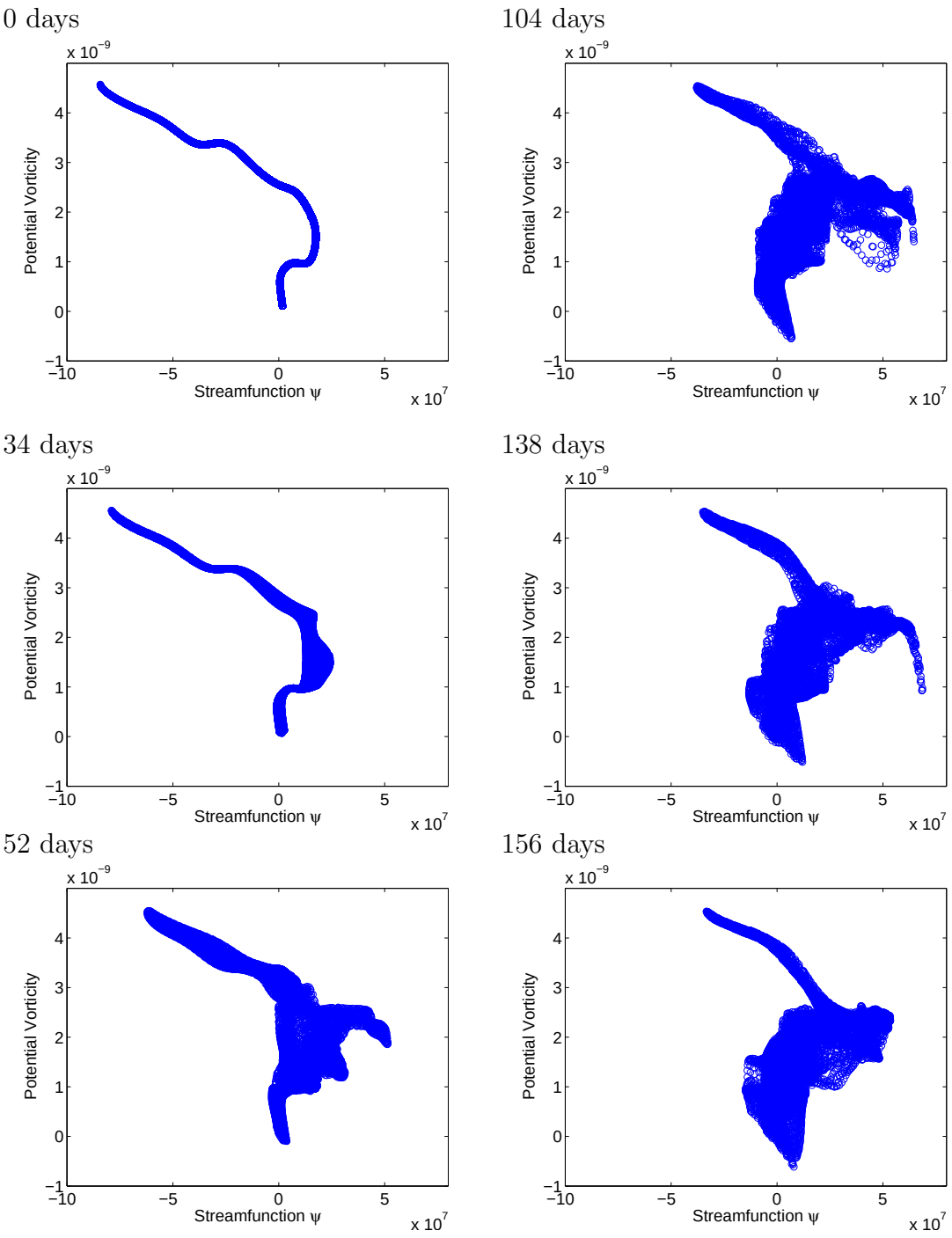

Figure 5.13: Scatter diagrams of streamfunction ψ against PV Q for various instants throughout the winter for the case of the 700m mountain for the days indicated.

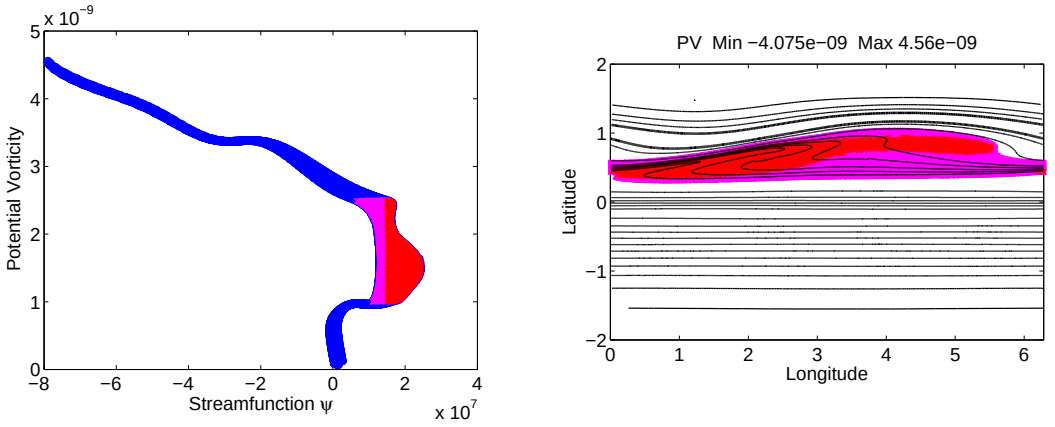

Figure 5.14: Scatter diagram of the streamfunction ψ against PV Q at 34 days along with the corresponding PV map. The coloured regions correspond to the same points on both plots. The red and magenta areas were chosen to coincide with the tongue of PV forming at this time.

compact throughout most of the simulations carried out here. In the case of the 2000m mountain the vortex gets almost completely eroded and the higher PV parts of the plots vary widely from the original compact form. When the vortex edge can be seen to be particularly sharp, such as toward the end of the 700m mountain simulation, the vortex edge ($Q \approx 3 \times 10^{-9}$) appears as the portion of the $\psi - Q$ space that is immediately above the large deviation from the compact curve.

In the case of the 700m mountain (Figure 5.13) the part of the $\psi - Q$ plots corresponding to the vortex gradually becomes less compact during the period of rapid mass removal from the vortex. When this period of rapid erosion of the vortex has slowed the relationship between ψ and Q for the air within the vortex again becomes closer and the upper parts of the $\psi - Q$ plots become again more compact. This can then be seen as an indicator that the rate of stripping has declined and the vortex has once more become isolated, as is the case with the other experiments where the rate of stripping reduces after some time.

The area of the plots which starts to become less compact when the tongues of air start to appear continues to become further from the original compact line as the area around the vortex becomes more turbulent, with the areas in the centre of the counter-rotating area lying furthest form the line. As the PV in the area

around the vortex becomes more well mixed the area of high ψ values in the $\psi - Q$ plots becomes more uniformly distributed to the right of the original compact line.

The vortex edge and surf zone can then be picked out from looking at the $\psi - Q$ plots, as the areas remaining close to the compact line, and the area showing the largest departure from the original line respectively.

Comparing the different wave 1 simulations, those in which more mass is removed from the vortex have a smaller compact part at the top of the $\psi - Q$ space, and in the case of the 2000m mountain this part is not present at all as the vortex is completely eroded by the end of the simulation.

It is not obvious what the cause of the reduction in the rate of stripping is in the case of several of the mountain heights. It is possible that for lower forcing amplitudes the vortex becomes eroded at a slow enough rate that numerical diffusion means that the edge of the vortex doesn't form a sufficiently sharp PV gradient to inhibit further stripping. This would mean that the inner contours of the vortex interior are then eroded once the outer ones have been sufficiently depleted, such as in the case of the 500m mountain here. For larger forcings the stripping of the contours at the vortex edge would then proceed at a sufficient rate as to build up the gradient necessary to inhibit further stripping. If the forcing is again increased past a certain level the amplitude would be enough to stimulate stripping of higher valued contours, meaning that more mass would be able to be removed from the vortex.

5.4.5 Investigating the effect of different mountain heights on the rate of mass removal for a Wave 2 forcing

Figure 5.15 shows the results for the same experiments as Figure 5.7 performed for a wave 2 forcing. Again the mountain is grown with a value of $\tau = 8\text{x}10^6$s to several intermediate heights, remaining at that height for the remainder of the model run. The lines at the top of the plots show the times when the various mountains reach their maximum heights.

When the mountain is grown to the full height of 2000m the removal of mass

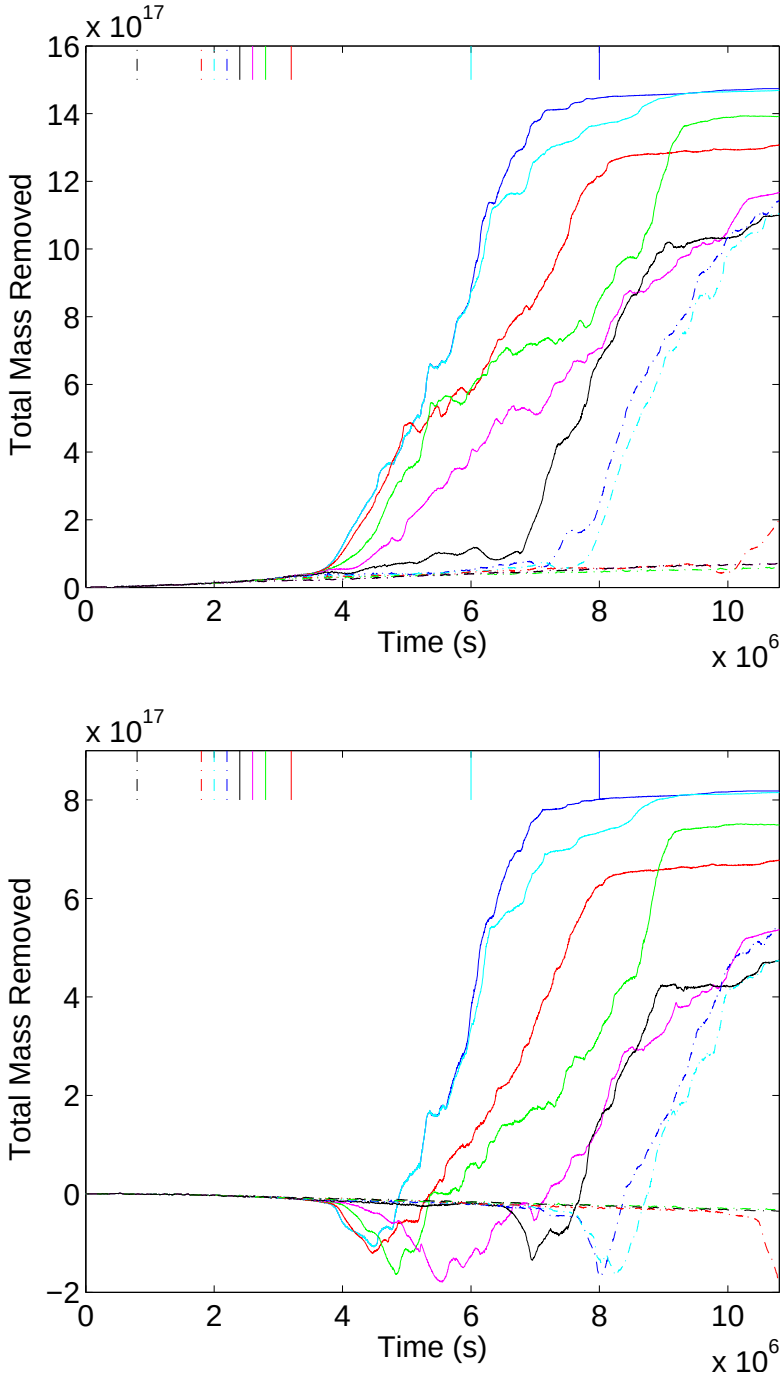

Figure 5.15: Mass removed from the two red PV contours in Figure 5.10 on the edge of the vortex and the surf zone. The top figure is the outer PV contour and the bottom figure is the inner one. The mountain was frozen at various heights (the solid blue line is the full 2000m mountain, the solid cyan line is 1500m, 800m (solid red line), 700m (solid green line), 650m (magenta), 600m (black), 550m (dashed blue line), 500m (dashed cyan line), 450m (dashed red line), 400m (dashed green line), 200m (dashed black line).

begins at a similar time after the start of the model run as it does in the case of the wave 1 forcing above, around 50 model days from the start of the run. The pattern of the mass flux from the PV contour also looks similar, although not identical. The amount of mass moved into the contour in the bottom plot in the figure is much larger in the case of the wave 2 forcing than it is for the wave 1 forcing. When mass starts to be removed from this contour it also does so at a faster rate for the wave 2 case.

The mass removal for the 1500m mountain starts identical to the 2000m case but at around 63 model days, when the mountain reaches its maximum height the rate of removal slows. Toward the end of the model run the total amount of mass removed from the vortex again becomes very close to the 2000m case.

For the runs where the mountain is grown to a height of greater than 650m, here the 700m and 800m runs (red and green solid lines), the initial mass removal from the PV contour is very similar to that of the 2000m mountain. After a period of roughly 20 days from when the rapid mass removal begins the lower final mountain height runs slow in the rate of removal of mass from the contour. There is another acceleration in each of the cases shown here, with the 800m mountain case accelerating in the rate of stripping after another period of roughly 20 days and the 700m mountain stripping more slowly for a period of roughly 60 days before accelerating to roughly the original rate of mass removal.

The mass removal for the case of the 650m mountain begins at the same time as the 700m and 800m cases but at a slower rate. This removal continues at roughly the same rate for nearly the entirety of the model run until around 115 model days when the rate begins to slow.

The black, blue dashed and cyan dashed lines in the plot, corresponding to final mountain heights of 600m, 550m and 500m respectively, have a very small rate of mass removal for a period of roughly 70 model days. After this the rate of stripping starts to increase to a rate similar to that of the 2000m mountain stripping rate. This period of stripping is much shorter than those of the runs in which the final mountain height is larger, lasting for around 25 model days in this case before the

rate of stripping decreases.

PV maps for the 500m mountain show that as the area surrounding the vortex starts to become more turbulent and a surf zone starts to form the vortex starts to become stretched in the way that if does for larger mountain heights. This stretching and erosion by the anticyclones which form near the edge is not large enough to cause the vortex to split. Instead it becomes more steadily eroded and remains centred over the pole. Once it has been eroded sufficiently the criteria of Equation (5.18) shows that the vortex undergoes an SSW, though it still remains centred on the pole. This appears to be due to the symmetric nature of the forcing, meaning that the vortex can't be effectively displaced from the pole as would happen in the real winter stratosphere.

In the wave 1 forcing runs the contour undergoes negligible removal of mass for a forcing of magnitude 200m but any larger forcing initiates significant further stripping of mass. All of this stripping appears to start occurring at similar times to each other but at different rates, roughly 40 model days from the start of the run. In contrast for the case of the wave 2 forcing this negligible mass removal continues up to a forcing amplitude of 400m, and when the forcing is increased to 450m the stripping does not start to become significant until over 100 model days have passed.

For the inner contour (bottom plot in Figure 5.15) the point where the rate of mass removal dramatically increases does not occur at the same time for all mountain heights as it does for the case of wave 1. The cases where the mountain is grown to 700m and above all start at roughly the same time (which is also roughly the same time at which the wave 1 case above starts), but when the mountain is grown to lesser heights the increase in the rate of stripping starts at gradually later times. The periods where the contour gains a significant amount of mass all last for fairly short periods of time, less than 20 model days for all experiments performed. This is in contrast to the case of wave 1 runs where the same contour with the 400m final mountain height contains a significant amount more mass than at the start of the run for a period of over 50 model days.

Once the contour shown in the bottom part of Figure 5.15 starts to lose mass in the cases where the stripping starts at roughly the same time as the 2000m final mountain height (the red and green lines in the figure) the average rate of loss in mass is lower when the final mountain height is smaller. The rate of mass removal for the case of the final height of 800m is at a fairly constant rate which is less than the 2000m run, and for the first 45 model days of mass removal the rate for the 700m mountain is again smaller, after which it increases for a period of 5 model days before reaching a plateau.

For the runs in which significant mass removal does not begin until later, here the runs shown by the magenta and black lines, the average rate at which the mass is removed is less than for the 2000m forcing amplitude but slightly larger than that of the 800m forcing. The rate of mass removal in each of these cases is similar to each other.

Similar to the case of the wave 1 forcing, the runs where the final height of the mountain is less than 450m have only a negligible amount of mass removal over the whole period of the model run. Again the mass change in the case of the 450m mountain doesn't begin to become significant until over 100 model days from the start of the model run. By the end of the model run this contour has increased more in mass than for the other wave 2 runs, and has not started to decrease.

For the first 100 days of the simulation the wave 2 runs are highly symmetrical as the vortex gets stretched and eventually breaks into two symmetrical pieces. The evolution of these two sub vortices continues to be similar to each other until after 100 days when one of these smaller vortices breaks down while the other remains intact.

In the case of both the wave 1 and the wave 2 forcing there is not a linear relationship between the maximum height of the mountain and the total amount of mass removed from the vortex by the end of the model run. For example in the case of the wave 1 forcing, for the first 90 to 100 model days the larger the maximum height of the mountain the larger the total amount of mass removed from the contour. However after this point the total mass loss for some of the smaller

forcing amplitudes becomes larger than those for which the maximum height is greater. The rate of mass loss for the 700m mountain case (red line in Figure 5.7) significantly slows between 70 and 80 model days and after 100 days the total mass removed is lower than the case where the maximum height of the mountain is 500m.

For the case of the wave 2 mountain there does not seem to be the same dramatic decrease in the rate of mass loss from the vortex as there is in some of the cases of the wave 1 mountain. There is still some crossing of the curves in Figure 5.15 indicating that some smaller mountain heights have more mass removed from the vortex than the case of larger mountain heights. This appears to be due to the fact that the edge of the vortex doesn't become strengthened in the same way that it does in the cases of the wave 1 forcing. This could be due to the fact that the vortex has split into two parts in the process of undergoing a model SSW, which then are more easily eroded than the single larger vortex.

In the case of the 700m wave 2 mountain there is an initial period of rapid mass removal from the vortex between 40 model days and 60 days before the rate of outward mass flux decreases. This period of slower mass removal lasts for a period of 100 model days interrupted by only a short period of more rapid mass removal. During this period the vortex initially splits into two before recombining briefly and splitting apart again. The intermediate phase of faster mass removal in Figure 5.15 coincides with this recombining of the two vortices. After splitting apart for the second time the vortices again reform. The reformed vortex then becomes eroded when the mass removal accelerates, though after the rate has flattened off at around 110 days the vortex starts to become more coherent and appears as a strong patch located over the pole with a strong edge, similar to what is seen for the 700m wave 1 case (Figure 5.10) but located more centrally over the pole.

5.5 Conclusions

A shallow water model has been used to investigate stripping of filaments from a model stratospheric polar vortex in relation to the amplitude and rate of growth of the forcing. The model SSWs produced here exhibit many of the features which

can be seen in real stratospheric sudden warmings.

It was found that when the rate of growth of the forcing was decreased, with the maximum amplitude kept constant, the vortex started to break down at successively lower amplitudes. In most cases this breakdown happened some time before the maximum amplitude of the forcing was reached, but in the case of the fastest growing forcing the SSW occurred after the maximum was reached. This suggests that once the forcing reaches a certain amplitude the vortex starts to become eroded which, after some time results in the breakdown of the vortex and an SSW like event.

A similar conclusion is reached from the experiments where the amplitude of the forcing is reduced while the rate of growth remains fixed. The stripping of mass from the vortex for this wave 1 forcing was initiated at a point some time after several of the maximum forcing amplitudes have been reached. This means that it isn't the direct effects of the forcing which is initialising stripping of the main vortex.

Wave activity $\mathcal{A}$ seems to be very well correlated with the removal of air from the vortex. The point where the vortex starts to break down corresponds almost exactly to the point where the wave activity integrated over the northern hemisphere reaches its maximum value.

The wave activity is then a much better measure of how much mass is removed from the vortex, being an integrated measure of the forcing.

The total amount of mass removed from the vortex over the course of the experiment is not proportional to the maximum amplitude of the forcing. There are certain cases, most prominently in the case of the wave 1 forcing but also present to a lesser degree for the wave 2 case, when the vortex edge appears to sharpen after a certain amount of mass has been removed from it. This then has the effect of inhibiting any further significant tongues of air from forming and being mixed into the surf zone. This does not happen for all cases and it is not quite clear what may cause this to happen in some cases but not in others. Cases when the forcing amplitude is less end up with more mass removed over the course of the experiment

than some of those with larger forcing amplitudes. An area of further exploration would be to see if this effect can be seen in more realistic multi levels models, and how the location of the just affects this effect.

This effect is seen to a lesser extent in the case of the wave 2 mountains. Here for a much smaller number of cases there are smaller forcing amplitudes which cause more mass to be stripped than for larger amplitudes. The difference in the total stripping experienced by vortices forced by different amplitudes for these cases is not as large as it is for the wave 1 cases.

Matthewman and Esler (2011) looked at the effect of topographic forcing height and surf zone PV parameter Ω on the onset of vortex splitting. They found that for a given surf zone parameter, when the forcing increases past a particular value a bifurcation takes place causing the system to transition into a state in which a splitting can occur. Comparing their results to those obtained here gives a possible explanation for the behavior seen here. In the results of Matthewman and Esler (2011) once the topography reaches a certain height the system undergoes a bifurcation and enters either a splitting or a high wave activity regime, with an area of oscillating vortex activity on the boundary of this region (see their Fig.2). This is consistent with the results seen here where once the mountain reaches 450m stripping starts to occur. For 500m and above the vortex undergoes SSW like behaviour. For some values of the forcing amplitude the vortex looks similar to the high wave activity (HW) regime. This suggests that the system may be on the border of the two regimes (HW snd splitting) from Fig.2a of Matthewman and Esler (2011). This would also account for the fact that some larger forcings do not induce SSWs while smaller ones do.

It is possible that as mass is stripped from the vortex reducing it in size, at some point the more compact vortex crosses a bifurcation threshold from a stable state in which no warmings occur into a SSW state, where it is able to split into two parts.

In contrast, Esler and Matthewman (2011) found that in the case of displacement SSWs the dynamics are much more complex than they are for the case of

vortex splitting events. The more varied results for the wave 1 experiments performed here appear to be in agreement with the conclusion of Esler and Matthewman (2011) in this respect. The theory of Esler and Matthewman (2011) does not explain the fact that some smaller forcings can produce SSWs while intermediate ones do not. There does not seem to be a bifurcation of the system for wave 1 forcing in the same way as there is for wave 2 forcing.

When this strengthening of the vortex occurs, $\psi - Q$ plots show a more compact region corresponding to the vortex itself with an area of widely spread area corresponding to the surf zone. This shows that the vortex region is close to free-mode form, though it is less clear what can be gained numerically from the relative spread of the two regions which can not be gained from the other diagnostics presented.

In both the wave 1 and wave 2 cases there seems to be a certain amplitude of forcing below which there is no significant stripping of air initiated. This threshold forcing is larger for the wave 2 forcing (around 450m) than for the wave 1 case (where all mountains larger than 200m initiate significant amounts of stripping). The difference in mass removed between the negligible case and the smallest where stripping is initiated is also much larger in the wave 2 case than the wave 1 case where once stripping starts it appears to carry on for far longer.

Using the criteria of Equation (5.18) to identify when SSW like events have occurred shows that they can be produced for fairly small forcing amplitudes. In the case of the wave 1 forcing the vortex looks similar to that of the real northern hemisphere polar vortex during a displacement event. In these cases Equation (5.18) defines an SSW to occur for forcings as small as 500m. In the case of the wave 2 forcing not all of the warmings produced resembled those seen in the stratospheric vortex. In the cases of smaller forcings the vortex remains centred exactly over the pole while Equation (5.18) defines an SSW to have occurred. For larger forcings the vortex can be seen to split into two parts and resemble more closely the split vortex composite of Seviour et al. (2013).

The jet shape and location have been kept fixed throughout the experiments, as well as the location of the mountain. It is likely that these factors play a role

in the rate and total amount of stripping experienced by the vortex. The values chosen in this study were chosen to be similar to what can be seen in the real winter stratosphere, but further experiments looking at the location and shapes of these would allow determination of the relative importance of these factors in relation to the amplitude or rate of growth of the forcing.

Chapter 6

Conclusions

In this thesis the dynamics of Stratospheric Sudden Warmings (SSWs) have been examined with an emphasis on the stripping of air from the vortex and what relation this has to the preconditioning of the vortex.

The conclusions of this work will be summarised followed by suggestions of further avenues of research which could follow.

6.1 Integral Diagnostics

Various integral diagnostics were calculated from ECMWF ERA-40 Reanalyses to diagnose stripping from the stratospheric polar vortex. The main questions answered in this chapter and their conclusions are presented below.

When does stripping occur in the period leading up to SSWs? How much stripping occurs? Are there significant differences in the amount of stripping across different vertical levels?

There are several periods in which significant amounts of stripping occur; the largest of these events can see up to 25% of the mass within the vortex removed. These stripping events typically last for periods of roughly 5 days. There is no preferred vertical level on which this stripping occurs, and all surfaces show significant stripping of mass. Larger stripping events typically show in the order of 10% of the mass within the vortex removed. There is not always a reduction of

the mass of the vortex of this order as it is replaced by downward movement of air from higher levels. Significant stripping events appear common across all vertical surfaces, though smaller ones do not have counterparts at all levels. Some stripping occurs concurrently on all vertical surfaces while others start on one level and propagate either upward or downward.

Is there a difference in the amount and timing of stripping preceding vortex splitting events and that preceding vortex displacement events? Is there a difference in the stripping preceding events occurring earlier in the winter than those occurring later?

There isn't a significant difference in the pattern or amount of stripping preceding splitting events when compared to displacement events. There is however a difference between the pattern and amount of stripping preceding SSWs which occur early in the winter compared to those which occur later in the winter.

For all warmings there is a large stripping event in the 10 days immediately preceding the warming. Those SSWs which occur late in the winter, in February and March, show several stripping events in the couple of months preceding the warming. These are all large stripping events in which around 10% of the mass within the vortex is stripped. For those SSWs which occur early in winter, in December and January, there is one large stripping event in the 10 days preceding the SSW while prior to this there are several smaller stripping events lasting for periods of only a couple of days and much smaller amounts of mass are stripped.

What role, if any, does this stripping play in the preconditioning of the vortex prior to SSWs? Is there a threshold of mass stripped from the vortex for an SSW to occur?

The role of the stripping in the preconditioning of the polar vortex is less clear. There is not a threshold amount of mass removed from the vortex for an SSW to occur. There is also no threshold mass below which the vortex must be brought for an SSW to occur.

There is a difference in the circulation at the vortex edge immediately prior to SSWs occurring between vortex displacement and vortex splitting events. Imme-

diately prior to displacement events the circulation takes larger values than it does immediately prior to vortex splitting events.

It appears that large stripping events are a necessary but not sufficient condition for SSWs to occur.

6.2 Lagrangian 'Circulation'

Integral diagnostics were calculated from ECMWF ERA-40 Reanalyses to calculate the Lagrangian meridional circulation in the stratosphere around the times of SSWs. The main questions answered in this chapter and their conclusions are presented below.

What are the main features of the Lagrangian circulation in and around the polar vortex?

Within the vortex, over most of the winter months, there is poleward and downward transport on higher levels and equatorward and downward transport on lower levels. In the early winter, when the vortex is strengthening, there is instead poleward and downward transport on the lower surfaces.

At the subtropical side of the surf zone area there is rising and poleward transport while on the vortex side there is downward and equatorward transport.

How does this Lagrangian circulation change around the time of SSWs?

Following SSWs the poleward flux of mass on the higher surfaces in and immediately around the vortex changes direction to be downward and equatorward. There is also a strengthening of the equatorward flux on the lower levels. This reversal is seen in all cases when SSWs have occurred, though the equatorward flow is weaker for SSWs occurring very early in the winter, and on higher surfaces there can still be poleward flux.

The area of equatorward flux extends only as far as the poleward side of the surf zone.

Following this outward flux of mass the pattern of transport in and around the vortex returns to one similar to that typical of November with poleward and

downward flux on the vortex edge of the surf zone on all levels.

6.3 Modelling

A shallow water model was used to investigate stripping in a model polar vortex, motivated by the results from the ERA-40 data. The main questions answered in this chapter and their conclusions are presented below.

How does the rate of growth of the mountain affect the amount of stripping of a model polar vortex?

As the rate of growth of the mountain decreases the vortex loses mass at a slower rate. The reduction in mass also starts before the maximum height of the mountain is reached for the slowest growing cases. This removal of mass lasts for a long time after the maximum height is reached.

How does the maximum height of the mountain affect the rate and amount of stripping in the case of a wave 1 shaped mountain?

When the maximum height of the mountain is reduced, the stripping starts at the same instant as that of the full height in the vast majority of the cases examined here. The maximum height of the mountain is not proportional to the total amount of stripping, but is strongly related to the initial rate of stripping. There is a limit to the rate at which stripping occurs, and as the maximum height is increased past a certain point, the rate of stripping remains very similar.

There are several cases where larger mountain heights produce less stripping than smaller mountain heights. The edge of the vortex appears to become sharper in these cases, and the surf zone becomes less turbulent, eventually becoming a region of smooth PV surrounding the vortex. It is not clear whether this is a consequence or a cause of the reduction in the rate of stripping.

When the mountain is grown to 200m or below no significant stripping is initiated.

How does the maximum height of the mountain affect the rate and amount of stripping in the case of a wave 2 shaped mountain?

For a wave 2 mountain, the threshold height of the mountain at which stripping

occurs is larger than it is for the wave 1 mountain. Once the threshold has been reached the total amount of mass stripped increases dramatically, in contrast with the wave 1 case. Also unlike the wave 1 case the stripping does not begin at the same point for differing mountian heights for the wave 2 case.

The system seems to undergo a bifurcation similar to that noted in Matthewman and Esler (2011) when a sufficient amount of mass has been removed. The vortex system then enters a state when a SSW can occur.

Similarly to the case of the wave 1 mountain the stripping initiates some time after the maximum height of the mountain has been reached in most cases. The lower the maximum height is, the longer the time after this height is reached when significant stripping begins.

How does the maximum height of the mountain compare to the onset of model SSWs?

While the model wave 1 SSWs show many of the features of real wave 1 SSWs, the maximum height of the mountain is not proportional to the time at which the SSW occurs. The wave 2 SSWs show less similarities to real SSWs

6.4 Further Work

There are several areas of stripping in the shallow water model vortex which were not examined here, such as the shape and location of the jet in relation to the mountain. The shallow water model, while useful, lacks many of the features of the full atmosphere. A further avenue of research would be to see if the features seen in the shallow water model are recreated in more realistic multi layer models, where more realistic vortices may be modelled.

Appendix A

Mass & Circulation balance

A.1 Theorems

The following is a list of identities which will be used in deriving of the Mass and Circulation balance equations which follow in sections section A.2 section A.3.

For any scalar function $\eta(\lambda, \phi, \theta, t)$, we have (on the northern hemisphere)

$$\int_{S_{Q,\theta}} \eta \, \mathrm{d}S = \int_{\widetilde{Q} \geq Q} \oint_{\Gamma_{\widetilde{Q},\theta}} \frac{\eta}{|\nabla_\theta \widetilde{Q}|} \, \mathrm{d}s \, \mathrm{d}\widetilde{Q} \tag{A.1}$$

as $\mathrm{d}S = \mathrm{d}s \, \mathrm{d}l$ with $\mathrm{d}l = |\mathrm{d}\mathbf{x}|$ being a length element normal to the PV contour $\Gamma_{\widetilde{Q},\theta}$ and $\mathrm{d}\widetilde{Q} = \left(\nabla_\theta \widetilde{Q}\right) \cdot \mathrm{d}\mathbf{x}$ and thus $\mathrm{d}l = \mathrm{d}\widetilde{Q}/|\nabla_\theta \widetilde{Q}|$.

We have

$$\frac{\partial}{\partial Q} \int_{S_{Q,\theta}} \eta \, \mathrm{d}S = - \oint_{\Gamma_{Q,\theta}} \frac{\eta}{|\nabla_\theta Q|} \, \mathrm{d}s. \tag{A.2}$$

We further have:

$$\frac{\partial}{\partial Q} \int_{S_{Q,\theta}} \eta \widetilde{Q} \, \mathrm{d}S \overset{\text{(A.2)}}{=} - \oint_{\Gamma_{Q,\theta}} \frac{\eta Q}{|\nabla_\theta Q|} \, \mathrm{d}s = -Q \oint_{\Gamma_{Q,\theta}} \frac{\eta}{|\nabla_\theta Q|} \, \mathrm{d}s \overset{\text{(A.2)}}{=} Q \frac{\partial}{\partial Q} \int_{S_{Q,\theta}} \eta \, \mathrm{d}S \tag{A.3}$$

The temporal evolution of any surface integral is given by:

$$\frac{\partial}{\partial t} \int_{S_{Q,\theta}} \eta \, \mathrm{d}S = \int_{S_{Q,\theta}} \frac{\partial \eta}{\partial t} \, \mathrm{d}S + \oint_{\Gamma_{Q,\theta}} \frac{\eta \frac{\partial Q}{\partial t}}{|\nabla_\theta Q|} \, \mathrm{d}s \overset{\text{(A.2)}}{=} \int_{S_{Q,\theta}} \frac{\partial \eta}{\partial t} \, \mathrm{d}S - \frac{\partial}{\partial Q} \int_{S_{Q,\theta}} \eta \frac{\partial \widetilde{Q}}{\partial t} \, \mathrm{d}S \tag{A.4}$$

Where $\widetilde{Q}$ is simply the values of Q to be integrated over.

Analogously, the vertical derivative is given by:

$$\frac{\partial}{\partial\theta}\int_{S_{Q,\theta}}\eta\,\mathrm{d}S=\int_{S_{Q,\theta}}\frac{\partial\eta}{\partial\theta}\,\mathrm{d}S+\oint_{\Gamma_{Q,\theta}}\frac{\eta\frac{\partial Q}{\partial\theta}}{|\nabla_\theta Q|}\,\mathrm{d}s\overset{(A.2)}{=}\int_{S_{Q,\theta}}\frac{\partial\eta}{\partial\theta}\,\mathrm{d}S-\frac{\partial}{\partial Q}\int_{S_{Q,\theta}}\eta\frac{\partial\widetilde{Q}}{\partial\theta}\,\mathrm{d}S \tag{A.5}$$

A.1.1 Equations of Motion

Continuity equation (mass conservation):

$$\frac{\partial\sigma}{\partial t}=-\nabla_\theta\cdot(\sigma\mathbf{v})-\frac{\partial\left(\sigma\dot{\theta}\right)}{\partial\theta} \tag{A.6}$$

PV advection (material conservation of PV for adiabatic flow):

$$\dot{Q}=\frac{DQ}{Dt}=\frac{\partial Q}{\partial t}+\mathbf{v}\cdot\nabla_\theta Q+\dot{\theta}\frac{\partial Q}{\partial\theta} \tag{A.7}$$

$$=\frac{\boldsymbol{\zeta}\cdot\nabla\dot{\theta}}{\rho}+\frac{\nabla\theta\cdot\nabla\times\mathbf{X}}{\rho} \tag{A.8}$$

which, using the small slope approximation, can be expressed in the form

$$\dot{Q}=\frac{1}{\sigma}\xi+\frac{1}{\rho}\frac{\partial\dot{\theta}}{\partial\theta}\zeta+\frac{1}{\sigma}\left(\frac{\partial v}{\partial\theta}\left.\frac{\partial\dot{\theta}}{\partial x}\right|_\theta-\frac{\partial u}{\partial\theta}\left.\frac{\partial\dot{\theta}}{\partial y}\right|_\theta\right) \tag{A.9}$$

Here ζ is the absolute vorticity, ξ is the vertical component of $\nabla\times\mathbf{X}$ taken at constant θ, where $\mathbf{X}$ is the friction, and u, v are the horizontal components of the velocity $\mathbf{v}$.

From Equation (A.6) and Equation (A.7) we easily get

$$\frac{\partial\left(\sigma Q\right)}{\partial t}=-\nabla_\theta\cdot(\sigma Q\mathbf{v})-\frac{\partial\left(\sigma Q\dot{\theta}\right)}{\partial\theta}+\sigma\dot{Q} \tag{A.10}$$

$$\frac{\partial\left(\sigma Q^2\right)}{\partial t}=-\nabla_\theta\cdot\left(\sigma Q^2\mathbf{v}\right)-\frac{\partial\left(\sigma Q^2\dot{\theta}\right)}{\partial\theta}+2\sigma Q\dot{Q} \tag{A.11}$$

With Gauss's theorem in two dimensions, we get

$$\int_{S_{Q,\theta}}\nabla_\theta\cdot\left(\sigma\widetilde{Q}\mathbf{v}\right)\,\mathrm{d}S=-\oint_{\Gamma_{Q,\theta}}\sigma Q\mathbf{v}\cdot\widehat{\mathbf{n}}\,\mathrm{d}s=Q\int_{S_{Q,\theta}}\nabla_\theta\cdot(\sigma\mathbf{v})\,\mathrm{d}S \tag{A.12}$$

and

$$\int_{S_{Q,\theta}}\nabla_\theta\cdot\left(\sigma\widetilde{Q}^2\mathbf{v}\right)\,\mathrm{d}S=-\oint_{\Gamma_{Q,\theta}}\sigma Q^2\mathbf{v}\cdot\widehat{\mathbf{n}}\,\mathrm{d}s=Q\int_{S_{Q,\theta}}\nabla_\theta\cdot\left(\sigma\widetilde{Q}\mathbf{v}\right)\,\mathrm{d}S \tag{A.13}$$

A.2 Mass Balance

Balance equation for the mass integral

The balance equation for the evolution of mass within PV contours is derived using the theorems of the previous two sections.

Starting with the time derivative of the mass

$$\frac{\partial \mathcal{M}_{Q,\theta}}{\partial t} = \frac{\partial}{\partial t}\int_{S_{Q,\theta}} \sigma \,\mathrm{d}S$$

and using Equation (A.4) gives

$$= \int_{S_{Q,\theta}} \frac{\partial \sigma}{\partial t}\,\mathrm{d}S - \frac{\partial}{\partial Q}\int_{S_{Q,\theta}} \sigma \frac{\partial \widetilde{Q}}{\partial t}\,\mathrm{d}S.$$

The product rule then gives

$$= \int_{S_{Q,\theta}} \frac{\partial \sigma}{\partial t}\,\mathrm{d}S - \frac{\partial}{\partial Q}\int_{S_{Q,\theta}} \left[\frac{\partial\left(\sigma\widetilde{Q}\right)}{\partial t} - \frac{\partial \sigma}{\partial t}\widetilde{Q}\right]\,\mathrm{d}S.$$

Equation (A.3) then allows this to be written as

$$\overset{(A.3)}{=} \int_{S_{Q,\theta}} \frac{\partial \sigma}{\partial t}\,\mathrm{d}S - \frac{\partial}{\partial Q}\int_{S_{Q,\theta}} \frac{\partial\left(\sigma\widetilde{Q}\right)}{\partial t}\,\mathrm{d}S + Q\frac{\partial}{\partial Q}\int_{S_{Q,\theta}} \frac{\partial \sigma}{\partial t}\,\mathrm{d}S$$

and simplifying

$$= \frac{\partial}{\partial Q}\left[Q\int_{S_{Q,\theta}} \frac{\partial \sigma}{\partial t}\,\mathrm{d}S - \int_{S_{Q,\theta}} \frac{\partial\left(\sigma\widetilde{Q}\right)}{\partial t}\,\mathrm{d}S\right].$$

Equations (A.6), (A.10) and (A.12) together then give the expression

$$= \frac{\partial}{\partial Q}\left[-Q\int_{S_{Q,\theta}} \frac{\partial\left(\sigma\dot{\theta}\right)}{\partial \theta}\,\mathrm{d}S + \int_{S_{Q,\theta}} \frac{\partial\left(\sigma\widetilde{Q}\dot{\theta}\right)}{\partial \theta}\,\mathrm{d}S - \int_{S_{Q,\theta}} \sigma\dot{Q}\,\mathrm{d}S\right]$$

which, when the brackets are expanded gives

$$= -\int_{S_{Q,\theta}} \frac{\partial\left(\sigma\dot{\theta}\right)}{\partial \theta}\,\mathrm{d}S - Q\frac{\partial}{\partial Q}\int_{S_{Q,\theta}} \frac{\partial\left(\sigma\dot{\theta}\right)}{\partial \theta}\,\mathrm{d}S + \frac{\partial}{\partial Q}\int_{S_{Q,\theta}} \left[\frac{\partial\left(\sigma\dot{\theta}\right)}{\partial \theta}\widetilde{Q} + \sigma\dot{\theta}\frac{\partial \widetilde{Q}}{\partial \theta}\right]\,\mathrm{d}S - \frac{\partial}{\partial Q}\int_{S_{Q,\theta}} \sigma\dot{Q}\,\mathrm{d}S.$$

Finally using Equation (A.3) gives

$$= -\frac{\partial}{\partial Q}\int_{S_{Q,\theta}} \sigma\dot{Q}\,\mathrm{d}S + \frac{\partial}{\partial Q}\int_{S_{Q,\theta}} \sigma\dot{\theta}\frac{\partial\widetilde{Q}}{\partial\theta}\,\mathrm{d}S - \int_{S_{Q,\theta}} \frac{\partial\left(\sigma\dot{\theta}\right)}{\partial\theta}\,\mathrm{d}S \quad \text{(A.14)}$$

$$= \mathcal{V}_{Q,\theta} - \int_{S_{Q,\theta}} \frac{\partial\left(\sigma\dot{\theta}\right)}{\partial\theta}\,\mathrm{d}S \quad \text{(A.15)}$$

where $\mathcal{V}_{Q,\theta} = -\frac{\partial}{\partial Q}\int_{S_{Q,\theta}} \sigma\dot{Q}\,\mathrm{d}S + \frac{\partial}{\partial Q}\int_{S_{Q,\theta}} \sigma\dot{\theta}\frac{\partial\widetilde{Q}}{\partial\theta}\,\mathrm{d}S$. Applying Equation (A.5) also gives the form given in Nakamura (1995)

$$\overset{\text{(A.5)}}{=} -\frac{\partial}{\partial Q}\int_{S_{Q,\theta}} \sigma\dot{Q}\,\mathrm{d}S - \frac{\partial}{\partial\theta}\int_{S_{Q,\theta}} \sigma\dot{\theta}\,\mathrm{d}S \quad \text{(A.16)}$$

A.3 Circulation Balance

Balance equation for the circulation

Here the balance equation for the time evolution of the circulation of PV contours is derived.

Starting with the time derivative of the circulation

$$\frac{\partial\mathcal{C}_{Q,\theta}}{\partial t} = \frac{\partial}{\partial t}\int_{S_{Q,\theta}} \sigma\widetilde{Q}\,\mathrm{d}S$$

and applying Equation (A.4) gives

$$= \int_{S_{Q,\theta}} \frac{\partial\left(\sigma\widetilde{Q}\right)}{\partial t}\,\mathrm{d}S - \frac{\partial}{\partial Q}\int_{SQ,\theta} \sigma\widetilde{Q}\frac{\partial\widetilde{Q}}{\partial t}\,\mathrm{d}S$$

which can be simplified to

$$= \int_{S_{Q,\theta}} \frac{\partial\left(\sigma\widetilde{Q}\right)}{\partial t}\,\mathrm{d}S - \frac{\partial}{\partial Q}\int_{S_{Q,\theta}} \left[\frac{\partial\left(\sigma\widetilde{Q}^2\right)}{\partial t} - \frac{\partial\left(\sigma\widetilde{Q}\right)}{\partial t}\widetilde{Q}\right]\,\mathrm{d}S.$$

Using Equation (A.3) this can be written

$$= \int_{S_{Q,\theta}} \frac{\partial\left(\sigma\widetilde{Q}\right)}{\partial t}\,\mathrm{d}S - \frac{\partial}{\partial Q}\int_{S_{Q,\theta}} \frac{\partial\left(\sigma\widetilde{Q}^2\right)}{\partial t}\,\mathrm{d}S + Q\frac{\partial}{\partial Q}\int_{S_{Q,\theta}} \frac{\partial\left(\sigma\widetilde{Q}\right)}{\partial t}\,\mathrm{d}S$$

and simplified to

$$= \quad \frac{\partial}{\partial Q}\left[Q\int_{S_{Q,\theta}}\frac{\partial\left(\sigma\widetilde{Q}\right)}{\partial t}\,\mathrm{d}S-\int_{S_{Q,\theta}}\frac{\partial\left(\sigma\widetilde{Q}^2\right)}{\partial t}\,\mathrm{d}S\right].$$

Equations (A.10), (A.11) and (A.13) allow this to be written as

$$\begin{aligned}= \quad & \frac{\partial}{\partial Q}\left[-Q\int_{S_{Q,\theta}}\frac{\partial\left(\sigma\widetilde{Q}\dot{\theta}\right)}{\partial\theta}\,\mathrm{d}S+Q\int_{S_{Q,\theta}}\sigma\dot{Q}\,\mathrm{d}S\right.\\ & \left.+\int_{S_{Q,\theta}}\frac{\partial\left(\sigma\widetilde{Q}^2\dot{\theta}\right)}{\partial\theta}\,\mathrm{d}S-2\int_{S_{Q,\theta}}\sigma\widetilde{Q}\dot{Q}\,\mathrm{d}S\right]\end{aligned}$$

which, expanding the brackets, becomes

$$\begin{aligned}= \quad & -\int_{S_{Q,\theta}}\frac{\partial\left(\sigma\widetilde{Q}\dot{\theta}\right)}{\partial\theta}\,\mathrm{d}S-Q\frac{\partial}{\partial Q}\int_{S_{Q,\theta}}\frac{\partial\left(\sigma\widetilde{Q}\dot{\theta}\right)}{\partial\theta}\,\mathrm{d}S\\ & +\int_{S_{Q,\theta}}\sigma\dot{Q}\,\mathrm{d}S+Q\frac{\partial}{\partial Q}\int_{S_{Q,\theta}}\sigma\dot{Q}\,\mathrm{d}S\\ & +\frac{\partial}{\partial Q}\int_{S_{Q,\theta}}\left[\frac{\partial\left(\sigma\widetilde{Q}\dot{\theta}\right)}{\partial\theta}\widetilde{Q}+\sigma\widetilde{Q}\dot{\theta}\frac{\partial\widetilde{Q}}{\partial\theta}\right]\,\mathrm{d}S-2\frac{\partial}{\partial Q}\int_{S_{Q,\theta}}\sigma\widetilde{Q}\dot{Q}\,\mathrm{d}S\end{aligned}.$$

Applying Equation (A.3) twice then gives

$$\begin{aligned}= \quad & -\frac{\partial}{\partial Q}\int_{S_{Q,\theta}}\sigma\widetilde{Q}\dot{Q}\,\mathrm{d}S+\frac{\partial}{\partial Q}\int_{S_{Q,\theta}}\sigma\widetilde{Q}\dot{\theta}\frac{\partial\widetilde{Q}}{\partial\theta}\,\mathrm{d}S\\ & -\int_{S_{Q,\theta}}\frac{\partial\left(\sigma\widetilde{Q}\dot{\theta}\right)}{\partial\theta}\,\mathrm{d}S+\int_{S_{Q,\theta}}\sigma\dot{Q}\,\mathrm{d}S\\ = \quad & Q\mathcal{V}_{\mathcal{Q},\theta}-\int_{S_{Q,\theta}}\frac{\partial\left(\sigma\widetilde{Q}\dot{\theta}\right)}{\partial\theta}\,\mathrm{d}S+\int_{S_{Q,\theta}}\sigma\dot{Q}\,\mathrm{d}S\end{aligned}$$

respectively. Equation (A.9) then gives

$$\begin{aligned}= \quad & Q\mathcal{V}_{Q,\theta}-\int_{S_{Q,\theta}}\zeta\frac{\partial\dot{\theta}}{\partial\theta}+\dot{\theta}\frac{\partial\zeta}{\partial\theta}\mathrm{d}S+\int_{S_{Q,\theta}}\xi\mathrm{d}S\\ & +\int_{S_{Q,\theta}}\zeta\frac{\partial\dot{\theta}}{\partial\theta}\mathrm{d}S+\int_{S_{Q,\theta}}\left(\frac{\partial v}{\partial\theta}\frac{\partial\dot{\theta}}{\partial x}-\frac{\partial u}{\partial\theta}\frac{\partial\dot{\theta}}{\partial y}\right)\mathrm{d}S\end{aligned}$$

and finally applying Stokes' theorem and grouping together terms gives

$$\begin{aligned} &= Q\mathcal{V}_{Q,\theta} + \oint_{\Gamma_{Q,\theta}} \mathbf{X} \cdot \mathrm{d}\mathbf{l} + \int_{S_{Q,\theta}} \dot{\theta}\frac{\partial \zeta}{\partial \theta} + \left(\frac{\partial v}{\partial \theta}\frac{\partial \dot{\theta}}{\partial x} - \frac{\partial u}{\partial \theta}\frac{\partial \dot{\theta}}{\partial y}\right) \mathrm{d}S \\ &= Q\mathcal{V}_{Q,\theta} + \oint_{\Gamma_{Q,\theta}} \mathbf{X} \cdot \mathrm{d}\mathbf{l} + \int_{S_{Q,\theta}} \frac{\partial}{\partial x}\left(\dot{\theta}\frac{\partial v}{\partial \theta}\right) - \frac{\partial}{\partial y}\left(\dot{\theta}\frac{\partial u}{\partial \theta}\right) \mathrm{d}S \\ &= Q\mathcal{V}_{Q,\theta} + \oint_{\Gamma_{Q,\theta}} \mathbf{X} \cdot \mathrm{d}\mathbf{l} + \int_{\Gamma_{Q,\theta}} \dot{\theta}\frac{\partial \mathbf{v}}{\partial \theta} \cdot \mathrm{d}\mathbf{l} \end{aligned} \tag{A.17}$$

Bibliography

M.H.P. Ambaum and B.J. Hoskins. The nao troposphere-stratosphere connection. Journal of Climate, 15(14):1969–1978, 2002.

D.G. Andrews, J.R. Holton, and C.B. Leovy. Middle atmosphere dynamics. Academic Pr, 1987. ISBN 0120585766.

M.P. Baldwin and T.J. Dunkerton. Stratospheric harbingers of anomalous weather regimes. Science, 294(5542):581–584, 2001.

M.P. Baldwin and T.J. Dunkerton. Propagation of the arctic oscillation from the stratosphere to the troposphere. Journal of Geophysical Research: Atmospheres (1984–2012), 104(D24):30937–30946, 1999.

N. Butchart and E.E. Remsberg. The area of the stratospheric polar vortex as a diagnostic for tracer transport on an isentropic surface. Journal of the atmospheric sciences, 43(13):1319–1339, 1986. ISSN 0022-4928.

N Butchart, SA Clough, TN Palmer, and PJ Trevelyan. Simulations of an observed stratospheric warming with quasigeostrophic refractive index as a model diagnostic. Quarterly Journal of the Royal Meteorological Society, 108(457):475–502, 1982.

A.J. Charlton and L.M. Polvani. A new look at stratospheric sudden warmings. part i: Climatology and modeling benchmarks. J. Cli., 20:449–469, 2007.

J. Cohen and J. Jones. Tropospheric precursors and stratospheric warmings. Journal of climate, 24(24):6562–6572, 2011.

D.G. Dritschel and M.E. McIntyre. Multiple jets as pv staircases: the phillips effect and the resilience of eddy-transport barriers. Journal of the Atmospheric Sciences, 65(3):855–874, 2008.

T. Dunkerton. On the mean meridional mass motions of the stratosphere and mesosphere. Journal of the Atmospheric Sciences, 35(12):2325–2333, 1978.

Joseph Egger and Klaus-Peter Hoinka. Zonal mean circulations for two conserved meridional coordinates. Quarterly Journal of the Royal Meteorological Society, pages n/a–n/a, 2014. doi: 10.1002/qj.2373.

H. Ertel. Ein neuer hydrodynamischer erhaltungssatz. Naturwissenschaften, 30: 543–544, 1942.

J.G. Esler and N.J. Matthewman. Stratospheric sudden warmings as self-tuning resonances. part ii: Vortex displacement events. Journal of the atmospheric sciences, 68:2505–2523, 2011.

M. Fisher, A. O'Neill, and R. Sutton. Rapid descent of mesospheric air into the stratospheric polar vortex. Geophysical research letters, 20(12):1267–1270, 1993.

Peter Haynes and Emily Shuckburgh. Effective diffusivity as a diagnostic of atmospheric transport: 1. stratosphere. Journal of Geophysical Research: Atmospheres (1984–2012), 105(D18):22777–22794, 2000.

P. Hitchcock, T.G. Shepherd, and G.L. Manney. Statistical characterization of arctic polar-night jet oscillation events. Journal of Climate, 26(6):2096–2116, 2013.

J.R. Holton, P.H. Haynes, M.E. McIntyre, A.R. Douglass, R.B. Rood, and L. Pfister. Stratosphere-troposphere exchange. Reviews of Geophysics, 33(4):403–440, 1995.

B.J. Hoskins, M.E. McIntyre, and A.W. Robertson. On the use and significance of isentropic potential vorticity maps. Quarterly Journal of the Royal Meteorological Society, 111(470):877–946, 1985.

M. Juckes. A shallow water model of the winter stratosphere. Journal of Atmospheric Sciences, 46:2934–2956, 1989.

Martin Juckes. A generalization of the transformed eulerian-mean meridional circulation. Quarterly Journal of the Royal Meteorological Society, 127(571):147–160, 2001.

M.N. Juckes and M.E. McIntyre. A high-resolution one-layer model of breaking planetary waves in the stratosphere. Nature, 328:590–596, 1987.

K. Labitzke. Interannual variability of the winter stratosphere in the northern hemisphere. Monthly Weather Review, 105:762–770, 1977.

K. Labitzke. The amplification of height wave 1 in january 1979: A characteristic precondition for the major warming in february. Monthly Weather Review, 109 (5):983–989, 1981.

K. Labitzke and B. Naujokat. The lower arctic stratosphere in winter since 1952. Sparc Newsletter, 15:11–14, 2000.

K. Labitzke, B. Naujokat, and M. Kunze. The lower arctic stratosphere in winter since 1952: an update. Sparc Newsletter, 24:27–28, 2005.

L.R. Lait. An alternative for potential vorticity. Journal of Atmospheric Sciences, 51:1754–1759, 1994.

B. Legras and D. Dritschel. Vortex stripping and the generation of high vorticity gradients in two-dimensional flows. In Advances in Turbulence IV, pages 445–455. Springer, 1993.

B. Legras, D.G. Dritschel, and P. Caillol. The erosion of a distributed two-dimensional vortex in a background straining flow. Journal of Fluid Mechanics, 441:369–398, 2001. ISSN 0022-1120.

V. Limpasuvan, D.W.J. Thompson, and D.L. Hartmann. The life cycle of the northern hemisphere sudden stratospheric warmings. Journal of climate, 17(13): 2584–2596, 2004.

Annarita Mariotti, Bernard Legras, and David G Dritschel. Vortex stripping and the erosion of coherent structures in two-dimensional flows. Physics of Fluids (1994-Present), 6(12):3954–3962, 1994.

T. Matsuno. A dynamical model of the stratospheric sudden warming. Journal of the Atmospheric Sciences, 28(8):1479–1494, 1971.

N.J. Matthewman. A Vortex Dynamics Perspective on Stratospheric Sudden Warmings. PhD thesis, University College London, 2009.

N.J. Matthewman and J.G. Esler. Stratospheric sudden warmings as self-tuning resonances. part i: Vortex splitting events. Journal of the atmospheric sciences, 68:2481–2504, 2011.

N.J. Matthewman, J.G. Esler, A.J. Charlton-Perez, and L.M. Polvani. A new look at stratospheric sudden warmings. part iii: Polar vortex evolution and vertical structure. Journal of Climate, 22:1566–1585, 2009.

M.E. McIntyre. Potential vorticity. Encyclopedia of Atmospheric Sciences, 2:685–694, 2003.

M.E. McIntyre and T.N. Palmer. Breaking planetary waves in the stratosphere. Nature, 305(5935):593–600, 1983.

M.E. McIntyre and T.N. Palmer. The surf zone in the stratosphere. Journal of atmospheric and terrestrial physics, 46(9):825–849, 1984.

M.E. McIntyre and T.N. Palmer. A note on the general concept of wave breaking for rossby and gravity waves. Pure and Applied Geophysics, 123(6):964–975, 1985.

A. Miller, H. Schmidt, and F. Bunzel. Vertical coupling of the middle atmosphere during stratospheric warming events. Journal of Atmospheric and Solar-Terrestrial Physics, 2013.

D.M. Mitchell, L.J. Gray, J. Anstey, M.P. Baldwin, and A.J. Charlton-Perez. The influence of stratospheric vortex displacements and splits on surface climate. Journal of Climate, 26(8):2668–2682, 2013.

R. Müller and G. Günther. A generalized form of laits modified potential vorticity. Journal of Atmospheric Sciences, 60:2229–2237, 2003.

N. Nakamura. Modified lagrangian-mean diagnostics of the stratospheric polar vortices. i: Formulation and analysis of gfdl skyhi gcm. Journal of the atmospheric sciences, 52(11):2096–2108, 1995.

Noboru Nakamura. Two-dimensional mixing, edge formation, and permeability diagnosed in an area coordinate. Journal of the atmospheric sciences, 53(11): 1524–1537, 1996.

W.A. Norton. Breaking rossby waves in a model stratosphere diagnosed by a vortex-following coordinate system and a technique for advecting material contours. Journal of the atmospheric sciences, 51(4):654–675, 1994.

Judith Perlwitz and Nilt Harnik. Observational evidence of a stratospheric influence on the troposphere by planetary wave reflection. Journal of Climate, 16(18), 2003.

L.M. Polvani and R. Saravanan. The three-dimensional structure of breaking rossby waves in the polar wintertime stratosphere. Journal of the atmospheric sciences, 57(21):3663–3685, 2000.

Lorenzo M Polvani, DW Waugh, and R Alan Plumb. On the subtropical edge of the stratospheric surf zone. Journal of the atmospheric sciences, 52(9):1288–1309, 1995.

P.L. Read, P.B. Rhines, and A.A. White. Geostrophic scatter diagrams and potential vorticity dynamics. Journal of Atmospheric Sciences, 43:3226–3240, 1986.

M.R. Schoeberl, L.R. Lait, P.A. Newman, and J.E. Rosenfield. The structure of the polar vortex. Journal of Geophysical Research: Atmospheres,

97(D8):7859–7882, 1992. ISSN 2156-2202. doi: 10.1029/91JD02168. URL http://dx.doi.org/10.1029/91JD02168.

W.J.M. Seviour, D.M. Mitchell, and L.J. Gray. A practical method to identify displaced and split stratospheric polar vortex events. Geophysical Research Letters, 40(19):5268–5273, 2013.

T.G. Shepherd. Transport in the middle atmosphere. J. Meteorol. Soc. Jpn., 85: 165–191, 2007.

K.P. Shine and J.A. Rickaby. Solar Radiative Heating Due to Absorption by Ozone. In R.D. Bojkov and P. Fabian, editors, Ozone in the Atmosphere, page 597, 1989.

A.H. Sobel and R.A. Plumb. Quantitative diagnostics of mixing in a shallow water model of the stratosphere. Journal of the atmospheric sciences, 56(16):2811–2829, 1999.

R.T. Sutton. Lagrangian flow in the middle atmosphere. Quarterly Journal of the Royal Meteorological Society, 120:1299–1321, 1994.

D.W.J. Thompson and J.M. Wallace. Regional climate impacts of the northern hemisphere annular mode. Science, 293(5527):85–89, 2001.

D.W.J. Thompson, M.P. Baldwin, and J.M. Wallace. Stratospheric connection to northern hemisphere wintertime weather: Implications for prediction. Journal of Climate, 15:1421–1428, 2002.

J. Thuburn and V. Lagneau. Eulerian mean, contour integral, and finite-amplitude wave activity diagnostics applied to a single-layer model of the winter stratosphere. Journal of the Atmospheric Sciences, 56(5):689–710, 1999. ISSN 1520-0469.

J Thuburn, CJ Cotter, and T Dubos. A mimetic, semi-implicit, forward-in-time, finite volume shallow water model: comparison of hexagonal–icosahedral and cubed sphere grids. Geoscientific Model Development Discussions, 6(4):6867–6925, 2013.

L. Tomassini, E.P. Gerber, M.P. Baldwin, F. Bunzel, and M. Giorgetta. The role of stratosphere-troposphere coupling in the occurrence of extreme winter cold spells over northern europe. Journal of Advances in Modeling Earth Systems, 4 (4), 2012.

S.M. Uppala, P.W. Kållberg, A.J. Simmons, U. Andrae, V. Bechtold, M. Fiorino, J.K. Gibson, J. Haseler, A. Hernandez, G.A. Kelly, et al. The era-40 re-analysis. Quarterly Journal of the Royal Meteorological Society, 131(612): 2961–3012, 2005.

D.W. Waugh, R.A. Plumb, R.J. Atkinson, M.R. Schoeberl, L.R. Lait, P.A. Newman, M. Loewenstein, D.W. Toohey, L.M. Avallone, C.R. Webster, et al. Transport out of the lower stratospheric arctic vortex by rossby wave breaking. Journal of Geophysical Research: Atmospheres (1984–2012), 99(D1):1071–1088, 1994.

Matthew AH Wittman, Andrew J Charlton, and Lorenzo M Polvani. The effect of lower stratospheric shear on baroclinic instability. Journal of the atmospheric sciences, 64(2), 2007.

T Woollings, A Charlton-Perez, S Ineson, AG Marshall, and Giacomo Masato. Associations between stratospheric variability and tropospheric blocking. Journal of Geophysical Research: Atmospheres (1984–2012), 115(D6), 2010.

C. Zülicke and E. Becker. The structure of the mesosphere during sudden stratospheric warmings in a global circulation model. Journal of Geophysical Research: Atmospheres, 118(5):2255–2271, 2013.